High-Efficiency Organic Photovoltaics for Indoor and Outdoor Applications

Lin Xie, BEng. (Hons.), MSc (Merit)

Thesis submitted to the University of Nottingham for the
Degree of Doctor of Philosophy in Chemical Engineering

May 2023

ABSTRACT

With the rapid development of the economy, non-renewable resources such as fossil fuels and natural gas are being depleted. One solution to maintain sustainable development is to utilize solar energy, which can be harvested directly through photovoltaic (PV) technology to produce electricity. In recent years, organic solar cells (OSCs)/organic photovoltaics (OPVs) in the PV field have attracted more and more attention due to their advantages of low cost, flexibility, light weight, and large area producibility using roll-to-roll technology. They are a promising candidate for realizing environmentally-friendly and low-cost PV technology that can convert irradiance into electrical power.

In addition to utilizing sunlight that is only available outdoors, artificial light supplied indoors can also be collected and converted into electricity. As the market for IoT nodes (such as sensors, watches, calculators, remote controls, hearing aids, and monitors) used in relatively mild indoor environments rapidly grows, the demand for artificial light energy harvesters to supply continuous and cordless power for indoor environments has emerged. When the illuminance is switched from 1-sun to dim light, the PV technology that adopts organic material as the photon capture layer is called indoor organic photovoltaics (IOPVs).

However, achieving a breakthrough in energy transfer efficiency, whether in indoor or outdoor environments, is still a challenge. To address this challenge, the aim of this study is to improve the power conversion efficiency (PCE) of the OPVs system by designing novel molecules that can be applied under different spectra, optimizing processing technology, and studying the underlying principles of efficiency improvement. In summary, the study can be divided into three main parts:

The first part focuses on improving device performance that can be applied under both outdoor and indoor environments by designing a novel molecule resulting in a compromise absorption spectrum and studying the influence of different processing technologies under outdoor and indoor conditions. A novel asymmetric acceptor

TB-4Cl, modified from Y6, was designed and synthesized to create a trade-off absorption spectrum that can be applied under both artificial light and sunlight. Furthermore, processing technology optimization was carried out. Two different processing methods, conventional bulk-heterojunction (C-BHJ) and sequential deposition bulk-heterojunction (SD-BHJ), were compared to study their difference under sunlight and artificial light. The optimal devices of PM6:TB-4F produced PCE of 14.44% and 15.24% for C-BHJ and SD-BHJ, respectively, under the illumination of AM1.5. For 1000-lux LED illumination, devices showed PCE of 16.82% and 21.05% for C-BHJ and SD-BHJ, respectively. SD-BHJ showed comparable performance than C-BHJ under sunlight. However, the PCE was significantly increased by 25% for SD-BHJ compared to C-BHJ under artificial light because of the strong influence of trap-assisted recombination and dark current on PCE in the condition of low carrier density. Our result indicates that asymmetric molecule with blue-shifted spectrum fabricated by SD-BHJ can be a promising candidate to be applied in the indoor environment to harvest sunlight and artificial light simultaneously.

The second part focuses on improving the performance of IOPVs through the systematic modification of molecules to tune the intramolecular charge transfer (intra-CT) and intermolecular charge transfer (inter-CT) in order to achieve high PCEs under indoor environments. I carefully investigated the effects of asymmetric skeleton and non-chlorination on terminal groups by thoroughly evaluating the photovoltaic performance and analyzing the intra-CT and inter-CT processes. Two new acceptors with an A-$D_1A'D_2$-A structure were designed and synthesized to compare the performance of an asymmetric backbone with two specified end groups. At the condition of 1000-lux illumination, the TB-SCl acceptor with the halogenous end group, 2-(6-oxo-5,6-dihydro-4H-cyclopenta[c]thiophen-4-ylidene) molononitrile (1), coupled with PM6 acquired a PCE of 19.7%. The TB-S with non-halogenous end group, 2-(6-oxo-5,6-dihydro-4H-cyclopenta[b]thiophen-4-ylidene) molononitrile (2), blended with PM6 yielded a higher PCE of 23.3%. In comparison, symmetric molecule BTP-2ThCl only produced a low PCE of 14.6%. The results indicate that tuning the intra-CT and inter-CT processes through reducing a fused ring to form an asymmetric skeleton and increasing the electronic density of the end group, based on the Y6 series molecule, is an effective strategy to increase the PCE of IOPVs. And our investigation can provide molecular design guidance for IOPVs.

The final part of the study aims to investigate the correlation among the eigen-properties of asymmetric skeleton non-fullerene (ASNF) molecules, the morphology of the active layer, and the photovoltaic performance of ternary organic photovoltaic (OPV) devices. Two wider bandgap ASNF acceptors, named TB-S1 and TB-S1-O, were synthesized based on TB-S. These three ASNF molecules have similar skeletons but different terminal groups or alkyl/alkoxy side chains which were incorporated into the host system PM6:BTP-eC9 as a third component, respectively. Interestingly, all the binary OPV devices for ASNF acceptors produced significantly higher V_{OC} than that of the PM6:BTP-eC9 system (0.949-1.120 *vs.* 0.837 V), however, only incorporating TB-S1-O into the host system had a positive effect of V_{OC} improvement. The alkoxy substituted TB-S1-O showed a cascade energy level alignment, a good absorption complementarity and an excellent compatibility with PM6/BTP-eC9. Moreover, the PM6:BTP-eC9:TB-S1-O ternary film exhibited an ideal interpenetrating network, leading to reduced ΔE_{nonrad} and enhanced charge transfer. As a result, the PCE was increased from 17.36% (binary film) to 18.14% (ternary film) when TB-S1-O was blended into the PM6:BTP-eC9 system due to the increase in V_{OC} and J_{SC}. In contrast, the incorporation of TB-S and TB-S1 formed an inferior morphology and thus failed to reduce voltage losses, resulting in a poorer PCE of 16.16% and 16.18%, respectively. This work reveals that alkoxy substitution on asymmetric backbone is an efficient method to construct the third component for high-performance ternary organic solar cells.

PUBLICATIONS

(1) **L. Xie**, A.Lan, Q.Gu, S.Yang, W. Song, J. Ge, R. Zhou, Z.Chen, J. Zhang, X. Zhang, D. Yang, B. Tang, T. Wu, and Z. Ge, Alkoxy Substitution on Asymmetric Conjugated Molecule Enabling over 18% Efficiency in Ternary Organic Solar Cells by Reducing Non-Radiative Voltage Loss, ***ACS Energy Letter***, 8 (2022) 361-371[1]. (This work is related to the content of Chapter 6 with permission from ACS Energy Letter, 8 (2022) 361-371. Copyright, 2023, American Chemical Society).

(2) **L. Xie**, J. Zhang, W. Song, J. Ge, D. Li, R. Zhou, J. Zhang, X. Zhang, D. Yang, B. Tang, T. Wu, and Z. Ge, Rational tuning of intermolecular and intramolecular interactions enabling high-efficiency indoor organic photovoltaics, ***Nano Energy*** 9(2022)107414[2]. (This work is related to the content of Chapter 5 with permission from Nano Energy 9(2022)107414. Copyright, 2022, Elsevier).

(3) **L. Xie**, J. Zhang, W. Song, L. Hong, J. Ge, P. Wen, B. Tang, T. Wu, X. Zhang, Y. Li, and Z. Ge, Understanding the Effect of Sequential Deposition Processing for High-Efficient Organic Photovoltaics to Harvest Sunlight and Artificial Light, ***ACS Applied Materials & Interfaces*** 13(2021) 20405-20416 [3]. (This work is related to the content of Chapter 4 with permission from ACS Applied Materials & Interfaces 13(2021) 20405-20416. Copyright, 2021, American Chemical Society).

(4) **L. Xie**, W. Song, J. Ge, B. Tang, X. Zhang, T. Wu, and Z. Ge, Recent progress of organic photovoltaics for indoor energy harvesting, ***Nano Energy*** 82 (2021) 105770[4]. (This work is related to the content of Chapter 2 with permission from Nano Energy 82 (2021) 105770. Copyright, 2021, Elsevier).

(5) J. Ge, L. Hong, H. Ma, Q. Ye, Y. Chen, **L. Xie**, W. Song, D. Li, Z. Chen, K. Yu, J. Zhang, Z. Wei, F. Huang, and Z. Ge, Asymmetric Substitution of End-Groups Triggers 16.34% Efficiency for All-Small-Molecule Organic Solar Cells, ***Advanced materials*** (2022) 2202752.

(6) W. Song, K. Yu, J. Ge, ***L. Xie***, R. Zhou, R. Peng, X. Zhang, M. Yang, Z. Wei,

and Z. Ge, Entangled structure morphology by polymer guest enabling mechanically robust organic solar cells with efficiencies of over 16.5%, ***Matter*** 5 (2022) 1877-1889.

(7) D. Li, J. Wang, **L. Xie**, J. Ge, R. Zhou, Q. Gu, D. Yang, J. Zhang, and Z. Ge, Crystallinity modulation of donors by heteroatom side-chain engineering and solvent additive achieving 14.3% all-small-molecule organic solar cells, ***Journal of Materials Chemistry A*** 10 (2022) 9635-9642.

(8) X. Chen, J. Zhang, C. Liu, Q. Lou, K. Zheng, X. Yin, **L. Xie**, P. Wen, C. Liu, and Z. Ge, TADF Molecule as an Interfacial Layer with Cascade Energy Alignment Enabling High Open-Circuit Voltage for 3D/2D Perovskite Solar Cells, ***ACS Applied Energy Materials*** 4 (2021) 11112-11120.

(9) J. Wang, R. Peng, J. Gao, D. Li, **L. Xie**, W. Song, X. Zhang, Y. Fu, and Z. Ge, Ti3C2Tx/PEDOT:PSS Composite Interface Enables over 17% Efficiency Non-fullerene Organic Solar Cells, ***ACS Applied Materials & Interfaces*** 13 (2021) 45789-45797.

(10) W. Song, K. Yu, E. Zhou, **L. Xie**, L. Hong, J. Ge, J. Zhang, X. Zhang, R. Peng, and Z. Ge, Crumple Durable Ultraflexible Organic Solar Cells with an Excellent Power-per-Weight Performance, ***Advanced Functional Materials*** 31 (2021) 2102694.

(11) Z. Chen, W. Song, K. Yu, J. Ge, J. Zhang, **L. Xie**, R. Peng, and Z. Ge, Small-molecular donor guest achieves rigid 18.5% and flexible 15.9% efficiency organic photovoltaic via fine-tuning microstructure morphology, ***Joule*** 5 (2021) 2395-2407.

(12) Z. Xia, J. Zhang, X. Gao, W. Song, J. Ge, **L. Xie**, X. Zhang, Z. Liu, and Z. Ge, Fine-Tuning the Dipole Moment of Asymmetric Non-Fullerene Acceptors Enabling Efficient and Stable Organic Solar Cells, ***ACS Applied Materials & Interfaces*** 13 (2021) 23983-23992.

(13) J. Zhang, Y. Han, W. Zhang, J. Ge, **L. Xie**, Z. Xia, W. Song, D. Yang, X. Zhang, and Z. Ge, High-Efficiency Thermal-Annealing-Free Organic Solar Cells Based on an Asymmetric Acceptor with Improved Thermal and Air Stability, ***ACS Applied Materials & Interfaces*** 12 (2020) 57271-57280.

(14) J. Ge, L. Hong, W. Song, **L. Xie**, J. Zhang, Z. Chen, K. Yu, R. Peng, X. Zhang, and Z. Ge, Solvent Annealing Enables 15.39% Efficiency All-Small-Molecule Solar Cells through Improved Molecule Interconnection and Reduced Non-Radiative Loss, ***Advanced Energy Materials*** 11 (2021) 2100800.

(15) W. Song, Y. Liu, B. Fanady, Y. Han, **L. Xie**, Z. Chen, K. Yu, X. Peng, X. Zhang, and Z. Ge, Ultra-flexible light-permeable organic solar cells for the herbal photosynthetic growth, ***Nano Energy*** 86 (2021) 106044.

(16) J. Zhang, Q. Wei, N. Fei, M. Zhao, **L. Xie**, L. Cao, X. Zhang, G. Xie, T. Wang, and Z. Ge, Simple-Structured Blue Thermally Activated Delayed Fluorescence Emitter for Solution-Processed Organic Light-Emitting Diodes with External Quantum Efficiency of over 20%, ***ACS Applied Materials & Interfaces*** 13 (2021) 12305-12312.

(17) Y. Han, W. Song, J. Zhang, **L. Xie**, J. Xiao, Y. Li, L. Cao, S. Song, E. Zhou, and Z. Ge, Annealing-free efficient organic solar cells via an alkylbenzene side-chain strategy of small-molecule electron acceptors, ***Journal of Materials Chemistry A*** 8 (2020) 22155-22162.

(18) K. Yu, W. Song, Y. Li, Z. Chen, J. Ge, D. Yang, J. Zhang, **L. Xie**, C. Liu, and Z. Ge, Achieving 18.14% Efficiency of Ternary Organic Solar Cells with Alloyed Nonfullerene Acceptor, ***Small Structures*** 2 (2021) 2100099.

AUTHOR CONTRIBUTION

Lin Xie conceived the experimental design, device fabrication, modelling, and calculation by herself. Lin Xie did the following characterizations by herself: *J-V* test, exciton dissociation efficiency, EQE test, UV-vis test, charge mobility test, electrochemical workstation test, TEM, AFM, PL, contact angle measurement, surface thickness test, accurate incident light power measurement. Lin Xie designed and synthesized material with the assistances of Jinsheng Zhang. TPV/TPC test and Photo-CELIV were performed by Ling Hong. Energy loss measurement was carried out by Ai Lan. GIWAXS was tested by Jianqi Zhang, TOF-SIMS was performed by ceshigo Inc.

ACKNOWLEDGEMENT

First, I would like to express my sincere gratitude to all my supervisors, Prof. Bencan Tang, Prof.Tao Wu from the University of Nottingham, Ningbo China, and Prof. Ziyi Ge from Ningbo Institute of Materials Technology and Engineering, Chinese Academy of Sciences, for giving me a valuable supervision and providing constructive guidance and funding support throughout my research.

Many thanks to Dr. Daobin Yang, Dr. Ruixiang Peng, Dr. Chang Liu, Dr. Wei Li, Dr. Mengjing Yang, and Dr Lisa Xie as lead teachers in Chinese Academy of Sciences, who shared extensive knowledge of photovoltaics principles and synthesis knowledge to me.

I wish to acknowledge the valuable advice for my study and living during my PhD period provided by Jessica Wang from the graduate school, the University of Nottingham, Ningbo China, and Fang Yang and Yiling Chen from the graduate school, Ningbo Institute of Materials Technology and Engineering, Chinese Academy of Sciences.

Additionally, special shout out to my colleagues, Wei Song, Jinsheng Zhang, Jinfeng Ge for their great assistance and at every stage of my PhD research. We often discuss the problems related to the semiconductors and molecule synthesis. Without them, I cannot finish this thesis. I would like to thank my other colleagues in Chinese Academy of Sciences, Dandan Li, Jie Wang, Zhichuan Wang, Yuanyuan Meng, Rong Zhou, Qun Gu, Jiasen Zhang, Shixiao Bu, Zhenyu Chen, Liang Cao, Yufang Han, Bing Han, Zihao Xia, Shuncheng Yang, Hongqian Wang, Pengyu Yan, Qinrui Ye, Ruikun Cao, and Shuyuan Lin, for a treasured time spent together as a research team and in social settings. Many thanks to Ai Lan and Jingtao Zhu from the from the University of Nottingham, Ningbo China who assisted me to test voltage loss.

At the last, I would like to convey my heartfelt appreciation to my boyfriend Haochenzi Zhang, who encouraged and supported me to pursue this wonderful

journey. I am truly grateful to my parents, Zhimin Xie and Liuxi Qin, who always support me to chase my dream and always give me unconditional love. Their care and encouragement are my motivation to strive forward.

TABLE OF CONTENTS

LIST OF FIGURES

LIST OF TABLES

LIST OF ABBREVIATIONS

Abbreviation	Identification
λ	Wavelength
τ	The charge carrier lifetime
C	Light speed
$\eta_{\text{diss}}/\eta_{\text{coll}}$	Exciton dissociation /charge collection efficiency
h	Planck constant
A	Effective area
AFM	Atomic force microscopy
AM1.5	Air mass 1.5
ANF/ ASNF (A-D_1A'D_2-A)/ ATNF(A_1-DA'D-A_2)	Asymmetric non-fullerene/ asymmetry skeleton typed non-fullerene/ asymmetry terminal typed non-fullerene
BHJ/C-BHJ	Bulk heterojunction, conventional bulk heterojunction
CA	Contact angles
CFL	Compact fluorescent lamps
CV	Cyclic voltammetry

DFT	Density functional theory
e	Elementary charge
E_Λ	Light power spectrum
E_{ox}	Oxidation potential
EQE	External quantum efficiency
E_{red}	Reduction potential
E_{Fn}	Electron quasi-Fermi levels
E_{Fp}	Hole quasi-Fermi levels
EFTEM	Energy-filter TEM
E_{g}	Optical bandgap
ETL	Electron transport layers
ESP	Molecular electrostatic potential
f_{whm}	Full width at half maxima
FF	Fill factor
GIWAXS	Grazing-incidence wide-angle X-ray scattering
HOMO	Highest occupied molecular orbital
I_0	Reverse dark saturation current

Intra-CT/inter-CT	The intramolecular charge transfer / intermolecular charge transfer
IoTs	Internet of Things
IOPVS	Indoor organic photovoltaics
IP	In plane profiles from GIWAXS
I_{Ph}, $I_{\mathrm{Ph,sun}}$ And $I_{\mathrm{Ph,room}}$	Photocurrent, photocurrents under AM1.5, indoor illuminance conditions
IPV	Indoor photovoltaics
k	Boltzmann constant
P_{in}, P_{out}, P_{Room},P_{Sun}	Input power, Output power, illuminance intensity under indoor environment, the illuminance power of solar spectrum without infrared region
PCE	Power conversion efficiency
P(E,T)	Exciton dissociation efficiency or probability

PET	Polyethylene terephthalate
Photo-CELIV	The photo-induced charge-carrier extraction in a linearly increasing voltage
PL	Photoluminescence
PSCs	Perovskite Solar Cells
PVs	Photovoltaics
q	Elementary charge
TPV/TPC	Transient photovoltage measurement/ transient photocurrent measurement
J_0/ J_{mp}/J_{max} /J_{ph}/ J_{light}/ J_{dark}/ J_{sat}	Reverse saturation current density/current at the point of maximal output power/maximal current/ photocurrent/the current under AM1.5 illumination/ the current under dark condition/the saturation current density
J_{SC}	Tested short circuit current density
J_{cal}	Calculated short circuit current density

L_C	The coherent lengths
LEDs	Light-emitting diodes
LUMO	Lowest Unoccupied Molecular Orbital
n	The ideality factor (assumption as 1)
$N_\Lambda(\Lambda)$	Photon flux spectrum
NMR	Nuclear magnetic resonance
OOP	Out of plane profiles from GIWAXS
OPVs	Organic photovoltaic cells
OSCs	Organic solar cells
R_S	Series resistance
R_{sh}	Shunt resistance
RMS	Root-mean-square
SCLC	Space-charge-limited-current
SD	Sequential deposition
SVA	Solvent annealing
t	Time
T	Cell temperature
TA	Thermal annealing
TEM	Transmission electron microscope

TOF MS	Spectroscopy and time-of-flight mass spectrometry
TOF-SIMS	Time-of-flight secondary ion mass spectrometry
V	Photovoltage
V_{mp}	Voltage at the point of maximal output power
V_{OC}	Open circuit voltage
V_{loss}	Voltage loss
V_{eff}	Is defined as V_0 -V, where V_0 is the voltage when J_{ph}=0, and V is the applied bias voltage

LIST OF CHEMICAL NAMES

Abbreviation	Identification
Al	Aluminum
BDT	Benzodithiophene
BTA	Benzotriazole
BTP-eC9	2,2'- [[12,13-Bis(2-butyloctyl)-12,13-dihydro-3,9-dinonylbisthieno[2'',3'':4',5']thieno[2',3':4,5]pyrrolo[3,2-e:2',3'-g][2,1,3]benzothiadiazole-2,10-diyl]bis[methylidyne(5,6-chloro-3-oxo-1H-indene-2,1(3H)-diylidene)]]bis[propanedinitrile]
BTR	Benzodithiophene terthiophene rhodanine
CB	Chlorobenzene
CF	Chloroform
CN	Chloronaphthalene
Cl	Chlorine
CN-PPV	Poly(2,5,2',5'-tetrahexyloxy-8,7'-dicyano-di-p-phenylene vinylene
DR3TBDTT	(5z,5'e)-5,5'-(((4,8-bis(5-(2-ethylhexyl)thiophen-2-yl)benzo[1,2-b:4,5-b']dithiophene-2,6-diyl)bis(3,3''-dioctyl-[2,2':5',2''-terthiophene]-5'',5-diyl))bis(methaneylylidene))bis(3-ethyl-2-thioxothiazolidin-4-one)

F	Fluorine
H	Hydrogen
ICBA	Indene-C60 bisadduct
IDIC	2,2'-((2Z,2'Z)-((4,4,9,9-tetrahexyl-4,9-dihydro-s-indaceno[1,2-b:5,6-b']dithiophene-2,7-diyl)bis(methanylylidene))bis(3-oxo-2,3-dihydro-1H-indene-2,1-diylidene))dimalononitrile
IO-4Cl	3,9-bis[5,6-dichloro-1H-indene-1,3(2H)dione]-5,5,11,11-tetrakis(4-hexylphenyl)-dithieno[2,3-d:2',3'-d']-s-indaceno[1,2-b:5,6-b']dithiophene
ITIC	3,9-bis(2-methylene-(3-(1,1-dicyanomethylene)-indanone))-5,5,11,11-tetrakis(4-hexylphenyl)-dithieno[2,3-d:2’,3’-d']-s-indaceno[1,2-b:5,6-b’]dithiophene
ITIC-4F/IT-4F	3,9-bis(2-methylene-((3-(1,1-dicyanomethylene)-6,7-difluoro)-indanone))-5,5,11,11-tetrakis(4-hexylphenyl)-dithieno[2,3-d:2’,3’-d’]-s-indaceno[1,2-b:5,6-b’]dithiophene
ITIC-Th	3,9-bis(2-methylene-(3-(1,1-dicyanomethylene)-indanone))-5,5,11,11-tetrakis(5-hexylthienyl)-dithieno[2,3-d:2’,3’-d’]-s-indaceno[1,2-b:5,6-b’]dithiophene
ITO	Indium tin oxide

MEH-PPV	Poly[2-methoxy-5-(2-ethylhexyloxy)-1,4-phenylenevinylene
MgPc	Magnesium phthalocyanine
N3	2,2'-((2Z,2'Z)-((12,13-bis(3-ethylheptyl)-3,9-diundecyl-12,13-dihydro-[1,2,5]thiadiazolo[3,4-e]thieno[2",3":4',5']thieno[2',3':4,5]pyrrolo[3,2-g]thieno[2',3':4,5]thieno[3,2-b]indole-2,10-diyl)bis(methanylylidene))bis(5,6-difluoro-3-oxo-2,3-dihydro-1H-indene-2,1-diylidene))dimalononitrile
P3HT	Poly(3-hexylthiophene-2,5-diyl)
P3HOT	Poly(3-hexyloxythiophene)
PBDB-T	Poly[(2,6-(4,8-bis(5-(2-ethylhexyl)thiophen-2-yl)-benzo[1,2-b:4,5-b’]dithiophene))-alt-(5,5-(1’,3’-di-2-thienyl-5’,7’-bis(2-ethylhexyl)benzo[1’,2’-c:4’,5’-c’]dithiophene-4,8-dione)]
$PC_{61}BM$	[6,6]-Phenyl-C61-butyric acid methyl ester
$PC_{71}BM$	[6,6]-Phenyl-C71-butyric acid methyl ester
PCDTBT	Poly[N-9′-heptadecanyl-2,7-carbazole-alt-5,5-(4′,7′-di-2-thienyl-2′,1′,3′-benzothiadiazole)]
PDINO	3,3'-(1,3,8,10-Tetraoxoanthra[2,1,9-def:6,5,10-d'e'f']diisoquinoline-2,9(1H,3H,8H,10H)-diyl)bis(N,N-dimethylpropan-1-amine oxide)

PDTBTBZ-2Fanti	Poly[(5,6-bis(2- hexyldecyloxy)benzo[c][1,2,5]thiadiazole-4,7-diyl)-alt-(5,5'-(2,5-difluoro-1,4-phenylene)bis(thiophen-2-yl))]
PDTSTPD	Poly[2,6-(4,4'-bis(ethylhexyl)dithieno[3,2-b:2',3'-d]silole)-alt- (1,3-(5-octyl-4H-thieno[3,4-c]pyrrole-4,6(5H)-dione))]
PFN	Poly[(9,9-bis(3'-(N,N-dimethylamino)propyl)-2,7-fluorene)-alt-2,7-(9,9–Dioctylfluorene)]
PEDOT:PSS (4083) or 4083	Poly(3,4-ethylenedioxythiophene)-poly(styrenesulfonate) for HTL application
PEDOT:PSS (PH1000)	Poly(3,4-ethylenedioxythiophene)-poly(styrenesulfonate) for FTE application
PM6	Poly[(2,6-(4,8-bis(5-(2-ethylhexyl-3-fluoro)thiophen-2-yl)-benzo[1,2-b:4,5-B’]dithiophene))-alt-(5,5-(1’,3’-di-2-thienyl-5’,7’-bis(2-ethylhexyl)benzo[1’,2’-c:4’,5’-c’]dithiophene-4,8-dione)]
PPDT2FBT	Poly[(2,5-bis(2-hexyldecyloxy)phenylene)-*alt*-(5-fluoro-4,7-di(thiophen-2-yl)benzo[*c*][1,2,5]thiadiazole)] (PPDTFBT) and poly[(2,5-bis(2-hexyldecyloxy)phenylene)-*alt*-(5,6-difluoro-4,7-di(thiophen-2-yl)benzo[*c*][1,2,5]thiadiazole)]

PTB7	Poly[[4,8-bis[(2-ethylhexyl)oxy]benzo[1,2-b:4,5-b']dithiophene-2,6-diyl][3-fluoro-2-[(2-ethylhexyl)carbonyl]thieno[3,4-b]thiophenediyl]]
PTB7-Th	Poly[4,8-bis(5-(2-ethylhexyl)thiophen-2-yl)benzo[1,2-b;4,5-b']dithiophene-2,6-diyl-alt-(4-(2-ethylhexyl)-3-fluorothieno[3,4-b]thiophene-)-2-carboxylate-2-6-diyl)]
S	Sulphur
Si	Silicon
SiO_2	Silicon dioxide
TOL	Toluene
Y6	2,2'-((2Z,2'Z)-((12,13-bis(2-ethylhexyl)-3,9-diundecyl-12,13-dihydro-[1,2,5]thiadiazolo[3,4-e]thieno[2",3’':4’,5']thieno[2',3':4,5]pyrrolo[3,2-g]thieno[2',3':4,5]thieno[3,2-b]indole-2,10-diyl)bis(methanylylidene))bis(5,6-difluoro-3-oxo-2,3-dihydro-1H-indene-2,1-diylidene))dimalononitrile

CHAPTER 1

Introduction

1.1 Background

As the economy continues to advance at a breakneck pace, non-renewable resources such as fossil oil and natural gas are gradually dwindling. Consequently, renewable energy sources like wind power, tidal energy, solar energy, and geothermal energy have emerged as highly efficient alternatives for meeting our energy needs and ensuring an abundant supply of power. Studies show that solar energy is internationally recognized ideal alternative energy source, which can be directly utilized by human without restriction of facilities and locations. Solar energy as the inexhaustible ideal energy has overwhelming advantages compared with other renewable energies: (1) The solar energy barely decay. The irradiation from sun to the earth is over 80 million kW/s, which is high enough for the usage of all mankind. (2) The geographical distribution of solar energy is wide, and its utilization is convenient. (3) The solar energy is 100% clean energy, which is friendly to the environment and is sustainable to the earth.

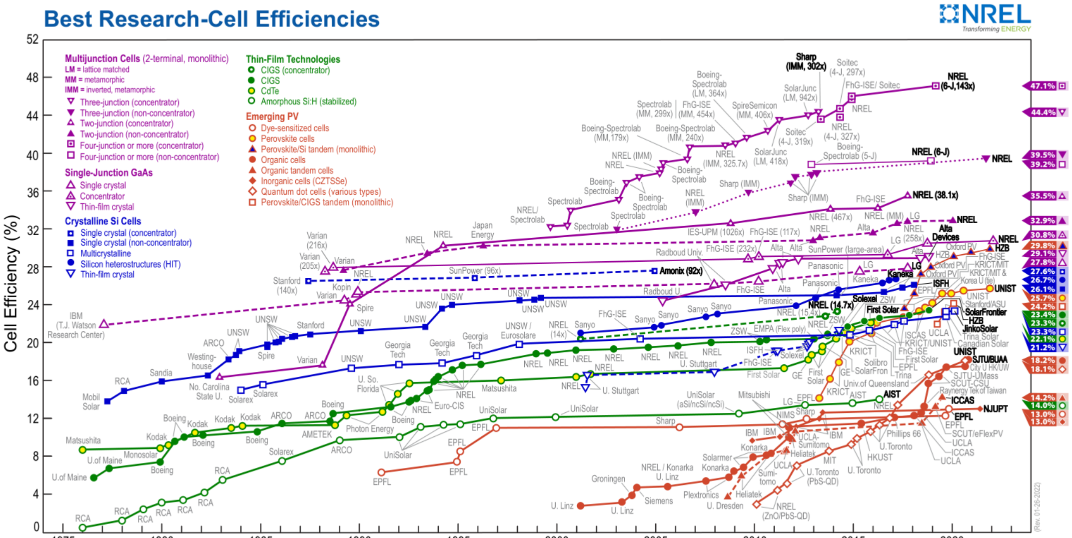

Figure 1.1. NREL maintains a chart of the highest confirmed conversion efficiencies for research cells for a range of photovoltaic technologies, plotted from 1976 to the present[5].

According to National Renewable Laboratory (NREL), photovoltaics includes five types: crystalline Si cells, single-junction GaAs, multijunction cells, thin-film technologies, and emerging PV. The highest conversion of different photovoltaics technologies has been summarized in **Figure 1.1**.

The first generation of solar cells are silicon-based, and they can be either monocrystalline or polycrystalline. These solar cells' extraordinary efficiency of over 22% and excellent longevity of 25 years make them the most developed PV technology currently available[6]. However, in order to achieve such high efficiency, the production of these solar cells calls for a comprehensive purification process and a thicker silicon absorption layer, which adds to the high energy usage and production expense. As a result, many potential substitutes for first-generation solar cells are being researched and produced.

Cadmium telluride (CdTe), and copper indium gallium selenide (CIGS) are the main types of thin-film solar cells that make up the second generation of solar cells[7]. These solar cells are substantially more affordable and capable of superior absorption even with a thin photoactive layer than their predecessor. Due to their increased efficiency and use of the heavy chemical cadmium, CdTe, solar cells show higher performance for next-generation PV technology. However, they pose several environmental risks. Although CIGS solar cells may efficiently absorb sunlight in a much thinner photoactive layer, it is important to consider the rarity and toxicity of indium and gallium.

The third generation of solar cells, which includes organic solar cells (OSCs) and perovskite solar cells, is the most recent innovation in the PV sector. These solar cells could eventually replace the first-generation silicon-based solar cells on the market. Most third-generation solar cells are now still in the development stage as researchers look for the ideal combination of cost, lifetime, and efficiency to outperform the first two generations. They have advantages of low cost, flexibility, light weight, and roll to roll large area producibility, which is a promising candidate to transfer irradiance to electrical power in the future[8-12]. Within the third generation of solar cell, perovskite solar cells (PSCs) show higher performance, better stability, and lower cost than organic solar cell. For instance, OSCs have a power conversion efficiency (PCE) above 18% and PSCs have a maximum possible PCE of 25.2%.

However, the theoretical value defined by the Shockley-Queisser (S-Q) model, which is based on the principle of detailed balance equating the photon flux into a device to the particle flux (photons or electrons) out of that device, limits the maximum achievable PCEs of various single-junction solar cells. According to this S-Q framework, photovoltaic semiconductors are unable to absorb photons with energies below their bandgaps (Eg), and photons with energies beyond their bandgaps also suffer from partial energy loss as a result of the thermalization of charge carriers, leaving around 45% of solar energy available for photovoltaic devices. The maximum possible V_{OC} are typically below their bandgaps if radiative recombination is assumed to be the only kind of charge recombination that devices may undergo because doing so is necessary for them to reach thermodynamic equilibrium. According to Shockley-Queisser limit, the ideal bandgap for the ideal bandgap energy for an AM1.5 is around 1.34 eV generating the maximum PCE of 33.7%[13]. Compared with perovskite, organic materials possess advantage that their bandgaps are tunable by modifying molecular structures leading to a desire bandgap that close to 1.34 eV. Moreover, OSCs can continuously optimize their morphology to enhance exciton dissociation and carrier transfer to inhibit non-radiative recombination. Therefore, OSCs have irreplaceable advantage which attract a lot of attentions.

Indoor artificial light can also be utilized as an energy source by the same device structure used for solar energy. As the market of IoT (Internet of Thing) nodes (e.g., sensors, watches, calculators, remote control, hearing aid, and monitors) used in relatively mild indoor environment rapidly grows, the demand of artificial light energy harvesters to supply continuous and cordless power for indoor environment has emerged. Therefore, OPVs can efficiently convert not only solar energy but also artificial illumination provided that the absorption spectrum of organic material appropriate covers according illuminated spectrum. Recently, with the continuous development and optimization for OPVs, the PCE of single junction has exceeded 19.17% under 1-sun illumination[14]. For the indoor energy harvesters, the highest organic indoor photovoltaic cell has exceeded the PCE of 30.89% under the 3000-lux LED[15].

To further improve the PCE of OPVs, three limitations must be addressed: (1) active materials do not have suitable absorption spectra, resulting in inadequate utilization of the emission spectrum of light sources (photons); (2) OPVs experience severe voltage loss due to non-radiative recombination; and (3) the inefficiency of exciton dissociation and free carrier transport leads to bimolecular recombination and trap-induced recombination. To overcome these issues, firstly, novel molecules should be designed and synthesized to fully absorb the photons of the irradiative spectra, and narrow bandgap materials should be synthesized for solar energy applications. Whereas wide bandgap material should be carried out when the light source is switched from solar illumination to artificial illumination. Secondly, new processing technology or ternary strategy are adopted to mitigate the non-radiative loss and enhance carrier transport, which can facilitate resulting in better morphology and thus achieving mitigated voltage loss and carrier recombination[12, 16].Thirdly, ternary strategy is treated as easy and direct method to improve PCE. Through doping the third active material, the photon absorption ability is enhanced due to the complementary absorption spectrum to harvest more photons. Moreover, the morphology of devices can be also optimized through doping the third material so that the extraction of carriers and devices stability are improved at the same time.

This chapter will summarize the work principles, rules to achieve high performance, and challenges of organic photovoltaics applied under outdoor and indoor environment, respectively. Based on the briefly introduction of photovoltaics, the aim and objective of my works to improve the performance of OPVs will be proposed.

1.2 Organic photovoltaics applied under outdoor environment

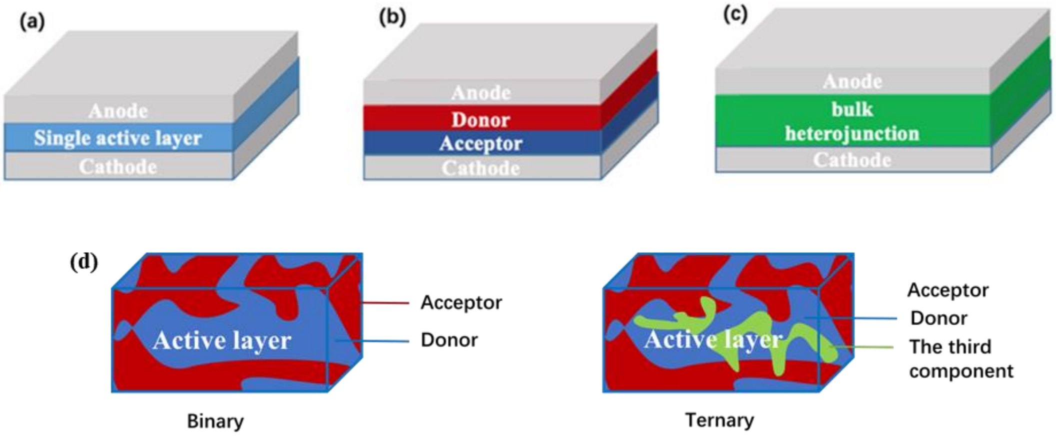

Figure 1.2. (a) single layer organic solar cells. (b) double layers organic solar cells. (c) bulk heterojunction organic solar cells. (d) binary and ternary system diagrams.

Tracing back to 1958, as shown in **Figure 1.2a**, the earliest OSCs of single layer structure were made of MgPc dye by Kearns and Calvin[17] which had lots of traps during excitons dissociation, resulting in ultra-low PCE. Over the next two decades, there was little innovation in the field of organic solar cells. In 1986, the breakthrough was made by Dr. Deng Qingyun of Kodak[18]. Organic materials used in OSCs were mainly organic dyes with high visible light absorption efficiency. Deng applied the idea of P-N junction of inorganic solar cells into the organic solar cell, fabricating a new structure of cells: double layer heterojunction (displayed in **Figure 1.2b**). Copper phthalocyanine acted as donor and tetra aryl perylene acted as acceptor, which had the PCE approaching 1%. Although the progress of OPVs still lag behind silicon-based solar cells, the bilayer structure was a successful idea, which brought new hope for the research of OSCs. Up to now, the structure of the two-layer heterojunction is still one of the focuses in the research of OSCs.

Later, based on the bilayer heterojunction structure, bulk heterojunction structure as shown in **Figure 1.2c** emerged. The concept of “hybrid heterojunction” is mainly aimed at solving the limitations of exciton separation and carrier transport in the photoelectric conversion process. In a double layer solar cell, excitons can only be separated in the interface region even though the interface between the two layers of organic material has a large area. Excitons generated far away from the interface often recombine before they diffuse to the interface. Moreover, due to low carrier mobility of organic materials, carrier which dissociate at the interface easily recombine during moving towards the electrode. Long diffusion length and low carrier mobilities limit the photoelectric conversion efficiency of double layer structure which can be solved by bulk heterojunction (BHJ). The so-called “mixed heterojunction” is to mix the donor material and the acceptor material, through co-evaporation or spin-coating method to make a mixed film. The donor and acceptor form a single region in the mixing film, and excitons produced at any location can diffuse to the interface in a short distance between the donor and acceptor, thus improving the efficiency of charge dissociation. At the same time, the electrons and holes formed at the interface can also reach the electrode in a shorter length, to complement the shortage of low carrier mobility. Hence, BHJ structure attracted more and more researchers’ attention in recent years. BHJ can be classified into two categories: binary and ternary systems. Binary systems comprise a donor and an acceptor material. The donor absorbs light and donates electrons to the acceptor material, which then transports the electrons to the electrode to generate an electric current. Ternary systems include a donor material, an acceptor material, and a third component, which can be a small molecule or a polymer. The third component functions as a bridge between the donor and acceptor materials, facilitating exciton dissociation and charge transfer, thereby improving the efficiency and stability of OPVs.

As shown in **Figure 1.3**, the photoelectric properties of OPVs are evaluated by four parameters, which are V_{OC} (the open circuit of voltage), J_{SC} (current density in the condition of short circuit), *FF* (fill factor), and PCE (power conversion efficiency).

(1) J_{SC} is the current density when extra electric field is equal to zero. J_{SC} depends on the number of photon absorption, the efficiency of exciton dissociation, and the efficiency of carriers’ transportation and extraction. One of the most efficient

strategies to improve the J_{SC} is adopting suitable materials of both donors and acceptors to cover the spectrum of light source.

(2) V_{OC} is the voltage when current equals zero. In other words, when external electric field is equal to built-in electric field, free carriers in the active layer are all recombined.

(3) $FF = J_{mp} \times V_{mp}/J_{SC} \times V_{OC}$, which represents the ratio between the maximal output power and the product of short circuit current density multiplied by open circuit voltage. *FF* is decided by the competition between the carriers' collection and recombination. Recombination mechanisms comprise bimolecular recombination and trap-induced recombination (Shockley-Read-Hall). The trade-off between the phase separation and crystallinity is an effective way to generate interpenetrating network morphology and thus increase the *FF*. There are several processing methods to optimize the morphology of active layers, such as solvent annealing (SVA), thermal annealing (TA), sequential deposition (SD), additive type, solution concentration, and dissolving temperature et.al.

(4) PCE describes the maximal output power divided by the input power, that is PCE = $J_{\mathrm{SC}} \times V_{\mathrm{OC}} \times FF/P_{\mathrm{in}}$. The better PCE means the higher photon utilization. The P_{in} for 1-sun illumination is 100 mW cm^{-2}.

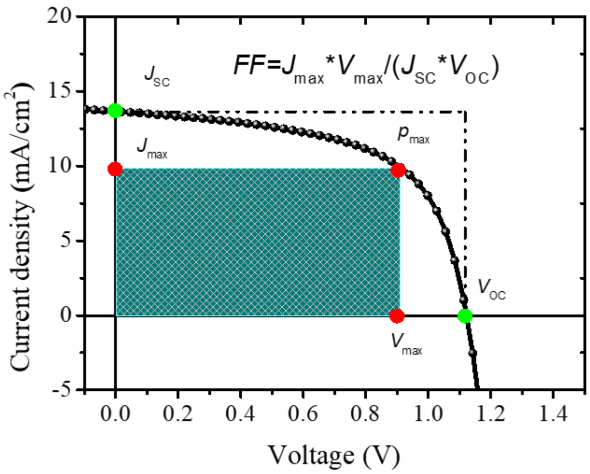

Figure 1.3. The parameters are used to evaluate the photoelectric properties of OPVs.

1.3 Indoor organic photovoltaics

Clean energy plays a significant role to replace gradually exhausted non-renewable energy resources, such as fossil fuel, thus, unprecedented demand for energy harvesting technologies utilizing sustainable energy has been reported[19-22]. Various solar power harvesters that convert solar energy to power have attracted dramatically attention nowadays. Among abundant types of PVs, OSCs have unique advantages including tunability of energy level, flexibility, low-cost, transparency, light weight, and large-area roll to roll processability [23-25]. These advantages make the prospects of OSCs surpass traditional silicon-based solar cells in the near future[26]. In laboratory, standard testing condition (AM1.5) that simulates the spectrum of the sun with an intensity of 100 mW cm^{-2} is universally adopted to evaluate the photoelectric properties of OSCs[27].

However, photovoltaic technologies can be used not only for outdoor applications, such as traditional solar plants, household rooftop solar systems, public lighting, solar-powered transportation, but also for indoor devices to utilize indoor light sources comprising wearable solar technology, portable electronics, and the IoTs as described in **Figure 1.4a** [28-30] . The definition of IoTs is automatically wireless communication between unique identifiers of things (various electronic devices) via internet. Real time data and digital information can be collected and exchanged through terminal devices, sensors, health monitors, and so on, which are adopted for smart home, factories, retail sectors and wearable technology. This huge number of applications which are independent and off-the-grid require abundant power supplier to operate. To replace non-self-rechargeable batteries that drive indoor applications at intervals is non-automatic and unintelligent. Therefore the successive power supplement via indoor photovoltaics (IPVs) which harvest energy from ambient lighting source is necessary in the near future[31]. Numerous studies about IPVs have been carried out. The photoelectric properties of IPVs are evaluated by four parameters, which are V_{OC}, J_{SC}, FF, and PCE, which are exactly same with OSCs (explained in **section 1.2.1**). The artificial indoor lighting sources include light-emitting diodes (LEDs), compact fluorescent lamps (CFL), halogen lamps, and incandescent light bulbs. The spectra of differently and frequently used dim lights are illustrated in **Figure 1.5**. The optical spectra for indoor light sources are mainly distributed from 400 nm to 750 nm, which are similar to the visible spectrum region of human eyes. The detail spectrum is dependent on the specific light source, color rendering and intensity.

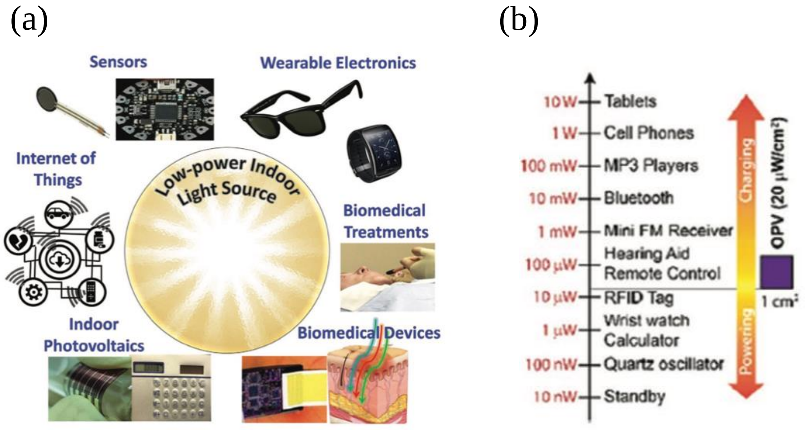

Figure 1.4. (a) Devices acquire power from indoor photovoltaics under dim lighting conditions [32]. Copyright 2018, Wiley. (b) Electrical energy requirements for various application devices supplied by a 1 cm^2 IPV cell under indoor lighting conditions[32]. Copyright 2018, Wiley.

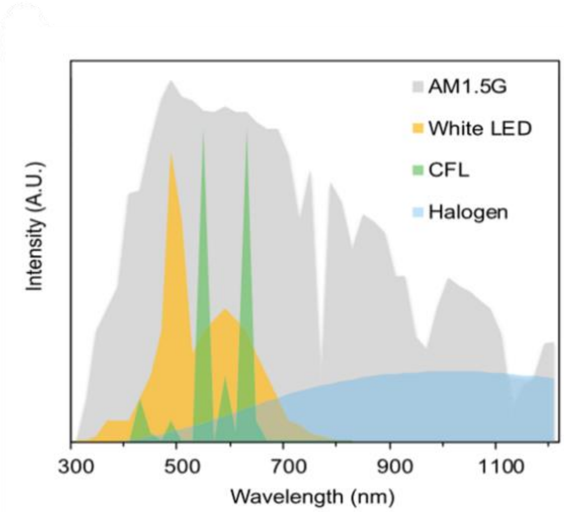

Figure 1.5. Output spectra of different indoor light sources: AM1.5 (grey), white LED (orange), CFL (green), halogen (blue) [31]. Copyright 2019, ScienceDirect.

The promising and rising market for IPVs by utilizing the micro energy derives from the huge demand for energy-autonomous applications. In 2017, the business market for IPVs was only \$ 140 million, which was far below \$ 100 billion-market for solar power devices. However, the quickly rising demand of IPVs for indoor applications boosts the market growth, and the global market for annual IPVs is predicted to be over \$ 850 million by 2023 and has the potential to keep growing in the following years[31].

There are a few studies of IPVs, comprising indoor organic photovoltaics (IOPVs) [33, 34], crystallized Si cells [35, 36], dye-sensitized solar cells [33, 34], PSCs [37, 38], and III–V compound semiconductor cells-GaAs[32, 35]. IOPVs possess outstanding properties of readily tunable chemistry and physics. Crystalline silicon cells[39, 40] and perovskite cells[41, 42] are more efficient than organic and dye-sensitized cells under outdoor condition but show lower performance compared with IOPVs under indoor conditions. In contrast to dye-sensitized material, organic materials possess advantages of more cost-efficiency, large-area producibility and these advantages lead to an advanced stage as a near commercial technology. **Figure 1.4b** illustrates the low power requirements for various indoor wirelessly interconnected devices supplied by a 1 cm^2 IPV cells, which prove that IPVs are promising candidates to harvest energy under weak light conditions. For example, the PCE of IOPVs so far is around 30% with the input power of 0.5021 mW cm^{-2}, hence, the output power is equal to ca. 150 μW cm^{-2} which is adequate to drive many electronic applications [15].

1.4 Key challenges

Since the first report about three decades ago, OPVs have been treated as a promising third-generation solar technology due to their advantages of light weight, cheap, flexibility, roll-to-roll producibility, and semi-transparency. The above-mentioned advantages just complement the shortage of traditional silicon solar cells. However, efficiency, lifetime and production cost are the three major obstacles that hinder large-scale production and the commercialization of OPVs[6]. To address these obstacles, a great attention focuses on the development of high-efficiency, stable, and easy-processing and cost-effective technology. According to Shockley-Queisser limit, the ideal bandgap for the ideal bandgap energy for an AM1.5 is around 1.34 eV generating the maximum PCE of 33.7% and for an indoor light source is around 1.9 eV producing the maximum PCE of 60%. According to the latest reports, the maximum PCE has exceeded 19.17%[43-45] under the illumination of AM1.5 and 29.4% under 1000-lux LED illumination[46].

The extraordinary progress in OPVs depends on the continuously emerging new materials, innovative device fabrication technologies, and the reveal of connection among film morphology, molecular packing, and photoelectric properties. How to further improve PCE of OPVs to close to Shockley-Queisser limit, some challenge should be solved.

(1) Novel non-fullerene molecule skeleton should be designed. Although Y6 and its derivatives as key materials have made remarkable breakthrough in efficiency, the minor changes such as replacing alkyl chain and terminal group usually results in limited improvement. Hence, radical change should be provided such as new skeleton, such as asymmetric skeleton acceptors.

(2) Having a comprehensive comprehension of the interrelation among "structure-property-performance" is crucial. At present, the discovery of high-efficiency molecules is frequently the result of chance. Besides, there is a pressing need to develop ternary strategies for material design. Ternary strategy is a feasible way to further increase PCE of OPVs by simply adding the third material into the host materials. Most third component incorporated host system result in reduced PCE. Only by characterizing effective devices can the reason for the performance enhancement be inferred. However, the process of screening for high-efficiency molecules can be time-consuming for researchers. Hence, providing guidance on the design and selection of appropriate molecules for the active layer is crucial.

Recently, there has been a rise in low-power off-grid applications that are connected to the internet, and this has led to a significant increase in the scale of IPVs markets. In this context, IOPVs technology as branch of OPVs is a promising contender for entering the IPVs market in the near future. Besides the challenge of OPVs discussed above, there are some development guidance for IOPVs.

(1) Lack of mechanism study on how to achieve highly efficient IOPVs when the illuminance is switched from 1-sun to dim light.

(2) Appropriate wide bandgap material design: the maximum theoretical PCE of IOPVs under indoor conditions is approximately 60%, which is significantly higher than that of silicon-based photovoltaics. However, the obtained PCE for IOPV so far is only approaching 30%. Therefore, wide bandgap acceptor should be carried out so that the emission spectrum of light source can be well covered by the absorption spectrum of active layer and active layer can generate high V_{OC}. Moreover, less trap mediated recombination and minimum V_{loss} are also necessary to achieve high performance under indoor environment.

(3) Inaccurate measurement of incident power: As recent progress about IOPVs summarized before, the light sources, illumination, color temperature, and apparatus that meter the incident emission power have not been uniformed and regulated. In other words, there is no generally accepted standards like solar cells to evaluate the performance of IOPVs. Therefore, it is not easy to directly compare their efficiency and performance. Hence, it is urgent to develop a standard system to measure the photoelectric properties of IOPVs. Considering capital expenditure of manufacturers, the economical mode to produce IOPVs is essential to ensure low cost for production in small volume. Moreover, as a higher PCE may be achieved under a stronger indoor light intensity, a large proportion of work about IOPVs adopts an incident intensity above 1000 lux. However, only commercial venues or hospitals use illuminance above 1000 lux which is not common in most of the buildings, therefore, a lower intensity ranging from 200-500 lux is recommended for

general places and is more suitable for the evaluation of IOPVs.

1.5 Aim and Objectives

Briefly, to speed up the commercialization of OPVs, the device's performance should be improved to fulfill the requirement of market and the PCE of OPVs should be at least comparable to Si-based PVs (18.5%-26%). Reviewing the development of OPVs, three general approaches have been adopted to improve OPVs' performance, namely material design (e.g., design, modification, and synthesis of novel organic material used as active layer to absorb photon), morphology control (e.g., morphology control of photoactive layer through different processing methods and the third material doping etc.) and device engineering (e.g., modification of electrode layer, interfacial layer, or photoactive layer). Among these approaches, the novel molecule design contributes the most to improve the performance of OPVs. For morphology and device engineering, their improvement is based on the threshold of performance produced by active material used. Therefore, to realize performance of OPVs enhancement, the aim of this research focuses on design and synthesis of novel molecules coupled with morphology control. Herein, a series of asymmetric non-fullerene acceptors, the derivatives of Y-series, are designed and synthesized to achieve high-efficiency organic photovoltaics for indoor and outdoor applications, respectively. Furthermore, the processing technology is conducted to further improve devices' performance. Moreover, ternary strategy is adopted to further improve the performance of chosen host system and the "structure-property-performance" correlation is investigated.

The aims and objectives of this research are:

i) Novel molecules design to utilize sunlight and artificial light: a series of asymmetric non-fullerene acceptors, the derivatives of Y-series, are designed and synthesized to achieve high-efficiency organic photovoltaics for indoor and outdoor applications, respectively. Y-series possess the structure of A-DA'D-A. The modification focuses on central core, donor moiety, terminal groups, and alkyl side chains. Herein, 5 novel molecules based on asymmetric non-fullerene acceptors are obtained (shown in **Figure 1.6**).

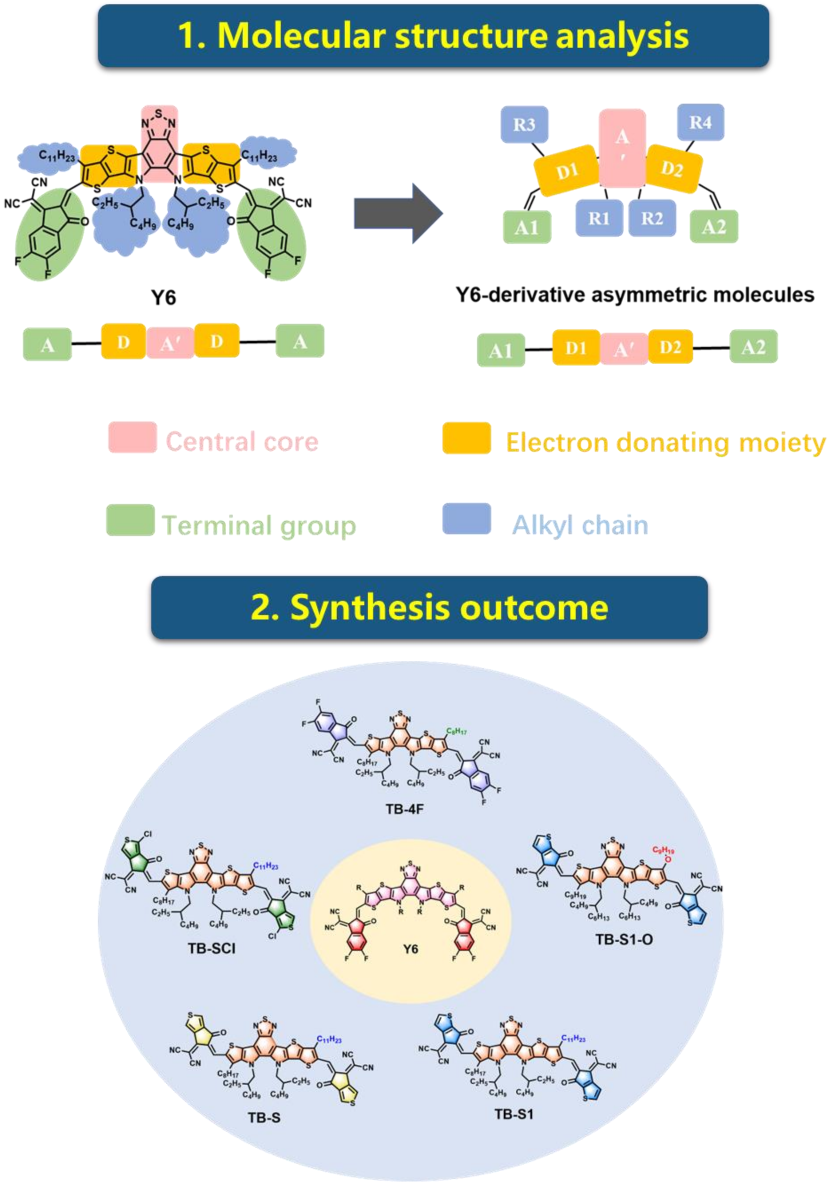

Figure 1.6. Molecular structure design and aimed acceptor design.

ii) The processing technology is conducted to further improve devices' performance. To explain the mechanism of how to achieve highly efficient

IOPVs when the illuminance is switched from 1-sun to dim light through studying V_{loss}, trap state, carrier recombination mechanism, dark current density, and different processing technologies (sequential deposition bulk-heterojunction (SD-BHJ) and conventional bulk-heterojunction (C-BHJ)).

iii) To thoroughly understanding the “structure-property-performance” correlation via molecular design in the ternary strategy section.

1.6 Outline of Thesis

The outline of this thesis will be discussed in brief as shown in the following:

Chapter 1 introduces the background and objectives of this study. It basically states what is OPVs, why do OPVs have advantages in PV markets, how do OPVs work, the research gap of this field, and aim of this research to readers. In the scope of OPVs, IOPVs is a novel research branch in OPVs, which attracts more and more attention recently as the market of IoT nodes used in relatively indoor environment rapidly grows. Therefore, this chapter also briefly introduces importance, necessity, challenge for IOPVs.

Chapter 2 provides a comprehensive review of the literature on OPVs and IOPVs. The chapter covers the progress made in the development of OPVs and IOPVs, including donor and acceptor molecules, binary and ternary systems. Additionally, this chapter outlines the key factors for achieving high performance and discusses a precise method for measuring the incident power of IOPVs.

In Chapter 3, you will find a comprehensive account of the experimental methodology employed in this study. The primary objective of this chapter is to furnish a detailed explanation of the molecule design and device fabrication process. Additionally, the equipment and techniques utilized for the characterization of the samples are outlined.

Chapter 4 provides deep insight into the difference of sequential deposition bulk-heterojunction (SD-BHJ) and conventional bulk-heterojunction (C-BHJ) based on novel small molecule TB-4Cl to harvest sunlight and artificial light. TB-4Cl was modified from the star acceptor Y6 by reducing a thiophene fused ring on the skeleton with blue-shifted absorption spectrum relative to Y6, and higher EQE response, which can as OSCs and IOPVs simultaneously. Comprehensive insights and underlying reason on the necessity of SD-BHJ for highly efficient OPVs under dim light condition are provided and revealed. This chapter discusses that asymmetric molecule with blue-shifted spectrum fabricated by SD-BHJ can be a promising candidate applied in the indoor environment to harvest sunlight and artificial light simultaneously.

Chapter 5 discusses strategy adopted for IOPVs to tune the intramolecular charge transfer (intra-CT) and intermolecular charge transfer (inter-CT) to achieve high PCEs under indoor environment in the combination of changing skeleton from symmetry to asymmetry and end group from chlorination to non-chlorination. Two new acceptors, TB-S and TB-SCl with an A-D_1A'D_2-A structure are designed and synthesized to compare the performance of an asymmetric backbone with two specified end groups under the dim light condition. The influence of asymmetric skeleton and non-chlorination strategies on devices are systematically investigated in this chapter through thoroughly evaluation of photovoltaic performance combined with analysis of intra-CT and inter-CT.

Chapter 6 illustrates the ternary strategy to enhance the performance of OPVs. The “structure-performance” correlation of the third component in the ternary device are demonstrated clearly from the aspect of material’s eigen-properties. Two wider bandgap asymmetry skeleton typed non-fullerene acceptors (ASNF), named TB-S1 and TB-S1-O, were modification from TB-S. These three ASNF molecules have similar skeletons but different terminal groups or alkyl/alkoxy side chains are incorporated into the host system PM6:BTP-eC9 as a third component, respectively. This chapter reveals that alkoxy substitution on asymmetric backbone is an efficient method to construct the third component for high-performance ternary organic solar cells.

A summary of the current research and proposal of future work are included in

Chapter 7.

CHAPTER 2

Literature review

2.1 Literature review of OPVs

The bulk heterojunction structure (BHJ) is most adopted to form active layer of OPVs which is shown in **Figure 2.1b**. In BHJ system, donor and acceptor are well mixed and form rational phase separation. The device structure (**Figure 2.1c**) contains active layers, the mixture of electron donors and acceptors (BHJ), electron transfer layer, hole transfer layer, anodes, and cathodes. The working principal of heterojunction photovoltaic cells are shown in **Figure 2.1a**. The process of photon transfer in organic photovoltaic devices typically involves four steps: (1) photons are absorbed by the active layers, which consists of donor and acceptor materials, resulting in the production of excitons, bound states of electrons and holes that are attracted to each other by Coulomb forces. (2) excitons diffuse to the interlayers of donors and acceptors. (3) excitons are dissociated into free carriers (electrons and holes). (4) free carriers are transported and collected by the electrodes (anode and cathode). The typical diffusion length of excitons is between 5 nm to 20 nm. Therefore, in order to achieve high exciton dissociation efficiency, the phase separation length of the active layers should be similar to the diffusion length. If the length of phase separation is too long, excitons will suffer severe recombination before excitons diffusing to the interlayer of acceptor and donor so that free carriers cannot be efficiently produced. Moreover, free carriers should be also effectively collected by the electrodes to generate the electricity. However, the free carries are motivated by the driving force that is built-in electric field. The magnitude of electric field depends on the difference between the Highest Occupied Molecular Orbital (HOMO) of donors and Lowest Unoccupied Molecular Orbital (LUMO) of acceptors. The electric field is also related to V_{OC} of OPVs. Furthermore, a high work function metal is used to collect holes and a low work function metal is adopted to extract electrons, in which the free carriers are easier to be collected in the short circuit condition. The performance of device is dependent on properties of adopted materials and the morphology formed by mixing acceptor and donor.

The swift progress of OPVs can be attributed to the continuous development of novel materials and optimization of the active layer's morphology. Over decades, researchers have designed new donors and acceptors in order to acquire improved absorption spectra, enhanced charge transfer ability, suitable bandgap, preferred phase separation with intermolecular interpenetrating network. The active layer's morphology can be further optimized by utilizing alternative deposition techniques or implementing ternary strategies, which enhance the efficiency of exciton dissociation and charge transfer. Thus, it is essential to comprehend the advancements in main materials and ternary strategies to enhance the performance of the host system.

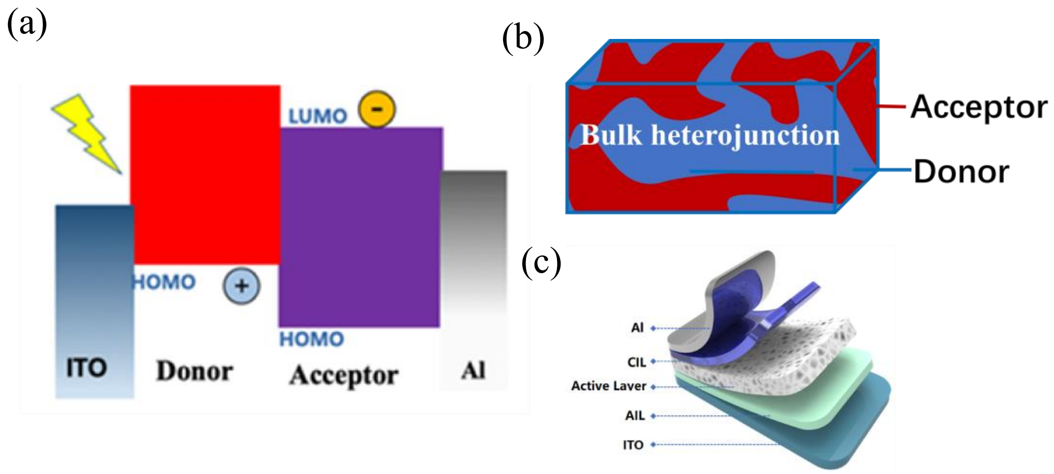

Figure 2.1. (a) The working principal of organic photovoltaic cells. (b) the diagram of BHJ. (c) device’s architecture.

2.1.1 Donor materials for binary device

In the past few decades, the development of heterojunction OSCs was rapid. In 1995, A.J.Heeger’ s group[47] and Friend’s group[48] firstly reported Ca/MEH-PPV:PC$_{61}$BM /ITO and Al/MEH-PPV:CN-PPV/SiO_2/ITO organic heterojunction structures, respectively. Heterojunction structure is that donor materials and the acceptor materials are mixed to form an active layer to harvest solar energy, in which two types of materials interpenetrate, forming numerous P-N junctions. The earliest polymer material for donor is polythiophene as shown in **Figure 2.2**. Since 2000, based on the P3HT:PCBM devices, the PCE has improved to 3%-5%[49]. This system has been further improved to maximal PCE of 6.6% through optimizing the thickness of anode modification interlayer PEDOT:PSS(4083)[50]. However, the narrow absorption rage of P3HT limits active layer to harvest the photons from long wavelength. Besides improving alkyl chain, Yongfang Li et al. also applied styryl moiety and thiophene vinyl into polythiophene forming PEHPVT and PT5, respectively[51, 52]. The results revealed that these materials featured with two peaks in the absorption spectra, which came from side chain absorption and main chain, respectively. In the following, Lijun Huo et al. adopted the strategy of adding alkoxy chain and sulfydryl chain obtaining P3HOT and P3HST. The substituent of alkoxy leaded to the lifting of HOMO yielding worsen PCE. Although sulfydryl substituent enabled down shifting HOMO with broader absorption range, the PCE was still quite low (0.34%).

A big progress was made by introducing benzodithiophene (BDT) unit, that is electron donating material moiety, into donor molecular structure to down shift HOMO level. As shown in **Figure 2.3**, BDT materials possess conjugate rigid plane structure, which is beneficial to π-π stacking and thus contributing to better free carrier transportation. In 2008, Jianhui Hou's group first applied BDT unit into polymer donor with D-A structure that facilitated intramolecular push and pull interaction and effectively tuned energy level and thus adjusted absorption spectrum[53]. The typical BDT-based material is PBDB-T[54] which has the absorption range from 400 nm to 700 nm. This type of polymer features temperature dependent aggregation effect which leads to molecular chains loose under the condition of heating and results in fiber aggregation structure when the temperature is cooling down. This effect conduces the mixing of donor and acceptor resulting in good morphology and suitable phase separation facilitating charge transfer.

Besides adopting BDT as D moiety, benzotriazole (BTA) was also adopted as A moiety, such as J_{51}[55]. In 2019, Liming Ding et al. introduced benzothiadiazo dithiophene into BDT-based polymer donor synthesizing the star novel donor, D18, which first realized over the PCE of 18%[56]. In order to decrease bandgap, quinoid was adopted to replace BDT, such as PTB7 series[57]. Thienothiophene can stabilize the quinoid vibration which realize not only decrease bandgap but also improve charge transfer efficiency. In addition to modifying the whole backbone, some special halogen and group can be introduced into molecule to adjust bandgap and absorption properties. The F atom was used to replace H in the structure of PBDB-T resulting in PM6[58], which obtained the high PCE of 17.8% ascribing from enhanced non-covalent interaction. Furthermore, Cl atom with stronger withdrawing ability was also be adopted to obtain PM7[59] featured lower bandgap and thus bathochromic shift.

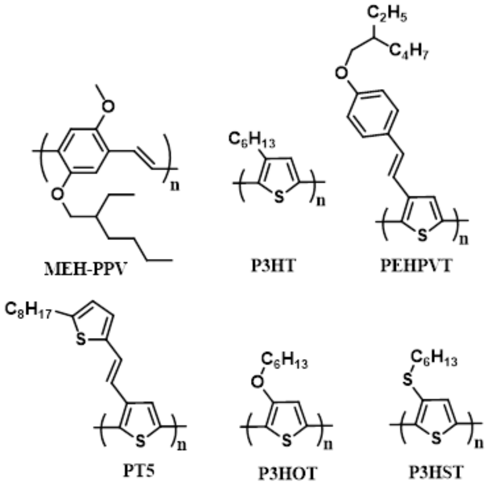

Figure 2.2. Polythiophene donor materials.

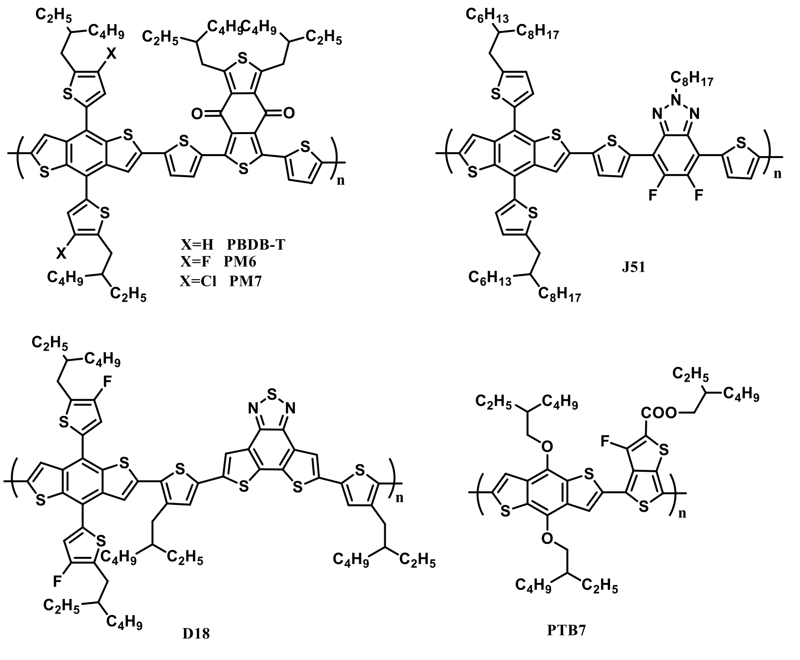

Figure 2.3. BDT polymer donor materials.

2.1.2 Acceptor materials for binary device

The earliest acceptor materials were fullerene derivatives as displayed in **Figure 2.4**. As the dissolution ability of fullerene is poor, phenyl butyrate was introduced into the fullerene to obtain $PC_{61}BM$ and $PC_{71}BM$ which can dissolve well in chloroform (CF), chlorobenzene (CB), and toluene (TOL), and possess lower LUMO and high carrier mobility. BTR:$PC_{71}BM$ [60] acquired PCE of 9.03%, and DR3TSBDT:$PC_{71}BM$ achieved PCE of 9.6%. In addition, through introducing two indenes by addition reaction, ICBA was formed[61] which coupled with P3HT showed a higher V_{OC} of 0.84 V and PCE of 5.44%. However, the inherent drawbacks of fullerene derivatives hinder their development: (1) their bandgap do not well match the spectrum of indoor and outdoor light sources. (2) their energy levels are hard to adjust by modifying their structures. Consequently, non-fullerene acceptors were quickly developed.

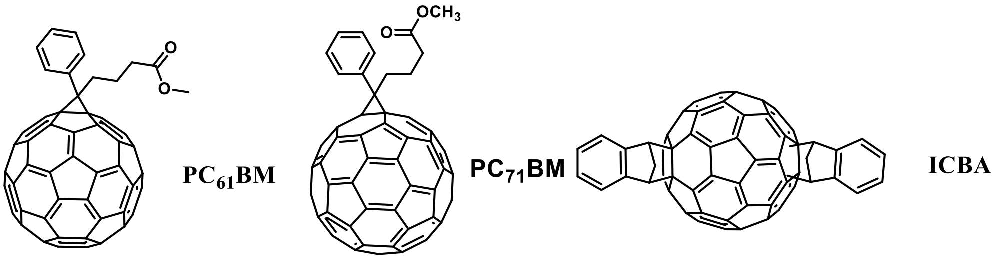

Figure 2.4. Molecular structure of fullerene acceptor materials.

The typical non-fullerene acceptor structure is A-D-A small molecular materials. In the type of A-D-A structures, the main chain adopts indacene multiple fused rings as D moiety and indanone as end groups and A moiety, well known as ITIC series. In 2015, Xiaowei Zhan reported the most classical molecule, ITIC, mixed with PTB7-Th showing the PCE of 6.8%[62]. The end group of ITIC has strong electron-withdrawing group, cyanogroup, which has strong pull electron ability leading to decrease bandgap. Also, the planarity of indanone facilities the stacking of acceptors among molecules. Subsequently, the progress on modification of ITIC mainly focused on the engineering main chain, side chain, and end group. On the aspect of main chain, Yanming Sun focused on modifying the fused ring to obtain a series of asymmetric molecules, such as TPTT-4F[63]. On the aspect of side chain engineering, the common modification was the replacement of alkyl thiophene group to alkyl phenyl, such as ITIC-Th. For the modification of end group, the adjustment of benzene was frequent. Jianhui Hou and Shu Kong So introduced F atom into end group to obtain ITIC-4F which exhibited wider absorption and better molecular interaction and thus ITIC-4F the high PCE of 12.1%[64]. Recently, Qingdong Zheng group abandoned indacene structure and adopted cyclization reaction forming thiophene ring and furan ring in the main chain to acquire novel A-D-A small molecule acceptors, M8 and M34. M34 realized the high PCE of 15.24%[65].

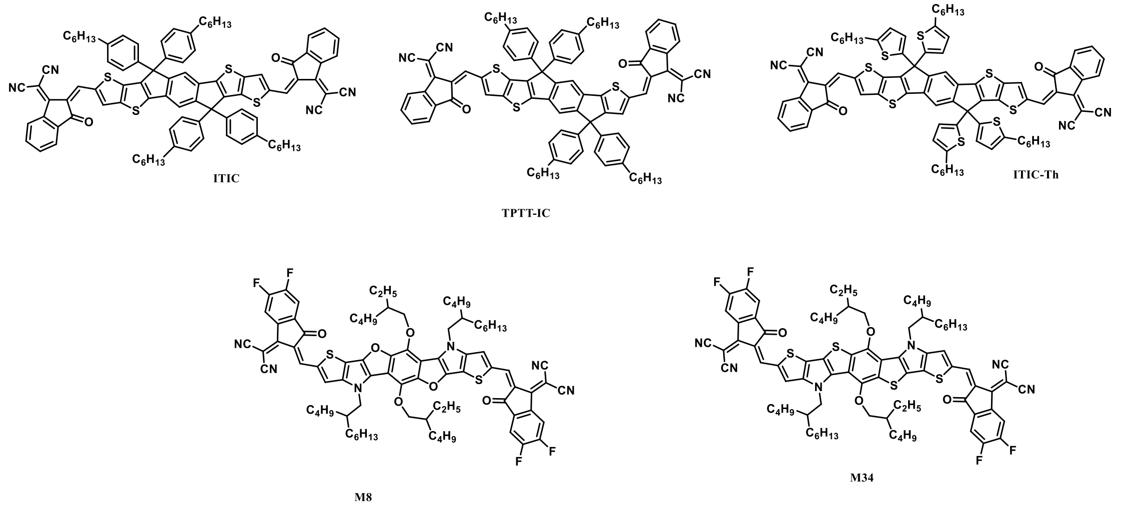

Figure 2.5. Molecular structure of ITIC series acceptor materials.

However, the series of ITIC molecules have the property of relative wide bandgap leading to the poor spectrum overlap of sun illumination. To further widen absorption, Yingping Zhou adopted electron-withdrawing core, benzothiadiazole, instead of indacene, obtaining stat molecule Y6, the structure of A-DA'D-A, which realized the high PCE of 15.7%[66]. Based on the novel backbone of Y6, benzotriazole (BTA) was introduced to replace benzothiadiazole to acquire Y11 with the PCE of 16.54%[67]. These results implied the superiority of the core of electron-withdrawing ability. In addition, the side chain engineering was in the following in the molecular development progress. He Yan studied the influence of side chain structure on the N atom. The result suggested that 3-ethyl heptyl alkyl side chain, named N3, realizing better solubility and photoelectronic properties, which showed the PCE of

15.98%[68]. Moreover, Jianhui Hou through adjusting the alkyl chain synthesized BTP-eC9 which adopted nonane on the thiophene ring and 2-butyl-octyl alkyl chain on the pyrrole ring, showing the high PCE of 17.8%[69]. However, the mentioned molecules above are only aimed at the application under sun irradiation, the molecules applied under indoor environment should be developed.

Table 2.1. Binary OPV performance under AM1.5 conditions.

Active layer	PCE (%)	V_{OC} (V)	J_{SC}(mA cm^{-2})	*FF*	Ref
P3HT:PCBM	3-5	0.66	8–12	50-65	50
J_{51}:IDSe-T-IC	6	0.91	15.2	62	55
PTB7-Th:ITIC	6.8	0.81	14.21	59.1	62
BTR: $PC_{71}BM$	9.03	0.9	13.8	72.86	60
PM6:ITIC-4F	12.1	0.85	18.73	76	64
PM6:M34	15.24	0.91	23.63	70.66	65
PM6:Y6	15.7	0.83	25.3	74.8	58
PM6:Y11	16.54	0.833	26.74	74.33	67
PM7:IT-4F	12.11	0.81	23.23	68.25	59
PM6:BTP-eC9	17.8	0.839	26.2	78.3	69
D18:Y6	18.22	0.859	27.70	76.6	56
PTB7: $PC_{71}BM$	7.4	0.74	14.5	68.97	57
P3HT:ICAB	5.44	0.84	9.67	0.67	61

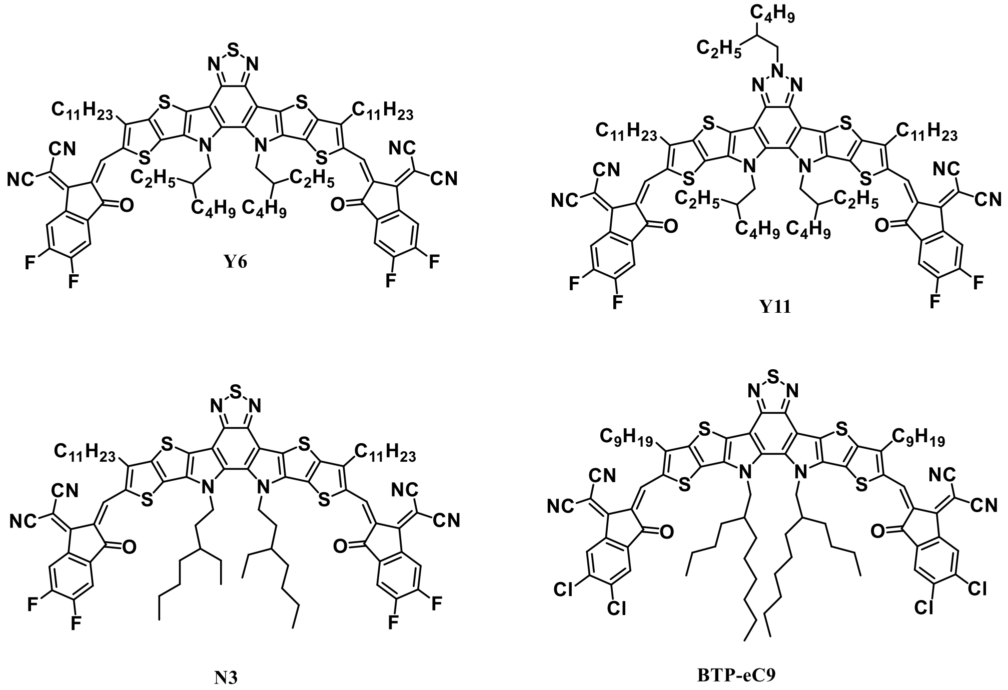
Y6 Y11 N3 BTP-eC9

Figure 2.6. Molecular structure of Y-series acceptor materials.

2.1.3 The research progress of ternary organic solar cells

Table 2.2. Ternary OPV performance under AM1.5 conditions.

Active layer	PCE (%)	V_{OC} (V)	J_{SC} (mA cm^{-2})	*FF*	Ref
DR3TBDTT:PC$_{71}$BM:PC$_{61}$BM	3.04	0.67	10.5	42.5	70
DR3TBDTT: PC$_{71}$BM:ICBA	5.11	0.76	14.2	47.1	70
SM:SM-Cl:IDIC	10.29	0.921	16.05	69.58	71
PBDB-T:IBC-F:IE4F-S	15.06	0.887	22.83	74.4	72
PM6:Y6: PC$_{71}$BM	16.67	0.85	25.7	76.35	73
PM6:BTP-eC9:MOIT-M	18.5	0.87	27.4	77.3	74
PM6:BTP-H2:L8-BO	19.2	0.892	26.68	80.7	75

The ternary strategy is a simple and effective approach to enhance the performance of the host system in organic photovoltaic devices. Ternary strategy through adding the third component into the photoactive layer to broaden the adsorption range is applied so that increases the light-harvesting capability based on a proven highly efficient binary heterojunction structure. Moreover, the third component can also enhance exciton separation, carrier transportation and devices stability. Ternary organic photovoltaic cells contain two types: two donors' systems and two acceptors' systems (D1:D2:A or D:A1:A2). D2 and A2 represent the third material as guest donor and guest acceptor, respectively, incorporated into host binary system. In comparison with the binary OSCs, ternary OSCs may contain one or more several advantages showing in the following: 1) the third material can broaden the adsorption range or extend the extinction coefficient resulting in higher photon absorption; 2) the third component can facilitate exciton dissociation and free carrier transport leading to higher J_{SC} and thus higher device performance; 3) the morphology of active layer can be improved by introducing the third material which can facilitate the formation of intermolecular interpenetrating network and thus minimize carrier recombination. 4) the aligned energy level can be formed by introducing the third component which facilitates the voltage loss resulting in higher V_{OC}. Ternary strategy maintains the simple process of binary devices, which contains three materials in active layers.

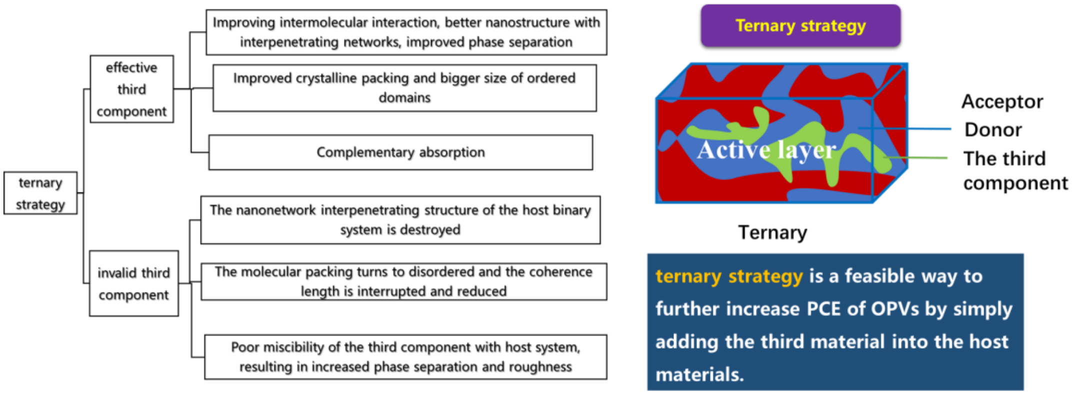

Figure 2.7. The description of effective third material and invalid third material for ternary strategy.

For an ideal ternary OPV, the following features should be included simultaneously. 1) The third component showing complementary absorption (for better photon harvesting) and aligned energy levels are necessary, which is beneficial to obtain high J_{SC} and V_{OC} [76, 77]. When three materials with different and complementary absorption wavelength are combined, the overall absorption spectrum can be broadened to absorb photons from light source, resulting in a higher photon harvesting efficiency leading to a higher J_{SC}. When the energy levels of the third material and host materials are well-aligned, it enables efficient charge transfer between the materials which is beneficial to generating efficient charge separation and transport for achieving higher V_{OC}. If the energy levels are not aligned, it may lead to energy losses and thus lower V_{OC}. 2) The introduction of a third component can reduce $\Delta E_{\mathrm{nonrad}}$. This is crucial for enhancing the V_{OC} in OPV, which is mainly determined by the electroluminescence quantum efficiency (EQE_{EL}) of the device [78]. Many studies have demonstrated that the low highest occupied molecular orbital (HOMO) or lowest unoccupied molecular orbital (LUMO) offset between the donor and acceptor could increase hybridization between the local exciton (LE) and charge transfer (CT) states, which can achieve a high luminescence of the CT state, resulting in a small $\Delta E_{\mathrm{nonrad}}$[79, 80]. 3) Enhancement of exciton dissociation and charge transfer achieved by the formation of ideal BHJ morphology, which are highly correlated with improvements in J_{SC} and FF in ternary OPVs. Recently, several studies demonstrated that the third component has favorable compatibility with the donor and acceptor of host system and is crucial for forming ideal BHJ morphology[81-83]. However, it is hard to control the morphology of blend film, especially in ternary systems. In ternary systems, incorporating an additional donor or acceptor material can lead to a more complex BHJ morphology. If the morphology exhibits a better nano-interpenetrating network, it indicates that the additional material has successfully created additional interfaces and pathways for exciton dissociation, increasing the likelihood of free charge formation. However, in many cases, the addition of extra material can lead to a worse morphology, resulting in a significant decrease in the PCE of the system.

In 2015, Park groups[70] utilized two fullerene acceptors to fabricate ternary devices. The structures of DR3TBDTT:$PC_{71}BM$:$PC_{61}BM$ and DR3TBDTT: $PC_{71}BM$:ICBA achieved PCE of 3.04% and 5.11%, respectively. In 2019, Ziyi Ge [71] group reported ternary non fullerene all small molecular structure devices SM:SM-Cl:IDIC which obtained the PCE of 10.29%. In 2013, Thompson's group[84] observed V_{OC} varied with increasing ratio of ICBA based on the structure of P3HT:ICBA:$PC_{61}BM$ and proposed alloy mode mechanism to explain the variation of V_{OC}. Tylor [85] in 2013 introduced dye small molecule SQ into P3HT:$PC_{71}BM$ and improved PCE to 4.5%, following by proposing energy transfer mechanism between two donors. Huang and coworkers [86] doped BTR into INI-Th:$\mathrm{PC_{71}BM}$ in 2017, and the PCE improved from 9.21% to 10.37%. Li's group [72] increased the PCE from 13.7% to 15.06% based on the structure of PBDB-T:IBC-F:IE4F-S. In 2019, Ziyi Ge et al. [73] doped $PC_{71}BM$ into highly efficient binary system PM6:Y6, then, the PCE have improved from 15.7% to 16.67%. In addition, N3 which is the derivative of Y6, and the structure of PM6:N3:$PC_{71}BM$ attained the PCE of 16.74%. Chen's group[75] demonstrated that the guest acceptor, BTP-H2, processing strong intermolecular interaction and near-zero HOMO offset with donor resulting in enhanced hole transfer and reduced ΔE_{nonrad}. As a result, PM6:BTP-H2:L8-BO exhibited the high PCE of 19.2% compared to binary system (18.5%) which ascribed to the more balance between the electron and hole and higher V_{OC}. The principle of that two compatible acceptors is effective to enhance PCE in the ternary strategy was claimed by Zhang's group[74]. In this work, MOIT-M as the third component displayed complementary absorption and cascaded energy level combined with good miscibility with BTP-eC9 resulting in promoted morphology which produced higher PCE of 18.5% with lower $\Delta E_{\mathrm{nonrad}}$ compared with that of binary system (17.4%). Sun and the co-authors[87] proposed that qualified third acceptors can be synthesized by sharing the same central unit with the host acceptor and a single fluorinated terminal group. The result implied that BTP-F, Y6-F, and L8-BO-F as the third material successfully improved the charge transfer, morphology, and reduced $\Delta E_{\mathrm{nonrad}}$ and thereby realized improved PCE in all ternary devices.

2.2 The progress of indoor organic photovoltaics

OPVs applied under the outdoor condition refers to the use of solar panels to generate electricity from sunlight. Indoor OPV, known as IOPV, refers to the use of solar panels to generate electricity from indoor light sources, such as artificial lighting or sunlight that has entered a building. The relationship between OPV and IOPV is that they both use the same working principles to generate electricity, but they are optimized for different environments. Outdoor OPV panels are designed to withstand outdoor conditions with broader irradiation spectrum, while indoor OPV panels are optimized for lower light levels and the specific spectrum (narrower) of artificial light.

In this section, the principles of achieving high efficiency in indoor environment are summarized. Subsequently, IOPVs performance characterization is outlined, where the reason why spectrometer is used to ensure the incident light intensities rather than lux meter is explained. Next, the reviews of progress are carried out to show the big progress achieved for IOPVs technology.

2.2.1 Principles to achieve high efficiency of IOPVs

2.2.1.1 Theoretical maximum PCE

According to the detailed balance limit theory, theoretical calculations for maximum PCE of photovoltaic devices by the methodology of Shockley and Queisser [88] are shown in **Figure 2.8a**. Theoretical calculations reveal that the optimal bandgap for indoor light source is ca.1.9 eV, whereas the optimal bandgap energy for AM1.5 is ca. 1.34 eV[33, 88]. The optimal bandgap energy under indoor lighting is relative to the range of the indoor lighting spectrum which the wider bandgap of active material producing larger V_{OC} will better cover. Because of the narrow range distribution of the indoor light sources, the photons of irradiance can be sufficiently utilized by organic materials, and the maximum theoretical efficiency is close to 60%. Moreover, the narrower band of spectra, the less transparency and thermalization losses[89]. Compared with indoor light sources, the upper-limit calculative efficiency under AM1.5 doesn't exceed 40%. Due to the tunable bandgap of OPVs based on molecular design, the photoelectric properties of IOPV can get closer and closer to the maximum theoretical efficiency. The bandgap of crystalline silicon is ca. 1.1 eV which corresponds to the optimal bandgap under solar illuminance, hence, silicon-based cells can achieve impressive efficiency under the AM1.5. On the contrary, silicon-based cells with narrower bandgap produce lower PCE for the indoor lighting conditions compared with organic-based PVs [90-93]. Although PCE of OPVs is lower than that of the crystalline silicon cells under solar simulator owing to low absorption in the near infrared (NIR) region, sufficiently transferring photons and tunable bandgap make IOPVs acquire higher efficiency under indoor illumination conditions with narrower spectra and weaker intensities. On the other hand, compared with other IPVs with adjustable bandgap (e.g., dye-sensitized cells, GaAs), IOPVs possess the superiorities in low-cost, roll to roll producibility, and large area solution processability. In sum, the bandgap of active material should be designed and synthesized being close to ca. 1.9 eV to maximize the PCE in indoor environment.

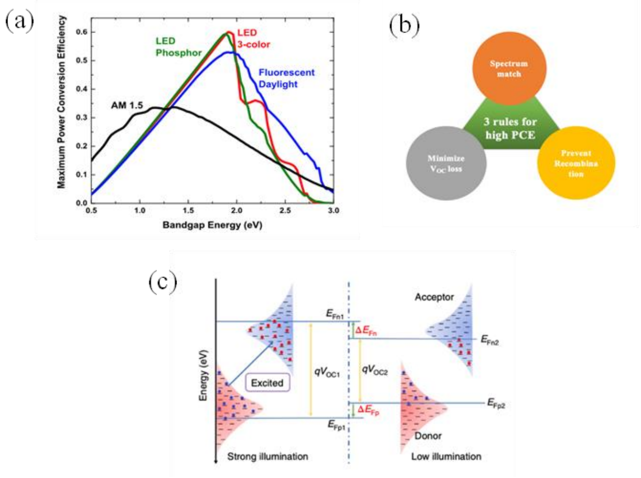

Figure 2.8. (a) Bandgap of active material dependent theoretical maximum PCE under different lighting sources demonstrating an ideal bandgap energy near 1.9 eV for ambient conditions[89]. Copyright 2015, IEEE. (b) Three rules in order to achieve high PCE for IPV under indoor lighting sources. (c) The quasi-Fermi levels of donors and acceptors under strong and weak illuminations[94]. Copyright 2019, Nature energy.

2.2.1.2 Three Important Rules

In order to achieve a high PCE, three rules are suggested to be applied. The first rule is that the photoresponse of the active material should maximally match the spectrum of the indoor light source. For OSCs under AM1.5, the low-bandgap active material is pursued to extend the absorption edge in the NIR region [66] and the maximal PCE is approaching 18% [56]. When testing these high efficiency OSCs in indoor condition, their efficiency cannot be improved significantly because the emission power spectra of LED and CFL range approximately from 400 to 750 nm, whose intensities are smaller than 1 mW cm^{-2} [95]. Therefore, the optimally overlapped spectra between emission and absorption is critical, which can sufficiently transfer the incident photons into light current, thereby minimizing transparency losses. In addition, a high external quantum efficiency (EQE) is also necessary to mitigate the thermalization of photogenerated charges[94].

Secondly, when the intensities decrease from AM1.5 to indoor light conditions, the carrier density dramatically declines, at which trap mediated recombination significantly suppresses electrodes to efficiently collect charge carriers [95-97]. Under weak light intensity, trap can impact not only EQE and FF but also V_{OC} [98]. Decreasing the density of trap state via effective phase-separation control and the increment of domain purity. Through employing highly crystalline active material, adjusting the interfacial ingredient ratio of donor and acceptor, electrode interlayer, and/or adopting ternary blend system, the morphology near the interface can be optimized to decrease the trap state density[99]. Kwon [100] stated that larger phase separation can mitigate interfaces of active layer so that contribute to more compact film and smaller leakage currents.

The third rule is that the loss of V_{OC} should be suppressed as much as possible. When the 1-sun illumination is changed to indoor lighting conditions, the V_{OC} of devices decrease unavoidably, because the intensities of lighting sources drop significantly. V_{OC} is defined by the electron and hole quasi-Fermi levels of semiconductors[101]:

$$V_{\mathrm{OC}} = 1/q(E_{\mathrm{Fn}} - E_{\mathrm{Fp}}) \qquad \text{Equation (2.1)}$$

Where q is the elementary charge, E_{Fn} is the electron quasi-Fermi levels and E_{Fp} indicates hole quasi-Fermi levels. As displayed in **Figure 2.8c**, E_{Fn} and E_{Fp} are correlative to the illumination intensities of lighting sources. Decreasing light intensity, E_{Fn} shifts down and E_{Fp} shifts up, which explains that why the illuminances declination leads to the decrease of V_{OC}[102]. How to make sure the V_{OC} is large in dim light conditions that is essential for achieving high PCE. The relationship between the V_{OC} and photocurrent (I_{ph}) is shown [101, 103-105]:

$$V_{\mathrm{OC}} = \frac{nKT}{q}\ln\left[\frac{I_{\mathrm{ph}}(V_{\mathrm{OC}})}{I_0} + 1 - \frac{V_{\mathrm{OC}}}{R_{sh}I_0}\right] \approx \frac{nKT}{q}\ln\left[\frac{I_{\mathrm{ph}}}{I_0}\right] \qquad \text{Equation (2.2)}$$

Where *n* is the ideality factor (assumption as 1), *k* is the Boltzmann constant, *T* is the cell temperature, q is the electron charge, R_{sh} is the shunt resistance, and I_0 is the reverse dark saturation current. Based on this expression, So's group concluded that minimizing the I_0 can contribute to maximize V_{OC} [106]. Under 1-sun condition, the leakage current is 3 order magnitudes less than I_{ph}, so the shunt resistance of 10^4 Ω cm^2 is enough to maintain V_{OC}. Under dim lighting conditions, the carrier density is extremely low and the leakage current plays an important role that impact the V_{OC} [15, 107]. Steim' group [108] suggested that a minimum R_{sh} of 85000 Ω cm^2 and maximum R_{s} of 50 Ω cm^2 are necessary for IOPVs under weak light conditions. On the contrary, a $\mathrm{R_{sh}}$ of 1000 Ω cm^2 or higher and a R_{s} of 3 Ω cm^2 or lower are required to acquire high efficiency for outdoor solar cells. Integrated OPV cells, which are applied in both, indoor and outdoor environment, need a R_{sh} of 85000 Ω cm^2 or higher and a R_{s} of 3 Ω cm^2 or lower. Furthermore, the loss of V_{OC} under room light is shown as:

$$\Delta V = \frac{nKT}{q}\ln\frac{I_{\mathrm{ph,sun}}}{I_{\mathrm{ph,room}}} \qquad \text{Equation (2.3)}$$

Where $I_{\mathrm{ph,sun}}$ and $I_{\mathrm{ph,room}}$ represent the photocurrents under AM1.5 and indoor illuminance conditions, respectively. Normally, I_{ph} increases with the increment of incident illuminance power (P). P_{sun} (100 mW cm^{-2}) is the illuminance intensity of the sun, and P_{room} is the illuminance intensity under indoor environment. Hence $P_{\mathrm{sun}}\theta$ means the illuminance power of solar spectrum without infrared region. θ is the fraction of light corresponding the wavelength smaller than 780 nm (the upper limit of the photopic region). Therefore, the Equation (2.3) can be rewritten as:

$$\Delta V \approx \frac{nKT}{q} \ln \frac{P_{\mathrm{sun}}\theta}{P_{\mathrm{room}}} \qquad \text{Equation (2.4)}$$

Hence, simulate $\mathrm{V_{OC}}$ under indoor lighting sources can be expressed as:

$$V_{\mathrm{OC,room}} \approx V_{\mathrm{OC,sun}} - \frac{nKT}{q} \ln \frac{P_{\mathrm{sun}}\theta}{P_{\mathrm{room}}} \qquad \text{Equation (2.5)}$$

So' group compared V_{OC}s of one specific OPV device under the solar spectrum without infrared region and under the 300-lux indoor light source, respectively, resulting in a computed $\Delta V \approx 0.166$ V. In other words, when the OPV is applied from solar illuminance to dim illuminance, an additional voltage loss of ca. 0.166 V is unavoidable. For OPVs under 1-sun illumination, the energy loss (E_{loss}) arises from free carrier recommendation losses and the charge transfer (CT) losses. The reported E_{loss} in the most efficient OSCs is typically 0.5–0.6 eV under AM1.5[109, 110]. $E_{\mathrm{loss}}$is the offset between the optical bandgap of acceptor and the measured qV_{oc} which is written as:

$$E_{\mathrm{loss}} = E_{\mathrm{g}} - qV_{\mathrm{oc}} \qquad \text{Equation (2.6)}$$

Where E_{g} is the optical bandgap derived from the absorption onset λ_{onset} (= 1240/ λ_{onset}). Hence, we can assume that the total voltage loss is 0.666-0.766 V under indoor conditions as the extra voltage loss of 0.166 V is unavoidable when lighting conditions are changed from 1-sun to dim lights. Therefore, we can conclude that a high V_{OC} under AM1.5 and a small voltage loss (V_{loss}) in indoor environment are essential for the IOPVs to achieve a high V_{OC} under indoor environment. If a wide bandgap material has E_{g} of 1.8 eV, a high V_{OC} of ca. 1 V under artificial lights are achievable.

2.2.2 IOPVs Performance Characterization

2.2.2.1 The description of lighting intensity

It should be noted that the lighting intensity of AM1.5 is represented with radiometric units of W m^{-2} or mW cm^{-2}. Outdoor 1-sun illumination which simulates the intensity of AM1.5 is 100 mW cm^{-2}. Whereas, the indoor lighting intensity is expressed in photometric units of lumens or lux, which is correlative with the spectral luminous efficiency of human eyes versus visible light wavelength. The illumination intensity of indoor conditions are 2 orders of magnitude less than AM1.5. The intensity of 1-sun approximately equals to 100,000 lux [27, 32, 111]. The illumination intensities adopted to test indoor photovoltaic cells are frequently under 200, 500 and 1000-lux, respectively, for most of the recent studies. These illumination intensities represent the illumination requirement for different indoor places. For example, 200-lux is used for living rooms and corridors; 500-lux is recommended for offices and classrooms; 1000-lux is suitable for supermarkets and operating rooms.

Chen et.al indicated that the sensitivity of human eyes varies with wavelength distributed over the visible spectrum[112]. In other words, the efficiency that produce a visual response of different wavelengths is defined as luminous efficiency of human eyes. For measuring the photometry based on a uniform standard, International Commission on Illumination created the spectral luminous efficiency curves which are shown in **Figure 2.9**. There are two situations, one is light-adapted condition (the "photopic" or $V\ (\lambda)$ function), and the other one is dark-adapted condition (the "scotopic" or $V'\ (\lambda)$ function). The photopic condition $V\,(\lambda)$ described as good lighting conditions is used for almost all the measurements. The illuminance intensity E_{V} (unit: lux) is derived from the emission spectrum collected from spectrometer and $V\,(\lambda)$, which is displayed in Equation (2.9).

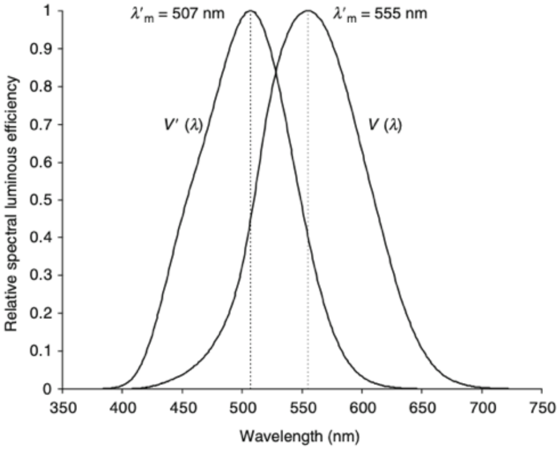

Figure 2.9. Commission International de l'Eclairage (CIE) photopic and scotopic luminous efficiency functions V(λ) and V' (λ) [112].Copyright 2016,Springer.

2.2.2.2 Accurate Photoelectric Parameter Measurement

The fixed illuminance intensity is used to supply solar energy with calibrating by the certificated standard silicon solar cell. Unlike solar simulator, there is no specified indoor lighting source and no uniform standard for testing the IOPVs. In order to precisely measure the PCEs of an IOPV harvesting energy from a non-standard illumination condition, the incident light intensity should be accurately evaluated at each time. Hence wavelength resolved spectra of different indoor light sources are universally measured with a calibrated spectrometer. A spectrometer with an optical fiber measures the absolute emission power spectrum that is equipped with a cosine corrector. Cosine correctors are optical diffusers on the end of fibers to collect signal from 180° field of view.

Both the illumination intensity (unit: lux) and incident power density P_{in} (unit: mW cm^{-2}) of the different indoor lighting sources (e.g. LED, Fluorescent, halogen) with various color rending (e.g. warm white: 2700K; cold white: 6500K) can be integrated from the emission power spectrum (unit: µW cm^{-2} nm^{-1}) measured from the spectrometer. PCE = P_{out}/P_{in}, and $P_{out} = V_{OC} \times J_{SC} \times FF$ is output power of photovoltaic cells. Photon flux spectrum $N_\lambda(\lambda)$ (unit: n s^{-1} cm^{-2} nm^{-1}) is calculated from light power spectrum E_λ (unit: μw cm^{-2} nm^{-1}). The detail Equation is shown:

$$N_\lambda(\lambda) = \mathrm{E}_\lambda . e\lambda/hc \qquad \text{Equation (2.7)}$$

Where e is the elementary charge, λ is the wavelength, h corresponds to the Planck constant and c is the light speed. Subsequently, the incident theoretical integral current density (unit: μA cm^{-2}) can be integrated by the following Equation:

$$J = \int_0^\infty N_\lambda(\lambda)\mathrm{d}_\lambda . e \qquad \text{Equation (2.8)}$$

The illuminance intensity (E_V) can be integrated by the following Equation:

$$E_\mathrm{V} = K_\mathrm{m} \int_0^\infty E_\lambda(\lambda) . V(\lambda)\mathrm{d}_\lambda \qquad \text{Equation (2.9)}$$

Where the coefficient K_m equals 683 lm/W, and E_λ represents emission spectrum. $V(\lambda)$ as described in **Figure 2.9** is luminous efficiency functions for human eyes. Based on the EQE curve and normalized emission power curve, J_SC can be calculated from incident integral current density J by the following Equation:

$$J_\mathrm{sc} = \int_0^\infty N_\lambda(\lambda) . EQE(\lambda)\mathrm{d}_\lambda . e \qquad \text{Equation (2.10)}$$

It should be noted that a low precise lux meter used to measure indoor illuminance conditions will lead to great error. In addition, the calculated current based on the combination of *EQE* curve and photon flux spectrum cannot be acquired to prove the accuracy of the measurement results.

Furthermore, the spherical probes installed for lux meters are not suitable for metering the incident emission power of the planar IOPVs [94]. Hence, an enlarged PCE is evaluated ascribed to big errors. For a instance, an overestimated PCE was obtained under 1000-lux illumination tested by a lux meter [113].

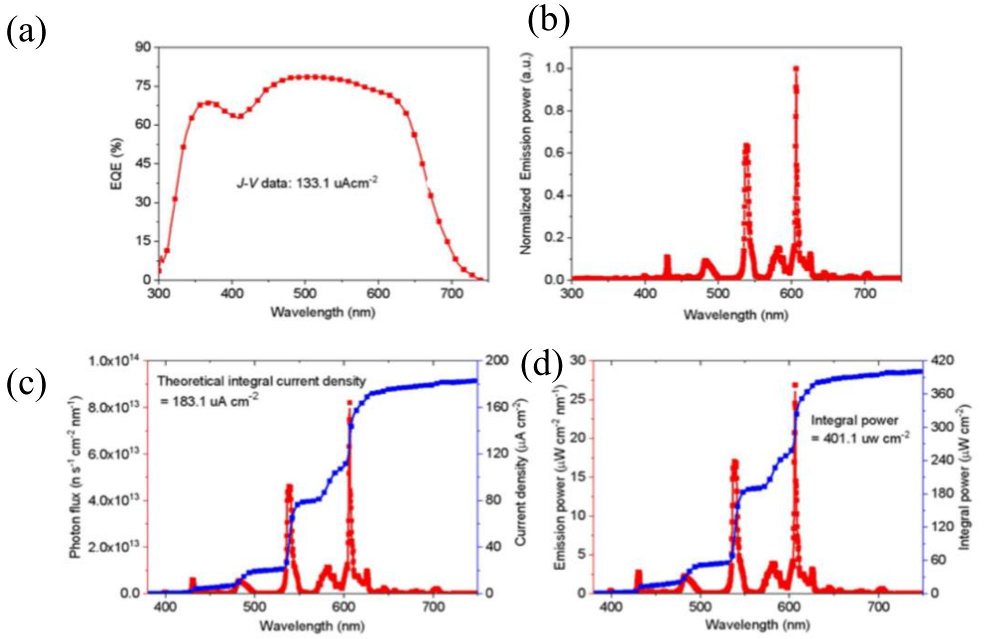

Figure 2.10. (a) The EQE curve and (b) the normalized emission spectrum under the 1000-lux florescent lamp in the example reference [113].Copyright 2018, Royal society of chemistry. (c) Derived photo flux and integral current density spectra of incident illumination. (d) Converted emission power and integrated power spectra of incident illumination[94]. Copyright 2019, Springer Nature.

Verification work of overestimated PCE was demonstrated by Hou's group[94]. Under the 1000-lux illumination measured by a lux meter rather than a spectrometer, the short circuit current density of device measured from *J-V* data is 133.1μA cm^{-2} with the calculated incident power (P_{in}) of 278 μW cm^{-2}. Based on the EQE curve as shown in **Figure 2.10a** and the normalized emission power curve displayed in **Figure 2.10b**, the photon flux spectrum (**Figure 2.10c**) corresponding the measured current density is inverse deduced by Equation (2.10). Next, the maximum theoretical integral current of incident light converted from the photon flux spectrum is calculated as 183.1 μA cm^{-2}. Subsequently, the emission power illustrated in **Figure 2.10d** of the lighting source is obtained. The integral power spectrum is further transformed, and the integrated power is 401.1 μW cm^{-2} (1607-lux). Hence, based on PCE = P_{out}/P_{in}, the real P_{in} is higher than lux meter measured power, which leads to the exaggerated PCE. In other words, lux meter is too rough to confirm incident power and results in imprecise PCE.

The *J-V* measurement signals are recorded by a source-measure unit. The photoelectric properties under different devices under AM1.5 and different indoor lighting sources are measured and compared. Thus, V_{OC}, J_{SC}, *FF*, and PCE are collected, followed by further studying the deeper reasons of their performance. As described in voltage loss minimization section, an active layer material coupled with the specified indoor lighting condition with the minimal V_{loss} is desirable. EQE measurement of the OPV cells is carried out to evaluate photoresponse capability and to verify that whether the integral current densities are consistent with measured J_{SC}. As dim lighting conditions are in 100-1000-lux range to fulfill human various visual requirement, which are only 0.1%-1% of 1-sun illuminance, the solar intensity varies from 100 mW cm^{-2} to 0.1 mW cm^{-2} to evaluate the slopes of the V_{OC} versus light intensity, and J_{SC} versus light intensity, respectively. If the slope of J_{SC} at weak light conditions is close to 1, the bimolecular recombination is weak. If the slope of V_{OC} is close to $\frac{KT}{q}$, it suggests that the bimolecular recombination is sole. Hence, through evaluating the slopes at weak light intensities, whether the trap-assisted recombination is serious can be conducted.

According to the Shockley Equation, J_{SC} can be expressed as:

$$J_{\mathrm{SC}} = \frac{1}{1+R_{\mathrm{s}}/R_{\mathrm{sh}}}\left[J_{\mathrm{ph}} - J_0\left\{\exp\left(\frac{|J_{\mathrm{SC}}|R_{\mathrm{s}}A}{nKT/q}\right) - 1\right\}\right] \qquad \text{Equation (2.11)}$$

Where R_{s} is series resistance, R_{sh} is shunt resistance to which the leakage current is related, J_{ph} is photo-generated current and J_0 is reverse saturation current density. Corresponding to Equation (2.11), the large $R_{\mathrm{s}}A$ results in small J_{SC} under solar illuminance. However, when light sources are switched from AM1.5 to indoor illuminance, the section $\exp\left(\frac{|J_{\mathrm{SC}}|R_{\mathrm{s}}A}{nKT/q}\right) - 1$ is negligible as the J_{SC} dramatically decreases to the level that is much lower than the thermal voltage nKT/q, even multiplied by a large $R_{\mathrm{s}}A$. Nevertheless, a large R_{sh} is not only essential to maintain high V_{OC} but also to decrease $\mathrm{R_s/R_{sh}}$ so that high J_{SC} and

PCE can be achieved. The reverse current in the dark is related to the leakage current which can be measured by J-V measurement in dark. Due to small J_{SC} under dim light environment, the increased R_s that arises from large area fabrication and/or adopting cost-effective PEDOT:PSS (PH 1000) to replace high-cost ITO electrodes will not significantly affect the devices photoelectric properties. Hence, OPV cells under indoor condition is suitable for commercialization owing to large surface processability and low-cost superiority[90, 96, 108].

Briefly, a desired PCE can be obtained owing to matching absorption spectrum, low V_{loss}, high EQE response, relatively low trap recombination, and extremely high shunt resistance with low leakage current.

2.2.3 Literature review of IOPVs

2.2.3.1 Fullerene acceptors

Mid bandgap donors blended with wide bandgap fullerene acceptors ($PC_{61}BM$, $PC_{71}BM$, ICBA) have been reported in the last few years, which produce PCEs ranged from 13% to 28% under artificial lights (**Table 2.3**). The successful outcomes based on fullerene acceptors arise from the overlapping spectra between active layers and ambient lights. Also, the weak intensities of dim lights compared with AM1.5 avoid causing photodimerization for fullerene and morphology instability [95].

In 2017, different polymer coupled with various fullerene derivatives were investigated, in which P3HT:ICBA achieved best PCEs of 13.76% and 13.05% under 500-lux illuminance of fluorescent tube and LED lamp, respectively[28]. In comparison with P3HT: ICBA, the systems of P3HT: $PC_{61}BM$ and PBDTTT-EFT: $PC_{71}BM$ produced less PCEs, because of the less energy offsets between the HOMO of polymer donors and LUMO of fullerenes resulting in lower V_{OC}. Hence, the performance of device can be maximized though increasing the energy difference between HOMO of donors and LUMO of acceptors.

The impact of solvent vapor annealing (SVA) time was investigated by Tsoi et.al[113]. The system BTR: $PC_{71}BM$ annealed by tetrahydrofuran with 2 - 5 minutes achieved the optimal PCE of 28.1%. The optimal SVA treatment time could achieve the appropriate film morphology in which the growing crystallization and the enlarged phase separation were balanced. They demonstrated that $V_{\mathrm{mp}}/V_{\mathrm{OC}}$ (V_{mp} is the voltage at the maximum power point) was stable, when the light intensities of sun varied from 1 to 0.1, which indicated that the fractional-voltage method was suitable to track the maximum power points (MPPs) of the low power consumption applications. Furthermore, Yu's group [114] illustrated that BTR dissolved in non-halogenated solvents exhibits high efficiency, which can be coated on substrates by the large-scale-print technology of slot-die coating.

In 2019, Shim's group [115] investigated the performance of BTD based wide bandgap donor PDTBTBz-2F$_{\mathrm{anti}}$ with fullerene acceptor PC$_{71}$BM under artificial lighting conditions, in comparison with other donors which are P3HT, PBDB-T, PTB7, respectively. The PCE of 23.1% under 1000-lux of LED exceeded that of Si-based IPVs (16.3%). The good photoelectric performance under indoor condition was ascribed to low leakage current, matching spectrum, deeper HOMO leading to lager V_{OC} (0.817 V). The finite-difference time-domain (FDTD) method was adopted to simulate the power absorption ratios for different devices in order to study the importance of spectrum match between the lighting sources and active layers. They suggested the spectrum match ratio was consistent with J_{SC}. Owing to the optimal power absorption ratio of among all the studied devices, the J_{SC} of PDTBTBz-2F$_{\mathrm{anti}}$-based cells was highest which agreed with the best PCE. Shim's group revealed that the work function (5.5 eV) of PDTBTBz-2F$_{\mathrm{anti}}$ was slightly deeper than that of holes transporting layer PEDOT:PSS (5.2eV) which could induce the depletion of holes, thus lead to bigger V_{loss} under 1-sun illuminance. However, due to the lower carrier densities under dim light conditions, the quasi-fermi level of PDTBTBz-2F$_{\mathrm{anti}}$ became shallower than PEDOT: PSS and could be in charge of the minimum V_{loss} (9%) when switched light sources compared with other donors mixed with PC$_{71}$BM (P3HT:20%, PDBD-T:12%, PTB7:11%).The research indicated that the influence of $\mathrm{R_s}$ in *FF* was negligible under dim light conditions. On the contrary, $\mathrm{R_{sh}}$ played an important role in determining *FF*, which was revealed through analyzing the semi-empirical equation of *FF*.

Table 2.3. Fullerene-based IOPV performance under dim light conditions.

Active layer	Light source	Illumination (lux)	PCE (%)	V_{OC} (V)	J_{SC} (mA cm^{-2})	Ref
P3HT: ICBA	FL	500	13.76	0.73	0.05	[28]
P3HT: $PC_{61}BM$	FL	500	9.59	0.43	0.062	[28]
PBDTTT-EFT: $PC_{71}BM$	FL	500	13.14	0.58	0.063	[28]
BTR: $PC_{71}BM$	FL	1000	28.1	0.791	0.133	[113]
PDTBTBz-$2F_{anti}$: $PC_{71}BM$	LED	1000	23.1	0.817	0.1124	[115]
P3HT: $PC_{71}BM$	LED	1000	9.4	0.498	0.0737	[115]
PBDB-T: $PC_{71}BM$	LED	1000	15.3	0.669	0.0902	[115]
PCDTCT: $PC_{71}BM$	FL	300	16.6	0.41	0.0277	[96]
PTB7-Th: $PC_{71}BM$	LED	890	11.63	0.62	0.092	[116]
PM6: $PC_{71}BM$	LED	1000	18.1	0.784	0.0941	[117]
PPDT2FBT:$PC_{71}BM$	LED	1000	16	0.587	0.117	[118]

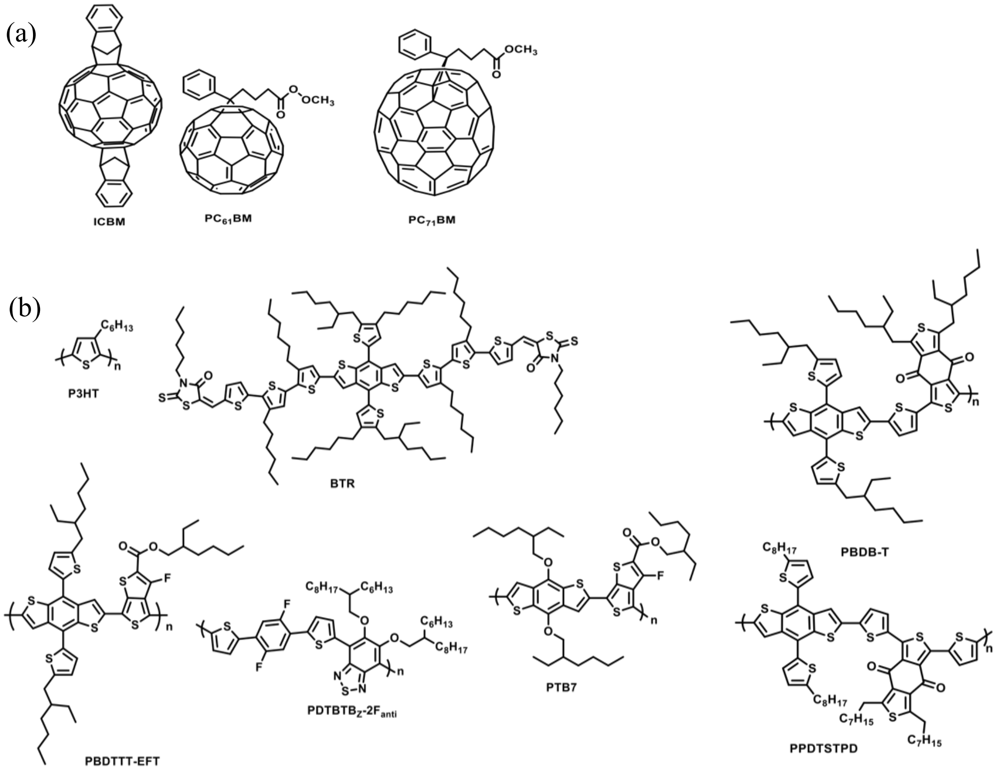

Figure 2.11. (a) chemical structures of fullerene derivatives. (b) Chemical structures of donors applied in fullerene-based devices.

In order to study the influence of thickness of active layers on PCE under weak illuminations, the thickness of PPDT2FBT:$\mathrm{PC_{70}}$BM-based photoactive layer was increased from 170 nm to 760 nm under intensity of 1000-lux, PCEs locate between 13% and 16% with thickness tolerant J_{sc} and *FF* values [118], where the optimal thickness was 390nm. In comparison with exact thickness processed by spin coating in lab, the thickness in large-scale production is less accurate, therefore, a certain thickness tolerance property of IOPVs is desirable [24, 119-121]. Small's group [122] demonstrated that one of the reasons why the thickness of active layer >200 nm leading to poor PCE is the accumulation of space charge in the active layer resulting in increased carrier recombination loss[123]. However, when the light intensity dropped from 100 to 11.4 mW $\mathrm{cm^{-2}}$, the space-charge limited photocurrent with thick active layer of 409 nm decreased because the space charge accumulation is proportional to the light intensity. Woo' s group[124] analyzed that the thick active layer is more suitable for IOPVs because a thicker layer may increase R_{sh} to cause a lower leakage current without serious carrier recombination loss. The results of the optimal PCEs with the thickness of 130 nm under AM1.5 and the thickness of 230 nm under dim light, for PPDT2FBT: $PC_{70}BM$-based photoactive layer, support Woo's assumption.

2.2.3.2 Non-fullerene Acceptors

The fullerenes located at the UV-vis region made the blend film's absorption spectrum match well with the LED and FL emission spectra, but the relatively deeper LUMO of fullerenes cause larger V_{loss} and low absorbance in visible spectrum resulted in relatively lower J_{SC}. Moreover, non-tunability of energy level of fullerene derivatives makes photoelectric performance hardly improved. Therefore, non-fullerene acceptors are explored for IOPVs (as displayed in **Figure 2.12**).

Kwon and coworkers [100] in 2019 demonstrated the effect of chlorination of PBDB-TS (**Table 2.4**). The polymer donors of PBDB-TS, PBDB-TS-3Cl, PBDB-TS-4Cl which have the core of BDT-Th were coupled with donor ITIC, respectively. Under outdoor condition, chlorination didn't exhibit perceptible effect on the performance. However, under fluorescent lamp, the best PCE of 21.7% was achieved by PDBD-TS-4Cl based devices, followed by the PCE of PDBD-TF-3Cl based devices (20.4%) and the quite low PCE of non-chlorination PBDB-TS based devices (5.2%). Kwon summarized that the performance improvement of chlorination of the polymer under artificial lamps were owing to efficient harvesting for fewer photons, the better morphology with better charge mobility, lower leakage current, and smaller V_{loss}.

In 2019, Hou' s group [117] fabricated 1 cm^2 PM6:ITCC, PM6:IT-4F, PM6: $PC_{71}BM$ devices, respectively, to verify the possibility of large-area processability. ITCC-based device achieved 1.1V and 0.962 V under illuminance of 1-sun and 1000-lux LED, respectively, compared with $PC_{71}BM$-based device of 0.945V and 0.784V, and IT-4F-based devices of 0.872 V and 0.712V. The PCE 22% of ITCC based devices surpassed that of $PC_{71}BM$-based devices (18.1%) and IT-4F-based devices (20.8%) under 1000-lux LED (2700 k). Although the trap-assisted recombination became more and more serious with decreasing the solar intensities from 100 mW cm^{-2} to 0.1 mW cm^{-2}, the trap-mediated charge recombination of ITCC-based was minor than that of $PC_{71}BM$-based and IT-4F-based under weak illumination, leading to better performance. They also revealed that the strong illumination and heat were the main reasons for PCE decline of IPV cells. In contrast to strong illumination, the devices showed much greater stability under continuous dim light illumination. Moreover, Hou verified that if the lux meter was used to measure the indoor lighting intensities, a large error would be caused. The input power of illumination should be accurately measured by spectrometer in order to correctly evaluate the performance of devices.

Hou' s group [94]further synthesized a new wide bandgap non-fullerene acceptor IO - 4Cl blended with PM6 which achieved 26.1% PCE and a literally large V_{OC} of 1.1 V under 1000-lux LED (2700 k). The structure of A-D-A was commonly adopted in non-fullerene acceptors[125-130]. This device possessed remarkable stability. IO-4Cl ranged from 450 to 700 nm with a wide optical bandgap of 1.8 eV. Through investigating the reason of high V_{OC}, a radiative recombination above the gap ΔE_1 of ca. 0.28 eV, a radiative recombination below the gap ΔE_2 of ca. 0.07 eV, and a non-radiative recombination ΔE_3 of ca. 0.25 eV were measured. Both low ΔE_2 and ΔE_3 contributed a relatively small V_{loss}. In order to prove the large-area processability for IOPVs, even 4-cm^2 devices through blade-coating process showed 23.9 % PCE with a thicker active layer. As shown in **Figure 2.13a**, by increasing the external additional series resistor, the devices performance under AM1.5 and 500 lux-LED were observed. In comparison with almost constant PCEs under weak illumination, the photoelectric performances under outdoor condition decreased obviously, as mentioned before, which implies that IOPVs are insensitive to series resistance Also, the devices showed remarkable stability under continuous illumination over 1000 h (**Figure 2.13b**), which demonstrated that the gentle light intensity can better maintain the stability of cells.

Yan et.al (31) in 2020 focused on the influence of electron transporting layers on the IOPVs under weak illumination. An acceptor Y6-O was blended with PBDB - TF which was applied with different electron transporting layers, PDINO (HOMO:

-6.21 eV) and PFN (HOMO: -5.61 eV), respectively. The work functions of cathode electrode Al applied different interlayers were measured by ultraviolet photoelectron spectroscopy (UPS). As shown in **Figure 2.13c**, the work function (WF) downshifted from 4.22 to 3.97 eV when applied with PDINO on Al, and WF shifted from 4.22 to 4.11.9 eV when applied with PFN. Although both interlayers could reduce the WF of cathode Al to improve electrons extraction, the Δh, the difference between the HOMO of the interlayer and the fermi level of the cathode, which expressed the hole blocking barrier, were different. The PDINO based devices with the Δh of 2.31 eV was larger than that of PFN based devices (1.49 eV), which indicated that the hole blocking ability of PDINO was better. The photoelectric properties of two types of interlayers' cells were similar under AM1.5, whereas PCE of PDINO-based was 30.02% and PCE of PFN-based was 22.47% under 1650-lux LED (3000 k). Yan' s group speculated that the worse trap-assisted recombination occurred in PFN based devices with low carrier density under weak light intensities due to the smaller Δh compared with the PDINO based devices. However, the influence of these two interlayers could be negligible under strong light intensities because of their high carrier density.

2.2.3.3 Ternary Strategy for IOPVs

Ternary BHJ approaches have been testified as a useful way to further enhance performance of OPVs in both outdoor and indoor environments. The ternary strategy includes two structures which are D1:D2:A (two donors and one acceptor) and D:A1:A2 (one donor and two acceptors), where the extra third component can broaden the photon utilization of the emission spectrum, promote charge transfer, improve BHJ morphology, and prevent active layer degradation[131-135].

Ternary strategy was applied to improve the performance of IOPVs by So' group (29). PDTSTPD as the ternary composition was doped into PCDTBT:$PC_{71}BM$ (**Table 2.5**) resulting in the PCE improvement increased from 16.5% to 20.8% under the 300-lux fluorescent lamp (2700 k). The ternary device showed improved hole mobility and passivated shallow traps ascribed to dope with the third component. In contrast to binary devices, ternary devices had higher V_{OC} of 0.89V under 1-sun illuminance, while 0.73V under dim light irradiance was achieved. Ternary-based cells had higher J_{SC} than binary-based cells owed to the complementary absorption spectrum of the third component to better utilize the emission of indoor tube. Moreover, the ternary films showed narrower band tail and improved hole mobilities, indicating shallow traps near the band edges are mitigated[136, 137].

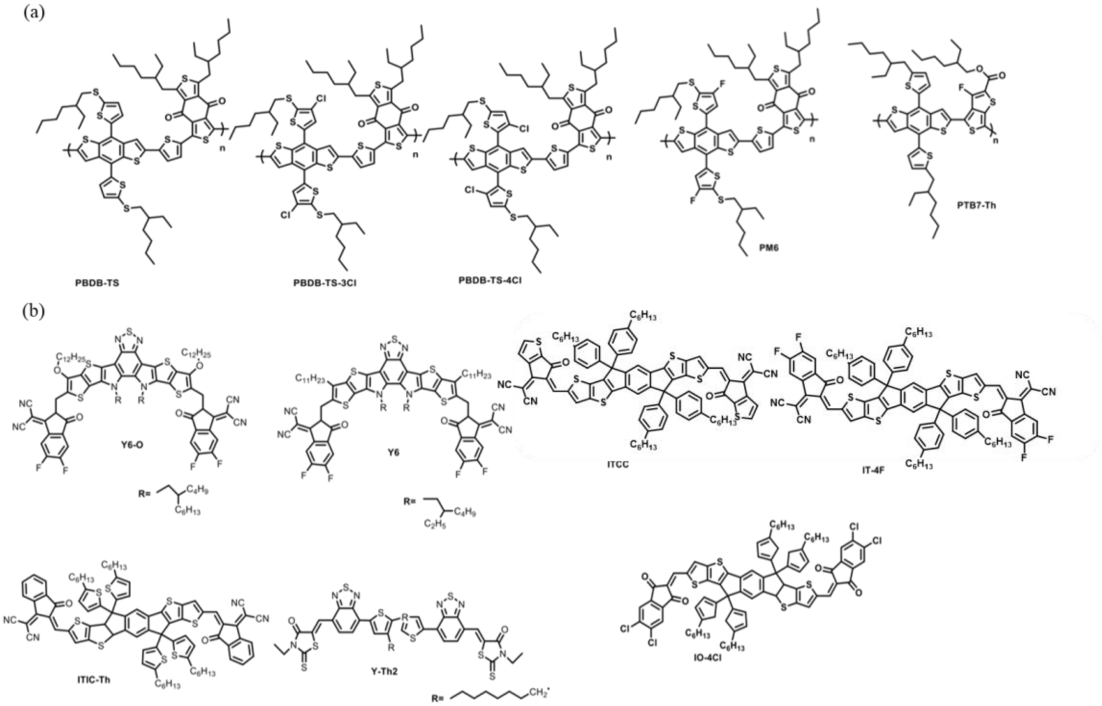

Figure 2.12. Chemical structures of (a) donors and (b) acceptors adopted in non-fullerene based IOPV devices.

Ko et al. [138] investigated D1:D2:A and D:A1:A2 models, which were PBDB-T:PTB7-Th: $PC_{71}BM$ and PBDB-T:ITIC-Th: $PC_{71}BM$ (**Figure 2.13e**), yielding PCE of 20.12% (V_{OC} = 0.63 V, J_{SC} = 159.99 μA cm^{-2} , and *FF* = 65.06%) and 26.4% (V_{OC}= 0.72 V, J_{SC} = 157.94 μA cm^{-2} , and *FF* = 54.43%) under 1000-lux LED, respectively. The result showed that both approaches improved performances of cells when referenced to binary blend with PCE of 15.23% (V_{OC} = 0.61 V, J_{SC} = 140.15 μA cm^{-2}, and *FF* = 49.6%). The result implied that the third non-fullerene acceptor, ITIC-Th, self-organized at the interface of polymer: fullerene, forming cascade ternary junction can result in less charge recombination, higher V_{OC} and

PCE compared with binary blend[139]. However, in comparison with D:A1:A2, additional donor, PTB7-Th failed in forming self-optimized ternary junction formation, suffering relatively severe charge recombination. The authors concluded that the third component should be compatible with the host materials and preferably emerge at interfaces of donor and acceptor in order to form cascade energy levels.

A new non-fullerene acceptor, Y-Th2 was designed by Yang's group[95], which has a structure of dual acceptor-donor-dual acceptor (A1-A2-D-A2-A1). Devices made of PM6:Y-Th2:Y6 offers the PCE of over 16% under AM1.5 and achieves the PCE of 22.7% under 1000-lux LED. The HOMO and LUMO of Y-Th2 aligned between those of binary host, thereby may facilitate efficient carrier transportation due to the cascade energy level. The bandgap of synthesized acceptors was higher than that of donor, PM6. Therefore, this acceptor complemented the absorption spectra of PM6 and Y6 in the short wavelength region with a high absorption coefficient in order to harvest extra photons. Moreover, the result of Grazing-incidence wide-angle X-ray scattering (GIWAXS), exhibited more packed face-on orientation for ternary blend compared with PM6:Y6, which could enhance intermolecular transportation. Transmission electron microscopy (TEM) demonstrated preferential bi-continues interpenetrating network structure after doping 5 wt% Y-Th2. The reported ternary active layer can be applied in both solar cells and indoor light harvesters because of its excellent PCE under outdoor and indoor conditions.

2.2.3.4 Molecular design and industrialization perspectives

Leclerc et al.[95] summarized molecular design perspective for high-efficient IOPVs. The bandgap of NFAs should be increased by increasing the electronic density of end group [140-142] or decreasing the backbone planarity[143, 144]. Compared with NFAs mixed with donors, fullerene acceptors in devices often exhibit lower V_{OC} due to worse aligned energy level and larger V_{loss}. In order to enlarge V_{OC}, a molecular design strategy of decreasing the electron-withdrawing properties of the A moiety in A-D-A leads to upshift LUMO[145], as demonstrated for IO-4Cl[94]. Also, downshifting HOMO level of donor is necessary.

Although higher intensities usually result in higher PCE, Mario [95] stated that lower intensities of 200-500 lux is more practical to evaluate the photoelectric property of indoor energy harvesters because the lower radiances are representative for most indoor conditions. Moreover, in comparison with fluorescent tubes, LED lamps have advantages of longer mean lifetime, cheaper cost and more efficient energy conservation, which should be as the standardized illuminance light source during measurement. Mathews et.al [31] provided the technology and market overview for IPV cells. A series of low-power consumption protocols that have been realized to fulfill various application of IoT technologies, requires 60 million IPV cells to harvest indoor light sources. Hence, the market (**Figure 2.13f**) of IPV cells is predicted to be huge in the near future, and the capital demand of IPVs and wireless sensors (WS) continues to rise to $ 850 million and $ 10 billion by 2023, respectively. Mathews predicted that the manufacturing cost of organic IPV cells will range from 0.001$ cm^2 to 0.03 $ cm^{-2} in the next 5 years. Researchers have to pay attention to materials and production in an economical way for ensuring low cost IPV cells at a small-scale production. Furthermore, they mentioned that to develop universally agreed and uniform standards for evaluating IPV cells performance is necessary.

Table 2.4. Non-fullerene based IOPV performance under dim light conditions.

Active layer	Light source	Illumination (lux)	PCE (%)	V_{OC} (V)	J_{SC} (mA cm^{-2})	Ref
PM6: Y6-O	LED 3000k	1650	30.89	0.84	0.245	[15]
PM6: ITCC	LED 2700k	1000	22	0.962	0.095	[117]
PM6: IT-4F	LED 2700k	1000	20.8	0.712	0.113	[117]
PBDB-TS:IT-4F	FL	500	5.3	0.36	0.0668	[100]
PBDB-TS-3Cl:IT-4F	FL	500	20.4	0.64	0.0628	[100]
PBDB-TS-4Cl:IT-4F	FL	500	21.7	0.64	0.0649	[100]
PM6: IO-4Cl	LED 2700k	1000	26.01	1.10	0.09	[94]

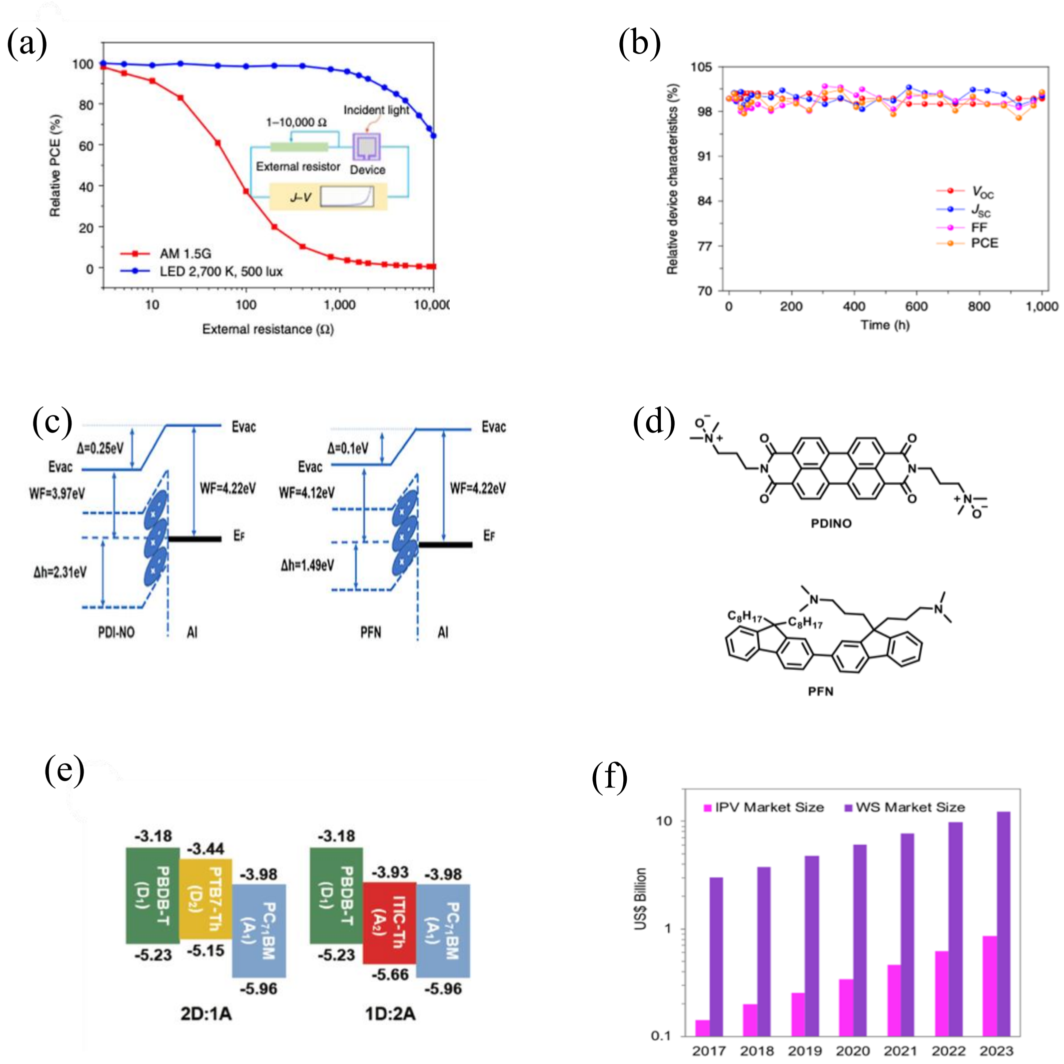

Figure 2.13. (a) Photovoltaic performance varying with the external resistance under AM1.5 and 500-lux LED, respectively[94] . (b) Compared with initial photovoltaic performance, dependence of relative device characteristics on time under continuous illumination with the temperature of 25°C - 30°C and humidity of 40%-60%[94]. Copyright 2019, Nature. (c) The energy level outline of PDINO, PFN and Al[15]. Copyright 2020, Science Direct. (d) The molecular structures of electron transport layers of PDINO and PFN. (e) Energy levels of D1:D2:A and D:A1:A2 models incorporating the third component PTB7-Th as D2 or ITIC-Th as A2 in PBDB-T[138]. Copyright 2019, Wiley. (f) The predicted market size of IPV and WS [31]. Copyright 2019, Science Direct.

Table 2.5. Ternary IOPV performance under dim light conditions.

Active layer	Light source	Illumination (lux)	PCE (%)	V_{OC} (V)	J_{SC} (mA cm^{-2})	Ref
PCDTBT: PDTSTPD: PC$_{71}$BM	FL 3000k	300	20.8	0.73	0.0333	[106]
PBDB-T: PTB7-Th: PC$_{71}$BM	LED	1000	18.99	0.63	0.158	[138]
PBDB-T: ITIC-Th: PC$_{71}$BM	LED	1000	26.4	0.72	0.1579	[138]
PM6: Y-Th2:Y6	LED	1000	22.33	0.701	0.032	[95]

CHAPTER 3

Methodology

3.1 Introduction

This chapter provides a comprehensive elaboration of the experimental work carried out in Chapters 4, 5, and 6, which involved the synthesis and device fabrication of TB-4F, TB-S, TB-SCl, TB-S1, and TB-S1-O. It contains detailed information about the materials and equipment employed in the study, the procedures used for device fabrication, and the methods used for device characterization.

3.2 Materials and solvents

Table 3.1. List of materials for device fabrication and their corresponding information.

Material name	Specification	Manufacturer
PM6	>98%	Solarmer Materials, Inc.
BTP-2ThCl	>98%	Solarmer Materials, Inc.
Y6	>98%	Solarmer Materials, Inc.
BTP-eC9		Solarmer Materials, Inc.
PDINO	>98%	Solarmer Materials, Inc.
PEDOT:PSS (4083)	Clevios P VP AI 4083 1.3-1.7% solid conten	Heraeus
1,8-iodooctane(DIO)	N/A	Tokyo Chemical Industry Co., Ltd.
1-chloronaphthalene (CN)	N/A	Tokyo Chemical Industry Co., Ltd.

CS_2	> 97.0%	J&K Inc
The indium-doped tin oxide (ITO)-coated glass	1.1 mm thick, ≤15 Ω/ square	Yaoke Inc
Polyethylene terephthalate (PET)	Thickness: < 0.2 mm Sheet resistance: n/a	South China Xiangcheng Technology Co., Ltd.

Table 3.2. List of materials for synthesis and their corresponding information.

Material name	Specification	Manufacturer
Petroleum ether	analytically pure	Sinopharm
Dichloromethane	analytically pure	Sinopharm
trichloromethane	analytically pure	Sinopharm
Pyridine	analytically pure	Sinopharm
acetone	99.9%	Sinopharm Chemical Reagent Co., Ltd.

iso-propanol	99.9%	Sinopharm Chemical Reagent Co., Ltd.
triphenyl phosphine	＞ 98%	J&K Chemicals
potassium carbonate	＞ 98%	Sinopharm
potassium iodide	＞ 98%	Sinopharm
o-dichlorobenzene	analytically pure	J&K Chemicals
N-N dimethyl formamide	analytically pure	Sinopharm
phosphorus oxychloride	＞ 98%	J&K Chemicals
dichloroethane	analytically pure	Sinopharm
miso-propanol	HPLC	Beijing Energy Engineering Technologies Co,.Ltd.

2-Ethylhexyl bromide	analytically pure	Sinopharm
ethyl acetate	analytically pure	Sinopharm
11,12-bis(2-ethylhexyl)-1,8-dioctyl-11,12-dihydro-[1,2,5]thiadiazolo[3,4-e]thieno[2',3':4,5]pyrrolo[3,2-g]thieno[2',3':4,5]thieno[3,2-b]indole-2,9-dicarbaldehyde	＞ 98%	Synthesis by our group [146]
2-(5,6-difluoro-3-o,,kxo-2,3-dihydro-1H-inden-1-ylidene)malononitrile	＞ 98%	Synthesis by our group [146]
Tetratriphenylphosphine palladium	＞ 98%	Beijing Energy Engineering Technologies Co,.Ltd.
4,7-dibromo-5,6-dinitrobenzo[c][1,2,5]thiadiazole	＞ 98%	hyperchemical
tributyl(4-octylthiophen-2-yl)stannane	＞ 98%	hyperchemical
tributyl(6-undecylthieno[3,2-b]thiophen-2-yl)stannane	＞ 98%	hyperchemical

2-(1-chloro-6-oxo-5,6-dihydro-4H-cyclopenta[c]thiophen-4-ylidene)malononitrile	> 98%	hyperchemical
2-(6-oxo-5,6-dihydro-4H-cyclopenta[c]thiophen-4-ylidene)malononitrile	> 98%	hyperchemical
2-(6-oxo-5,6-dihydro-4H-cyclopenta[c]thiophen-4-ylidene)malononitrile	> 98%	hyperchemical
11,12-bis(2-ethylhexyl)-1-octyl-8-undecyl-11,12-dihydro-[1,2,5]thiadiazolo[3,4-e]thieno[2',3':4,5]pyrrolo[3,2-g]thieno[2',3':4,5]thieno[3,2-b]indole-2,9-dicarbaldehyde	> 98%	synthesized by myself
11,12-bis(2-butyloctyl)-1-nonyl-8-(nonyloxy)-11,12-dihydro-[1,2,5]thiadiazolo[3,4-e]thieno[2',3':4,5]pyrrolo[3,2-g]thieno[2',3':4,5]thieno[3,2-b]indole-2,9-dicarbaldehyde	> 98%	eFlexPV Limited
2-(6-oxo-5,6-dihydro-4H-cyclopenta[c]thiophen-4-ylidene)malononitrile	> 98%	eFlexPV Limited

2-(6-oxo-5,6-dihydro-4H-cyclopenta[b]thiophen-4-ylidene)malononitrile	> 98%	eFlexPV Limited
2-(6-oxo-5,6-dihydro-4H-cyclopenta[b]thiophen-4-ylidene)malononitrile	> 98%	eFlexPV Limited

3.3 Apparatus

Table 3.3. List of instrumentations and their corresponding information.

Instrument Name	Specification	Manufacturer
UV-Vis Spectrophotometer	LAMBDA 950	Perkinelmer, Inc.
Transmission Electron Microscopy (TEM)	Talos™ F200X	Thermo Fisher Scientific, Inc.
Atomic Force Microscopy (AFM)	Dimension 3100	Veeco Instruments, Inc.
Surface Profiler	Dektak 150	Newport Corporation
J-V Measurement (Solar Simulator)	Oriel Sol3A	Newport Corporation

J-V Measurement (Digital Source)	Keithley 2440	Tektronix, Inc.
Quantum Efficiency Measurement System (EQE)	QE-R	Enli Technology Co., Ltd.
Ultrasonic Cleanser	SK8200H	Kudos Ultrasonic Instrument Co., Ltd.
Photoluminescence Spectroscopy (PL)	FL3-111	Horiba
Cyclic Voltammetry	Electrochemical Workstation (CHI660C)	Artisan Scientific Corporation Dba Artisan Technology Group
UV-Ozone Box	BZS250GF-TC	Huiwo Technology Co., Ltd.
Spin Coater	SPIN-1200D	Midas System Co., Ltd.
Heating Plate (With Magnetic Stirrer)	C-MAG HS 7	IKA ® Works
Vacuum Deposition and Glove Box	N/A	M. Braun Inertgas-Systeme Gmbh

Contact angle test	CAM 200	Biolin Scientific
^{1}H NMR	Bruker Dmx-400	Bruker Switzerland
Time-of-Flight Mass Spectrometer	LC-Q-TOF	Ab Sciex
Time-of-flight secondary ion mass spectrometry (TOF-SIMS)	OF-SIMS 5 iontof	PHI NanoTOFII
Spectrometer	Maya Pro 2000	Ocean Optics
GIWAXS	D/Max-Ttriii(Cbo)	Rigaku
Photo-CELIV, TPC/TPV	All-In-One Characterization Platform Paios	Fluxim AG, Switzerland
Highly Sensitive EQE	PECT-600	Enlitech
Electroluminescence (EL) And Electroluminescence	REPS	Enlitech

Quantum Efficiency (EQE EL) Measurements		
Spin coater	SPIN-1200D	Midas System Co., Ltd.

3.4 Materials design and synthesis

3.4.1 Understanding the effect of sequential deposition processing for high-efficient organic photovoltaics to harvest sunlight and artificial light

The newly designed acceptor TB-4F was synthesized according to Scheme 3.1. Compound 1 was synthesized referring to our previous work[146].

Take 400 mg of compound 1 (11,12-bis(2-ethylhexyl)-1,8-dioctyl-11,12-dihydro[1,2,5]thiadiazolo[3,4e]thieno[2',3':4,5]pyrrolo[3,2g]thieno[2',3':4,5]thieno [3,2-b]indole-2,9-dicarbaldehyde) and 500 mg of compound **2** (2-(5,6-difluoro-3-oxo-2,3-dihydro-1H-inden-1-ylidene)malononitrile) into a 100 mL flask. Then, evacuate the flask and purge it with argon gas. Next, 30 mL of anhydrous CF solution and 1.5 mL of pyridine solution were added into the flask. The mixture was heated and stirred at 60℃ for 4 h, then it was cooled down to room temperature. A dropper was used to slowly drop the solution into a methanol solution, and the mixture was settled overnight. The sediment was filtered and PE:CF=1:3 column chromatography was adopted to obtain the product TB-4F. Then, CF and methanol were used for two times of recrystallization, followed by PE:CF=1:2 column chromatography for the obtained product. n-hexane and CF were used to further recrystallize twice to obtain 300mg of blue-black solid.

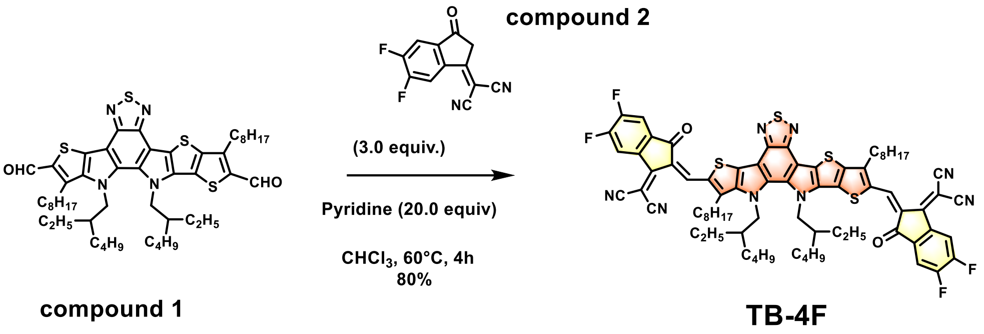

Scheme 3.1. Synthesis route to TB-4F.

TB-4F was confirmed by ^{1}H NMR spectroscopy and TOF MS:

^{1}H nuclear magnetic resonance (NMR) spectroscopy and time-of-flight mass spectrometry (TOF MS) confirmed that TB-4F was successfully synthesized. ^{1}H NMR (400 MHz, Chloroform-d) δ 9.19 (d, J = 16.6 Hz, 1H), 8.57 (dd, J = 10.0, 6.4 Hz, 1H), 7.71 (q, J = 7.0 Hz, 1H), 4.75 (d, J = 7.7 Hz, 1H), 4.55 (s, 1H), 3.23 (t, J = 8.0 Hz, 1H), 2.02 (d, J = 7.5 Hz, 1H), 1.88 (p, J = 8.1 Hz, 2H), 1.76 (s, 1H), 1.52 (d, J = 8.2 Hz, 2H), 1.40 – 1.25 (m, 9H), 0.88 (h, J = 3.7 Hz, 3H).

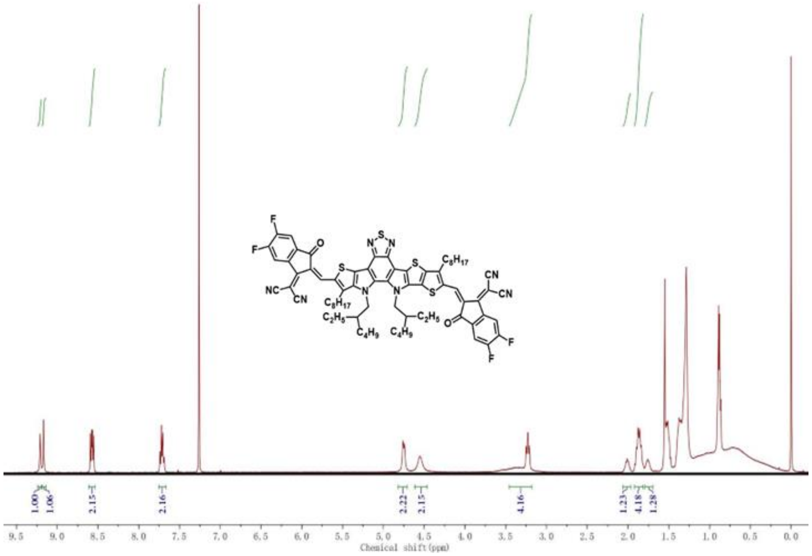

Figure 3.1. 1H NMR spectrum of TB-4Cl.

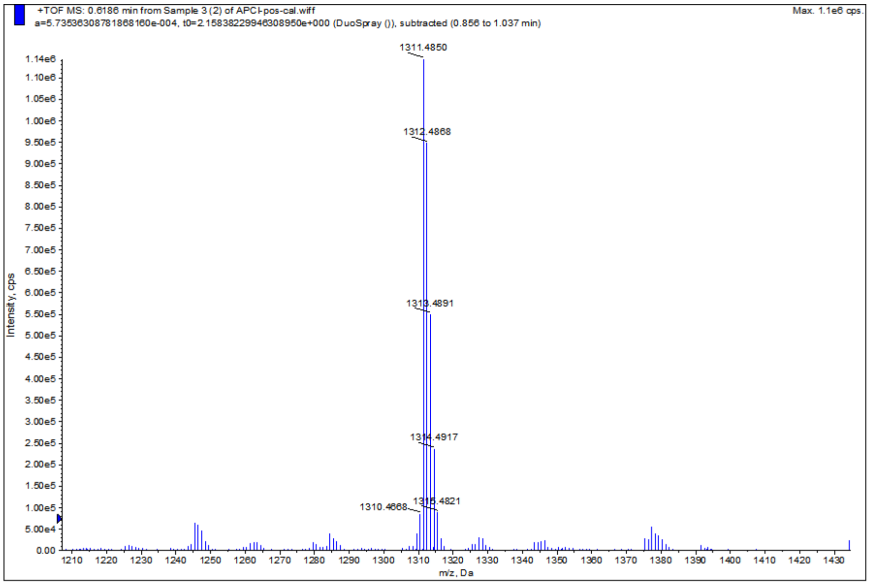

Figure 3.2. TOF spectrum of TB-4Cl.

3.4.2 Rational tuning of intermolecular and intramolecular interactions enabling high-efficiency indoor organic photovoltaics

The newly designed acceptor TB-SCl and TB-S were synthesized according to **Scheme 3.2**. Compound BTP-2ThCl was synthesized referred reported work[147].

Compound 3 4,7-dibromo-5,6-dinitrobenzo[c][1,2,5]thiadiazole (10 g) and compound tributyl(4-octylthiophen-2-yl)stannane (15 g) were weighed into a 500 mL three-necked flask. 250 mL of anhydrous toluene solvent was added and stirred while simultaneously evacuating the flask under nitrogen protection three times. Then 0.3g of $Pd((PPh)_3)_4$ was added into the flask. Then the flask was heated up to 110°C and shielded from light. After 2 h of reaction, the heater was turned off and let it cool to room temperature naturally. The product was poured into a 1L separatory funnel and was washed with dichloromethane (DCM) repeatedly to reduce loss. Then, approximately 5-6 times the volume of deionized water was added into the flask and shake it. The flask was standed for a while until the solution separates into two layers. The DCM solution in the lower layer was collected from the bottom of the flask. This process was repeated several times until the upper liquid become clear to remove impurities from the aqueous solution. Finally, the obtained DCM solution was dried by rotary evaporation and silica gel powder was added. Column chromatography with a mobile phase of petroleum ether (PE): dichloromethane (DCM) = 3:1 was used to remove unreacted raw materials and by-products, and 5.2g of red compound 2 (5,6-dinitro-4-(4-octylthiophen-2-yl)-7-(6-undecylthieno[3,2-b]thiophen-2-yl)benzo[c][1,2,5]thiadiazole) was obtained with a yield of about 50%.

Compound 4 (5.2 g) and compound tributyl(6-undecylthieno[3,2-b]thiophen-2-yl)stannane (10 g) were weighed into a 500 mL three-necked flask. Add 150 mL of ultra-dry toluene and 0.4g of $Pd((PPh)_3)_4$. The reaction temperature was maintained at 110°C for about 12 h. Then extraction was performed (consistent with the above operation). After removing the residual solvent with a rotary evaporator, silica gel powder was added for column chromatography. The mobile phase was PE:DCM=3:1, and a deep red solid compound 3 (5,6-dinitro-4-(4-octylthiophen-2-yl)-7-(6-undecylthieno[3,2-b]thiophen-2-yl)benzo[c][1,2,5]thiadiazole) of 4.8g was obtained.

Compound 5 (2 g) and $P(Ph)_3$ (8 g) were weighed into a 100 mL three-necked flask. Then the flask was vacuumed and purged with nitrogen for protection. Then 20 mL of o-dichlorobenzene was injected into the flask, followed by vacuuming and flushing with nitrogen three times. Finally, the flask was heated and stirred at 180°C for 36 h. After the reaction was completed, silica gel powder was directly added into the flask and petroleum ether (PE) was used for column chromatography to remove o-dichlorobenzene and impurities dissolved in PE. Then all products were washed with ethyl acetate, spin dry, and transfer four times with 5 mL of DMF into a 100 mL three-necked flask. 1-bromo-2-ethylhexane, Na_2CO_3 and KI were added into the flask that was then vacuumed and purged with nitrogen. Furthermore, the flask was heated and stirred at 95°C for 24 h, followed by cooling to room temperature. The mixture was poured into a 500 mL separating funnel, the flask was rinsed with ethyl acetate (EA) and deionized water, and extract repeatedly until the aqueous phase was relatively clear. After spin drying, DCM and water were used for further extraction. After spin drying the final extract, silica gel powder was added the flask and PE:DCM=2:1 was adopted for column chromatography, finally 0.82g of yellow oily liquid compound 4 (11,12-bis(2-ethylhexyl)-1-octyl-8-undecyl-11,12-dihydro-[1,2,5]thiadiazolo[3,4-e]thieno[2',3':4,5]pyrrolo[3,2-g]thieno[2',3':4,5]thieno[3,2-b]indole) was obtained.

0.4g of compound **6** was weighted into a 100 mL three-necked flask, 30 mL of 1,2-dichloroethane and 2.5 mL of DMF were added into the flask respectively. The flask was evacuated and flushed with nitrogen, followed by storing in an ice bath and adding 5 mL of $POCl_3$. The flask was stirred at low temperature for 2 h, then was gradually heated up to 90°C and stirred for 12 h. Then the flask was cooled to room temperature and the reaction solution was dropwise added to a saturated solution of sodium carbonate, and the solution was continuously stirred overnight. Then DCM was used to extract the product. The extracted product was dried and was mixed with silica gel powder. Subsequently, PE:EA=10:1 as the mobile phase was adopted for separation and purification. After recrystallization, 0.4g of light yellow solid compound **5** (11,12-bis(2-ethylhexyl)-1-octyl-8-undecyl-11,12-dihydro-[1,2,5]thiadiazolo[3,4-e]thieno[2',3':4,5]pyrrolo[3,2 g]thieno[2',3':4,5] thieno[3,2-b]indole-2,9-dicarbaldehyde) was obtained.

Compound TB-SCl:

Compound 7 (200 mg) and compound 8 2-(5,6-dichloro-3-oxo-2,3-dihydro-1H-inden-1-ylidene)malononitrile (500 mg) were dissolved in $CHCl_3$. While pyridine was added dropwise slowly under nitrogen, the mixture gradually turned blue and black. After reacting overnight at 60°C, a dropper was used to slowly drop the solution into a methanol solution which was settled overnight. The sediment was filtered and PE:CF=1:3 column chromatography was used to obtain the product TB-4F. Then, CF and methanol were used for two times of recrystallization, followed by PE:CF=1:2 column chromatography for the obtained product. n-hexane and CF were used to further recrystallize twice to obtain 180 mg of dark-blue solid.

Compound TB-S:

Compound 7 (200 mg) and compound 9 2-(6-oxo-5,6-dihydro-4H-cyclopenta[c]thiophen-4-ylidene)malononitrile (500 mg) were dissolved in $CHCl_3$. While pyridine was added dropwise slowly under nitrogen, the mixture gradually turned blue and black. After reacting overnight at 60°C, a dropper was used to slowly drop the solution into a methanol solution which was settled overnight. The sediment was filtered and PE:CF=1:3 column chromatography was used to obtain the product TB-4F. Then, CF and methanol were used for two times of recrystallization, followed by PE:CF=1:2 column chromatography for the obtained product. n-hexane and CF were used to further recrystallize twice to obtain 168 mg of dark-blue solid.

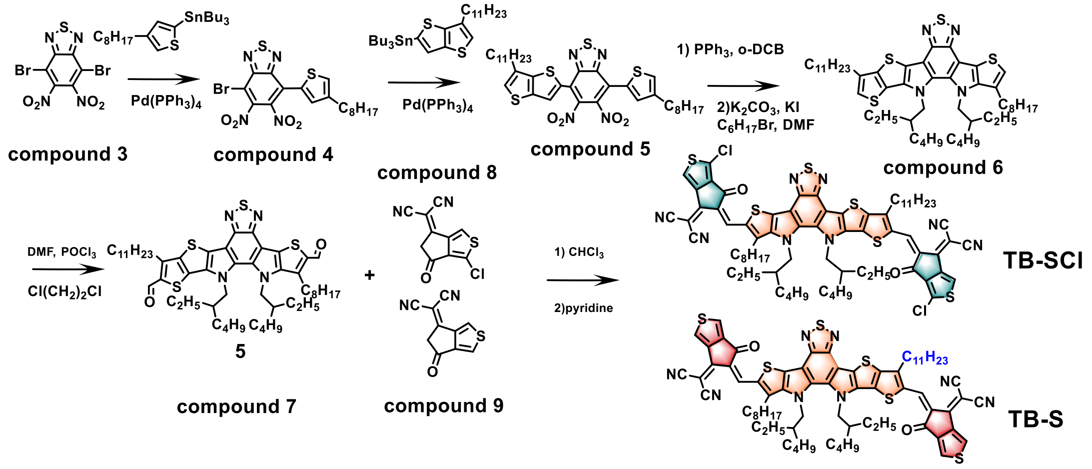

Scheme 3.2. Synthesis route to TB-SCl and TB-S.

Compound 6, compound 7, TB-SCl, and TB-S were confirmed by ^{1}H NMR spectroscopy and TOF MS:

11,12-bis(2-ethylhexyl)-1-octyl-8-undecyl-11,12-dihydro-[1,2,5]thiadiazolo[3,4-e] thieno [2',3':4,5] pyrrolo[3,2-g]thieno[2',3':4,5]thieno[3,2-b]indole (compound **6**): 1H NMR (400 MHz, CDCl3) δ 7.05 (s, 1H), 7.01 (s, 1H), 4.61 (d, J = 7.3 Hz, 2H), 4.48 (d, J = 7.4 Hz, 2H), 2.92 (t, J = 7.6 Hz, 2H), 2.82 (t, J = 7.7 Hz, 2H), 2.06 – 1.95 (m, 1H), 1.92 – 1.80 (m, 4H), 1.78 – 1.69 (m, 1H), 1.53 – 1.20 (m, 34H), 1.13 – 0.33 (m, 38H).

11,12-bis(2-ethylhexyl)-1-octyl-8-undecyl-11,12-dihydro-[1,2,5]thiadiazolo[3,4-e] thieno [2',3':4,5] pyrrolo [3,2-g]thieno[2',3':4,5]thieno[3,2-b]indole-2,9-dicarbaldehyde (compound **7**): 1H NMR (400 MHz, CDCl3) δ 10.15 (s, 1H), 10.15 (s, 1H), 4.63 (d, J = 7.6 Hz, 2H), 4.48 (d, J = 6.5 Hz, 2H), 3.20 (t, J = 7.7 Hz, 4H), 1.92 (dt, J = 11.8, 6.1 Hz, 6H).

2,2'-((5Z,5'Z)-((11,12-bis(2-ethylhexyl)-1-octyl-8-undecyl-11,12-dihydro-[1,2,5]thiadiazolo[3,4-e]thieno[2',3':4,5]pyrrolo[3,2-g]thieno[2',3':4,5]thieno[3,2-b]indole-2,9-diyl) bis (methanylylidene)) bis(1-chloro-6-oxo-5,6-dihydro-4H-cyclopenta[c]thiophene-5,4-diylidene))dimalononitrile (TB-SCl): 1H NMR (600 MHz, CDCl3) δ 9.13 (s, 1H), 9.10 (s, 1H), 4.73 (s, 2H), 4.55 (s, 2H), 3.22 (s, 4H), 1.98 (s, 1H), 1.86 (s, 4H), 1.76 (s, 1H).

2,2'-((5Z,5'Z)-((11,12-bis(2-ethylhexyl)-1-octyl-8-undecyl-11,12-dihydro[1,2,5]thiadiazolo[3,4-e]thieno[2',3':4,5]pyrrolo[3,2-g]thieno[2',3':4,5]thieno[3,2-b]indole-2,9-diyl)bis (methanylylidene)) bis (6-oxo-5,6-dihydro-4H-cyclopenta [c]thiophene-5,4-diylidene)) dimalononitrile (TB-S): 1H NMR (400 MHz, CDCl3) δ 9.13 (s, 1H), 9.09 (s, 1H), 8.39 (s, 2H), 7.96 (s, 2H), 4.73 (d, J = 7.6 Hz, 3H), 4.54 (s, 3H), 3.22 (s, 4H), 2.00 (s, 1H), 1.86 (d, J = 7.7 Hz, 4H), 1.75 (s, 1H).

2,2'-((5Z,5'Z)-((12,13-bis(2-ethylhexyl)-3,9-diundecyl-12,13-dihydro-[1,2,5]thiadiazolo[3,4-e] thieno[2'',3'':4',5']thieno[2',3':4,5]pyrrolo[3,2-g]thieno[2',3':4,5]thieno[3,2-b]indole-2,10-diyl)bis(methanylylidene))bis(1-chloro-6-oxo-5,6-dihydro-4H-cyclopenta[c]thiophene-5,4-diylidene)) dimalononitrile (BTP-2ThCl): was synthesized referred reported work[147]. 1H NMR (400 MHz, CDCl3) δ 9.08 (s, 2H), 8.17 (s, 2H), 4.75 (s, 4H), 3.22 (s, 4H), 2.09 (s, 2H), 1.87 (s, 4H), 1.38 – 0.96 (m, 48H), 0.86 (t, J = 6.8 Hz, 7H), 0.75 – 0.65 (m, 12H).

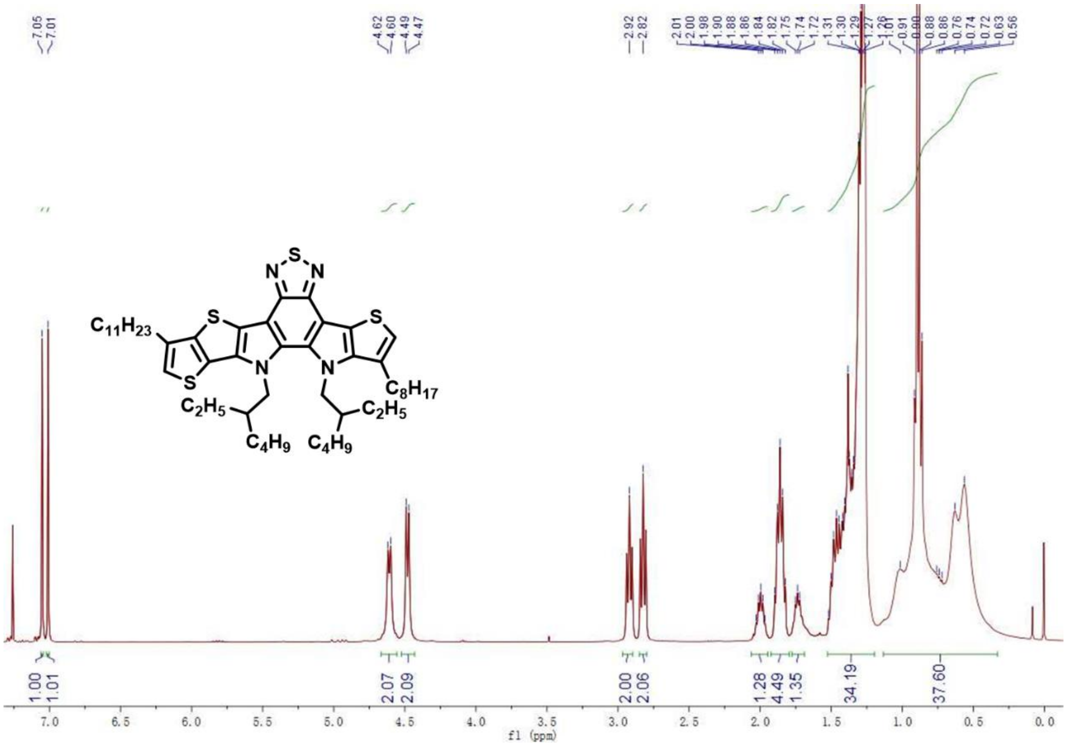

Figure 3.3. 1 H NMR spectrum of compound 6.

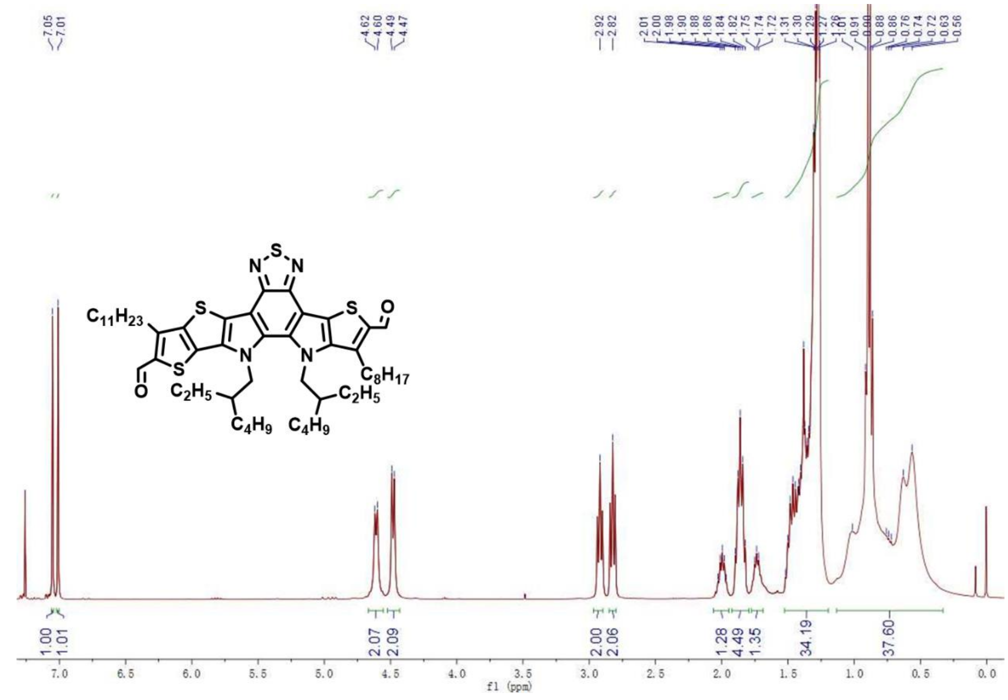

Figure 3.4. 1 H NMR spectrum of compound 7.

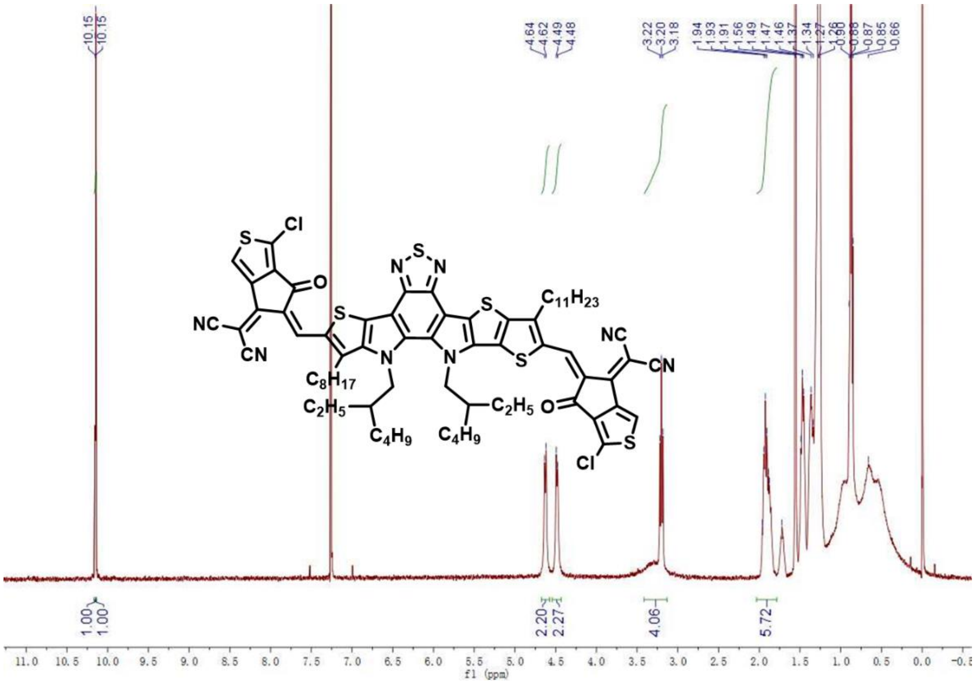

Figure 3.5. 1 H NMR spectrum of TB-SCl.

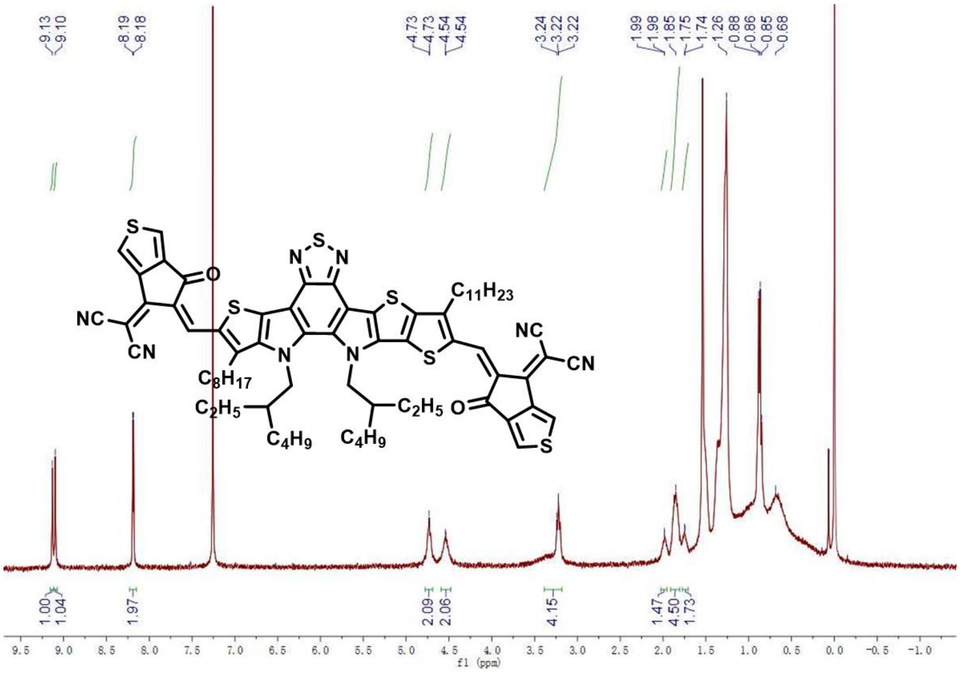

Figure 3.6. 1 H NMR spectrum of TB-S.

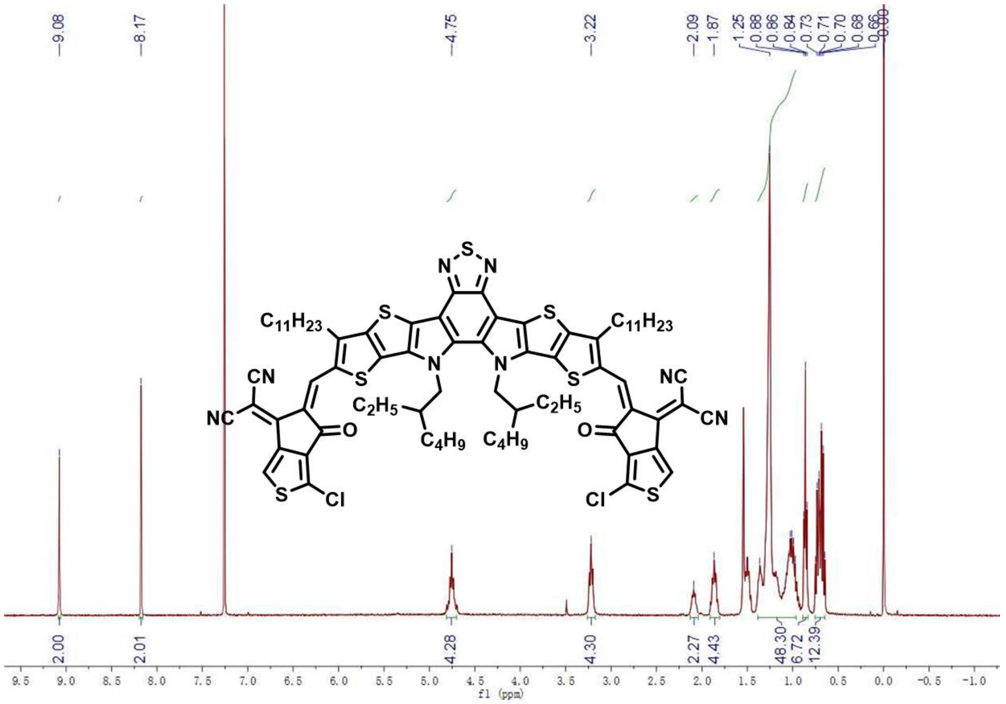

Figure 3.7. 1 H NMR spectrum of BTP-2ThCl.

3.4.3 Alkoxy substitution on asymmetric conjugated molecule enabling over 18% efficiency in ternary organic solar cells by reducing non-radiative voltage loss

The newly designed acceptor TB-S1 and TB-S1-O were synthesized according to **Scheme 3.3**. Compound **7** and TB-S was synthesized according to the reported work[2]. Compounds 9, 10 and 11 were purchased from eFlexPV Limited. TB-S1 and TB-S1-O were designed and synthesized as shown in the following:

Compound TB-S1:

Compound 7 (0.12 g) and compound 10 (0.0745 g) were dissolved in 60 mL CF, 0.5 mL pyridine was dropped under Argon gas. Then the reaction mixture was refluxed for 12 h. Afterwards, the reaction mixture was dropped to 400 mL methanol which precipitated a solid. The solid was filtered off, and purified by silica gel chromatography (eluent, petroleum ether: ethyl acetate=15:1) to afford a dark-green solid. The solid was recrystallized from a 3:1 volume ratio of CF and methanol mixture to afford compound TB-S1.

Compound TB-S1-O:

Compound 11 (0.267 g) and compound 10 (0.15 g) were dissolved in 60 mL CF, 0.5 mL pyridine was dropped under Argon gas. Then the reaction mixture was refluxed for 12 h. Afterwards, the reaction mixture was dropped to 400 mL methanol which precipitated a solid. The solid was filtered off, and purified by silica gel chromatography (eluent, petroleum ether: dichloromethane=1:3) to afford a dark-red solid. The solid was recrystallized from a 3:1 volume ratio of CF and methanol mixture to afford compound TB-S1.

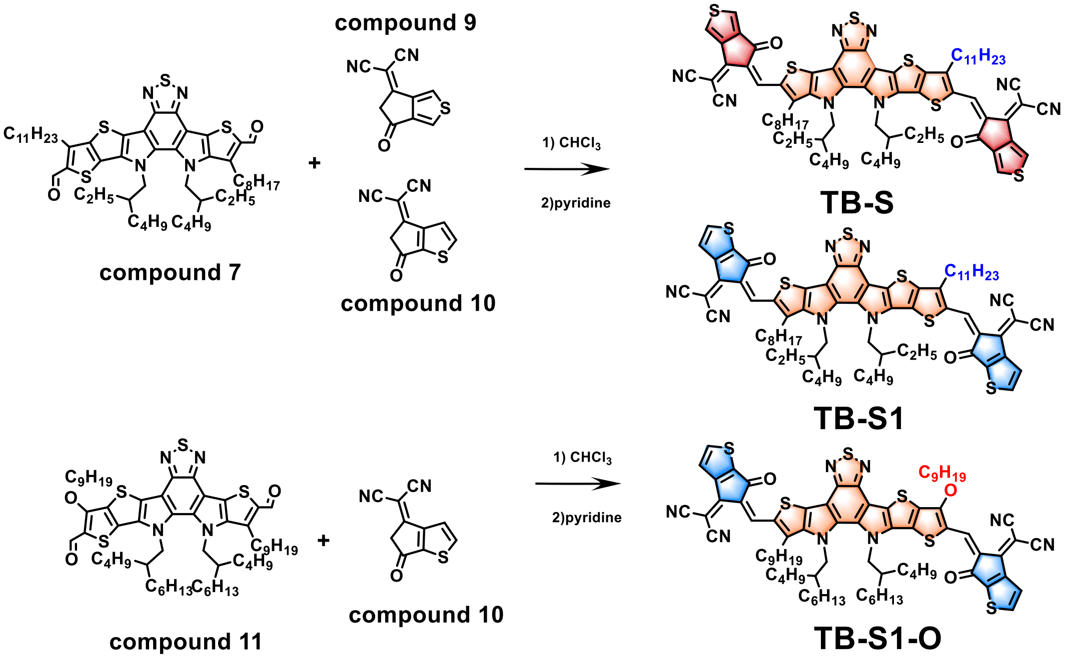

Scheme 3.3. Synthetic route for TB-S1 and TB-S1-O.

TB-S1 and TB-S1-O were confirmed by ^{1}H NMR spectroscopy and TOF MS:

Compound TB-S1:

Compound 7 (0.12 g, 0.129 mmol) and compound 10 (0.0745 g, 0.372 mmol) were dissolved in 60 mL CF, 0.5 mL pyridine was dropped under Argon gas. Then the reaction mixture was refluxed for 12 h. Afterwards, the reaction mixture was dropped to 400 mL methanol which precipitated a solid. The solid was filtered off, and purified by silica gel chromatography (eluent, petroleum ether: ethyl acetate=15:1) to afford a dark-green solid. The solid was recrystallized from a 3:1 volume ratio of CF and methanol mixture to afford compound TB-S1 0.04 g, yield 24%. ^{1}H NMR (400 MHz, $CDCl_3$, ppm,) δ: 8.95 (d, J = 12 Hz 2H,ArH), 7.97 (m, 4H ArH),4.73 (d, J = 7.6 Hz, 2H,NCH_2), 4.52 (s, 2H,CH_2), 3.20 (t, J = 8 Hz,4H,CH_2), 2.00 (s, 1H, CH), 1.86 (s, 4H, CH_2), 1.75 (s, 1H, CH),1.30-1.24 (m,42H,CH_2),0.895-0.864(m,18H,CH_3) . HR-TOF-MS (APCI) *m/z*: $[M+H]^+$ calcd for $C_{73}H_{81}N_8O_2S_6$, 1293.4807; found, 1293.4817.

Compound TB-S1-O:

Compound 11 (0.267 g, 0.2558 mmol) and compound 10 (0.15 g, 0.75 mmol) were dissolved in 60 mL CF, 0.5 mL pyridine was dropped under Argon gas. Then the reaction mixture was refluxed for 12 h. Afterwards, the reaction mixture was dropped to 400 mL methanol which precipitated a solid. The solid was filtered off, and purified by silica gel chromatography (eluent, petroleum ether: dichloromethane=1:3) to afford a dark-red solid. The solid was recrystallized from a 3:1 volume ratio of CF and methanol mixture to afford compound TB-S1 0.061 g, yield 17%. ^{1}H NMR (400 MHz, $CDCl_3$, ppm) δ: 9.13 (s, 1H,ArH), 8.97 (s, 1H, ArH), 7.99 (m, 4H, ArH), 4.77 (t, J = 6.4 Hz 2H,OCH_2), 4.69 (d, J = 7.6 Hz, 2H, NCH_2), 4.53 (s, 2H, NCH_2), 3.35 – 3.03 (m, 2H, CH_2), 2.09 – 1.97 (m, 4H, CH_2), 1.89 – 1.74 (m, 4H, CH_2), 1.31-1.19 (m, 56H,CH_2),0.91-0.79(m, 18H, CH_3). HR-TOF-MS (APCI) *m/z*: $[M+H]^+$ calcd for $C_{80}H_{95}N_8O_3S_6$, 1407.5851; found, 1407.5781.

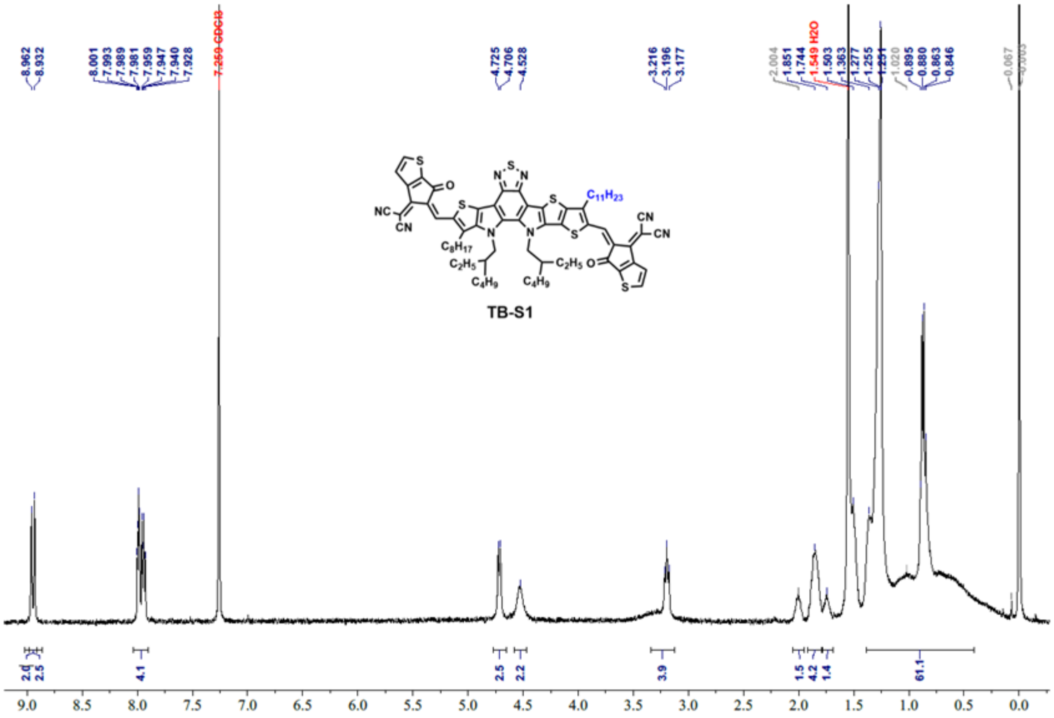

Figure 3.8. 1 H NMR spectrum of TB-S1.

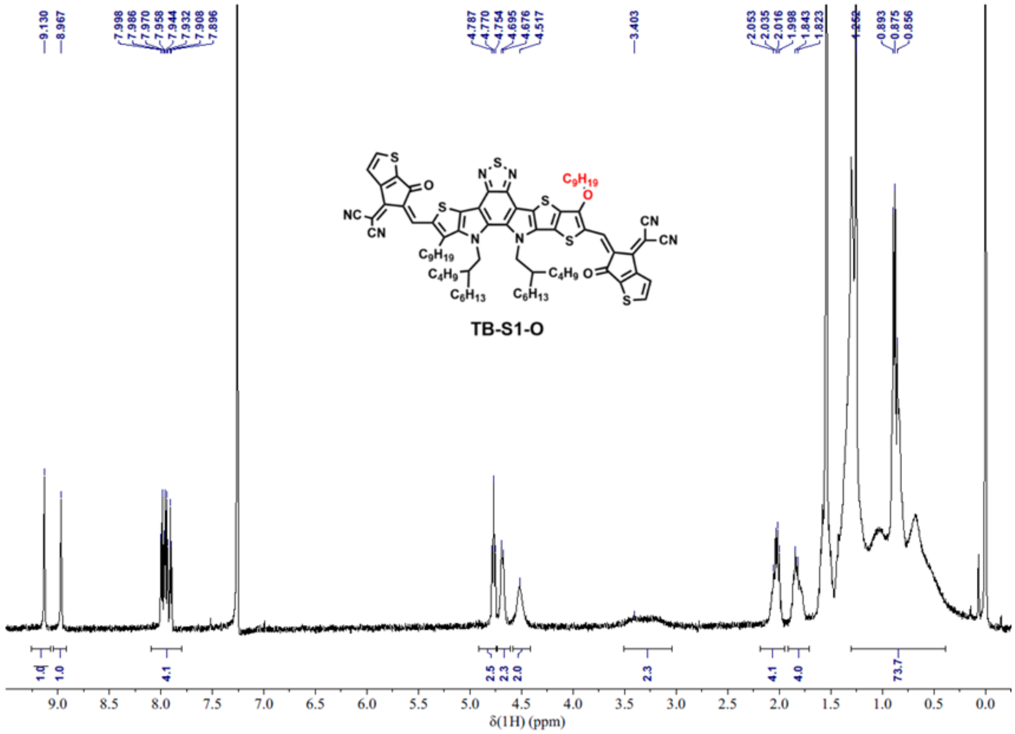

Figure 3.9. 1 H NMR spectrum of TB-S1-O.

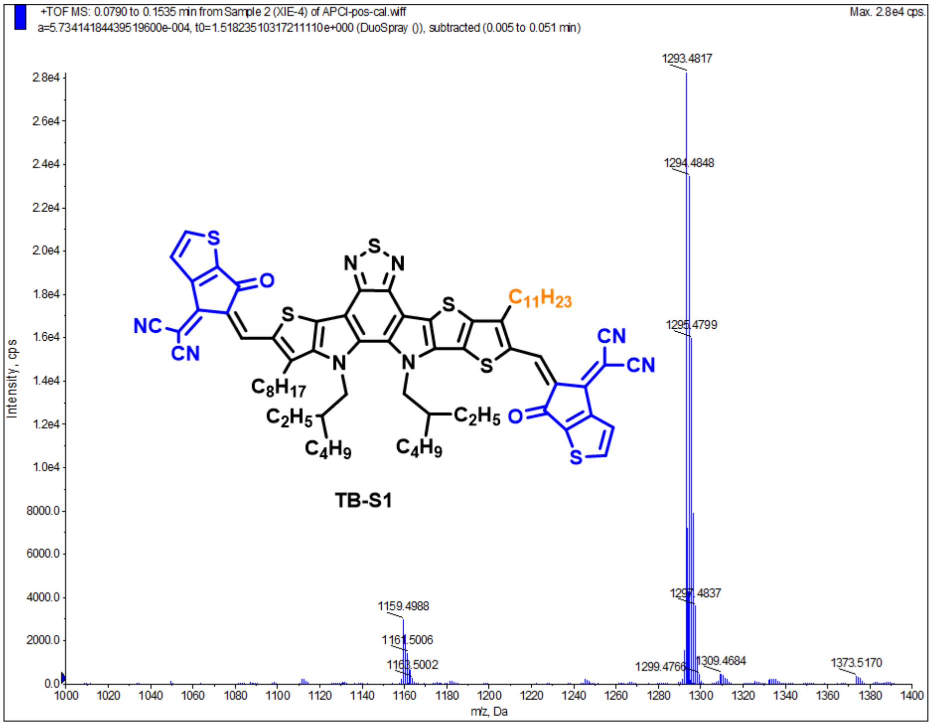

Figure 3.10. The mass spectrum of TB-S1.

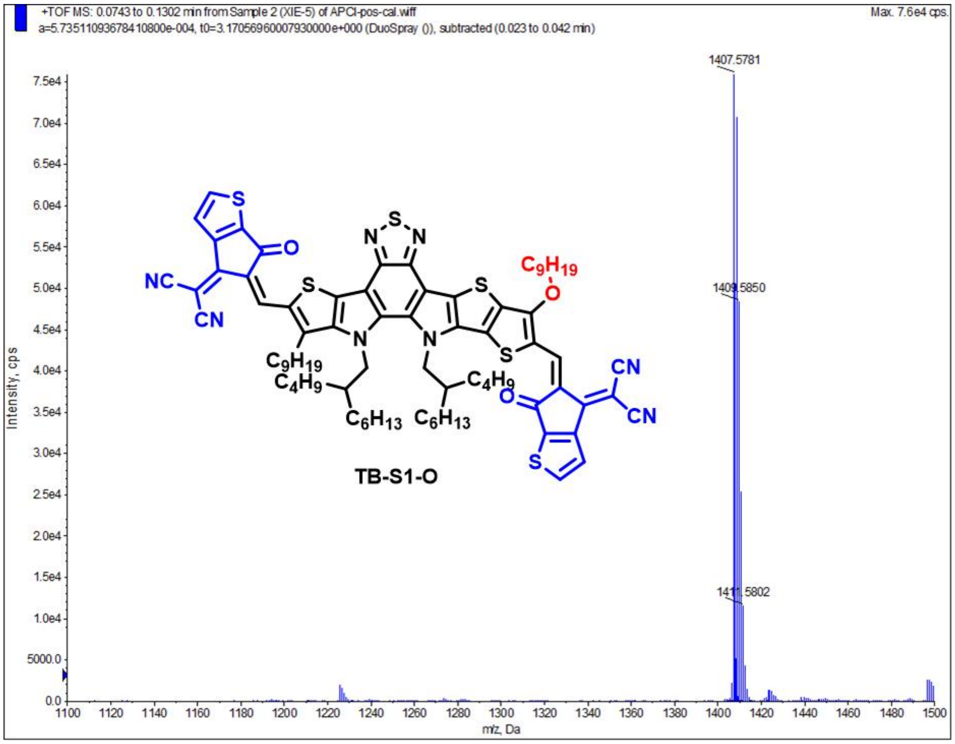

Figure 3.11. The mass spectrum of TB-S1-O.

3.5 Device fabrication

A device consists of a substrate (ITO/glass or PH1000/PET), a hole transport layer, an active layer, an electron layer, and a metal layer, which are deposited layer by layer. The materials that need to be deposited can be classified as either liquid or solid. The spin coating method is used to deposit liquid-processable materials such as PEDOT:PSS or organic materials dissolved in an organic solvent for the active layer, hole transport layer, and electron transport layer. Solid materials that cannot be processed in liquid form can be deposited using an evaporation machine, such as the Ag electrode. As shown in **Figure 3.12a**, ITO/glass substrates possess 2.5 mm width and 14.9 mm length ITO in the middle of glass. One device possesses 2 subcells.

For this project, the OPV devices were manufactured in batches, enabling the fabrication of up to 4 independent devices resulting in 8 independent subcells simultaneously. To ensure the reliability and reproducibility of the data, several experimental trials were conducted. The area of each device is 0.0625 cm^2 (2.5 mm ×2.5 mm). The device layout with mask is described in **Figure3.12b**. To prevent the collection of transverse space-charge flow, each device must be tested using a calibrated mask with an area of 0.04 cm^2, resulting in an active area of 0.04 cm^2 for each device.

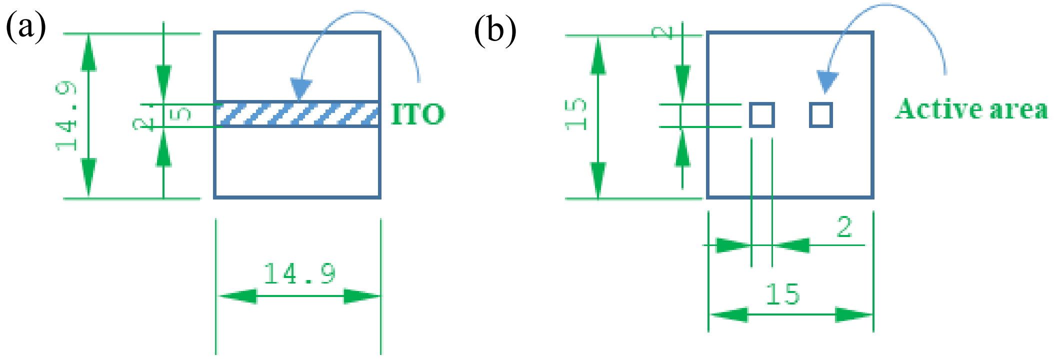

Figure 3.12. (a) the diagram of ITO on glass, and (b) device with calibrated mask resulting in an active area of 0.04 cm^2 for each subcell.

3.5.1 Understanding the effect of sequential deposition processing for high-efficient organic photovoltaics to harvest sunlight and artificial light

For conventional bulk heterojunction (**C-BHJ**) process, PM6 and TB-4F were mixed in CF and was spin-coated at the same time as shown in **Figure 3.13a**. For the process of sequential deposition processing (**SD-BHJ**) as shown in **Figure 3.13b**, PEDOT:PSS was firstly spin-coated onto ITO substrate, followed by spin-coating neat PM6 dissolved in CF. Subsequently, neat acceptor, TB-4F, dissolved in CF as well was spin-coated onto the bottom donor layer, thereby penetration of TB-4F into the PM6 film was formed through the swelling of polymer by the CF. Therefore, the vertical phase morphology was formed as depicted in **Figure 3.13b**. The optimal condition for SD-BHJ was determined by controlling the spin rate of PM6 with fixed concentration and varying the concentration of acceptors with fixed spin rate.

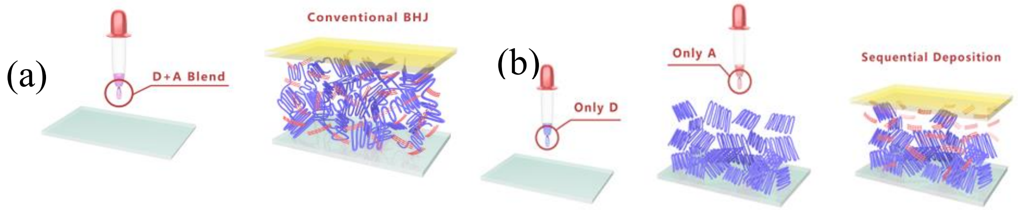

Figure 3.13. (a) the flow charts of conventional BHJ process, and (b) sequential deposition process.

Devices were fabricated with the conventional device structure of glass/ITO/PEDOT: PSS/Active layer/PFN-Br/Al. ITO-coated glass substrates were cleaned with detergent and ultrasonicated in deionized water, acetone and iso-propanol for 20 min each and subsequently blow-dried by nitrogen. The substrates were then subjected to a UV-ozone treatment step for 30 min. The PEDOT:PSS was spin-cast onto the ITO surface at 3000 rpm for 60 s, and baked at 130 °C for 20 min in air. The samples were then transferred into a dry nitrogen glove box (<10 ppm O_2).

SD-BHJ:

For the fabrication of SD-BHJ based on PM6/TB-4F: the neat PM6 in CF solution (7.5 mg mL$^{-1)}$ was spin-coated onto the PEDOT:PSS-coated substrates at different speeds (2500, 2000, 1500 rpm) and then TB-4F in CF solution (9, 10, 11 mg mL^{-1}) with 0.25% (volume fraction) chloronaphthalene (CN) was subsequently spin-coated at 3000 rpm on top of PM6 layer; CS_2 was used to process solvent-annealing (30 s) followed by 3 min thermal-annealing at 85 ºC.

C-BHJ:

For PM6:TB-4F-based C-BHJ devices, D/A ratio is 1:1.2 (16 mg ml^{-1}), which was dissolved and blended in CF with 0.5% (volume fraction) CN. Then, the solvent was spin-coated onto the substrates covered by PEDOT:PSS at 2500 rpm; CS_2 was used to process solvent-annealing (30 s) followed by thermal-annealing at 85 ºC for 3 min. Then, the solvent was spin-coated onto the substrates covered by PEDOT:PSS. For the cathode interlayer, PDINO was dissolved in methanol at the concentration of 1.5 mg ml^{-1} and spin-coated onto the photoactive layer at 3000 rpm for 1 min for all devices. Finally, a 100 nm Al electrode were deposited on top of the active layers through a shadow mask under a vacuum about 1×10^{-5} Pa. The active area was 0.04 cm^2.

3.5.2 Rational tuning of intermolecular and intramolecular interactions enabling high-efficiency indoor organic photovoltaics

Rigid device:

Devices were fabricated with the conventional device structure of glass/ITO/PEDOT:PSS/Active layer/PDINO/Al. ITO-coated glass substrates were cleaned with detergent and ultrasonicated in deionized water, acetone and iso-propanol for 20 min each and subsequently blow-dried by nitrogen. The PEDOT:PSS was spin-cast onto the ITO surface at 3000 rpm for 60 s, and baked at 130 °C for 20 min in air. The PM6:acceptors (1:1.2 weight ratio) were dissolved in CF and stirred overnight in a nitrogen-filled glove box. The optimal concentration for PM6:BTP-2ThCl, PM6:TB-SCl, and PM6:TB-S are 16 mg ml^{-1}. The active layer solution was spin-cast at 2500 rpm for 30 s. CS_2 was used to process solvent-annealing (2 min). For the cathode interlayer, PDINO was dissolved in methanol at the concentration of 1.5 mg ml^{-1} and spin-coated onto the photoactive layer at 3000 rpm for 1 min for all devices. Finally, a 100 nm Al electrode were deposited on top of the active layers through a shadow mask under a vacuum about 1×10^{-5} Pa. The active area was 0.04 cm^2. Although SD-BHJ has been figured out that it show superior performance under the indoor condition in comparison with C-BHJ (in chapter 4), the aim of this work is to demonstrate the relationship between performance and molecular design rather than processing technology, C-BHJ technology was adopted in this work to avoid plenty of parameter optimization so that lot of time can be saved.

Flexible device:

Preparation of PET (polyethylene terephthalate)/PH1000 flexible transparent electrodes (FTEs). The PET/PH1000 composite electrodes were made by simple solution processing method. 0.3vol% Zonyl FS300 was added in PH1000 aqueous solution and stirred for ~2h at room temperature. Filter the PH1000 mixture through 0.45 μm syringe filter and spin-cast at 1800 rpm to achieve a uniform film on the PET substrate then baked at 100℃ for 10 min on a hot plate. After that, methanesulfonic acid (99%, J&K Chemicals Inc.) was drop-coated on the surface of PH1000 films and retained for 10 min, then the acid-treated films were washed with DI water and ethanol for 3 times each to remove residual acid. Another 15 minutes of 100℃ thermal annealing was applied to dry the PET/PH1000 films. At last, PEDOT:PSS (Clevios P VP 4083) was spin-cast onto the substrate to obtain well-distributed PET/PH1000 composite electrodes. The other procedures are the same with rigid device.

3.5.3 Alkoxy substitution on asymmetric conjugated molecule enabling over 18% efficiency in ternary organic solar cells by reducing non-radiative voltage loss

Devices for PM6:BTP-eC9, PM6:TB-S1, PM6:TB-S1-O, PM6:BTP-eC9:TB-S, PM6:BTP-eC9:TB-S1, PM6:BTP-eC9:TB-S1-O were fabricated with the conventional device structure of glass/ITO/PEDOT:PSS/Active layer/PDINN/Ag. The fabrication process of PM6:TB-S refers to **section 3.5.2**. ITO-coated glass substrates were cleaned with detergent and ultrasonicated in deionized water, acetone, and iso-propanol for 20 min each and subsequently blow-dried by nitrogen. The PEDOT:PSS was spin-cast onto the ITO surface at 3000 rpm for 60 s, and baked at 130 °C for 20 min in air.

Binary device:

For binary devices, the ratio of donor:acceptor was kept in (1:1.2 weight ratio), therefore the weight of acceptor equaled to the weight of PM6 times 1.2. For the blended solutions of PM6:BTP-eC9, PM6:TB-S1, and PM6:TB-S1-O, the concentration of donor were kept at 7.5 mg ml^{-1} with 0.5wt% of total active material for 1,8-diiodooctane (DIO), therefore the volume of solvent (CF) to dissolve the mixture of donor and acceptors was calculated by dividing the weight of donor (mg) by the concentration 7.5 mg ml^{-1}. The mixture of donor and acceptor were dissolved in CF in a nitrogen-filled glove box and stirred overnight and heated at 40°C for 30min before fabrication. The active layer solution was spin coated at 4000 rpm for 30s to obtain a thickness of ~120 nm followed by 10 min thermal annealing at 100℃. For the cathode interlayer, PDINN was dissolved in methanol at the concentration of 1 mg ml^{-1} and spin-coated onto the photoactive layer at 2000 rpm for 1 min to obtain a thickness of ~5 nm without any annealing. Finally, a 150 nm Ag electrode were deposited on top of the active layers through a shadow mask under a vacuum about 1×10^{-5} Pa. The active area with calibration was 0.04 cm^2.

Ternary device:

For ternary devices, the ratio of donor:host acceptor:guest acceptor was kept in

(1:1.05:0.15 weight ratio), therefore the weight of acceptor equaled to the weight of PM6 times 1.05 for host acceptor and the weight of PM6 times 0.15 for guest acceptor. For the blended solutions of PM6:BTP-eC9:TB-S, PM6:BTP-eC9:TB-S1, PM6:BTP-eC9:TB-S1-O, the concentration of PM6 was kept at 7.5 mg ml^{-1} with 0.5wt% of total active material for DIO, therefore the volume of solvent (CF) to dissolve the mixture of donor and acceptors was calculated by dividing the weight of donor (mg) by the concentration 7.5 mg ml^{-1}. The mixture of donor and acceptor were dissolved in CF in a nitrogen-filled glove box and stirred overnight and heated at 40°C for 30min before fabrication. The active layer solution was spin-cast at 4000 rpm for 30s to obtain a thickness of ~120 nm followed by 10 min thermal annealing at 100℃. For the cathode interlayer, PDINN was dissolved in methanol at the concentration of 1 mg ml^{-1} and spin-coated onto the photoactive layer at 2000 rpm for 1 min to obtain a thickness of ~5 nm without any annealing. Finally, a 150 nm Ag electrode were deposited on top of the active layers through a shadow mask under a vacuum about 1×10^{-5} Pa. The active area with calibration was 0.04 cm^2.

3.6 Characterization

3.6.1 *J-V* measurement under 1-sun intensity condition, indoor condition, and dark condition

Once the device has been fabricated, it will be tested to conduct the PCE by *J-V* curve under the same international standard to allow a valid comparison between OPVs that produced by different research groups.

1-sun intensity:

The *J-V* curve of the device was tested by using a Keithley 2400 source meter under AM1.5, 100 mW cm^{-2} illumination conditions (using Newport OrielSol3A simulator). The light intensity simulator was calibrated using a NREL-certified silicon solar cell. PV performance of the device (such as J_{SC}, V_{OC}, *FF*) was measured by connecting two electrodes (bottom and top) through the outer circuit.

Data is automatically collected and recorded for each test. The data was plotted as current density vs voltage curve, yielding a typical *J-V* characteristics curve.

Indoor condition:

The *J-V* curve of the device was tested by using a Keithley 2400 source meter under artificial light. Light source is 3000k-LED light and its spectrum and incident power P_{in} was accurately measured by the spectrometer as described in section 3.6.17 (Maya2000 Pro, Ocean Optics). PV performance of the device (such as $J_{\mathrm{SC}}, V_{\mathrm{OC}}$, *FF*) was measured by connecting two electrodes (bottom and top) through the outer circuit. Data was automatically collected and recorded for each test. The data was plotted as current density vs voltage curve, yielding a typical *J-V* characteristics curve.

Dark condition:

The test method was similar to the 1-sun intensity process, but with the Newport OrielSol3A simulator switched off, resulting in zero illumination. The resulting data were plotted as a current density vs voltage curve, yielding a typical *J-V* characteristic curve under dark conditions.

3.6.2 Exciton dissociation efficiency calculation

Exciton dissociation efficiency of the device was tested by using a Keithley 2400 source meter under AM1.5, 100 mw cm^{-2} illumination conditions (using Newport OrielSol3A simulator) to obtain J_{light} and dark condition to obtain J_{dark}. Data was automatically collected and recorded for each test.

$$J_{\mathrm{ph}} = J_{\mathrm{light}} - J_{\mathrm{dark}} \qquad \text{Equation(3.1)}$$

$$V_{\mathrm{eff}} = V_0 - V \qquad \text{Equation(3.2)}$$

where $J_{\mathrm{light}}$and J_{dark} are the current densities under light and dark conditions. V_0 was the voltage value as $J_{\mathrm{ph}} = 0$ and V was the applied voltage. J_{sat} is the saturation current density, which is equal to J_{SC} when $V_{\mathrm{eff}} \geq 2.0$ V. The J_{ph} at short circuit condition or the maximum power output condition is defined as $J_{\mathrm{ph}}{}^{1}$and $J_{\mathrm{ph}}{}^{2}$, respectively. The exciton dissociation (η_{diss}) and charge collection efficiency (η_{coll}) can be evaluated according to the $J_{\mathrm{ph}}{}^{1}/J_{\mathrm{sat}}$ and $J_{ph}{}^{2}/J_{\mathrm{sat}}$, respectively.

The η_{diss} and η_{coll} were obtained according to the equation of $\eta = J_{\mathrm{ph}}/J_{\mathrm{sat}}$ (saturated current density) at the conditions of short circuit and maximum power output.

3.6.3 EQE (external quantum efficiency) measurement

EQE was measured using a quantum efficiency measurement system. The system used a monochromatic light source to irradiate the device at different wavelengths and then measured the intensity of reflected, transmitted, and absorbed light at each wavelength. By calculating the device's response to the incident light intensity, the EQE value of the device was obtained. EQE is an important photovoltaic parameter that reflects the device's response to light of different wavelengths and is a key indicator for evaluating the performance of photovoltaic devices. Measurements were conducted in a nitrogen-filled glovebox without device encapsulation. Quantum efficiency measurement system (QE-R, Enli Technology) with a 75W Xenon lamp source, whose light intensity was calibrated using a reference standard calibrated silicon probe (RC-S103011-G) from Enli Technology Limited, was used for measurements. The EQE performance of the device was generated and plotted into EQE and/or integrated J_{SC}.

3.6.4 UV-vis measurement

UV-visible (UV-vis) spectroscopy is a widely used analytical technique for measuring the absorbance or transmittance of a sample at different wavelengths of light in the ultraviolet and visible regions of the electromagnetic spectrum. The measurement was performed by passing a beam of light through the sample in a quartz cuvette. A detector on the other side of the cuvette measured the amount of light that was absorbed by the sample at each wavelength.

The quartz substrate (1.5×1.5 cm) was cleaned using an ultrasonic cleaner with a mixture of detergent, deionized water, acetone, and isopropanol. The substrate was then dried using N_2 flow and further treated with UV-ozone before use. The tested sample was spined onto the quartz. For example, to calculate the absorption of the TB-S1-O, the TB-S1-O solution was spined on the substrate directly at 4000 rpm for 30s followed by 10 min thermal annealing at 100℃. Subsequently, the sample was transferred for measurement using a LAMBDA 950 spectrophotometer (PerkinElmer). The resulting data was used to determine the absorbance or transmittance of the sample at different wavelengths.

3.6.5 Transient photovoltage measurement (TPV)/Transient photocurrent measurement (TPC) measurement

TPV and TPC tests are two common techniques used to characterize the optoelectronic properties of semiconductors. Here are the basic steps involved in a typical TPV/TPC test: Once the device has been fabricated, it was mounted onto a sample holder. A light source such as a laser was used to excite the device. TPV measurements study the photovoltage decay upon a small optical perturbation during various constant light-intensity biases and at open-circuit bias conditions. The device was illuminated at the open-circuit mode within 50 μs to allow photovoltage to reach steady state. Subsequently, the light was switched-off and the charge was extracted at the short-circuit mode by applying 100 Ω resistor. The subsequent voltage decay was then recorded to directly monitor bimolecular charge carrier recombination. The photovoltage decay kinetics of all devices follow a mono-exponential decay: V = A exp(-t/τ), where t represents the time and τ represents the charge carrier lifetime. The TPV signal can provide information about the carrier recombination lifetime and mobility of the device. TPC analysis measure the time-dependent extraction of photogenerated charge carriers. During the measurement, the device was set under short-circuit condition; a 200 μs light pulse was used allowing the current density to reach the steady-state condition followed by turning off the light. Under dark condition, trapping pattern were analyzed. The TPC signal can provide information about the carrier transport properties of the device.

3.6.6 Charge mobility calculation

Space-charge-limited-current (SCLC) measurement was adopted to investigate the carrier mobilities for all the devices. Electron-only devices were fabricated in a structure of ITO/Ag/Active Layer/PDINN or PDINO or PFN-Br /Ag, whereas hole-only devices were fabricated utilizing a structure of ITO/PEDOT:PSS/Active Layer/MoO_3/Ag. The fabrication conditions of the active layers followed the same procedure described in the section of device fabrication. The charge mobilities were determined by fitting the dark current measurement curves according to the Motto-Gurney law:

$$J = \frac{9}{8}\mu\varepsilon_r\varepsilon_0(\frac{V^2}{L^3}) \qquad \text{Equation(3.3)}$$

Where *J* is the current density, ε_0 is the permittivity of free space (8.85×10^{-14} F cm^{-1}), ε_r is the relative permittivity of the materials, μ is the charge mobility, V is the applied voltage, and *L* is the active layer thickness. The parameter ε_r is assumed to be 3, which is a typical value for organic materials.

3.6.7 Photo-induced charge-carrier extraction in a linearly increasing voltage (photo-CELIV)

The photo-CELIV measurements were adopted to test the mobilities of devices, which was tested by the all-in-one characterization platform Paios developed and commercialized by Fluxim AG, Switzerland. Photo-CELIV measurements through conducting the photo-induced charge-carrier extraction in a linearly increasing voltage (voltage ramp rate 203V ms^{-1}, delay time: 0s, offset voltage: 0 V, light-pulse length: 100 μs, maximum voltage: 2V) were performed at 100 % light intensities of LED lamp source at 200 mW cm^{-2} to calculate the carrier mobility of the device. The equation[148] of $\mu = \frac{2d^2}{3At_{max}^2} \times \frac{1}{1+0.36 {}^{\Delta J}/_{J_0}}$ was adopted to calculate the mobility, where $\Delta J = J_{max}$-J_0 (J_{max} is maximal current and J_0 is initial current), A is the voltage rise speed of applied voltage pulse, t_{max} is the time where the current reach the maximum, and d is the thickness of active layer.

3.6.8 Energy loss measurement

The energy loss was estimated by the measurements of electroluminescence (EL), electroluminescence external quantum efficiency (EQE$_{EL}$), and highly sensitive EQE (s-EQE). EL measurements were conducted using an external voltage/current source provided by the OSCs (REPS, Enlitech) that comprised a Si-CCD detector combined with a monochromator. EL measurement system used a high-sensitivity camera to capture the EL image of the device, which allowed for the visualization of the recombination and defect states within the device. EQE$_{EL}$ performed by REPS, Enlitech, which was a physical quantity that describes the light-emitting efficiency of optoelectronic devices. It referred to the ratio of the number of photons emitted by the device to the number of injected electrons under electric current injection. And it described that how much electrical energy was converted into light energy by the OPVs. s-EQE was measured using an integrated system (PECT-600, Enlitech), where the photocurrent was atmplified and modulated by a lock-in instrument. E_{loss} was described by the following equation in three parts (energetic difference between the singlet excited state and the CT state, radiative energy loss and non-radiative energy loss):

$$E_{\text{loss}} = E_{\text{g}} - eV_{\text{OC}} = (E_g - E_{\text{CT}}) + (E_{\text{CT}} - eV_{\text{OC}} - \Delta E_{\text{nonrad}}) + \Delta E_{\text{nonrad}}$$

$$= \Delta E_{\text{CT}} + \Delta E_{\text{rad}} + \Delta E_{\text{nonrad}} \qquad \text{Equation(3.4)}$$

where E_g is the bandgap estimated by the intersection point of normalized electroluminescence (EL) and normalized highly sensitive EQE (s-EQE) plots. ΔE_{CT} was determined by the energetic difference between the singlet excited state and the CT state. E_{CT} was acquired from the intersection point of fitting s-EQE and EL curves by dual curve fitting based on Marcus theory as shown in [149, 150]. The ΔE_{CT} means the reduced voltage because of the CT process. The rest two parts of E_{loss} are radiative energy loss (ΔE_{rad}) and ΔE_{nonrad}. ΔE_{nonrad} is defined as ΔE_{nonrad}= -kT ln(EQE_{EL}). Moreover, ΔE_{rad} was calculated from the energy loss equation. Therefore, each part of energy loss could be deduced.

3.6.9 Electrochemical workstation measurement

Electrochemical workstation measurement was used to test the HOMO (highest occupied molecular orbital) and LUMO (lowest unoccupied molecular orbital) levels of organic materials. In the electrochemical workstation, techniques such as cyclic voltammetry (CV) was used to obtain data on the reduction potential and oxidation potential. By analyzing this data, the HOMO and LUMO levels were calculated. The energy levels for organic material were measured by CV station, which was performed by using Ag/AgCl as reference electrode in anhydrous CH_3CN solution, and ferrocene/ferrocenium (Fc/Fc+) was used as internal reference. The HOMO and LUMO were calculated according to the following equations:

HOMO= -[E_{ox}+(4.8-E_{FC})] eV Equation(3.5)

LUMO= -[E_{red}+(4.8-E_{FC})] eV Equation(3.6)

Where E_{OX} is the onset of oxidation and the E_{red} relates to the reduction potential, respectively.

3.6.10 Transmission electron microscopy (TEM) measurement

TEM is a technique used to study the structure and properties of materials at the nanoscale. The sample preparation is described in the following: The ITO substrates of size 1.5×1.5 cm were cleaned using an ultrasonic cleaner with a solution of detergent, deionized water, acetone, and isopropanol. After drying with N_2 stream, the substrates were treated with UV-ozone prior to use. The sample was prepared as an ultra-thin specimen that was transparent to electrons. Therefore, PEDOT:PSS was deposited onto the substrate followed by the deposition of sample (active layer). Annealing the film for 5 min until dry, the substrate was soaked into deionized water to dissolve PEDOT:PSS, resulting in a thin film of active material floating on the surface of water. The separated films were attached to a copper mesh and transferred for measurement in a Talos™ F200X (Thermo Fisher). TEM images of the tested films were generated during measurement.

3.6.11 Atomic force microscopy (AFM) measurement

AFM is a technique used to analyze the surface topography and properties (heigh image and phase image) of materials at the nanoscale level. The steps involved in an AFM test are as follows: The quartz substrates of size 1.5×1.5 cm were cleaned using an ultrasonic cleaner with a solution of detergent, deionized water, acetone, and isopropanol. After drying with N_2 stream, the substrates were treated with UV-ozone prior to use. The active material was spined onto the substrate with its specified process. The sample was then mounted onto a sample holder of Dimension 3100 (Veeco Instruments). A suitable probe was selected based on the surface properties of the sample and the type of measurement to be performed. The probe was attached to a cantilever, which was used to scan the sample surface. The data obtained from the AFM test was analyzed to determine the surface properties of the sample.

3.6.12 Photoluminescence Spectroscopy (PL) measurement

PL is a non-destructive analytical technique used to study the optical properties of materials. It involves the measurement of the light emitted by a sample when it is excited by a light source. Here are the basic steps involved in a typical PL measurement (FL3-111): The quartz substrate (1.5×1.5 cm) was cleaned using an ultrasonic cleaner with a mixture of detergent, deionized water, acetone, and isopropanol. The substrate was then dried using N_2 flow and further treated with UV-ozone before use. The sample to be tested was then placed onto the quartz substrate and mounted onto a sample holder. The sample was excited using a light source, such as a laser, with the excitation wavelength selected based on the absorption spectrum of the sample. The emitted light was recorded by a detector as a function of time or wavelength. The resulting PL spectrum provided information on the sample's electronic and structural properties, and analysis of the peak positions, widths, and intensities could reveal details about the sample's band structure, defect states, and carrier dynamics.

3.6.13 Grazing-incidence wide-angle X-ray scattering (GIWAXS) measurement

GIWAXS measurement is a technique used to study the structure and orientation of thin films and surfaces. The general steps involved in GIWAXS measurement are as follows. The active layer was deposited on a silicon slice with the concentration of 20 mg ml^{-1}. The sample is usually thin enough to allow X-rays to penetrate and scatter. The GIWAXS instrument (D/Max-Ttriii(Cbo)) was set up by aligning the X-ray beam and detector, and adjusting the incidence angle of the beam. The incidence angle was typically kept small (0.05-2 degrees) to ensure that the X-rays graze the sample surface and minimize the background signal. The X-ray beam was directed at the sample and scattered X-rays were collected by the detector. The scattering pattern was recorded as a 2D image, with intensity as a function of scattering angle and position on the detector. The scattering pattern was analyzed to extract information about the sample structure and orientation. The π-π distance was estimated by the value of q through the equation of $\frac{2\pi}{q}$ and the coherence length (CCL) was calculated by the value of full-width at half-maximum (FWHM) through the equation of $\frac{2\pi}{\mathrm{FWHM}}$. This involved comparing the experimental sample to a reference sample to identify the crystal structure, size, and orientation of the sample.

3.6.14 Contact angle measurement

The quartz substrates with size of 1.5×1.5 cm, were cleaned using an ultrasonic cleaner with detergent, deionized water, acetone, and isopropanol. Moreover, they were dried using N_2 gas and treated with UV-ozone prior to use. Active materials were deposited on the substrate respectively. Following the deposition and drying of the films, samples were inserted into contact angle measurement. Subsequently, contact angles were measured by an optical contact angle meter. The contact angles (CA) of water and glycerol liquid drops was carried out to explore the compatibility between two materials. The surface energy (γ_s) is analyzed by Wu's model [151]. Contact angles were measured from spin-coated films by an optical contact angle meter(CAM 200). The surface energy was estimated by the Harmonic mean equations:

$$(1+cos\theta_1)\gamma_1 = 4(\frac{\gamma_1^d\gamma_s^d}{\gamma_1^d+\gamma_s^d}+\frac{\gamma_1^p\gamma_s^p}{\gamma_1^p+\gamma_s^p}) \qquad \text{Equation (3.7)}$$

$$(1+cos\theta_2)\gamma_2 = 4(\frac{\gamma_2^d\gamma_s^d}{\gamma_2^d+\gamma_s^d}+\frac{\gamma_2^p\gamma_s^p}{\gamma_2^p+\gamma_s^p})$$

$$\gamma_s = \gamma_s^d + \gamma_s^p$$

where γ_s^d represents the dispersive components, γ_s^p is the polar component. θ_1 and θ_2 are the contact angles of pure water and glycerol, respectively. H_2O: $\gamma_1 =$ 72.8 mJ m^{-2}, γ_1^d = 21.8 mJ m^{-2}, γ_1^p=51.0 mJ m^{-2}; glycerol: γ_2 = 63.4 mJ m^{-2} , γ_2^d =37.0 mJ m^{-2} , γ_2^p=26.4 mJ m^{-2}. γ_s is the surface energy.

Moreover, the degree of molecular miscibility for two molecules was acquired by the Flory-Huggins interaction parameter χ[151] as shown in the following:

$$\chi_{\mathrm{A-B}} \propto (\sqrt{\gamma_{\mathrm{A}}} - \sqrt{\gamma_{\mathrm{B}}})^2 \qquad \text{Equation (3.8)}$$

where γ_{A} represents the surface energy of component A, γ_{B} represents the surface energy of component B, which are calculated from Equation (3.7).

3.6.15 Film thickness measurement

To measure the surface roughness, the Dektak 150 instrument was used. The Dektak utilizes a stylus that was moved across the surface of the sample to record its height at various points. The collected data was then used to generate a topographic map of the sample's surface, providing information about its surface roughness. The quartz substrates with size of 1.5×1.5 cm, were cleaned using an ultrasonic cleaner with detergent, deionized water, acetone, and isopropanol. Moreover, they were dried using N_2 gas and treated with UV-ozone prior to use. Sample were deposited on the substrate respectively. The stylus size and scan length were selected. The stylus was moved across the surface of the sample, and the height of the surface was recorded at each point. The height data was analyzed to generate the thickness of the sample's surface.

3.6.16 Time-of-flight secondary ion mass spectrometry (TOF-SIMS) measurement

TOF-SIMS experiments were carried out by the Physical Electronics PHI TRIFT III spectrometer. Samples for TOF-SIMS were prepared using the same methods for the active layer for the organic photovoltaics. TOF-SIMS is an analytical technique used to analyze the chemical composition of a sample surface. The measurement step for TOF-SIMS involves the following steps: the quartz substrates with size of 1.5×1.5 cm, were cleaned using an ultrasonic cleaner with detergent, deionized water, acetone, and isopropanol. Moreover, they were dried using N_2 gas and treated with UV-ozone prior to use. Active materials were deposited on the substrate respectively. A beam of high-energy primary ions was directed towards the sample surface. The primary ions interacted with the atoms in the sample surface, causing the emission of secondary ions. The secondary ions were extracted from the sample surface using an electric field. The extracted secondary ions were accelerated and focused into a beam. The extracted secondary ions were then introduced into a time-of-flight mass spectrometer. The ions were accelerated by an electric field and pass through a flight tube. The time take for the ions to travel through the flight tube was proportional to their mass-to-charge ratio (m/z). The ions were detected by a detector at the end of the flight tube, and their m/z values were recorded. The data obtained from the TOF-SIMS measurement was analyzed to determine the chemical composition of the sample surface.

3.6.17 Accurate incident light power measurement

P_{in} is incident light power density which is the key parameter to calculate PCE. P_{in} should be measured carefully by wavelength resolved spectra spectrometer because there is no standard indoor light source by now. If P_{in} is roughly measured by an inaccurate lux meter, the result of PCE may be exaggerated. In order to precisely meter emission power of the LED (no standard requirement for indoor illumination) at each wavelength, the spectrometer (Maya2000 Pro, Ocean Optics) with an optical fiber equipped with a cosine corrector was adopted to accurately integrate the power at each wavelength obtaining the total P_{in}. The following steps are the detail step to test P_{in}:the Maya Pro 2000 Spectrometer was connected to the computer using the USB cable; the Ocean Optics SpectraSuite software was opened; the test parameters for spectral range of the test LED was from 400 nm to 850 nm. The position of LED lamp was fixed, and the distant between LED light source and the device was consistent with that between light source and the optical fiber. The light was turned off. The noise light was subtracted. The light was turned on and P_{in} was measured.

3.6.18 Flexibility and mechanical stability measurement

To assess the devices' mechanical stability and flexibility, devices were conducted to bending test. The test was carried out in a glove box filled with N_2 and without device encapsulation. In the bending test, the devices were positioned on a cylindrical surface with a radius of approximately 2.5 mm, while in the folding test, the devices were folded. The devices were subjected to a specific number (400 times and 1000 times) of repeated bending. Their performance that after bending test was measured to observe efficiency decrease resulting from extreme mechanical deformation compared with original performance.

3.6.19 Gaussian calculation

Density Functional Theory (DFT) is a quantum chemical calculation method used to calculate the electronic structure of molecules and materials. In DFT, the electronic density is the fundamental quantity that describes the system, and by solving a functional, the total energy and electron density distribution of the system can be obtained. Density functional theory (DFT) calculation by Gaussian 09 was performed to optimize the molecules. In order to simplify the calculation, all the side chains were simplified as methyl groups. The optimization conformations for molecules were calculated. DFT calculations based on B3LYP/6-31G(d,p) level (functional and basis set) along with simplification of long side chain to methyl, ethyl or methoxy moieties was carried out. The optimization conformation of molecules generated dipole moment, dihedral angle, calculated HOMO and LUMO number. The relaxed potential surface energy scans[152, 153] of rotamer were calculated based on B3LYP/6-31G(d,p) level by scanning 24 steps and each step rotating 15 degree.

Molecular electrostatic potential (ESP), were studied with Gaussian, Multiwfn[154] and VMD. The binding energy for neighboring acceptors were calculated using semi-empirical PM6 and corrected by basis set superposition error (BSSE). Notably, because of the asymmetric structures, there were two types of resulting conformation packing when the binding energy was calculating. Within two types of dimer packing, the one yields stronger binding energy was adopted. For symmetric structure, there was only one type of resulting conformation packing.

3.6.20 ^{1}H nuclear magnetic resonance (^{1}H NMR) spectroscopy for synthesis material

^{1}H NMR spectroscopy (Bruker Dmx-400, Bruker Switzerland) is a non-destructive analytical technique that can provide valuable information about the chemical environment of protons within a molecule. This technique is commonly used to confirm the structure and purity of synthesized materials, as well as to identify impurities or side products. Materials were dried in the oven under vacuum environment over 24 h to remove solvent. To perform ^{1}H NMR spectroscopy, the synthesized and purified powdery material was transferred into a nuclear magnetic tube and dissolved by chloroform-d, which was then inserted into a strong magnetic field and exposed to radiofrequency radiation. The resulting NMR spectrum provides information about the number, type, and relative positions of protons in the sample. The spectroscopic data obtained from ^{1}H NMR spectroscopy was used to verify the structure of TB-4F, TB-S, TB-SCl, TB-S1, and TB-S1-O molecules.

3.6.21 Time-of-flight mass spectrometry (TOF MS) for synthesis material

TOF MS (OF-SIMS 5 iontof, PHI NanoTOFI) is an analytical technique that can provide valuable information about the mass-to-charge ratio (m/z) of ions in a sample. This technique is often used to analyze the composition and purity of synthesized materials. In TOF MS, a sample was ionized and accelerated through a time-of-flight chamber, where the ions werr separated based on their m/z ratio. The resulting spectrum provided the information about the identity and abundance of ions in the sample. To obtain accurate results from TOF MS, the synthesized material was purified and dissolved in a suitable solvent with low concentration. This ensured that the resulting spectrum was free from interference and accurately represents the composition of the material.

CHAPTER 4

Understanding the effect of sequential deposition processing for high-efficiency organic photovoltaics to harvest sunlight and artificial light

4.1 Synopsis

As the rising market of IoT, a great number of attentions has been paid on the development of high-efficient OPVs utilizing artificial light. However, in a real indoor condition, the power density contribution of the artificial light cannot exceed 35% in the combination of indoor and outdoor irradiation, which indicates that the illumination of sunlight cannot be ignored during daytime. Hence, it is urgent to develop high-efficiency OPVs in indoor condition taking into account both sun and artificial light. In this work, a novel asymmetric molecule TB-4F was synthesized to trade off absorption spectrum that can be applied under both artificial light and sunlight. Conventional bulk-heterojunction (C-BHJ) has been figured out that due to non-optimal morphology some carriers failed to be efficiently collected. Herein, sequential deposition bulk-heterojunction (SD-BHJ) as an alternative fabrication method has successfully enhanced performance of OPVs, under both artificial light and sunlight, which was attributed to that favorable microstructure was vertically distributed in the active layer. Notably, the PCE was significantly increased by 25% for SD-BHJ compared to C-BHJ under artificial light owing to the strong effect of trap-assisted recombination and dark current on PCE in the condition of low carrier density. Our result indicates that asymmetric molecule with blue-shifted spectrum fabricated by SD-BHJ can be a promising candidate which can be applied in the indoor environment to harvest sunlight and artificial light simultaneously.

4.2 Introduction

4.2.1 The device applied under sunlight and artificial light

During past few years, as OPVs possess numerous advantages such as flexibility, semitransparency, low-cost, and large-scale processability[23-25], OPVs have drawn a lot of attention and obtained rapid development thanks to the molecular design of donors and acceptors and device engineering, with the PCE over 19.17%[14]. The development of (IoT) influences the research direction of OPVs. IoT refers to the connection of various physical devices through the internet, enabling communication and data exchange between the devices. Recently, the increasing market demand for IoT ecosystem with low power requirement in a range of 1-$100\mu W$[32] motivates the research interest of OPVs to harvest indoor illumination . These devices include a range of low-power devices such as remote controls, smartwatches, Wi-Fi devices, and communication devices. To operate efficiently and effectively, IoT devices need to have low power requirements to ensure that they consume minimal energy and can operate for extended periods. Some examples of IoT devices with low power requirements are: (1) Remote Controls: These are devices that allow users to control electronic appliances remotely. They are designed to be energy-efficient and have low power requirements to ensure long battery life. (2) Smartwatches: These are wearable devices that are equipped with various sensors and can perform a range of functions such as monitoring health, fitness, and sleep patterns. Smartwatches have low power requirements, and some models can operate for up to a week on a single charge. (3) Wi-Fi Devices: These include smart home devices such as thermostats, security cameras, and smart locks. They require low power to operate, and some models are designed to be battery-powered, making them easy to install and use. (4) Communication Devices: These include devices such as Bluetooth headsets, wireless earbuds, and wireless speakers. They require low power to operate and can be connected to other devices such as smartphones and laptops to enable communication and data transfer. Based on a great market prospect, indoor photovoltaics that can harvest weak illuminance and produce electricity have drawn more and more attention [28-30, 113, 115, 118]. IOPVs are new type of solar technology that utilizes light from indoor sources to generate electricity. Compared to traditional silicon-based photovoltaic technology, IOPV offers higher flexibility and lower cost. Recent studies have shown significant improvements in the efficiency and stability of IOPV through the use of new organic materials and improved fabrication processes.

Overall, the key to creating an effective IoT ecosystem with low power requirements is to design devices that are energy-efficient and can operate for extended periods without needing frequent charging or battery replacement. The emission spectrum of artificial light sources such as light-emitting diodes (LEDs) and fluorescent lamps typically ranges from 400 nm to 750 nm [31], which is similar to the wavelength range of visible light perceived by humans[112 155]. However, the irradiation in the indoor environment is complex and variable, and there is not only one emission spectrum present. During the 32-day measurement period (from January to February in 2013) with 15 min, to investigate the real illumination condition in a common room with a window, the measurement was performed by Ruhle' group to calculate the intensity contribution of artificial light in the common room where the indoor lighting was supplied by both sunlight and artificial light during daytime per day. The result implied that the proportion of artificial light was very small with the maximal value of 35% even in winter. Consequently, the irradiation of sunlight cannot be negligible and should be taken into consideration in the indoor condition. However, most studies focus on high-efficient OPVs applied either under AM1.5 or artificial light, which are not suitable for some devices installed in the specific indoor environment that are illuminated by sun during daytime and artificial light during daytime and nighttime. Hou's group demonstrated that devices based on PM6:IO-4Cl showed an amazing PCE of 26.01% under 1000-lux LED, but only yielded 9.8% under AM1.5[94]. Similarly, Yan's group designed FCC-Cl mixed with D18, which produced a PCE of 28.8% under 500-lux LED, but only produced a PCE of 13.1% under AM1.5[46]. It's worth noting that devices with high PCE under 1-sun illumination usually generate relatively low PCE under indoor lighting conditions. Therefore, highly efficient OPVs taking into account both sunlight and artificial light at the same time to uninterruptedly automatically power devices applied in indoor environment should be carried out as soon as possible. An example of a highly efficient OPV that takes into account both sunlight and artificial light to uninterruptedly power devices in an indoor environment is a smartwatch. For an instance, the OPV for smartwatch is designed with suitable absorption spectrum to cover the spectra of sunlight and artificial light, ensuring uninterrupted functionality even when the user is indoors for long periods of time. By using OPV that can be applicated under both indoor and outdoor environment, the smartwatch can reduce its dependence on traditional power sources and provide a more sustainable and convenient solution for users.

As shown in **Figure 4.1a**, to maximally utilize the solar irradiation, narrow bandgap active material should be synthesized to absorb the photon from near infrared (NIR) region[56, 66]. On the contrary, the emission spectrum of artificial light should be well-matched, thus wide bandgap material should be designed[94, 156]. However, considering that the indoor application harvest both sunlight and artificial light, the absorption spectrum of active layer should be traded off to balance the converge of AM1.5 and indoor light. Hence, the absorption onset should be ranged around 850 nm so that device can acquire decent PCE in both situations. In addition to suitable absorption spectrum, high EQE response is also necessary to produce high short circuit current density J_{SC}. For instance, ITIC-Th[138, 156] has a suitable absorption onset at 800nm. However, its relatively low EQE response gives rise to low J_{SC} resulting in low PCE of 8.43% and 16.92% under illumination of sunlight and artificial light, respectively.

4.2.2 The principal to achieve high PCE under low incident intensity

Moreover, It is worth noting that when the light intensity is switched from 1-sun illumination to simulate outdoor environment (100 mW cm^{-2}) to indoor light intensity ($\leq$1 mW cm^{-2}), according to $V_{\mathrm{OC}} = 1/q(E_{\mathrm{Fn}} - E_{\mathrm{Fp}})$ (where E_{Fn} is the electron quasi-Fermi levels and E_{Fp} is hole quasi-Fermi levels there)[101] , there is unavoidable voltage loss (V_{loss}) of 0.15-0.2 V because the gap between E_{Fn} and E_{Fp} varies with light intensity[94, 106]. To mitigate the V_{OC} loss, the dark current should be suppressed, explained by the equation of $V_{\mathrm{OC}} = \frac{nKT}{q}\ln\left[\frac{I_{\mathrm{ph}}(V_{\mathrm{OC}})}{I_0} + 1 - \frac{V_{\mathrm{OC}}}{R_{sh}I_0}\right] \approx \frac{nKT}{q}\ln\left[\frac{I_{\mathrm{ph}}}{I_0}\right]$ (where *n* is the ideality factor (assumption as 1), *k* is the Boltzmann constant, *T* is the cell temperature, q is the electron charge, R_{sh} is the shunt resistance, and I_0 is the reverse dark saturation current). According to the equation, V_{OC} is inversely proportional to natural logarithm of dark current which can significantly influence V_{OC} under dim light condition with low carrier density[157]. With the graduate decrease of light intensity, FF will rise at the beginning and subsequently decrease[158]. Therefore, maintaining high FF in indoor condition plays an important role in achieving high PCE. As the carrier density is low during low illumination, trap-assisted recombination is dominative in the mechanism of carrier recombination[159]. Therefore, suppressing trap-assisted recombination through morphology control can effectively improve FF under indoor condition. The PCEs of devices were calculated from $P_{out}/P_{in} \times 100\%$ (P_{out} is output power density $=V_{OC} \times J_{SC} \times FF$, P_{in} is incident light power density, J_{SC} is short circuit current density, FF is fill factor) , where P_{in} was measured carefully by wavelength resolved spectra spectrometer because there is no standard indoor light source by now. If P_{in} is roughly measured by an inaccurate lux meter, the result of PCE may be exaggerated. Based on precisely metering emission power of the 1000lux-LED at each wavelength by a spectrometer (Maya2000 Pro, Ocean Optics) with an optical fiber equipped with a cosine corrector, the integrated P_{in} is calculated as 305 μW cm^{-2} (**Figure 4.1b**). This method can provide more precise measurements of the input power and improve the accuracy of the calculated PCE value to ensure the meaningful comparison of IOPVs within the different research groups.

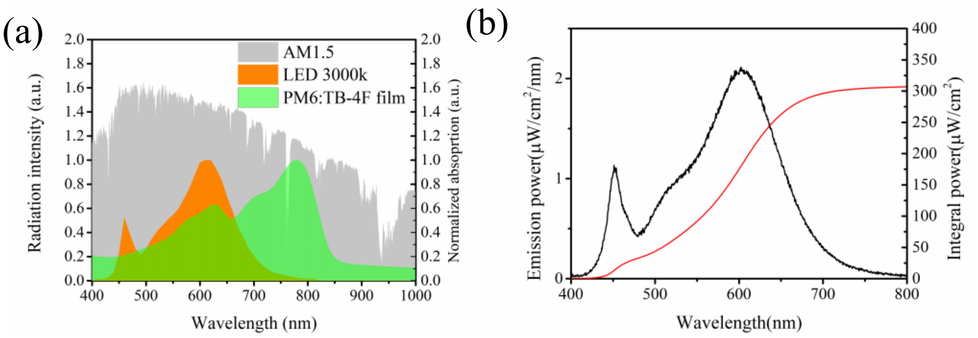

Figure 4.1. (a) The emission spectra of AM1.5 and LED, and the absorption spectrum of PM6:TB-4F. (b) the emission power and integral power of LED.

4.2.3 Different processing technology: conventional bulk heterojunction (C-BHJ) and sequential deposition bulk heterojunction (SD-BHJ)

Different processing technologies can lead to different morphologies, which can in turn affect the photovoltaic properties of the materials. For example, by controlling processing parameters such as additive concentration, processing temperature, and processing time in the solution, the morphology and molecular arrangement of organic materials can be controlled in order to improving their PCEs. Different morphologies may also result in changes in other properties of the material, such as carrier mobility and band structure. Therefore, when studying the performance of OPVs, the influence of processing technology on morphology and performance needs to be considered. In this chapter, when the light intensity changed from 1-sun to indoor weak illumination, the different processing technologies were studies and compared. To pursue effective exciton dissociation at the donor and acceptor interface, BHJ configuration[48, 160, 161], processing by spin-coating premixing solution of donor and acceptor resulting in bi-continuous interpenetrating network morphology, is popular in recent studies. Although an interpenetrating morphology with large interfacial area can be formed, there are some isolated phases that cannot connect electrodes due to excessively premixing so that free carriers fail to be collected[162]. Also, excessive phase separation, producing donor phase connected to cathode and acceptor phase connected to anode, causes non-geminate recombination. Sequential deposition BHJ (SD-BHJ), as the intermediate product of conventional BHJ (C-BHJ) and bilayer heterojunction is performed by spin coating neat donor and acceptor layer by layer. This is the effect way to mitigate the complexity of miscibility and self-organization of donor and acceptor arisen from C-BHJ processing. Previous reports have demonstrated an optimal p-i-n morphology in OPVs generated from SD-BHJ as a result of the perpendicular permeation and diffusion of top acceptor layer into bottom donor[163]. The distinction between SD-BHJ and bilayer heterojunction is solvent used to dissolve materials. Orthogonal solvents (solvent dissolves one material and cannot dissolve the other) are adopted in bilayer heterojunction to produce planer D-A interface[164, 165]. Whereas donor and acceptor in SD-BHJ process are dissolved in the same solvent. This approach is to use the same solvent where the acceptor is dissolved to swell the coated polymer layer to enable penetration of the acceptor into the first depositing layer forming a suitable gradient of the donor and acceptor distribution in vertical. Moreover, the optimization procedure of layer by layer enables each layer to be optimized separately. In terms of physical process of molecular reorganization during SD-BHJ process, Sun et al.[166]declared that conjugated polymer as donor is deposited on the substrate to form crystalline fiber structure in the first step followed by the amorphous region of donor permeated well by small molecule acceptor via swelling. Ko's group[167] adopted molecular dynamics simulation to perform theoretical study together with the experiment analysis to reveal that self-optimized molecular stratification resulting in improved molecular packing was realized during SD-BHJ process for quaternary OPVs. Min and coworkers[162] reported that adopting SD-BHJ process to produce OPVs based on J71:ITC6-IC and PTQ10:IDIC yielded better performance than those of C-BHJ OPVs. Jen' s group fabricated OPVs based on PM6:Y6-BO by SD-BHJ and C-BHJ, respectively. Optimal SD-BHJ device produced PCE of up to 17.2%, outperforming that based on C-BHJ (16.4%)[168]. SD-BHJ has been clarified that it possesses better carrier generation and transportation, and mitigated charge recombination[162, 168, 169], which is attributed to proper vertical distribution of p-i-n geometry leading to improved photovoltaic properties. However, this alternative processing methodology only received less concern, and no study has reported the application of SD-BHJ process into OPVs under the weak illumination. It is believed that the advantages of SD-BHJ will be further amplified when light source is switched from sunlight to artificial light because trap state significantly effects device's performance at low carrier density[157].

4.2.4 Objective of this work

In this work, a Y6's derivative[170] with asymmetric skeleton, named TB-4F, expected to show a blue-shifted absorption spectrum relative to Y6 and high EQE response, was designed and synthesized as a non-fullerene acceptor coupled with a polymer donor, PM6[171]. In indoor environments, the illumination conditions are a combination of sunlight and artificial light, which can vary depending on the weather and time of day. To account for this, two different processing technologies, namely SD-BHJ and C-BHJ processes, were employed to fabricate devices in order to investigate which technology offers better advantages under low illumination and their underlying reasons. The AM1.5 illumination was used to simulate solar irradiation, and a 1000-lux LED lamp was used as the indoor light source due to its longer mean lifetime and cost-effectiveness compared to fluorescent lamps. The newly designed acceptor TB-4F was synthesized and the specified synthesis procedure was included in **section 3.4.1**.

4.3 Results and discussion

4.3.1 Quantum calculation

For trade-off of absorption, reducing a thiophene ring of state-of-the-art molecule Y6 and changing the alky chain could be carried out to obtain the novel asymmetric acceptor TB-4F. The previous study in our group indicated that S-shaped conformation induced by the noncovalent interaction between S and O atoms[146]. The density functional theory (DFT) at B3LYP/6-31g** level was conducted to study the molecular properties. Its theoretical value of highest occupied molecular orbital (HOMO) and lowest unoccupied molecular orbital (LUMO) are -5.70eV and -3.61eV, respectively, matched well with energy levels of PM6. As shown in **Figure 4.2**, the LUMO and HOMO orbitals are evenly distributed along the molecular skeleton, which are beneficial to charge transfer within the molecular. It is notable that the LUMO of TB-4F does not distribute on the thiadiazole unit with electron-withdrawing ability, but on the electron-donating pyrrole moiety. Hence, the LUMO of TB-4F with removing a thiophane unit results in up-shifted LUMO in comparison with Y6. Moreover, TB-4F displays a larger dipole moment (1.5196 Debye) than that of Y6 (1.073 Debye). Lots of works justified that a large dipole moment can reinforce intermolecular interaction resulting in close packing of acceptor molecules and thus rendering more efficient charge transfer[172-175]. The intrinsic large dipole moment of asymmetric acceptor not only enhances intermolecular π-π stacking but also enable *FF* to be improved[174, 176]. The calculation indicates that in comparison with symmetric acceptor Y6, asymmetric acceptor TB-4F with S-shaped conformation has superiorities of blue-sifted absorption and more efficient charge transfer.

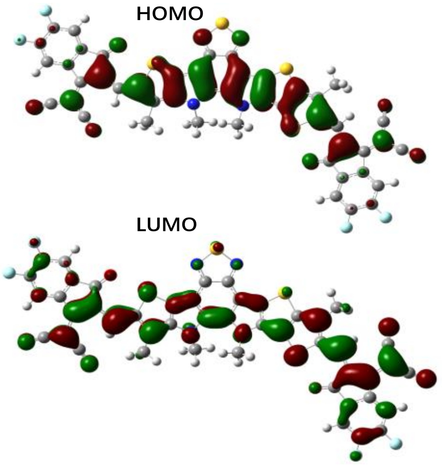

Figure 4.2. LUMO and HOMO distribution of TB-4F.

4.3.2 Photovoltaics and photoelectric properties

The energy levels for TB-4F were measured by CV which is displayed in **Figure 3.3a**. The LUMO and HOMO level of TB-4F were measured to be -4.13 and -5.84 eV (**Figure 4.3b**).

As shown in **Figure 4.4a**, compared to TB-4F in CF solution, TB-4F in the thin film shows bathochromic shift of 75 nm in the UV-vis absorption spectra, which is induced by strong intermolecular aggregation from solution to the solid state.

Figure 4.4d illustrates the normalized absorption spectra of thin films for PM6 and TB-4F. The absorption peak of medium bandgap acceptor, TB-4F, is at 790 nm with the absorption band ranged from 550nm to 880nm, which is desirable for the devices applied under indoor condition to harvest both sunlight through the window and LED light.

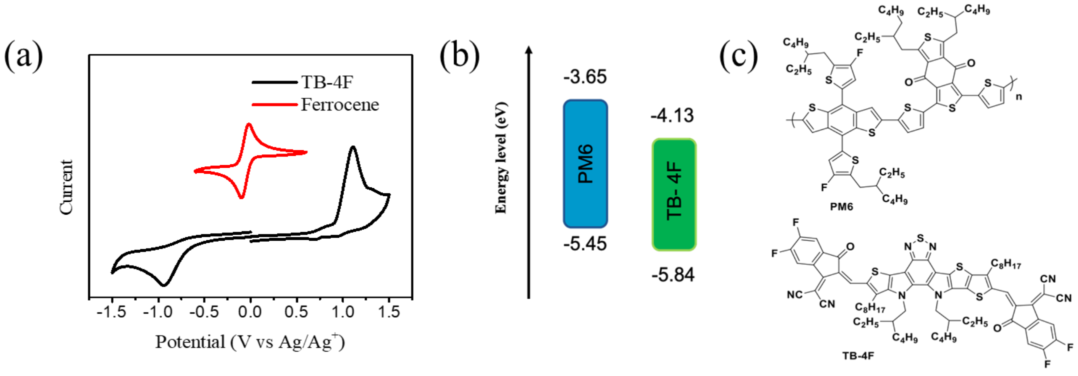

Figure 4.3. (a) CV curve of TB-4F. (b) LUMO and HOMO distribution of TB-4F. (c) Molecular structure of PM6 and TB-4F.

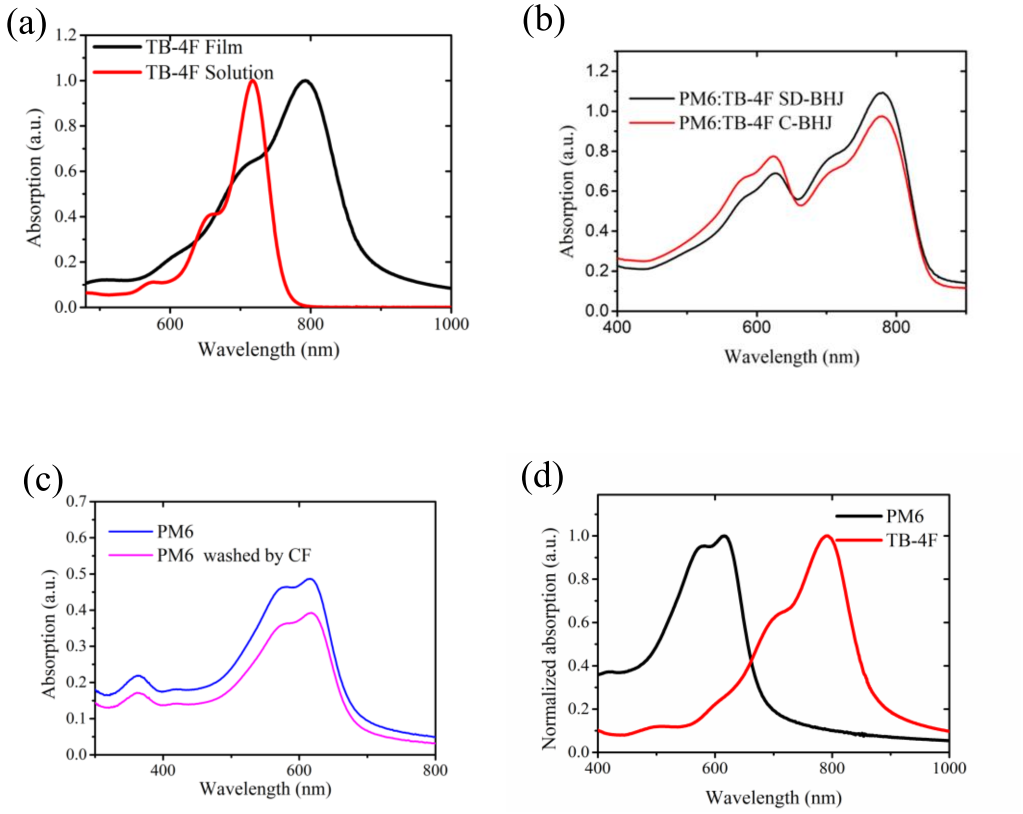

Figure 4.4. (a) UV-vis absorption spectra of TB-4F in solution and film, respectively. (b) UV-vis absorption spectra of PM6/TB-4F-based blend films with different fabrication methods. (c) UV-Vis absorption spectra of PM6 films with/without

washing by CF. (d) Normalized UV-vis absorption spectra of neat films of PM6 and TB-4F.

The PM6:TB-4F processed by SD-BHJ and C-BHJ were optimized tested under the condition of 1-sun intensity and were described in **Table 4.1-4.6**. SD-BHJ determined the optimal spin-coating rate for donor PM6 (7.5 mg ml^{-1}) by testing spin speeds of 1500, 2000, and 2500 rpm, while the acceptor TB-4F (10 mg ml^{-1}) was fixed at 3000 rpm The results showed that the optimal spin-coating rate for the donor was 2000 rpm The optimal concentration of the acceptor was then studied by spin-coating neat PM6 in CF solution (7.5 mg ml^{-1}) at 2500 rpm and TB-4F in CF solution at different concentrations (9, 10, 11 mg ml^{-1}) at 3000 rpm on top of the PM6 layer. The optimal concentration for TB-4F was found to be 10 mg ml^{-1}. The optimal ratio of donor to acceptor (D:A) was studied by spin-coating neat PM6 in CF solution (7.5 mg ml^{-1}) at different speeds and TB-4F in CF solution (10 mg ml^{-1}) at 3000 rpm on top of the PM6 layer. The results showed that the optimal D:A ratio was 1:1.2. The PM6:TB-4F ratio (1:1, 1:1.2, 1:1.4) was then optimized with a total concentration of 16 mg ml-1, and the optimal D:A ratio was found to be 1:1.2. Furthermore, the total concentration was optimized by fixing the D:A ratio at 1:1.2 and varying the concentration between 14, 16, and 18 mg ml^{-1}, with the optimal concentration being 16 mg ml^{-1}. **Table 4.5** summarizes the thickness of the active material based on the optimal fabrication condition for OPVs. For PM6:TB-4F based devices, the optimal condition for fabricating SD-BHJ was to spin-coat neat PM6 (7.5 mg ml^{-1}) with 2000 rpm and neat TB-4F (10 mg ml^{-1}) with 3000 rpm, while the optimal weight ratio of D:A for C-BHJ was found to be 1:1.2.

To study the effect of top layer on the bottom layer during deposition process, UV-vis absorption spectra of the blend film of PM6:TB-4F were measured. As depicted in **Figure 4.4b**, it is interesting that the region of donor in the film of SD-BHJ is lower than that of C-BHJ and the region of acceptor of SD-BHJ is higher than that of C-BHJ. As shown in **Figure 4.4c**, it is suggested that a small part of PM6 was washed by solvent during the deposition of the second layer [168]. Besides, the higher proportion of acceptor in D:A mixture for SD-BHJ in comparison with

C-BHJ lead to increased absorption in the region of acceptor.

Table 4.1. SD-BHJ photovoltaic parameters of devices (AM1.5) in which the neat PM6 in CF solution (7.5 mg ml^{-1}) was spin-coated at different speeds and TB-4F in CF solution (10 mg ml^{-1}) was spin-coated at 3000 rpm on top of PM6 layer.

AM1.5	Spin-coating rate of PM6 (rpm)	V_{OC} (V)	J_{SC} (mA cm^{-2})	FF	PCE (%)
PM6: TB-4F	2500	0.851	21.95	77.51	14.48(14.33±0.06)
PM6: TB-4F	2000	0.861	22.87	77.39	15.24(15.14±0.05)
PM6: TB-4F	1500	0.851	22.06	77.47	14.55(14.23±0.11)

The average parameters and s.d. were calculated from more than 5 independent cells.

Table 4.2. SD-BHJ photovoltaic parameters of devices (AM1.5) in which the neat PM6 in CF solution (7.5 mg ml^{-1}) was spin-coated at 2500 rpm and TB-4F in CF solution at different concentration was spin-coated at 3000 rpm on top of PM6 layer.

AM1.5	Concentration of TB-4F (mg ml^{-1})	V_{OC} (V)	J_{SC} (mA cm^{-2})	FF	PCE (%)
PM6: TB-4F	9	0.848	21.79	71.35	13.17(12.97±0.14)
PM6: TB-4F	10	0.861	22.87	77.39	15.24(14.99±0.07)
PM6: TB-4F	11	0.855	22.64	71.71	13.87(13.78±0.09)

The average parameters and s.d. were calculated from more than 5 independent cells.

Table 4.3. C-BHJ photovoltaic parameters of devices (AM1.5) in which the mixture of PM6:TB-4F at different ratio in the concentration of 16 mg ml^{-1}.

AM1.5	Ratio of D:A	V_{OC} (V)	J_{SC} (mA cm^{-2})	FF	PCE (%)
PM6: TB-4F	1:1	0.855	21.66	75.17	13.93(13.38±0.45)
PM6: TB-4F	1:1.2	0.849	21.93	77.56	14.44 (14.21±0.09)
PM6: TB-4F	1:1.4	0.838	21.51	76.74	13.85(13.58±0.31)

The average parameters and s.d. were calculated from more than 5 independent cells.

Table 4.4. C-BHJ photovoltaic parameters of devices (AM1.5) in which the mixture of PM6:TB-4F at the D:A ratio of 1:1.2 with different concentration.

AM1.5	Concentration (mg ml^{-1})	V_{OC} (V)	J_{SC} (mA cm^{-2})	FF	PCE (%)
PM6: TB-4F	14	0.83	20.67	75.68	12.99(12.49±0.31)
PM6: TB-4F	16	0.849	21.93	77.56	14.44(14.25 ± 0.14)
PM6: TB-4F	18	0.831	23.39	72.25	14.04(13.85±0.11)

The average parameters and s.d. were calculated from more than 5 independent cells.

Table 4.5. The thickness of active material based on the optimal fabrication condition for OPVs processed by SD-BHJ and C-BHJ, respectively.

Fabrication method	Component	Thickness (nm)
SD-BHJ	neat D	41.8
SD-BHJ	neat A	87.2
SD-BHJ	D+A	129
C-BHJ	D+A	125

The average parameters and s.d. were calculated from more than 5 independent cells.

Table 4.6. Reverse SD-BHJ photovoltaic parameters of device (AM1.5) in which the neat TB-4F in CF solution (10 mg ml^{-1}) was firstly spin-coated at 3000 rpm into the substrate and PM6 in CF solution (7.5 mg ml^{-1}) in CF solution was deposited at 2000 rpm on top of TB-4F layer.

AM1.5	V_{OC} (V)	J_{SC} (mA cm^{-2})	FF	PCE (%)
PM6: TB-4F (reverse SD-BHJ)	0.3	0.059	28.956	0.0052(0.0045±0.0003)

The average parameters and s.d. were calculated from more than 5 independent cells.

Table 4.7. The photoelectrical parameters of PM6:IT-4F based on SD-BHJ and C-BHJ under AM1.5.

AM1.5		V_{OC} (V)	J_{SC} (mA cm^{-2})	J^{a}_{cal} (mA cm^{-2})	FF	R_SA (Ω cm^2)	$R_{Sh}A$ (Ω cm^2)	PCE^b (%)	E_{loss} (eV)
PM6: TB-4F	C	0.849	21.93	21.28	77.56	3	2182	14.44 (14.25 ± 0.14)	0.61
PM6: TB-4F	SD	0.861	22.87	22.25	77.39	2.38	2926	15.24 (14.99±0.203)	0.598

$^{a}J_{cal}$ was obtained by integrating the EQE spectrum over that of the light source. ^{b}The average parameters and s.d. were calculated from more than 10 independent cells.

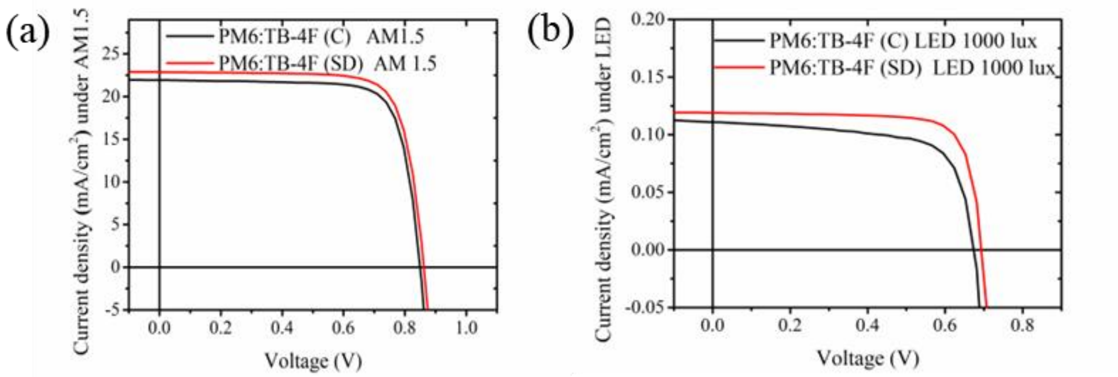

Figure 4.5. (a) *J–V* characteristics of PM6: TB-4F processed by C-BHJ and SD-BHJ under AM1.5. (b) *J–V* characteristics of PM6:TB-4F processed by C-BHJ and SD-BHJ under LED illumination.

I firstly measured the photovoltaic performance of OPVs under AM1.5 condition. The *J-V* curve of optimal device under illumination of AM1.5 is shown in **Figure 4.5a**. The detailed device parameters collected from the *J-V* curve are shown in **Table 4.7**. The optimal device of PM6: TB-4F based on C-BHJ with the optimal D/A weight ratio of 1:1.2 yielded the PCE of 14.44%, with a V_{OC} of 0.849 V, J_{SC} of 21.279 mA cm^{-2} and an *FF* of 0.775. When C-BHJ process was replaced by optimal SD-BHJ process, the V_{OC} increases to 0.861 V, with the increased J_{SC} of 22.87 mA cm^{-2} and a comparable *FF* of 0.774, resulting in a PCE of 15.24%. PM6:Y6 based on C-BHJ that was studied in our previous work produced the PCE of 15.9%, with a V_{OC} of 0.837 V, J_{SC} of 25.05 mA cm^{-2} and an *FF* of 0.758[146]. In comparison with Y6, TB-4F based devices show lower PCEs as the upshifted

LUMO leads to absorption sacrifice and thus lower J_{SC}. However, the upshifted LUMO resulting in better energy level with PM6 indicates higher V_{OC}.

As discussed above, the conformation of asymmetric acceptor with a large dipole moment usually enables *FF* to be enhanced. Hence, TB-4F-based devices yield higher FF than that of Y6-based devices. The EQE spectra (**Figure 4.6a**) of PM6:TB-4F processed by C-BHJ and SD-BHJ were measured and the integral currents were calculated to verify the accuracy of *J-V* curves. Moreover, it is worth to mention that SD-BHJ show better EQE response than that of C-BHJ in PM6:TB-4F indicating that the more efficient exciton generation and carrier transport were achieved by SD-BHJ. The integrated currents are 21.279 and 22.245 mA cm^{-2} for PM6:TB-4F of C-BHJ and SD-BHJ, respectively, which are consistent with J_{sc} of *J-V* curves. According to the equation: $E_{\mathrm{loss}} = E_{\mathrm{g}} - qV_{\mathrm{OC}}$ (where $E_{\mathrm{g}} = 1240/\lambda_{\mathrm{onset}}$), E_{loss}s are 0.61eV and 0.598eV for C-BHJ and SD-BHJ, respectively. The smaller E_{loss} for SD-BHJ agreed with the suppressed dark current and enhanced J_{SC} compared with C-BHJ.

Furthermore, we applied the optimal devices under the condition that light intensity was decreased from AM1.5 (100 mW cm^{-2}) to 1000-lux LED (305 μW cm^{-2}). Based on precisely metering emission power of the 1000lux-LED at each wavelength by a spectrometer (Maya2000 Pro, Ocean Optics) with an optical fiber equipped with a cosine corrector, the integrated P_{in} is calculated as 305 μW cm^{-2} (**Figure 4.1b**). The specified measurement for incident power and calculation for integral current under the illumination of artificial light are depicted in the section 2.2.3.

J-V curve under dim light condition is shown in **Figure 4.5b**. The detailed photovoltaics performances are summarized in **Table 4.8**. The maximum output power densities (P_{out}) are 51.02 and 64.23 μW cm^{-2} with PCE of 16.82% and 21.05% for PM6:TB-4F fabricated by C-BHJ and SD-BHJ, respectively. The photovoltaics performances are substantially improved under dim light condition in comparison with that under 1-sun condition, due to the narrower emission spectrum of LED. In the term of different processing methods, SD-BHJ OPVs yield better PCE than that of C-BHJ with the increment of 25%, which was attributed from mitigated E_{loss}, high *FF* maintained under dim condition, and better EQE response leading to higher J_{SC}.

This result suggests that SD-BHJ is more suitable than C-BHJ under dim light condition, which can be applied in manufacture process for the indoor application. Because P_{in} under dim light condition is 3 orders less than that under AM1.5, inaccurate J_{SC} arising from imprecise P_{in} will give rise to a PCE with big error. Hence, integrated current calculated in the combination of EQE curve and photo flux of LED was necessary in this work to ensure the accuracy of results. However, this verification step was absent in some work studying indoor energy harvesting. As shown in **Figure 4.7** and **Table 4.8**, the integral current densities, which are 0.1172 mA cm^{-2} and 0.1157 mA cm^{-2} for SD-BHJ and C-BHJ under the 1000-lux LED illumination, respectively, were calculated and confirmed the reliability of photovoltaic performance under indoor condition.

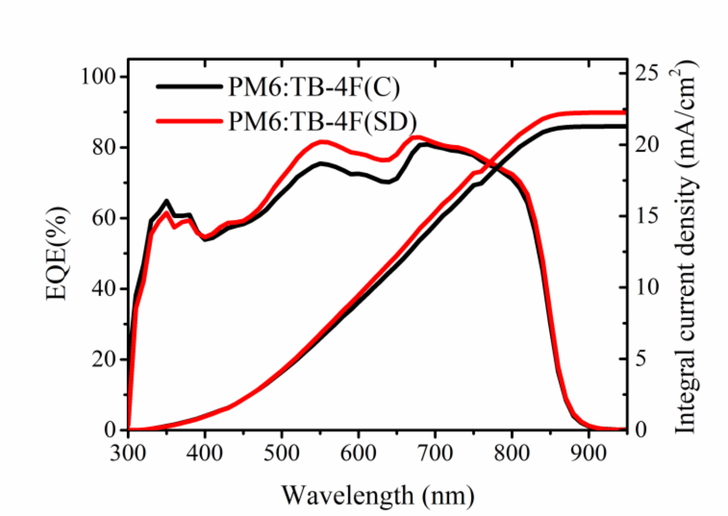

Figure 4.6. The corresponding EQE spectra of PM6:TB-4F processed by C-BHJ and SD-BHJ under AM1.5. (b) Photon flux over 1000-lux LED (3000k) and the corresponding integrated current density spectra of PM6:TB-4F OSCs.

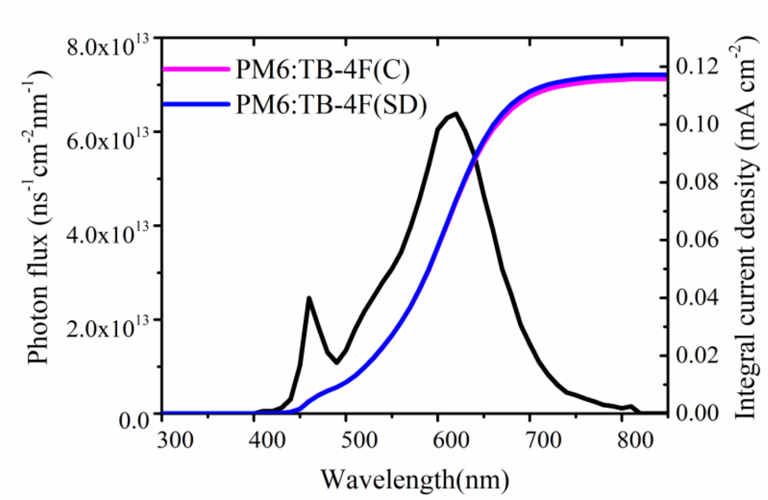

Figure 4.7. Photon flux over 1000-lux LED (3000k) and the corresponding integrated current density spectra of PM6:TB-4F OSCs.

Table 4.8. The photoelectrical parameters of PM6:IT-4F based on SD-BHJ and C-BHJ under 1000 lux-LED.

Indoor		V_{OC} (V)	J_{SC} (mA cm^{-2})	J^{a}_{cal} (mA cm^{-2})	FF	R$_S$A (Ω cm^2)	R$_{Sh}$A (Ω cm^2)	PCE^b (%)	P$_{out}$ (μW/cm^2)	E$_{loss}$ (eV)
PM6: TB-4F	C	0.674	0.111	0.116	68.66	478	58078	16.82 (16.47 ± 0.26)	51.02	0.785
PM6: TB-4F	SD	0.693	0.119	0.117	77.89	274.6	204161	21.05 (20.4 ± 0.43)	64.23	0.766

[a]J_{cal} was obtained by integrating the EQE spectrum over that of the light source.
[b]The average parameters and s.d. were calculated from more than 10 independent cells.

Notably, the advantages of SD-BHJ were largely enhanced and broadened when illuminated by the artificial light. To further clarify the underlying reasons why SD-BHJ can achieve significantly improved PCE under weak illumination, carrier transport evaluation and recombination characteristics were assessed. Photoluminescence (PL) spectra of neat PM6, TB-4F, and their corresponding blended films were measured to study the underlying reasons for the improved performance of devices fabricated by SD-BHJ. As illustrated in **Figure 4.8a,b**, the neat PM6 film and PM6:TB-4F films, were excited at the wavelength of 570 nm; the neat TB-4F film and PM6:TB-4F films were excited at the wavelength of 770 nm. The neat PM6 and TB-4F possess emission peaks for PL spectra at 674nm, and 829nm, respectively. The PM6:TB-4F films show significantly quenched PL intensities of PM6 and TB-4F. It is notable that SD-BHJ OPVs show enhanced quenching for PL spectra than that of C-BHJ OPVs, which proves that SD-BHJ possesses more efficient charge transfer property[177, 178]. Therefore, superior donor/acceptor interfaces can be formed in the SD-BHJ.

Subsequently, in order to demonstrate the acceptor phase vertically distributed in the whole active layer in the SD-BHJ, time-of-flight secondary ion mass spectrometry (TOF-SIMS) was adopted to detect characteristic group of donor, acceptor, and PEDOT:PSS. According to TOF-SIMS depth plots (**Figure 4.9**), the signal of SO_3^- (PEDOT:PSS) increases with the decrease of F^- (PM6 and TB-4F) and CN^- (TB-4F), which hints that, during sequential deposition, acceptor has successfully distributed throughout the whole vertical profile of active layer and a large portion of acceptor has been inserted into the donor, thus forming a continuous pathway for exciton dissociation and carrier extraction.

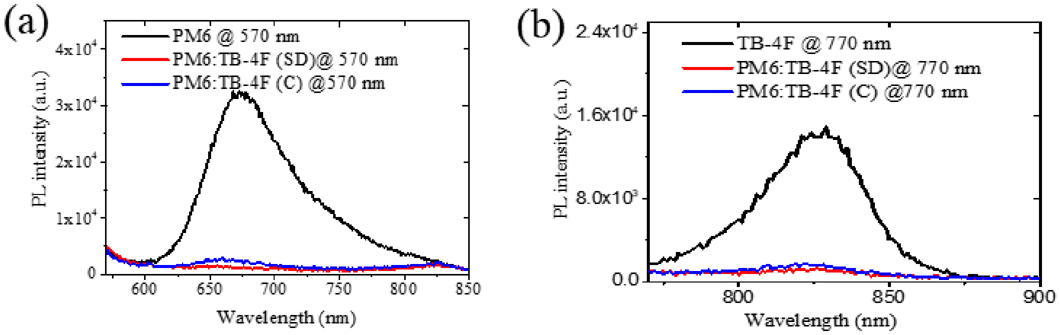

Figure 4.8. PL spectra of pristine films and blend films excited at 570 nm for PM6 (a) and at 770 nm for TB-4F (b), respectively.

In order to oppositely verify the vertical stratification of donor and acceptor produced by SD-BHJ, the reverse SD-BHJ was fabricated, and its photoelectrical performance was tested as shown in **Figure 4.10** and **Table 4.6**, where TB-4F was deposited as the first layer and PM6 was subsequently spin coated as the second layer. This result indicated that if donor to acceptor ratio was high on the top of layer and low on the bottom of layer, the excitons failed to be effectively dissociated and carriers were inefficiently extracted.

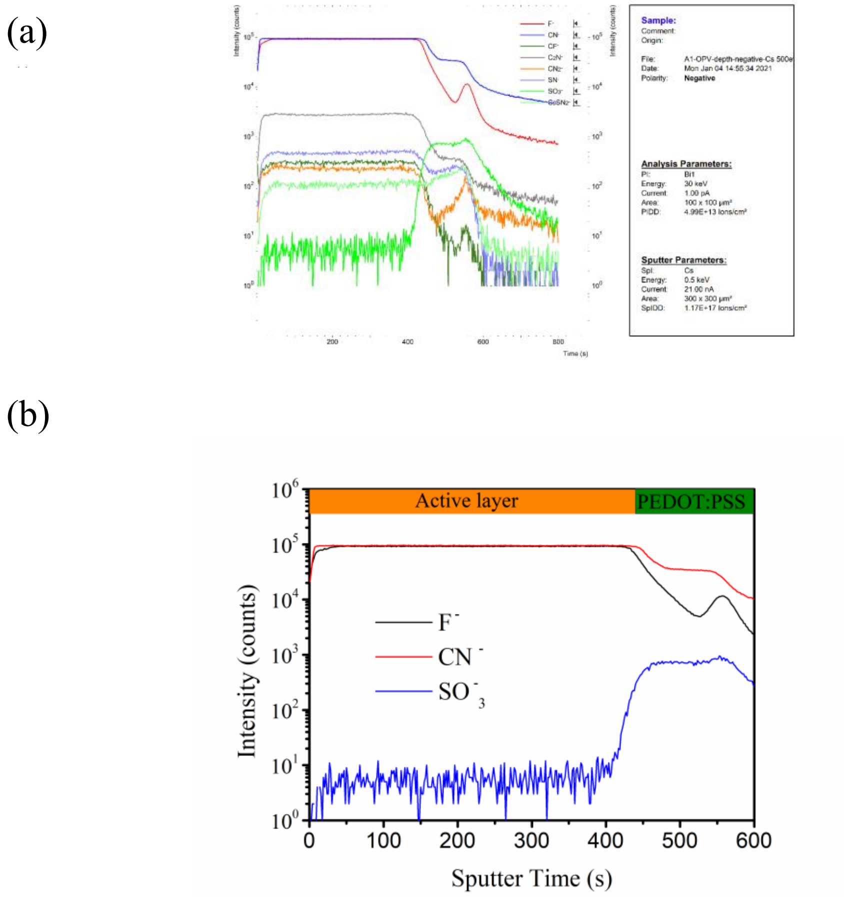

Sample:
Comment:
Origin:

File: A1-OPV-depth-negative-Cs 500e
Date: Mon Jan 04 14:55:34 2021
Polarity: **Negative**

Analysis Parameters:
PI: Bi1
Energy: 30 keV
Current: 1.00 pA
Area: 100 x 100 µm²
PIDD: 4.99E+13 Ions/cm²

Sputter Parameters:
SpI: Cs
Energy: 0.5 keV
Current: 21.00 nA
Area: 300 x 300 µm²
SpIDD: 1.17E+17 Ions/cm²

Figure 4.9. (a) TOF-SIMS result for sequential processing PM6:TB-4F-based SD-BHJ. (b) TOF-SIMS depth plots for the PM6: TB-4F based SD-BHJ.

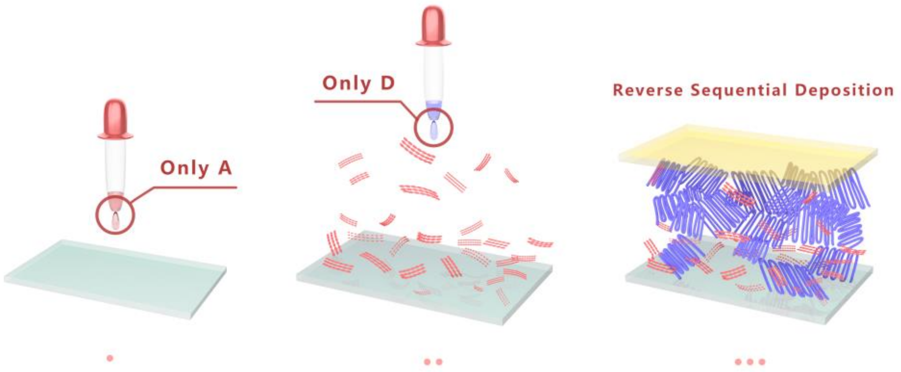

Figure 4.10. The schematic diagram of reverse SD-BHJ.

In order to demonstrate the impact of SD-BHJ on the carrier transport properties, the photo-induced charge-carrier extraction in a linearly increasing voltage (photo-CELIV) was applied to examine the devices as displaying in **Figure 4.11** [179]. The mobility of faster carrier's component was measured as $6 \times 10^{-4}\ c\mathrm{mV}^{-1}\mathrm{s}^{-1}$ for PM6:TB-4F (SD-BHJ), which was much higher than that of PM6:TB-4F(C-BHJ) with $9.5 \times 10^{-5}\ c\mathrm{mV}^{-1}\mathrm{s}^{-1}$. This result indicated that SD-BHJ was beneficial to carrier extraction leading to higher J_{SC}. The trap state characterization was performed from transient photocurrent measurement (TPC) (see **Figure 4.12**). When the light was switched off at 200 μs, the equilibrium between the carrier trapped and escaping was disrupted. Under dark condition, trapping pattern was stopped and only escaping pattern remained. Consequently, only carriers escaping from trap state contributed to decay current[180], which means that the faster decay, the less trap-assisted recombination center is. The decay rate of PM6:TB-4F (SD-BHJ) is faster than that of PM6:TB-4F (C-BHJ) which implies that SD-BHJ possesses less trap state. Also, the faster rate of charge extraction is beneficial to the enhancement of J_{SC} and FF. In the following, transient photovoltage measurement (TPV) was measured to study the recombination mechanism as depicted in **Figure 4.12**, which was deducted by the carrier lifetime. The device was illuminated at the open-circuit mode. Subsequently, the light was switched-off and the charge was extracted at the short-circuit mode. The carrier lifetime for SD-BHJ is 1.83 μs and for C-BHJ is 1.8 μs. The slower decay of photovoltage for SD-BHJ means bimolecular recombination is less, which is in favor of the improvement of J_{SC} and FF. Further giving insights into charge-carrier recombination for two fabrication methods, devices were also assessed by measuring the dependence of V_{OC} and J_{SC} of the devices on the light intensity (P_{light}). The dependence of V_{OC} on P_{light} is plotted in **Figure 4.13a** for PM6:TB-4F OSCs. If the slope of the fitting line closes to $2kT/q$, monomolecular recombination (trap-assisted) is dominate. Whereas, the slope close to $1kT/q$ means that bimolecular recombination is the main recombination way[181]. **Figure 4.13b** shows the relationship between J_{SC} and P_{light} according to the equation: $J_{\mathrm{SC}} \propto P_{light}{}^{\alpha}$, where $\alpha = 1$ represents that all the carriers are effectively swept out prior to the bimolecular recombination and monomolecular recombination is sole[182]. Herein, kT/q values equal 1.1684 kT/q and 1.0904 kT/q for C-BHJ and SD-BHJ of PM6:TB-4F, respectively. This implies that SD-BHJ possess less trap states or recombination centers owing to superior morphology[183], which is more suitable for low illumination with low density carriers and leads to higher FF that has been discussed in the introduction section. Moreover, α= 0.946 for SD-BHJ is closer to 1 than that of C-BHJ with α=0.938. This result indicates that, compared with C-BHJ, SD-BHJ shows suppressed bimolecular recombination.

The charge generation and extraction properties were studied by the dependence of photocurrent (J_{ph}) on effective voltage (V_{eff}). $J_{\mathrm{ph}} = J_{\mathrm{light}}$-$J_{\mathrm{dark}}$, where J_{light} indicates the current under AM1.5 illumination, and J_{dark} represents the current under dark condition. V_{eff} is defined as V_0 -V, where V_0 is the voltage when J_{ph} = 0, and V is the applied bias voltage. The charge collection capability ($P(E, T)$) can be evaluated by the equation: $P(E, T) = J_{\mathrm{ph}}/J_{\mathrm{sat}}$, where J_{sat} is the saturated current at V_{eff} is larger than 2 V[184]. The plots of J_{ph} versus V_{eff} is shown in **Figure 4.14a** for PM6:TB-4F based devices of SD-BHJ and C-BHJ. The value of $P(E, T)$ = 0.979 for SD-BHJ with J_{sat} of 23.36 mA cm^{-2} is higher than that of 0.974 with J_{sat} of 22.5 mA cm^{-2} for C-BHJ, implies that SD-BHJ possesses ability of more efficient charge generation and carrier extraction. This also indicates that more D/A interface channels for exciton dissociation and effectively vertical composition of TB-4F distribution for carrier extraction can be formed in the process of SD-BHJ. Devices fabricated in SD-BHJ show less dark current than that of C-BHJ as described in **Figure 4.14b** in log-sale and **Figure 4.14c** in linear-scale.

The dark current can be deduced from the current density at the voltage of -0.5 V (reverse voltage). According to the equation of $V_{\mathrm{OC}} = \frac{nkT}{q} \ln\left[\frac{I_{\mathrm{ph}}}{I_0}\right]$, it is well known that the dark current at low bias voltage is related to leakage current [185]. While light current equals that the photogenerated current subtract leakage current, so thus impacts J_{SC}. Besides, dark current, I_0 can make V_{OC} decrease as the increase of

I_0 leading to the decline in the section of $\ln\left[\frac{I_{\text{ph}}}{I_0}\right]$, thus resulting in the loss of V_{OC}. Hence, suppressing dark current can also mitigate V_{OC} loss, especially, under low illumination with weak photogenerated current, I_{ph}. Consequently, the V_{OC} for PM6:TB-4F processed by SD-BHJ is higher than that processed by C-BHJ under both sun and indoor light illumination. In addition, under low illumination, the effect of series resistance (R_s) and R_{sh} is quite different from that illuminated under AM1.5. As shown in Shockley's equation expressed as: $J_{\text{SC}} = \frac{1}{1+R_s/R_{\text{sh}}}\left[J_{\text{ph}} - J_0\left\{\exp\left(\frac{|J_{\text{SC}}|R_s A}{\text{n}kT/q}\right) - 1\right\}\right]$, where J_{ph} represents photo-generated current density and J_0 represents reverse saturation current density. As J_{SC} is much lower than the thermal voltage nkT/q when illuminated by artificial light, the section of $\exp\left(\frac{|J_{\text{SC}}|R_s A}{\text{n}kT/q}\right)$ becomes negligible, which means that the effect of R_s is not so crucial. In terms of R_s/R_{sh}, the larger R_{sh}, the higher J_{SC} is. The R_{sh} for SD-BHJ is larger than that of C-BHJ under weak illumination leading to the higher J_{SC}.

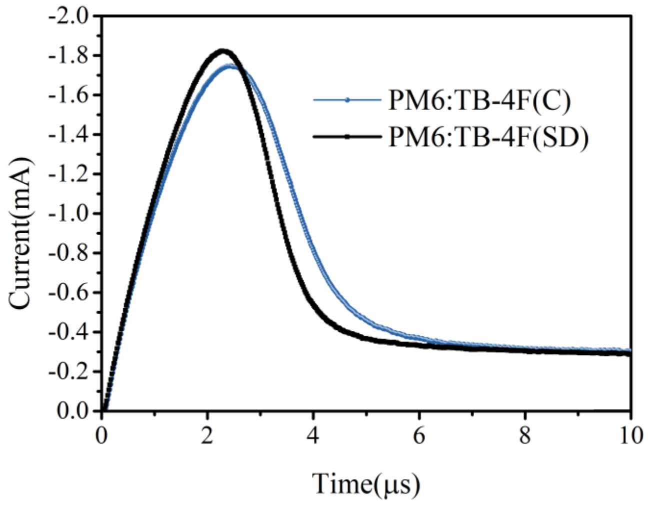

Figure 4.11. Photo-CELIV curves of PM6: TB-4F based OSCs fabricated by SD-BHJ and C-BHJ.

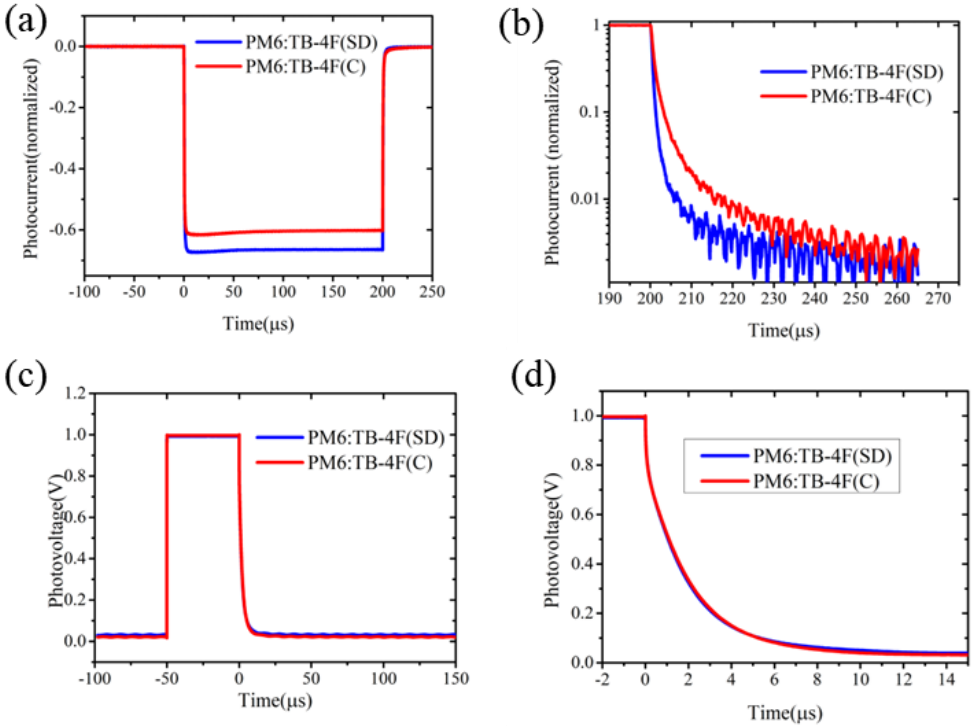

Figure 4.12. (a) Decay curves from transient photocurrent spectroscopy. (b) Normalized photocurrent decay in the log scale after light turned off at 200 μS. (c) Decay curves from transient photovoltaic spectroscopy. (d) Normalized photocurrent decay after light turned off at 0 μS.

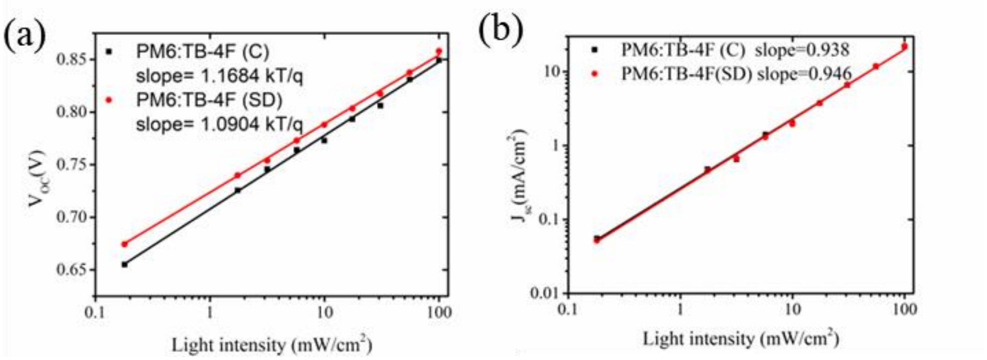

Figure 4.13. The dependence of V_{OC} (a) and J_{SC} (b) on light intensity for optimized C-BHJ OSCs and SD OSCs of PM6: TB-4F.

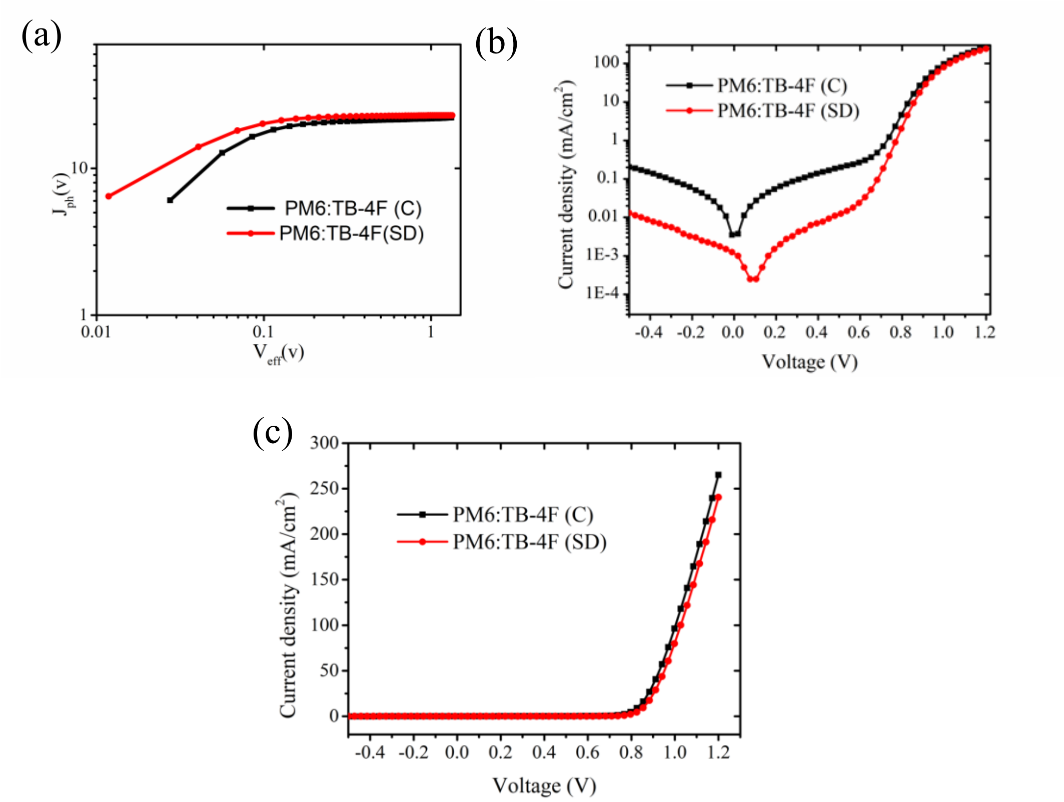

Figure 4.14. (a) J_{ph} versus V_{eff} plots of the optimized C-BHJ and SD-BHJ of PM6: TB-4F OSCs. (b) The current density (log scale) as a function of the voltage the optimized C-BHJ and SD OSCs for PM6: TB-4F under dark. (c) The current density (linear scale) as a function of the voltage for (SD and C) PM6:TB-4F under dark condition.

4.3.3 Morphology

Atomic force microscopy (AFM) and transmission electron microscope (TEM) were used to investigate the microstructure of film processed by SD-BHJ and C-BHJ. As depicted in **Figure 4.15 a,b**, the roughness values for the SD-BHJ and C-BHJ for PM6: TB-4F were measured to be 2.54 and 4.87 nm, respectively. Because SD-BHJ features vertical distribution with higher component of TB-4F on the top of active layer and the roughness of neat TB-4F (**Figure 4.16**) is smooth (0.315 nm), SD-BHJ exhibits smaller root-mean-square (RMS) surface roughness value than that of C-BHJ. Usually, the surface roughness is related to the crystallinity of active layer[186]. As shown **Figure 4.15e**, we can deduce that the crystallization property of TB-4F is weaker than that of the blended film of PM6:TB-4F, which explains the reason why SD-BHJ shows smaller RMS. In general, the smoother surface is beneficial to charge transfer and allows active layer to form ohmic contact with electrodes. The phase patterns (**Figure 4.15c,d**) show that finer fibrous network morphology and less phase separation domains in SD-BHJ. The smaller domain may be conducive better charge separation leading to higher EQE and J_{SC}, which makes big difference in PCE under weak illumination[187]. The TEM images between SD-BHJ and C-BHJ are markedly different **(Figure 4.17**). A network of fibrils is observed in SD-BHJ image, which may be formed by the pre-crystallized fiber of PM6 at the first step and the mixture of TB-4F and the amorphous section of PM6 at the second step. Whereas the coarser morphology is visible for C-BHJ which is probable the result of overmixed C-BHJ.

Grazing-incidence wide-angle X-ray scattering (GIWAXS) was carried out to study the crystallinity and the molecular orientation of the neat donor and acceptor and corresponding blend film processed by SD-BHJ and C-BHJ, respectively, as depicted in **Figure 4.15e,f**. The neat PM6 and TB-4F exhibit a face-on orientation which is conducive to transport carriers to substrate. Moreover, PM6:TB-4F (SD-BHJ) possesses strong π-π stacking, supported by the (010) peak with $q = 1.751$Å^{-1} ($d = 3.586$ Å) in the out of plane (OOP) direction. In the in-plane (IP) direction, the lamellar peak (100) indicates $q = 0.301$Å^{-1} ($d = 20.85$ Å). The combination of IP and OOP peaks verifies that the face-on orientation tendency of PM6:TB-4F (SD-BHJ). It can be found that there is no big difference between SD-BHJ and C-BHJ, as PM6:TB-4F (C-BHJ) displays a π-π peak at $q = 1.733$Å^{-1} (d=3,623 Å) in OOP direction and a lamellar peak at $q = 0.301$Å^{-1} (d=20.85 Å) in IP direction. Therefore, SD-BHJ can still maintains preferred face-on orientation without changing the molecular packing when compared with C-BHJ. Moreover. The coherent lengths ($\mathrm{L_c}$) in the (010) peak of OOP direction are assessed by the equation[188] of $\mathrm{L_c} = 2\pi\mathrm{k}/f_{\mathrm{whm}}$, where k equals 0.9 that is the shape factor and f_{whm} represents the half-width at the peak. The $\mathrm{L_c}$ were calculated to be 1.32 nm for SD-BHJ and 1.23 nm for C-BHJ, which implies that SD-BHJ possesses higher crystallinity that is conductive to better phase separation agreed with the improvement of charge dissociation and extraction.

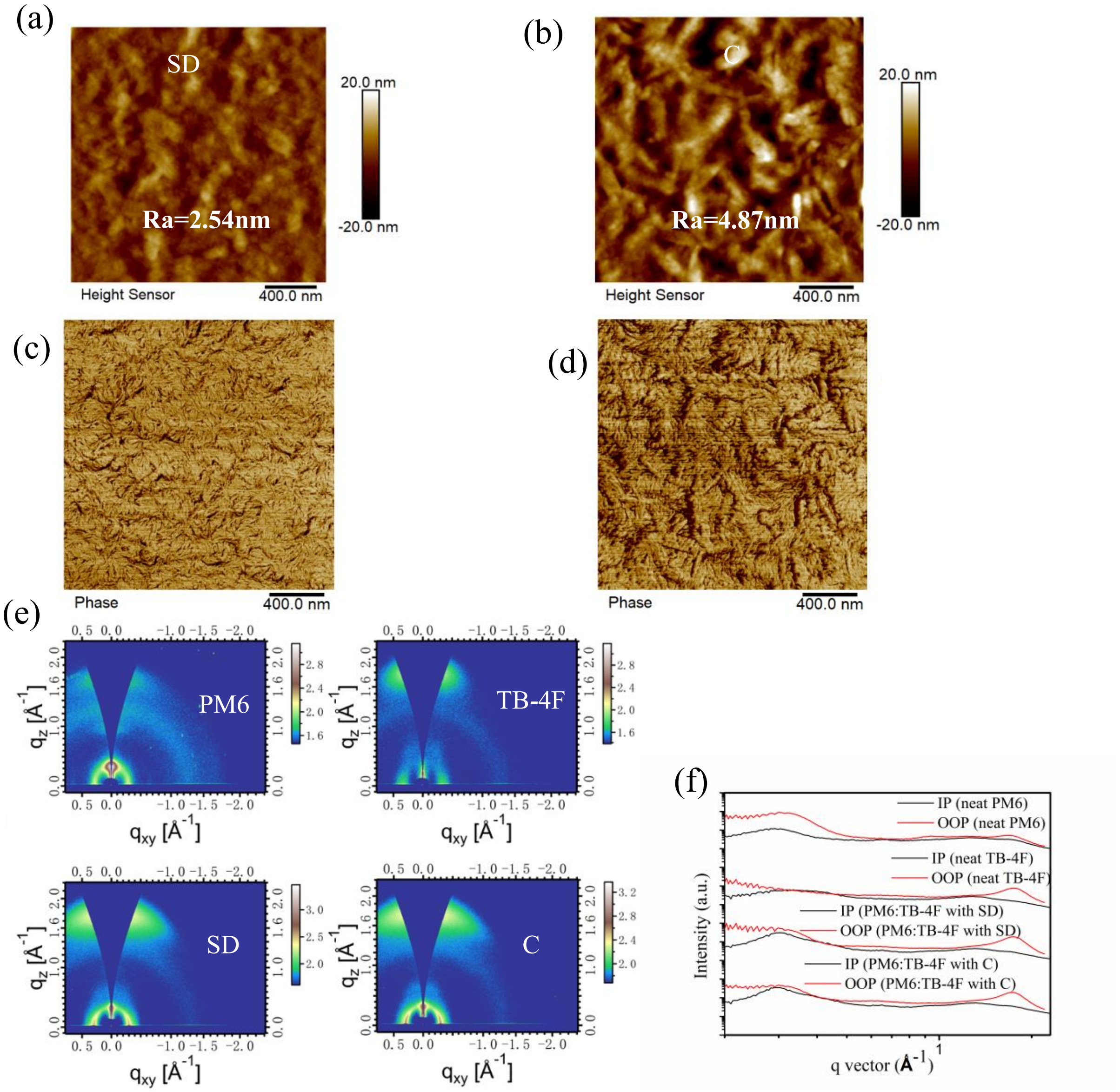

Figure 4.15. Tapping-mode AFM high images (2×2 μm) of SD OSCs (a) and C-BHJ OSCs (b) of PM6: TB-4F. Tapping-mode AFM phase images (2×2 μm) of SD OSCs (c) and C-BHJ OSCs (d) of PM6: TB-4F. (e) 2D GIWAXS images of neat films of PM6,TB-4F, and blend films of SD OSCs and C-BHJ OSCs of PM6: TB-4F. (f) GIWAXS intensity profiles along the in-plane (dotted line) and out-of-

plane (solid line) directions.

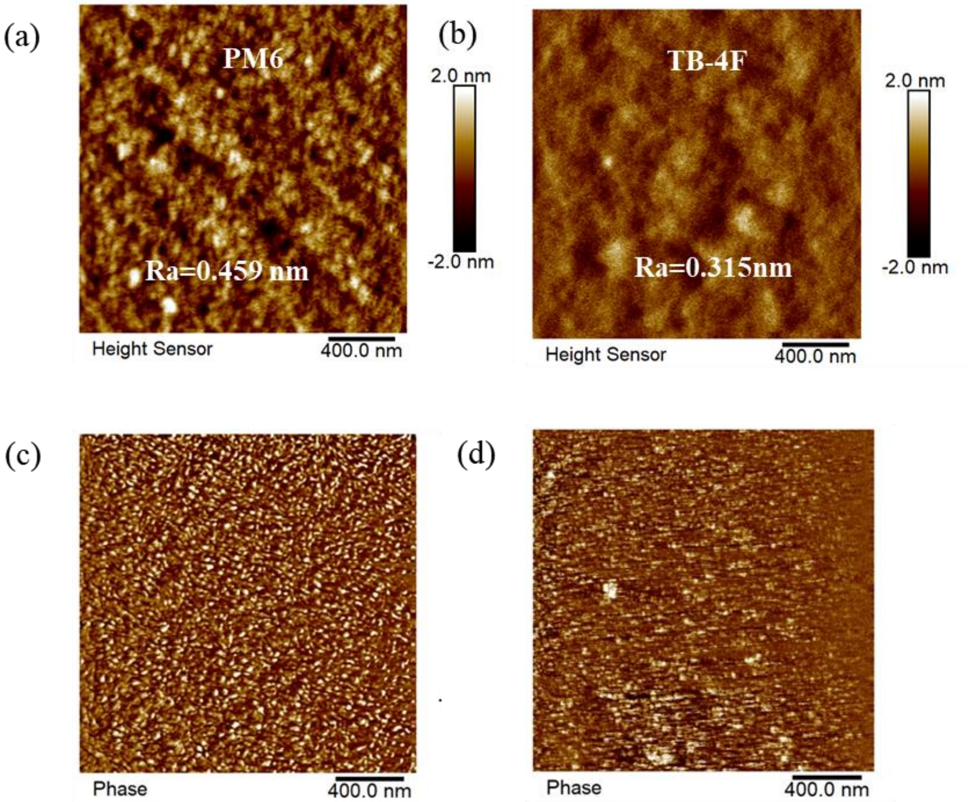

Figure 4.16. Tapping-mode AFM high images (2×2 μm) of neat PM6 in film (a) and neat TB-4F in film (b). Tapping-mode AFM phase images (2×2 μm) of neat PM6 in film (c) and neat TB-4F in film (d).

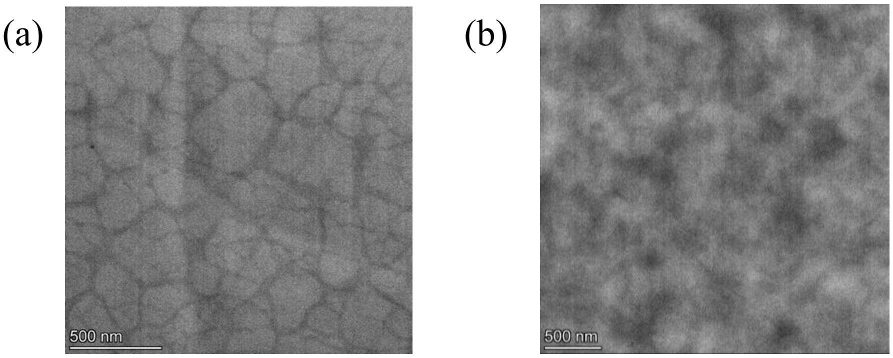

Figure 4.17. TEM of SD OSCs (a) and C-BHJ OSCs (b) for PM6:TB-4F.

4.4 Conclusion

We designed and synthesized an acceptor, TB-4F, with a trade-off of absorption spectrum ranged from 600 to 850 nm and relatively high EQE. PM6:TB-4F based OPVs were fabricated by C-BHJ and SD-BHJ, respectively. The optimal devices of PM6:TB-4F produced PCE of 14.44% and 15.24% for C-BHJ and SD-BHJ, respectively, under the illumination of AM1.5. For 1000-lux LED illumination, devices showed PCE of 16.82% and 21.05% for C-BHJ and SD-BHJ, respectively. SD-BHJ shows better performances under both sunlight and artificial light. Detailed characterizations imply that SD-BHJ process can produce better morphology in active layer than that of C-BHJ process so that more carriers were generated and extracted leading to higher J_{SC}, trap state and bimolecular recombination were mitigated resulting in improved *FF*, and leakage current was suppressed leading to higher V_{OC}. The advantages of SD-BHJ were further enhanced and broadened when illuminated by the artificial light, because the trap-assisted recombination and dark current can strongly affect PCE in the condition of low carrier density. Therefore, this work not only demonstrates that PM6:TB-4F based OPVs are a promising candidate installed for devices installed in a realistic room where sunlight and artificial light are available, but also testifies that SD-BHJ yields better PCE than that of C-BHJ, especially under dim light illumination.

CHAPTER 5

Rational tuning of intermolecular and intramolecular interactions enabling high-efficiency indoor organic photovoltaics

5.1 Synopsis

IOPVs are one of promising candidates for transferring artificial illumination to power the IoT. However, their power conversion efficiencies (PCE) are limited by the fact that only a few efficient non-fullerene acceptors are available for IOPVs. Herein, a new strategy is adopted to tune the intramolecular charge transfer (intra-CT) and intermolecular charge transfer (inter-CT) to achieve high PCEs under indoor environment in the combination of changing skeleton from symmetry to asymmetry and end group from chlorination to non-chlorination. The study reveals that, in comparison with symmetric molecule BTP-2ThCl, asymmetric structure TB-SCl possesses a smaller intra-CT resulting in higher V_{OC} and strengthened inter-CT for neighboring acceptors resulting in more efficient carrier collection and thus higher *FF*. Moreover, the non-chlorine molecule TB-S exhibits smaller intra and inter-CT leading to further promoting V_{OC} but smaller *FF* compared with TB-SCl under 1-sun illumination. When the illumination is switched to artificial light, the mitigated trap state, minimized leakage current, and suppressed non-radiative energy loss ($\Delta E_{\mathrm{nonrad}}$) enable a novel acceptor TB-S yielding high-efficiency rigid PCE of 23.3% which surpasses TB-SCl and flexible PCE of 20.02% which is one of the best PCE for flexible IOPVs. Our observation provides a new insight into molecule structure modification to promote the indoor photovoltaic performance.

5.2 Introduction

5.2.1 Requirement to achieve high PCE for IOPVs

Recently, OPVs have been reported as one of the promising candidates for indoor light harvester[32, 95]. The market requirement for transferring artificial light to electricity is getting to increase as the market of IoT rapidly grows[28-30, 159]. Also, benefiting from the tunable bandgap of non-fullerene organic acceptor material, flexibility, light weight, and its solution processability, OPV is one of validate candidates to drive vast off-grid low power consumption applications and can realize industrialization[23-25, 96, 189-193]. Different with sun simulator, LEDs as a popular light source are chosen to simulate indoor illumination, with emission wavelength from 400 to 750nm, whose spectrum is much narrower and weaker than that of 1-sun intensity for outdoor condition[4]. This suggests that the active layer for utilizing indoor spectrum is narrower than that for utilizing outdoor spectrum.

Nowadays, only a few reported PCE undergone accurate indoor organic photovoltaic (IOPV) measurement[194] reached over 26%[46, 94] and some reported PCEs are exaggerated and inaccurate. Hence, a spectrometer should be applied to accurately evaluate wavelength resolved spectrum of incident indoor light source to get the integrated intensity. The combination of EQE curve and photon flux curve derived from spectrometer can certify the accuracy of current density of device. The specified measurement is shown in **section 3.6.17**. How to achieve high PCE for IOPVs has already been declared, which comprises three elements[4] as shown in the following. (1) high V_{OC} requests wide bandgap [94]. (2) low voltage loss (V_{loss}) when light source is changed from 1-sun condition to artificial light condition, which demands small leakage current that is proportional to dark current [15, 101, 103-105, 107]. (3) high *FF* under dim light environment calls for suppressed trap recombination [95-98, 195]. A qualified IOPV device should fulfill criteria listed above. Therefore, the strategy to design active materials should be carried out to supply guidance for achieving high-efficiency IOPVs.

5.2.2 Summary of design principle for acceptor applied for IOPVs

In recent years, non-fullerene acceptors were designed and synthesized to have better absorption spectrum overlapped with LEDs emission spectrum. In the perspective of molecule design, in order to further improve the PCE of OPVs for indoor environment, the wide bandgap acceptor to better utilize artificial spectrum should be designed and synthesized with a certain bathochromic-shifted spectrum. The effective strategy to increase the bandgap of acceptor are summarized in the following: (1) a weak donor (D) moiety is introduced to replace strong D moiety to reduce the intramolecular charge transfer (intra-CT) so that effectively increase the bandgap of acceptor. Yan's group designed a new molecule that is neither the derivatives of ITIC nor Y6, named FCC-Cl, with a weak electron donating unit using a fluorenedicyclopentathiophene as the core in the structure of A-D-A yielding 29.4% efficiency under 1000-lux LED benefited from the decrease of LUMO and the reduction of intra-CT[196]. (2) the low electronic density end group (A unit) replaced by high electronic density can decrease the intra-CT leading to successfully blue-shift absorption spectrum. Hou's group modified the molecule of ITIC with a A-D-

A structure named IO-4Cl achieving 26% efficiency under 1000-lux condition[94]. Their cores are the same, but the end group of IO-4Cl possesses higher electronic density compared with that of ITIC due to the substitution of carbonyl unit for malononitrile group, leading to the increase of LUMO and thus the improvement of V_{oc} because of the decrease of intra-CT. However, derivatives of ITIC have relatively low EQEs.

Most reported high-efficiency IOPVs adopted fullerene-based[197, 198] and ITIC derivatives-based[94, 199] acceptors. However, the lack of tunability and deeper LUMO of fullerene derivatives, and relatively low extinction coefficient leading to low J_{SC} and inferior FF of ITIC series, in comparison with Y6 series, make the urgent of development of Y6 derivatives for IOPVs utilizing dim light. The star organic molecules, Y6 and its derivatives with A-DA'D-A structure possess superior absorption ability and high charge mobilities resulting high PCE under the illumination of 1-sun, but with broader spectrum leading to relatively lower V_{OC}, which is not quite suitable for harvesting artificial emission. Therefore, the modification of Y6 series resulting in higher V_{oc} used in IOPVs should be made. However, the reported works about Y6's derivatives for IOPV are rare. In 2021, Yan's group replaced D unit from thienothiophene to benzothiophene aiming reducing intra-CT and thus up shifting its LUMO. The blue-shifted molecule, LBT-SCl[196], achieved 25.1% PCE under the illumination of 1000-lux LED. Based on the huge potential from the structure of Y6 series applied in IOPVs, more attention should be pay on the modification of it.

5.2.3 Design strategy

Since Y6-series molecule[66] has been figured out with a highly efficient performance owing to good phase separation, high charge carrier mobilities, and high EQE, Y6-series molecule was chosen in this work to be reformed to better utilize the illumination of artificial light. As shown in **Figure 5.1**, two design strategies are described for high-efficiency IOPVs.

Strategy 1: TB-SCl was designed and synthesized derived from symmetric BTP-2ThCl[147] which produces higher V_{OC} and blue-shifted spectrum compared with Y6. Asymmetric backbone achieved by reducing a thiophene is chosen as the main chain inspired by numerous works showing that in comparison of symmetric analogue, asymmetric skeleton displayed higher *FF* and stronger intermolecular π - π stacking[146, 176, 200-203].

Strategy 2: by modifying the terminals with a weaker acceptor (A) unit [94], removing chlorine in the thiophene-fused end groups from TB-SCl, TB-S was obtained. The detailed synthesis schemes of TB-SCl and TB-S are illustrated in the **Section 3.4.2**. The aim products were synthesized with five-step reactions. Products were verified by ^{1}H nuclear magnetic resonance (NMR) spectroscopy. The corresponding spectra were shown in supporting information (SI). BTP-2ThCl was synthesized according to the reported work[147].

5.2.4 Objective of this work

In this work, inspired by the structure of a derivative of Y6, BTP-2ThCl[147], that can yield higher V_{OC} than Y6, an asymmetric framework was designed by reducing a fused ring in the D moiety. According to Huckel's molecular orbital method, reducing conjugated chain can yield HOMO resulting a boarder bandgap and blue-shifted absorption. Moreover, in order to further tune the bandgap of acceptors, end group was replaced from chlorination to non-chlorination for thienyl-fused indanone so that the weakening electron-withdrawing end group enables further up-shifted LUMO level. Herein, two new acceptors with an A-D_1A'D_2-A structure are designed and synthesized to compare the performance of an asymmetric backbone with two specified end groups. The TB-SCl acceptor with the halogenous end group, 2-(6-oxo-5,6-dihydro-4H-cyclopenta[c]thiophen-4-ylidene) molononitrile (1), coupled with PM6 to fabricate devices. The TB-S with non-halogenous end group, 2-(6-oxo-5,6-dihydro-4H-cyclopenta[b]thiophen-4-ylidene) molononitrile (2), blended with PM6 to make devices. The detailed synthesis route and deice fabrication process were summarized in **section 3.4.2** and **section 3.5.2**. In comparison, symmetric molecule BTP-2ThCl was adopted to fabricate devices to study the effect of molecular conformation. The performance of the fabricated devices was evaluated under different illumination conditions, specifically AM1.5 and 3000K LED lights with intensities of 200 lux, 500 lux, and 1000 lux, to obtain their corresponding PCEs. Although SD-BHJ has been figured out that it show superior performance under the indoor condition in comparison with C-BHJ, the aim of this work is to demonstrate the relationship between performance and molecular design, C-BHJ technology was adopted in this work to avoid plenty of parameter optimization so that save lot of time.

The objective of this study was to uncover the effects of removing a fused ring to form an asymmetric framework and subsequently enhancing the electronic density of the end group, based on the Y6 series molecule, on the modulation of intra-CT and inter-CT, and hence its influence on the PCE under indoor illumination.

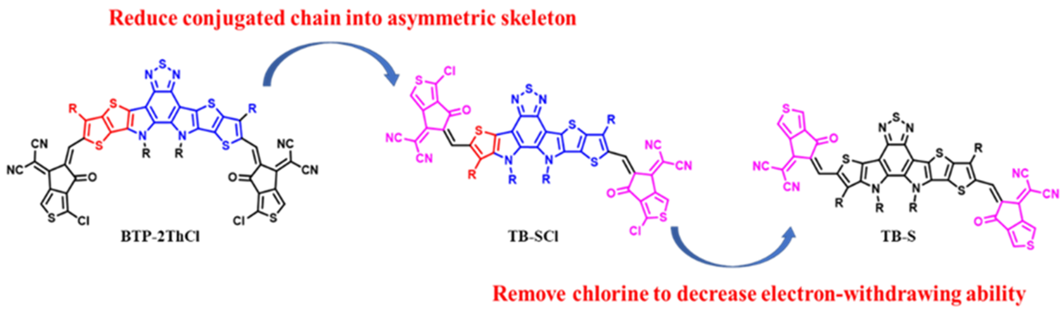

Figure 5.1. Molecules design strategies for IOPVs.

5.2 Results and discussion

5.2.1 Quantum calculation

DFT calculation by Gaussian 09 was performed to optimize the molecules of TB-SCl and TB-S. The optimization conformations for TB-SCl and TB-S were calculated. The results reveal that these two molecules possess the lowest energy when they in the nearly coplanar situations. Furthermore, B3LYP/6-31G(d,p) were executed to optimal conformation. Atomic charges were calculated from Multiwfn program. The binding energy for neighboring acceptors were calculated. Based on the theoretical calculation by Gaussian 09, molecular configurations for two novel acceptors applied in IOPVs, TB-SCl and TB-S, display S-type owing to the strong non-covalent interaction between S-O conformation locking. As displayed in **Figure 5.2,** the calculation reveals that the HOMO distributes on the donor unit of backbone and the LUMO spreads over the end group. The HOMO and LUMO for TB-SCl and TB-S are -5.672/-3.63 eV and -5.602/-3.533 eV, respectively. Compared with TB-SCl, the uplifted LUMO for TB-S is beneficial for acquiring higher V_{OC}.

For BTP-2ThCl, TB-SCl and TB-S, in order to evaluate the influences of (1) symmetric/asymmetric conformations for skeleton and (2) with/without halogen in the terminal groups, the comparisons of intra-CT and intermolecular charge transfer (inter-CT) for adjacent acceptors was investigated from the studies including intramolecular dipole moment (**Figure 5.3**) through calculating left-half-side molecules (as right-half sides are same), whole molecular dipole moment (**Figure 5.4**), molecular electrostatic potential (ESP), and binding energy calculated. ESP was studied with Gaussian, Multiwfn[154] and VMD. Binding energy was assessed and corrected by basis set superposition error (BSSE)). Notably, because of the asymmetric structures, there were two types of packing confirmation when the binding energy was calculating for TB-SCl and TB-S but only one for symmetric BTP-2ThCl. Within two types of dimer packing, the one yields stronger binding energy was adopted.

(1) Section 1: symmetric/asymmetric conformations for skeleton

On the aspect of intra-CT, the smaller intra-CT leads to larger V_{OC}. A common strategy adopted in OPV molecule design integrates push-pull nature of the alternating electron-rich and electron-deficient moieties promoting intra-CT upon photoexcitation. The larger dipole moment pointing from the end group to the core implies the enhanced intra-CT resulting in that more negative charge concentrated in A unit and more positive charge concentrated in D unit, namely excitons[204-208]. The study revealed that a delocalized exciton is formed under illumination within 150 fs timescale followed by localization and subsequently recombination[205, 209]. The bandgap between HOMO and LUMO increases leading to blue-shifted absorption provided that the intramolecular dipole moment decreases. The result of **Figure 5.3** shows that the intramolecular dipole moment decreases from 8.697 to 7.951 D for BTP-2ThCl and TB-SCl, respectively, suggesting that intra-CT was weaken by the modification from symmetricity to asymmetricity via reducing a thiophene ring, leading to a blue-shifted absorption spectrum. On the aspect of inter-CT for acceptors , compared with BTP-2ThCl, although TB-SCl possesses a little lower dipole moment of μ_m=2.16 D than that of BTP-2ThCl of μ_m=2.48 D, vectors in direction of X and Z for asymmetric TB-SCl which are μ_x=0.595 and μ_z=-0.61 D whereas nearly zero for BTP-2ThCl (**Figure 5.4**). The vector of dipole moment along packing directions is considered to intensify the inter-CT between neighboring molecules due to the trend of eliminating the dipole moment of the molecule resulting in enhanced molecule packing[176, 196, 210, 211]. This is beneficial for intermolecular interaction among adjacent molecules, which was verified by the calculation of binding energy. It is noteworthy that while there is only one mode of intermolecular packing for symmetric molecules, there are two modes for asymmetric molecules. The mode with a higher binding energy will be selected. As described in **Figure 5.5**, the calculated binding energy was -63.29 kcal/mol for TB-SCl that was stronger than that of BTP-2ThCl(-27.97 kcal/mol). The longer stacking distance is proportional to stronger intermolecular interaction verified by some studies[176, 202]. The stronger intermolecular interaction with longer stacking distance is in favor of enhancing molecular packing between neighboring molecules. This also benefits enhanced *FF* because excitons can diffuse longer distances owing to larger crystalline domains showed by many studies[212, 213], and thus avoids recombination at the interface of overmixed phases.

(2) Section 2: with/without halogen in the terminal groups

It has been figured out that LUMO can be shifted up by replacing the end group with the higher density one, so chlorine was removed for TB-S. In the terms of intra-CT, the intramolecular dipole moment of TB-S (7.369 D) is smaller than that of TB-SCl (7.951 D), implying that the elimination of chlorine in the end group resulting in decrease in intra-CT, and thus higher V_{OC}. Furthermore, as shown in **Figure 5.6-5.13**, decreased electrostatic potential (ESP) value in the terminal moiety of TB-S caused by the elimination of chlorine atom that possesses strong electron-withdrawing ability, resulting in increased electronic density so that weaken intra-CT and more blue-shifted absorption. Consequently, weakening intra-CT ability can acquire more matched absorption spectrum to LED emission spectrum. Another aspect, in consideration of dimer packing, the inter-CT of acceptors for TB-SCl is stronger than that of TB-S, as the calculated binding energy are -63.29 kcal/mole and -57.43 kcal/mole, respectively. This is because of omitted chlorine for TB-S resulting in decreased inter-CT as the lack of non-covalent bonds of Cl⋯S and Cl⋯H. Besides, the smaller dipole moment vectors of μ_x=-0.209 D and μ_z= 0.511 D for TB-S in the comparison in TB-SCl leading to reduced inter-CT. Briefly, there is a trade-off between weakened intra-CT to acquire blue-shifted spectrum and strength inter-CT to improve molecular stacking. Reducing intra-CT leads to a progressive increase in V_{OC}, but excessive weakening of intra-CT ultimately has a detrimental effect on inter-CT, resulting in inferior carrier transport.

ESP results indicate that ESP value of PM6 is opposite to the acceptors, which facilitates charge transfer from donor to acceptor[214, 215]. In **Figure 5.7b**, the surface area ESP distributions for TB-S, TB-SCl, and BTP-2ThCl gradually tend to more positive ESP value, which implies that their interactions for donor and acceptor are gradually increase[215]. However, the intense Donor-Acceptor intermolecular interaction can conduce high charge generation but also may lead to impure domain or overmixed domain, and thus carrier recombination and large nonradiative recombination. The reported research revealed that the mixed phase where the interface of donor and acceptor can strongly regulate charge generation and recombination[216]. Two extreme cases as completely mixed domains and pure domains are both detrimental to the efficiently charge transfer and thus only proper interaction between donor and acceptor conduce to charge extraction. Hence, excessive donor-acceptor intermolecular interactions leading to ultrafast timescale photocurrent but suffering quick recombination due to the overmixing domains and impure domains.

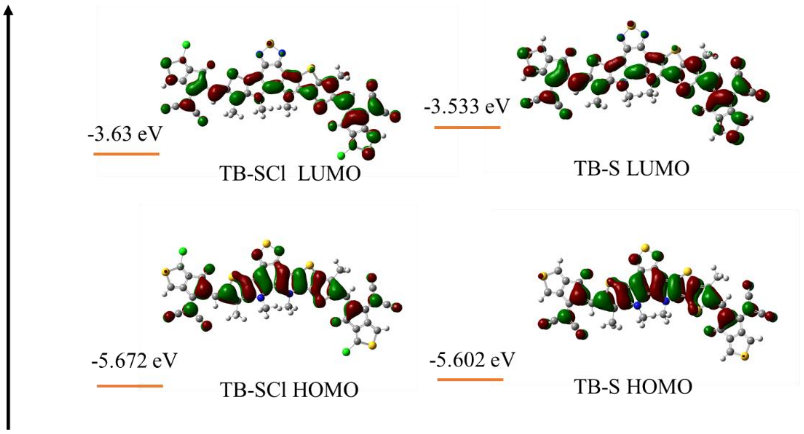

Figure 5.2. The frontier molecular orbitals obtained by DFT for TB-SCl and TB-S.

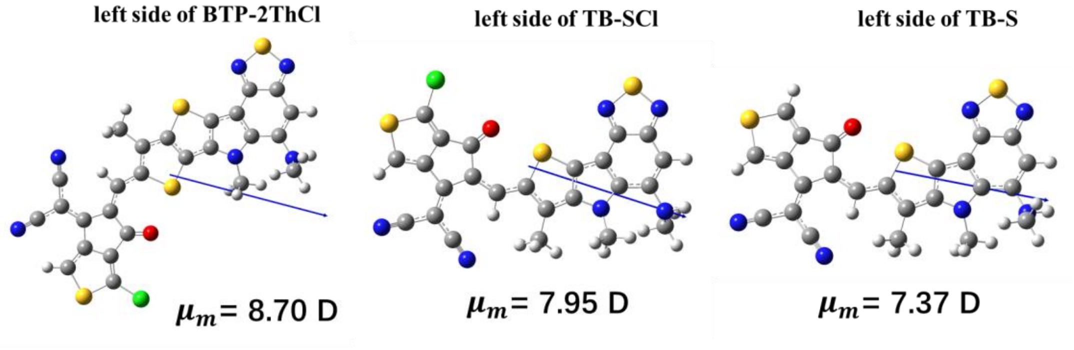

Figure 5.3. Theoretical calculation of the intramolecular dipole moments of left-half-side molecule for acceptors based on B3LYP/6-31(d.p).

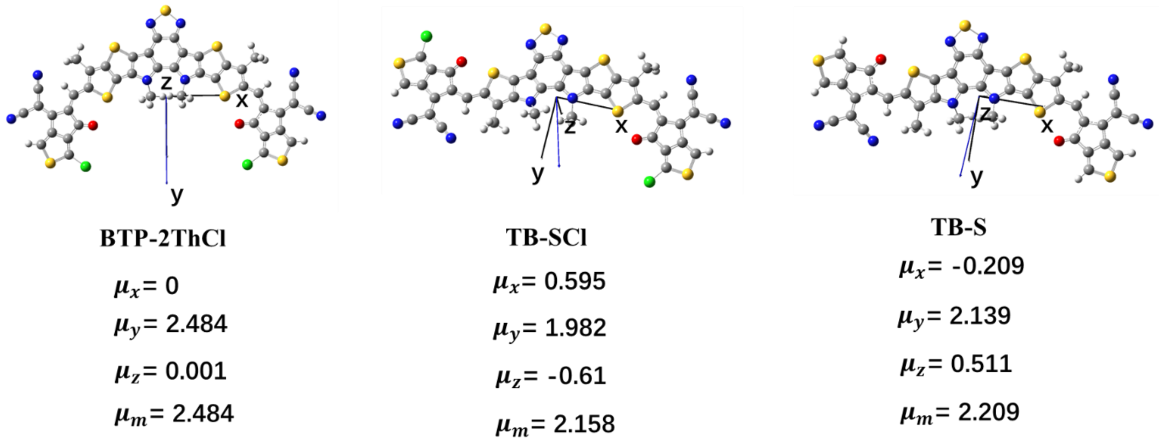

Figure 5.4. The dipole moment for the whole molecules for BTP-2ThCl, TB-SCl and TB-S.

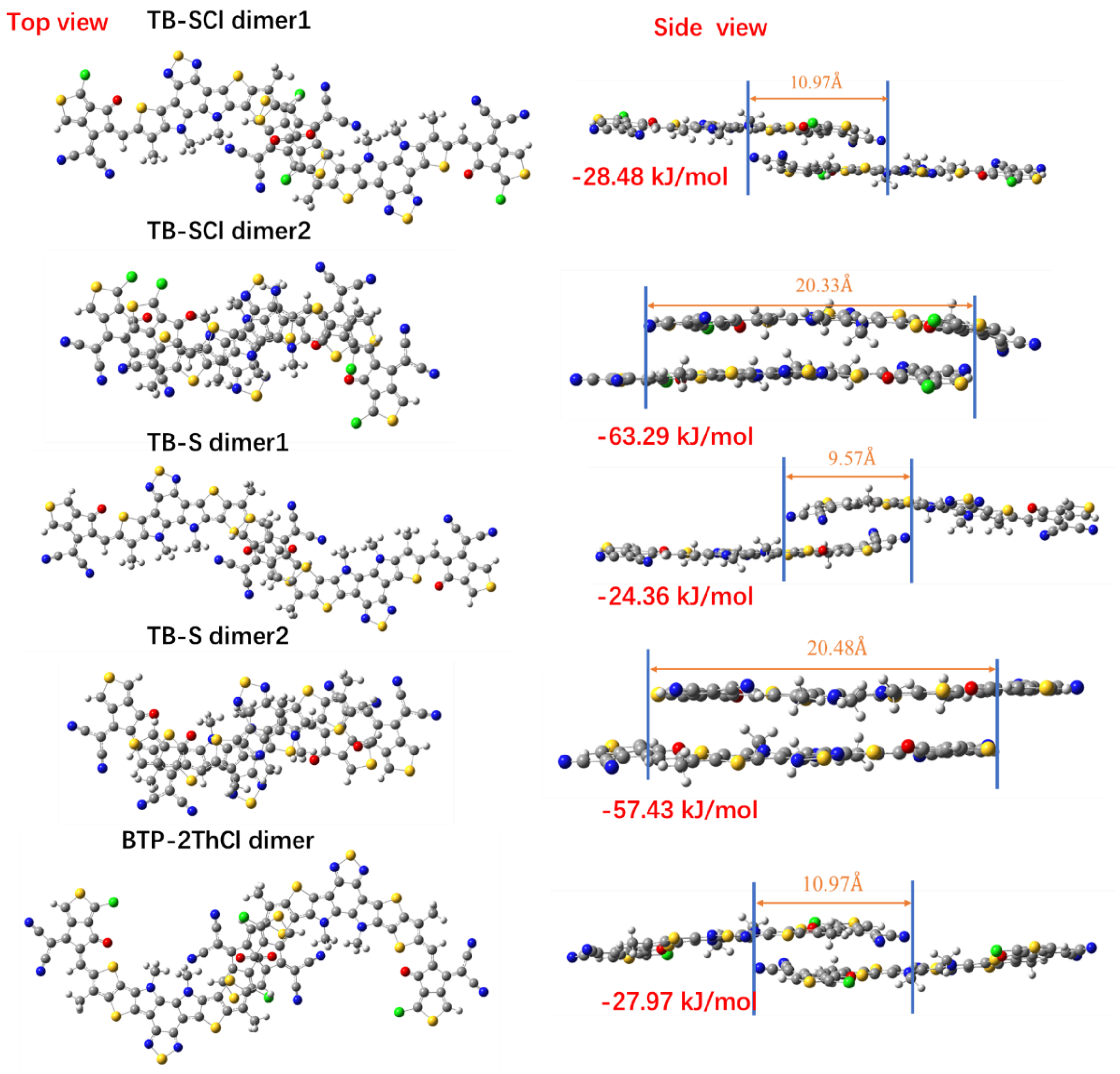

Figure 5.5. The results of theoretical simulations of TB-SCl and TB-S of dimer packing. For the asymmetric structures, there are two types of packing confirmation for TB-SC ne for symmetric BTP-2ThCl. Within two types of dimer packing, the one yields stronger binding energy is adopted.

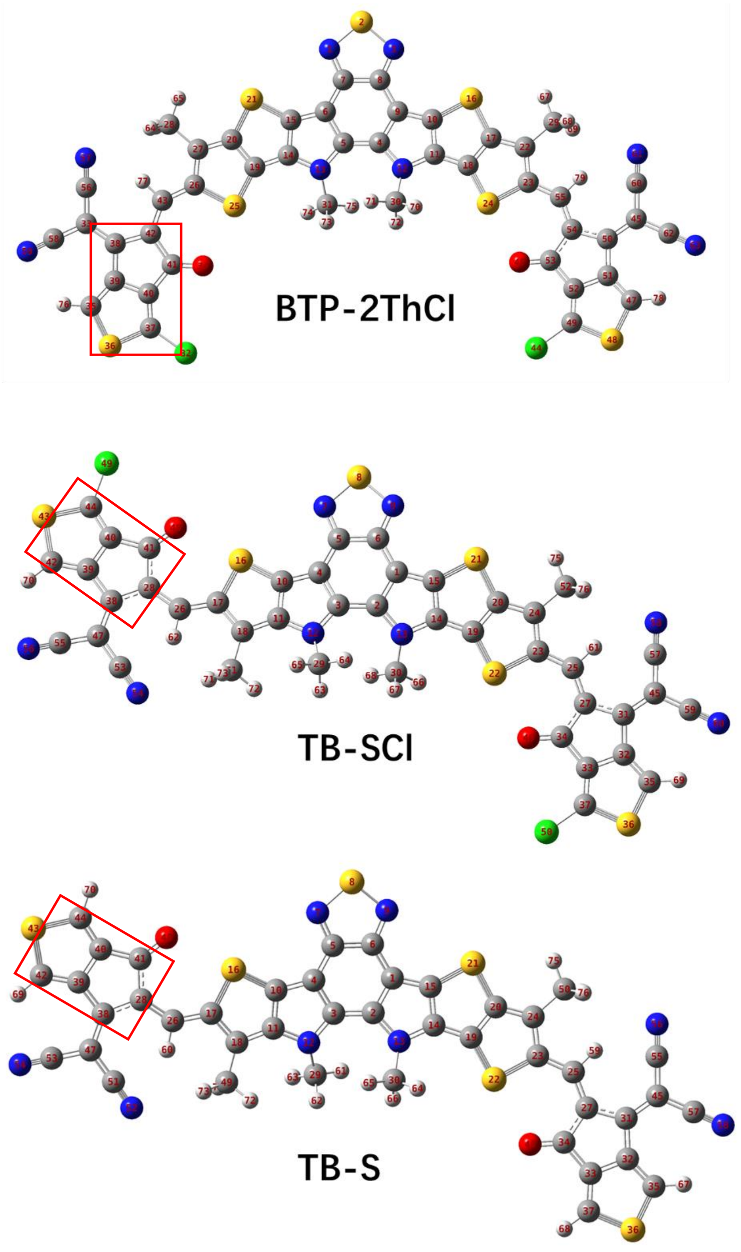

Figure 5.6. Atom labels of BTP-2ThCl, TB-SCl, and TB-S.

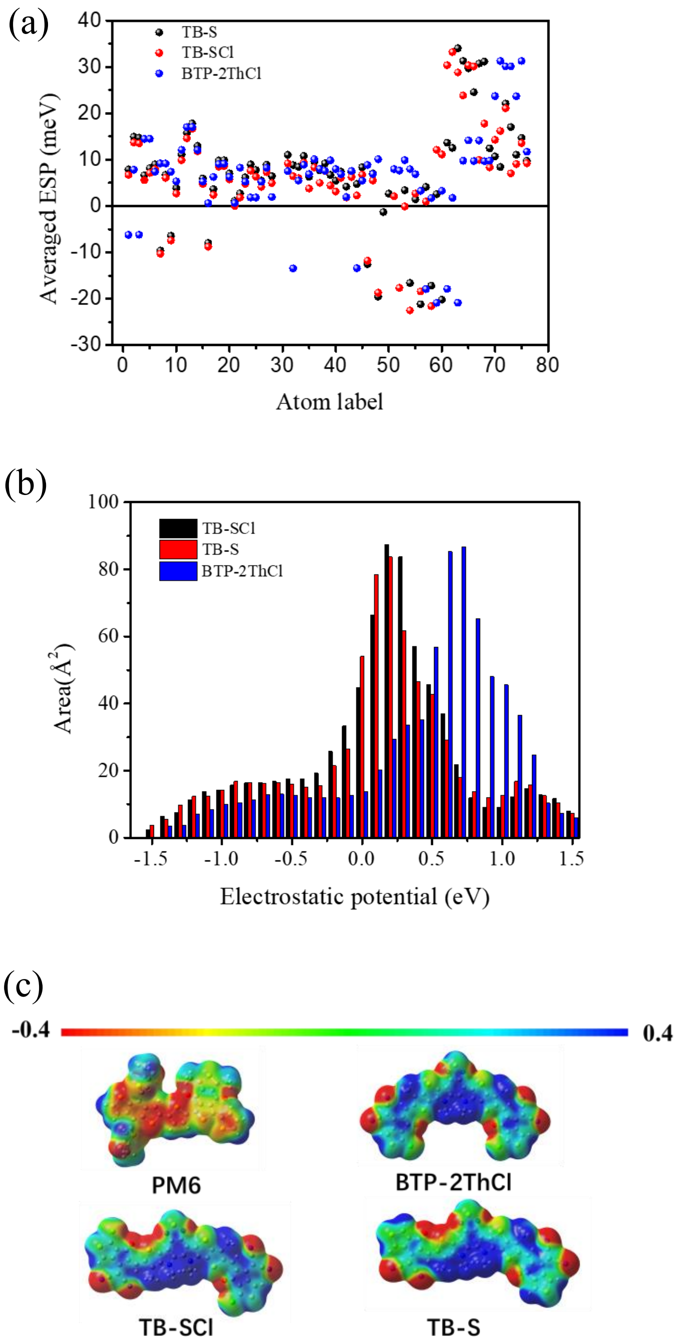

Figure 5.7. (a) ESP value for each atom of BTP-2ThCl, TB-SCl, and TB-S.(b) ESP area distributions of BTP-2ThCl, TB-SCl, and TB-S. (c) ESP of PM6, BTP-2ThCl, TB-SCl, and TB-S.

5.2.2 Photovoltaics and photoelectric properties

In order to study the photoelectric properties, the frontier orbital energy levels of BTP-2ThCl, TB-S and TB-SCl were evaluated by CV to calculate HOMO and LUMO, as depicted in **Figure 5.9**. The energy levels for materials are shown in **Figure 5.8**. The tested HOMO and LUMO are -5.56 eV and -3.97 eV, -5.67 eV and -3.94 eV, and -5.57 eV and -3.82 eV, for BTP-2ThCl, TB-SCl, TB-S, respectively.

This indicates that transforming skeleton into asymmetry and subsequently removing halogen in the terminal group can continuously decrease intra-CT and achieve wider bang gap to better cover LED emission spectrum. The corresponding UV-vis absorption spectra of neat donor and acceptors and blended film are described in **Figure 5.10**. TB-S in film (peak at 719 nm) shows more blue-shifted absorption than TB-SCl (peak at 784 nm) and BTP-2ThCl (peak at 833 nm) in films, which indicates the successful molecular modification. Bathochromic shift phenomenon is observed in both novel acceptors from solution to film presenting strong intermolecular existed in both blended films.

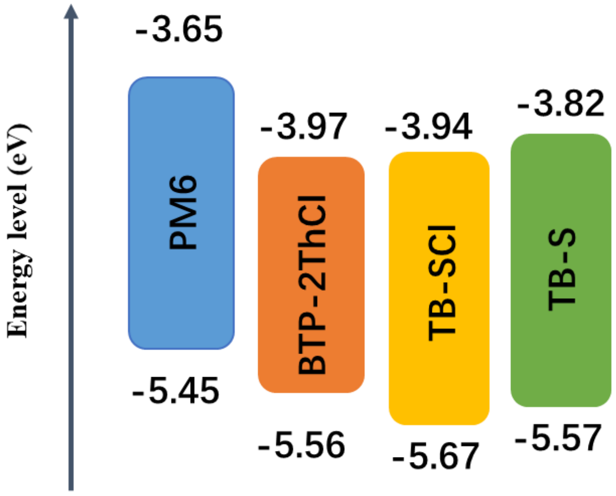

Figure 5.8. Energy levels of PM6, BTP-2ThCl, TB-SCl, and TB-S.

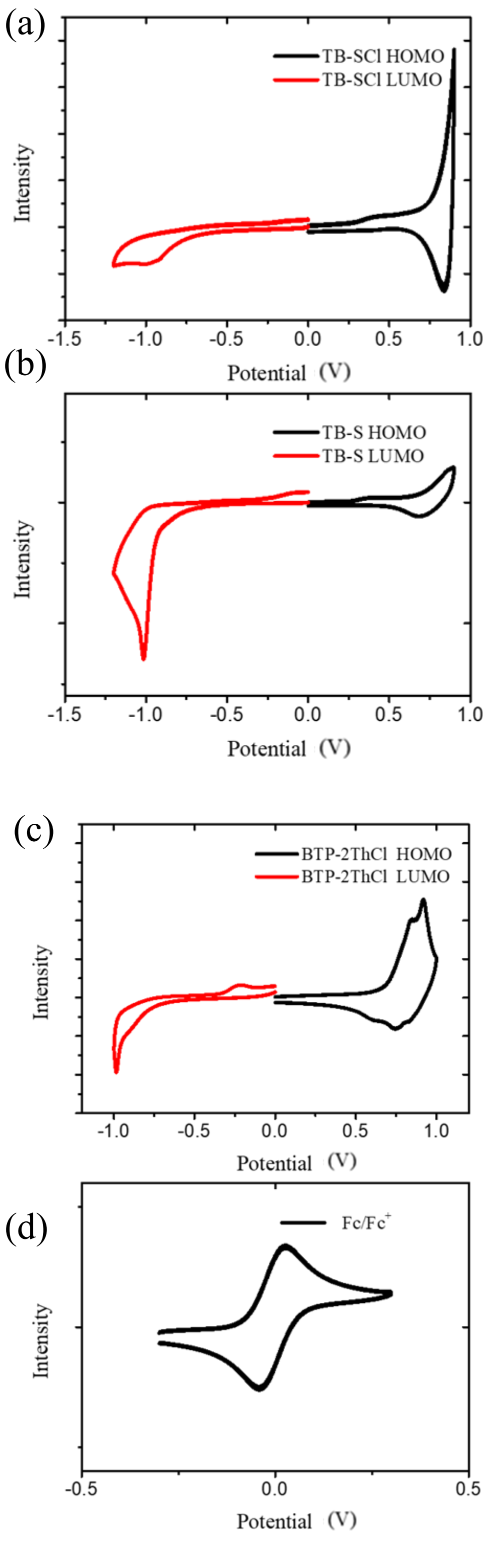

Figure 5.9. CV test for (a) TB-SCl, (b) TB-S, (c) BTP-2ThCl, and (d) Fc/Fc+.

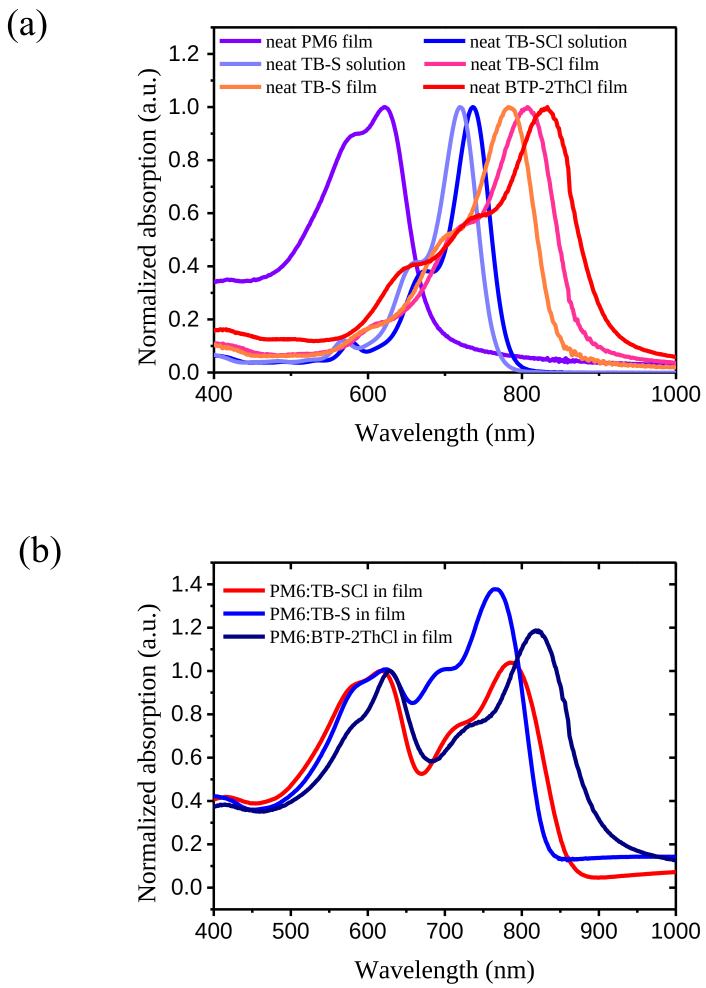

Figure 5.10. (a) absorption spectra of neat donor and acceptors in CF solution and film. (b) absorption spectra of blend films for PM6:BTP-2ThCl, PM6:TB-SCl, and PM6:TB-S.

3.3.2.1 Photovoltaic properties under AM1.5

A conventional structure of ITO/PEDOT:PSS/active layer/PDION/Al was adopted to investigate the photovoltaic performance under the illumination of 1-sun intensity (100 mW cm^{-2}). The relevant photovoltaic properties for PM6:BTP-2ThCl, PM6:TB-S, and PM6:TB-Cl based device are displayed in **Figure 5.11a** and **Table 5.1**. The optimal D:A equals to 1:1.2 for all active layers dissolved in CF. PM6:BTP-2ThCl based device delivered a PCE of 14.1%, with a V_{OC} of 0.885 V, a J_{SC} of 23 mA/cm^2, and an FF of 69.6. As asymmetric S conformation with reduced conjugation, the absorption shifted to blue leading to a certain loss in J_{SC} but an elevation in V_{OC} and FF. Therefore, PM6:TB-SCl based device yielded a better PCE of 14.8%, with a V_{OC} of 0.889 V, a J_{SC} of 22.76 mA cm^{-2}, and an FF of 73.2. When the electronic density in the terminal group was increased through eliminating the chlorine atom, the absorption was further blue shifted, which was attributed to the further decrease of intra-CT. So PM6:TB-S based device produced a higher V_{OC} of 0.949 V, a smaller J_{SC} of 20.19 mA/cm^2, and a similar FF of 72.4, and thus resulted in a PCE of 14.2%. **Figure 5.11b** shows the EQE curve of these three devices. It can be seen that the optimal devices based on the PM6:TB-SCl and PM6:TB-S exhibit superior photoresponse from 500 to 750 nm with the maximum value of 80%, suggesting efficient photon conversion and carrier collection attributed to their S conformations compared with U conformation. Although BTP-2ThCl has broader photoresponse leading to higher J_{SC}, the narrower and higher respond of asymmetric acceptors can better utilize the illumination of LED when are applied in indoor environment. The calculated J_{SC} are well consistent with the tested J_{SC} (within 5% error).

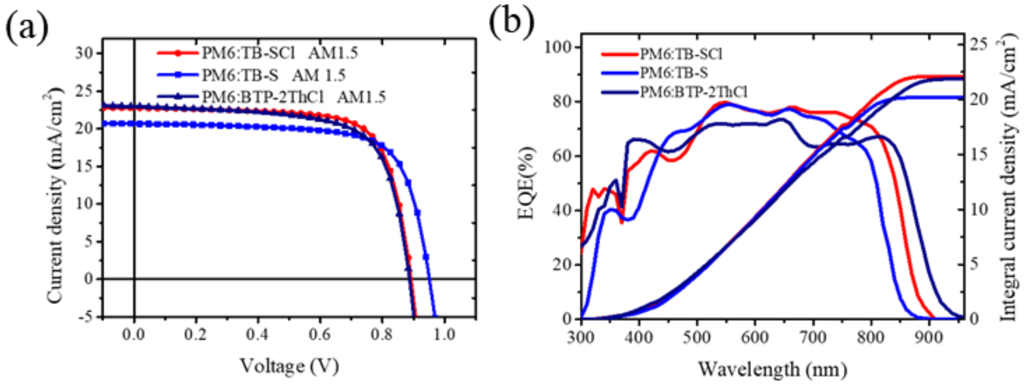

Figure 5.11. (a) *J-V* curves of OPVs fabricated by PM6:BTP-2ThCl, PM6:TB-SCl, and PM6:TB-S. (b) EQE curves of the corresponding OPVs.

Table 5.1. Photovoltaics parameters of the OPV cells under AM1.5G illumination.

AM1.5G	V_{OC} (V)	J_{SC} (mA cm^{-2})	$J^{a)}_{cal}$ (mA cm^{-2})	FF	R_SA (Ω cm^2)	$R_{Sh}A$ (Ω cm^2)	PCE$^{b)}$ (%)
PM6:BTP-2ThCl	0.885 (0.884±0.002)	23 (22.96±0.018)	21.87	69.6 (69.54±0.04)	2.83	783	14.14 (14.1±0.03)
PM6: TB-SCl	0.889 (0.885±0.003)	22.76 (22.55±0.196)	22.1	73.2 (71.53±1.76)	3.02	1562	14.81 (14.28±0.46)
PM6: TB-S	0.949 (0.947±0.001)	20.67 (20.52±0.200)	20.19	72.4 (72.28±0.81)	3.55	1492	14.20 (14.04±0.13)

[a)] Values were calculated from the integration of the EQE spectrum. [b)] Average values were obtained from 10 devices.

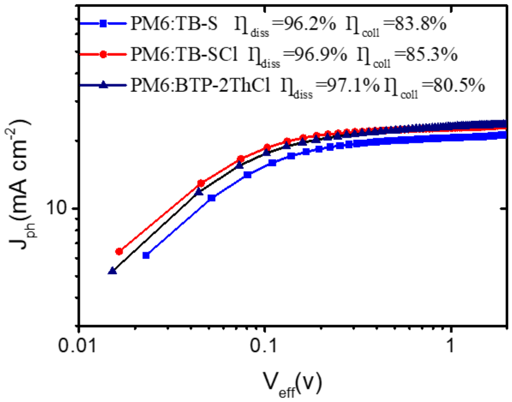

Figure 5.12. $J_{ph}-V_{eff}$ curves of three devices.

To get insight into the exciton dissociation (η_{diss}) and charge collection efficiencies (η_{coll}) of these three devices, the dependence of effective voltage (V_{eff}) and photocurrent density (J_{ph}) was evaluated (**Figure 5.12**)[217, 218]. The $\eta_{\text{diss}}/\eta_{\text{coll}}$ values are 97.1%/80.5%, 96.9%/85.3% and 96.2%/83.8% for BTP-2ThCl, TB-SCl, and TB-S based devices, respectively. Although BTP-2ThCl produced the highest J_{sat} and η_{diss} but showed the poorest η_{coll} resulting in the lowest FF owing to severe carrier recombination. The η_{diss} and η_{coll} for TB-SCl are slightly larger than TB-S based devices ascribed to chlorination leading to slightly molecular interaction. Overall, both PM6:TB-SCl and PM6:TB-S based devices enabled efficient charge generation and suppressed recombination, and thus exhibited balanced η_{diss} and η_{coll}.

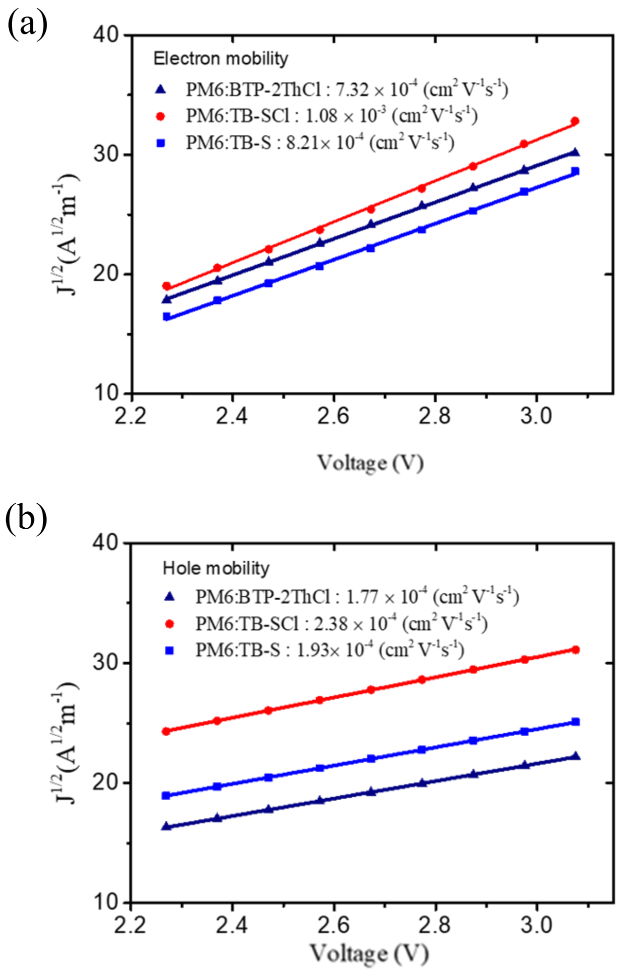

Figure 5.13. $J^{1/2}$ -V curves of electron (a) and hole (b) mobilities for all blended films.

The carrier mobility was investigated to assess their charge carrier mobilities via space-charge-limited-current (SCLC) as shown in **Figure 5.13**. The stronger interaction of asymmetric acceptors compared with symmetric acceptor contributes to a high electron mobility, eventually resulting a higher FF[219]. The result indicates that the electron mobility of TB-SCl-based film ($1.08\times 10^{-3} cm^2V^{-1}s^{-1}$) is much enhanced than that of BTP-2ThCl-based film ($7.32\times 10^{-4} cm^2V^{-1}s^{-1}$) due to improved inter-CT that is benefited by the asymmetric geometry. TB-S-based film

($8.21\times 10^{-4} cm^2V^{-1}s^{-1}$) shows decreased electron mobility that is attributed to non-chlorination leading to decrease intra-CT to achieve higher V_{OC} and thus decrease inter-CT among acceptors. For hole transfer ability, the hole mobilities for all films are similar, which are $1.77\times 10^{-4} cm^2V^{-1}s^{-1}$, $2.38\times 10^{-4} cm^2V^{-1}s^{-1}$, and $1.93\times 10^{-4} cm^2V^{-1}s^{-1}$ for BTP-2ThCl, TB-SCl, and TB-S-based films, respectively.

3.3.2.2 Photovoltaic properties under indoor environment

A 3000 K LED lamp with different incident intensities (1000 lux, 500 lux, 200 lux) was adopted as the light source simulating the indoor environment. Lux is a unit used to measure the amount of light that falls on a surface per unit area. The intensity of indoor artificial lighting is often measured in lux. For example, typical lux levels for different indoor lighting applications include: (1) 200 lux for simple orientation in hallways and stairs; (2) 500 lux for general office work, classrooms, and supermarkets; (3)1000 lux for detailed work such as reading, writing, and precision assembly; (4) 2000 lux for specialized visual tasks like inspection and medical examinations. Therefore, the PCEs of IOPVs applied under different indoor intestines were tested and compared. The incident intensities were accurately evaluated[194] by the spectrometer Maya pro 2000 (as described in **section 3.6.17**). The integrated input powers as described in **Figure 5.14** are 308.6 μW cm^{-2}, 161.77 μ W cm^{-2}, 68 μ W cm^{-2} for 1000-lux, 500-lux, and 200-lux illuminations, respectively. The relevant performances for IOPVs under indoor environment of different intensities are summarized in **Table 5.2**, **Figure 5.15** and **Figure 5.16**.

Under the illumination of 1000 lux, the PM6:TB-S performed the optimal PCE of 23.3% with a V_{OC} of 0.832 V, a J_{SC} of 110.9 μA cm^{-2}, and an *FF* of 74.1. For PM6:TB-SCl based device, the inferior PCE of 19.7% was achieved , with a V_{OC} of 0.725 V, a J_{SC} of 117.6 μA cm^{-2}, and an *FF* of 69.66. Whereas, PM6:BTP-2ThCl produced the lowest PCE under weak illumination of 14.57%, with a V_{OC} of 0.724 V, a J_{SC} of 109.8 μA cm^{-2}, and an *FF* of 56.59. The integrated current densities J_{cal}

under different indoor intensities for devices were derived from the combination of EQE curves and evaluated photon flux spectra, which show good agreement with the J_{SC} and thus confirms the reliability of our IOPVs test.

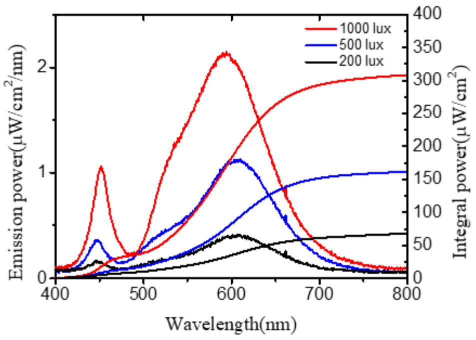

Figure 5.14. The integrated incident power of 1000 lux, 500 lux and 200 lux, respectively.

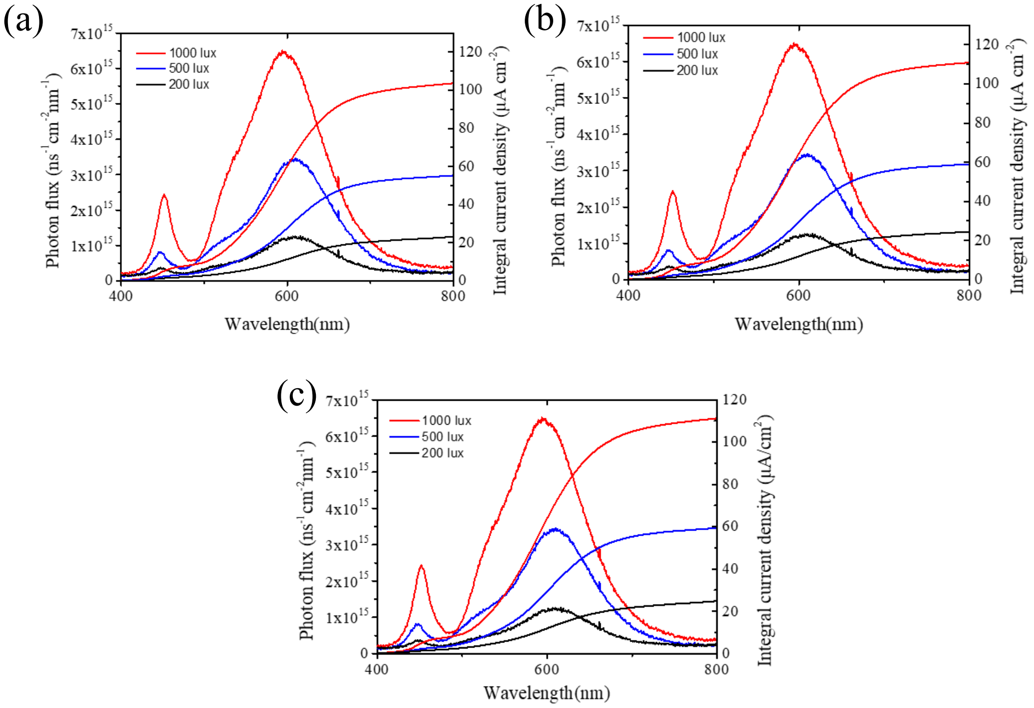

Figure 5.15. Input photon flux and integrated current density of 3000k-LED at 200, 500, 1000 lux for (a) PM6:BTP-2ThCl, (b) PM6:TB-SCl, and (c) PM6:TB-S based device, respectively.

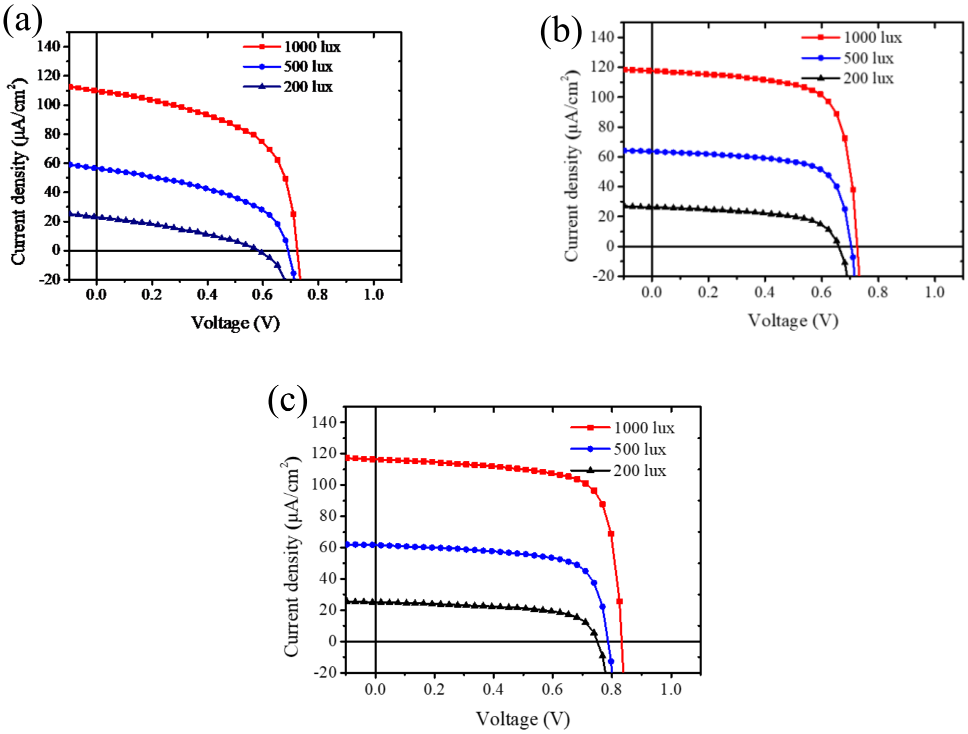

Figure 5.16. The *J*-*V* curves under indoor conditions with 200 lux, 500 lux, and 1000 lux intensities based on (a) PM6:BTP-2ThCl, (b) PM6:TB-SCl, (c) PM6:TB-S.

The blended films of PM6:BTP-2ThCl, PM6:TB-SCl, and PM6:TB-S shows comparable PCE under the illumination of sun. However, under the illumination of artificial light source, because the mismatch spectrum of BTP-2ThCl and LED and relatively low EQE response and low *FF*, the performance of PM6:BTP-ThCl yielded the worst PCE. It is worth noting that, although TB-S-based device showed a lower PCE than TB-SCl-based device under 1-sun illumination, when the light source was switched to dim light, the performance of PM6:TB-S surpassed that of PM6:TB-SCl. Therefore, the further characterizations were performed to demonstrate the performance of blended films under weak illumination.

It has been disclosed that, under the strong illumination, the bimolecular recombination is the dominant mechanism, but under the weak illumination, trap-induced recombination becomes the main mechanism affecting the IOPVs' performances[94]. This critical instruction suggests that when design material molecule structure and device constructure, trap state is the key defect which should be mitigated. To directly detect that different trap state for BTP-2ThCl, TB-S, and TB-SCl, the dependence of V_{OC} and light intensity as plotted in **Figure 5.17**.

In general, the slope closes to *kT*/*q* means the trap state is mitigated. It is can be found that, under sufficient carrier density, the calculated slopes are quite close to *kT*/*q* for PM6: BTP-2ThCl, PM6:TB-SCl, and PM6:TB-S which are 1.006 1.041, and 1.033, respectively, as bimolecular recombination mechanism is prominent. Notably, when the light density continuously decrease leading to insufficient carrier density, the calculated slopes enlarged to be 1.542, 1.397 and 1.346 for PM6: BTP-2ThCl, PM6:TB-SCl, and PM6:TB-S, respectively, implying that trap-induced recombination is dominant. Interestingly, the acceptor without halogen in the terminal group, TB-S, shows superior property of suppressed trap state in comparison of BTP-2ThCl and TB-SCl which is beneficial for achieving high *FF* value[4] (shown in **Figure 5.17b**) under dim light condition. The minimum trap state of TB-S is probably ascribed to the less ESP value of TB-S compared to TB-SCl and BTP-2ThCl that opposite to the ESP value of PM6 attributing to more proper Donor-Acceptor interaction[99].

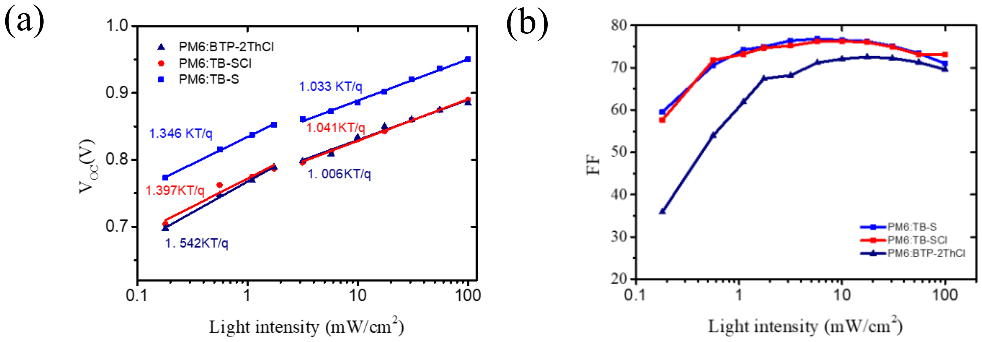

Figure 5.17. (a) V_{OC} and (b) *FF* versus light intensity (0.1-100 mW cm^{-2}) under solar simulator.

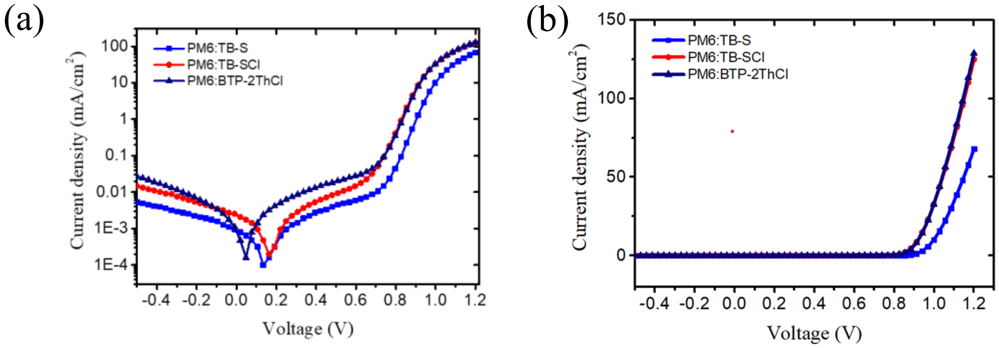

Figure 5.18. (a) The dark current density for the corresponding OPVs. (b) The current density (linear scale) as a function of the voltage for blended films under dark condition.

For leakage current, it is proportional to the dark current at the low bias voltage of -0.5V. As shown in **Figure 5.18**, TB-SCl-based device performed smaller dark current density than BTP-2ThCl-based device, implying that asymmetric acceptor exhibits suppressed leakage current. Moreover, TB-S-based device exhibits smaller dark current than TB-SCl-based devices, demonstrating that non-chlorination acceptor can further mitigate the leakage current. As the light current (I_{ph}) equals to the photogenerated current deducted leakage current (I_0), J_{SC} is affected by the I_0 that should be suppressed[15, 107]. Moreover, according to the expression of $V_{\mathrm{OC}} = \frac{\mathrm{n}KT}{q}\ln\left(\frac{I_{\mathrm{ph}}}{I_0}\right)$, in the condition of weak incident illumination resulting in low carrier density and thus low I_{ph}, the influence of I_0 will be amplified and predominant when the illumination is switched from 1-sun intensity to LED intensity. This implies that severe I_0 not only results in V_{loss} under strong illumination but also leads to much more serious V_{loss} under the weak illumination [196, 220, 221]. The TB-S based device has the minimum I_0 suggests that the strategy of non-halogen terminal group with asymmetric skeleton performs highest V_{OC} with the smallest V_{loss} when the light intensity significantly decreases. This is consistent with the result in the photovoltaic test in which the V_{OC} of TB-S devices showed ~0.06 eV higher than those of TB-SCl devices under the AM1.5G condition, but the V_{OC} of TB-S devices showed ~0.1 eV higher than those of TB-SCl devices under the LED light condition.

Table 5.2. Photovoltaics parameters of the OPV cells under 3000 K LED light with different light intensities.

Indoor	Intensity (lux)	V_{OC} (V)	J_{SC} (μA cm^{-2})	$J^{a)}_{cal}$ (μA cm^{-2})	FF	PCE$^{b)}$ (%)	P$_{out}$ (μW/cm^2)
PM6:BTP-2ThCl	1000	0.724 (0.723 ±0.001)	109.8 (109.6 ±0.184)	103.6	56.59 (55.69 ±0.56)	14.57 (14.3±0.16)	44.97
	500	0.690 (0.688 ±0.001)	56.57 (56.59±0.03)	55.23	46.69 (46.05 ±0.52)	11.27 (11.08 ±0.13)	18.23
	200	0.581 (0.567 ±0.016)	23.09 (23.06 ±0.046)	24.86	35.16 (34.06 ±0.71)	6.93 (6.55±0.25)	4.71
PM6: TB-SCl	1000	0.725 (0.724 ±0.001)	117.60 (117.30 ±0.28)	111.2	71.43 (71.26 ±0.08)	19.73 (19.62 ±0.05)	60.88
	500	0.704 (0.703 ±0.001)	63.6 (62.8±0.46)	59.34	68.73 (68.73 ±0.37)	19.00 (18.77 ±0.11)	30.25
	200	0.66 (0.660 ±0.001)	26.3 (26.3±0.035)	24.86	58.35 (58.07 ±0.48)	14.92 (14.82 ±0.12)	10.15
PM6: TB-S	1000	0.832 (0.826±0.01)	116.44 (114.86 ±2.23)	110.9	74.1 (74.15 ±0.76)	23.27 (22.8±0.5)	71.81
	500	0.786 (0.786 ±0.001)	61.53 (61.34±0.34)	58.96	69.1 (68.69 ±0.43)	20.65 (20.23 ±0.35)	33.41
	200	0.75 (0.749 ±0.001)	25.02 (24.83±0.43)	24.52	62 (61.03 ±0.70)	17.06 (16.68 ±0.39)	11.6

a) Values were calculated from the integration of the EQE spectrum. b) Average values were obtained from 10 devices.

The underlying reason of why TB-S with omitted chlorine in the terminal group can yield better performance under weak illumination was further studied. As summarized in the introduction section, besides low leakage current and suppressed trap state, high V_{OC} is one of main factors to achieve high IOPVs. First, the V_{loss} for TB-SCl and TB-S, was deduced. The total energy loss (E_{loss}) is originated from there parts[150, 222]: the energy offset between E_{g} and the energy of charge-transfer (CT) state, radiative recombination loss below the CT state, and non-radiative recombination loss. The corresponding parameters were summarized in **Table 5.3**. Normally, large E_{g} features high E_{loss}[94], however, TB-S based device possesses lower E_{loss} than TB-SCl based device. The underlying reason was studied by the electroluminescence (EL) and the highly sensitive EQE (s-EQE) spectra. As shown in **Figure 5.19 a,b**, $E_{\mathrm{g}}$was deducted from the intersection point of s-EQE and EL, and E_{CT} was obtained by the intersection point of fitting s-EQE and EL. $\Delta E_{\mathrm{nonrad}}$ was derived from electroluminescence external quantum efficiency ($\mathrm{EQE_{EL}}$).

The TB-S based device exhibits a reduced ΔE_{CT} in the comparison of TB-SCl based device. Moreover, PM6:TB-S blended film presenting higher $\mathrm{EQE_{EL}}$ of 1.28×10^{-4} than 2.86×10^{-5} for PM6:TB-SCl blended film, leads to the smaller $\Delta E_{\mathrm{nonrad}}$ of 0.233 eV than 0.272 eV. It has been declared that trap-induced recombination is associated with $\Delta E_{\mathrm{nonrad}}$, thus we suggest that TB-S exhibited suppressed trap states[222-224]. This is also consistent to ESP test. It is well known that $\Delta E_{\mathrm{nonrad}}$ contributes the main part of the V_{loss} and is the dominant factor hindering the performance of device. Therefore, this result implies that the elimination of chlorine in the end group not only possesses larger E_{g} but also mitigates the $\Delta E_{\mathrm{nonrad}}$ so that acquires higher V_{OC} under both strong and weak illuminations.

Table 5.3 Detailed V_{loss} for TB-SCl and TB-S based devices.

Device	V_{OC} (V)	E_{g} (eV)	E_{loss} (eV)	E_{CT} (eV)	ΔE_{CT} (eV)	ΔE_{rad} (eV)	$\Delta E_{\mathrm{nonrad}}$ (eV)
PM6: TB-SCl	0.889	1.41	0.521	1.4	0.01	0.239	0.272
PM6: TB-S	0.949	1.443	0.511	1.44	0.003	0.275	0.233

As shown in **Figure 5.19c**, the larger slopes of the dependence of V_{OC} on light intensity for all devices are observed under the weak illumination and low carrier density in comparison with under the strong illumination suggesting that trap-assisted recombination becomes prominent. This result is consistent with the observation where the V_{OC} of TB-S devices showed the higher values than those of

TB-SCl devices with ~0.06 eV and ~0.1 eV under the AM1.5G condition and the LED light condition, respectively.

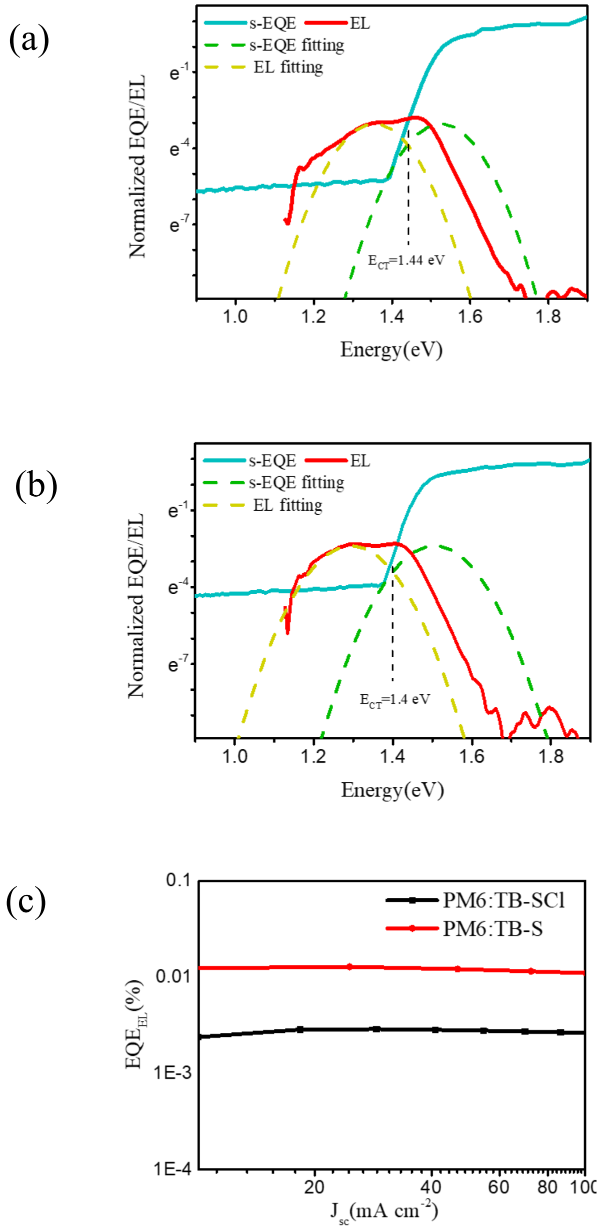

Figure 5.19. Normalized s-EQE and EL spectra of (a) PM6:TB-SCl, (b) PM6:TB-S.(c) EQE_{EL} spectra of the corresponding devices.

5.2.3 Morphology

To investigate the morphology of the blend film, atomic-force microscopy (AFM) and transmission electron microscope (TEM) tests were adopted. As shown in **Figure 5.20**, all blend films show smooth surfaces with small root-mean-square surface roughness (Rq) of 0.715nm, 0.838 nm, and 0.79 nm for PM6:BTP-2ThCl, PM6:TB-SCl, and PM6:TB-S, respectively. The smooth surfaces facilitate charge transfer and collection. As shown in phase images, asymmetric molecule based films presents larger phase separation than symmetric molecule based film implying that the stronger crystallinity of PM6:TB-SCl and PM6:TB-S is attributed to stronger inter-CT leading to larger aggregation. TB-S-based films displayed smaller phase separation than TB-SCl based film implying that non-chlorination of asymmetric acceptor resulted in less inter-CT. The TEM images demonstrate that the nano networks are formed in the bulk of all blends and no excessive phase segregation is showed. In comparison with BTP-2ThCl-based film, TB-SCl and TB-S-based films display larger phase separation and better interpenetrating networks, which is ascribed to larger intermolecular interaction of asymmetric acceptors, contributing to charge carrier mobility. Notably, chlorination of asymmetric acceptor, TB-SCl, features larger inter-CT than TB-S without chlorine leading to the slightly larger phase separation. Furthermore, in order to verify larger intermolecular interaction of asymmetric acceptor leading to larger phase separation, energy-filter TEM (EFTEM) was adopted to map the local elemental composition through the standard three-window method[225, 226]. Due to featured fluorine element for PM6 and featured chlorine for TB-SCl and BTP-2ThCl, the green filed images indicating the distribution of domain with featured element in blended films as shown in **Figure 5.21**. The film of PM6:TB-SCl presents larger domain of acceptor than the film of PM6:BTP-2ThCl indicating that the asymmetric acceptor possessing larger intermolecular interaction than the symmetric acceptor resulting in larger domain of acceptor indicating that the asymmetric acceptor possessing larger inter-CT among acceptors. All elements indicated in TB-S are also showed in PM6, so the domain of TB-S cannot be well mapped by EFTEM. The images mapped by PM6 indicate that TB-S based film possesses larger donor domain and smaller acceptor domain than TB-SCl based film implying that the end group without halogen leads to weaker inter-CT. The result of AFM and EFTEM also implies that asymmetric molecule-based films exhibit better morphology with proper domains owing to proper Donor-Acceptor intermolecular interaction which is consistent with the results of ESP calculation.

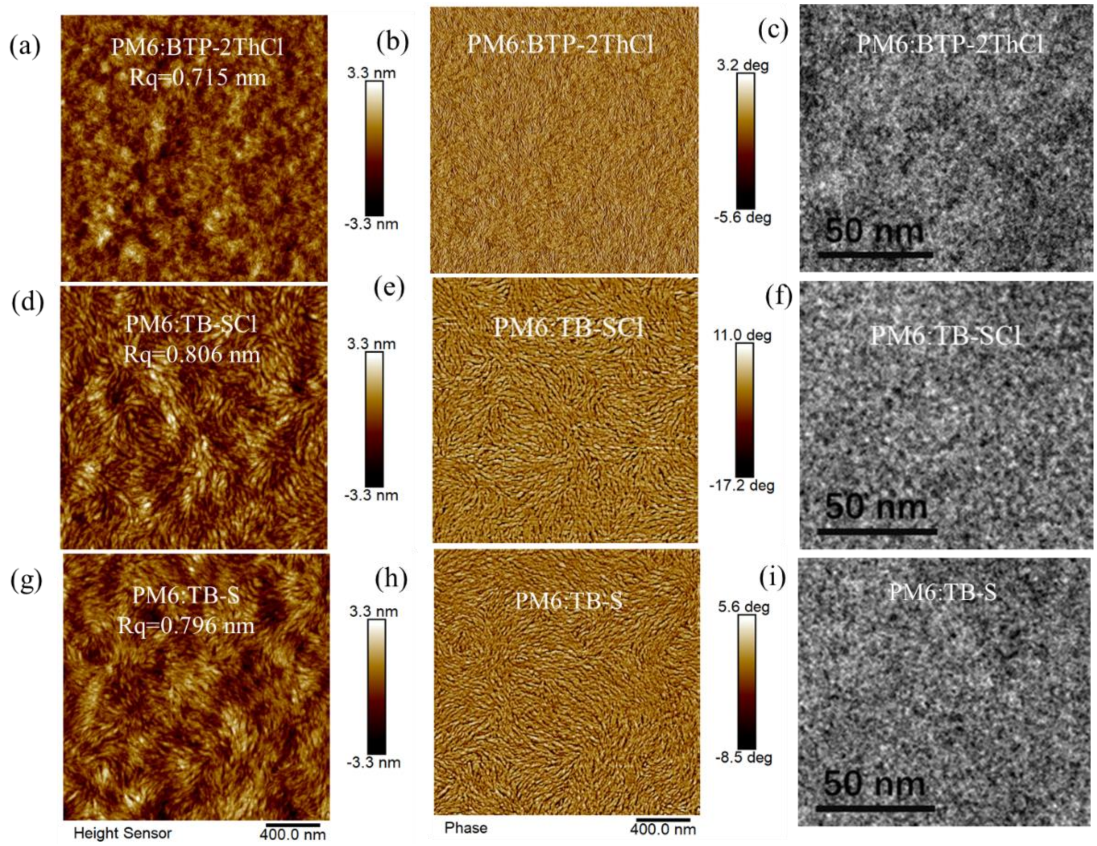

Figure 5.20. (a) AFM height, (b) phase, (c) TEM images of PM6:BTP-2ThCl. (d) AFM height, (e) phase, (f) TEM images of PM6:TB-SCl. (g) AFM height, (h) phase, (i) TEM images of PM6:TB-S.

Grazing incidence wide-angle X-ray scattering (GIWAXS) measurements were performed to study the molecular packing of neat and blend films. The two-dimensional GIWAXS patterns and their relevant scattering profiles in the in-plane (IP) and out of plane (OOP) directions are shown **Figure 5.22** and **Figure 5.23**, while the orientation and packing information are summarized in **Table 5.4**. As described in the 2D images, all neat acceptors exhibit apparently face-on orientation. The π-π stacking diffraction (010) locates at $q_z = 1.703\ \text{Å}^{-1}$, contributing to a π-π stacking distance of 3.687 Å for all acceptors. The crystalline domain sizes were calculated by comparing coherence length (CCL) using Scherrer equation[227]. The CCL was calculated as 22.232 Å, 23.053 Å, and 22.787 Å for BTP-2ThCl, TB-SCl, and TB-S, respectively.

Both asymmetric acceptors, TB-SCl and TB-S, possess longer CCL than symmetric acceptor, BTP-2ThCl, owing to asymmetric backbone and thus stronger inter-CT. The strong inter-CT can induce strong molecular packing and thus high CCL and high crystallinity that has been declared by many reports[196, 228, 229]. The result indicates that larger crystallite domain of acceptor with asymmetric structure are formed along π-π stacking direction with the same π-π stacking distance resulting in improved carrier mobilities and charge collection[230, 231]. This is consistent with the phase images in AFM results. Moreover, TB-SCl displays enhanced CCL than TB-S ascribed to stronger inter-CT benefiting for molecular stacking due to chlorination of terminal group.

For the blended films, PM6:BTP-2ThCl, PM6:TB-S and PM6:TB-SCl films display similar packing mode, retaining property like in neat PM6 film as polymer donor has a strong self-aggregation effect. The π-π stacking distance maintains at 3.687 Å for all blended films. The CCL at (010) are 23.209 Å , 23.219 Å, and 24.987 Å for PM6:BTP-2ThCl, PM6:TB-S and PM6:TB-SCl films, respectively, which indicates that asymmetric molecule exhibits slightly stronger inter-CT than symmetric molecule caused by the higher dipole moment vectors at the X and Z directions contributing to their higher charge mobilities and thus higher FF. Furthermore, the CCL result for blended films also indicates that the elimination of chlorine of terminal group leads to a little weaken of inter-CT due to the lack of non-covalent bonds of Cl⋯S and Cl⋯H.

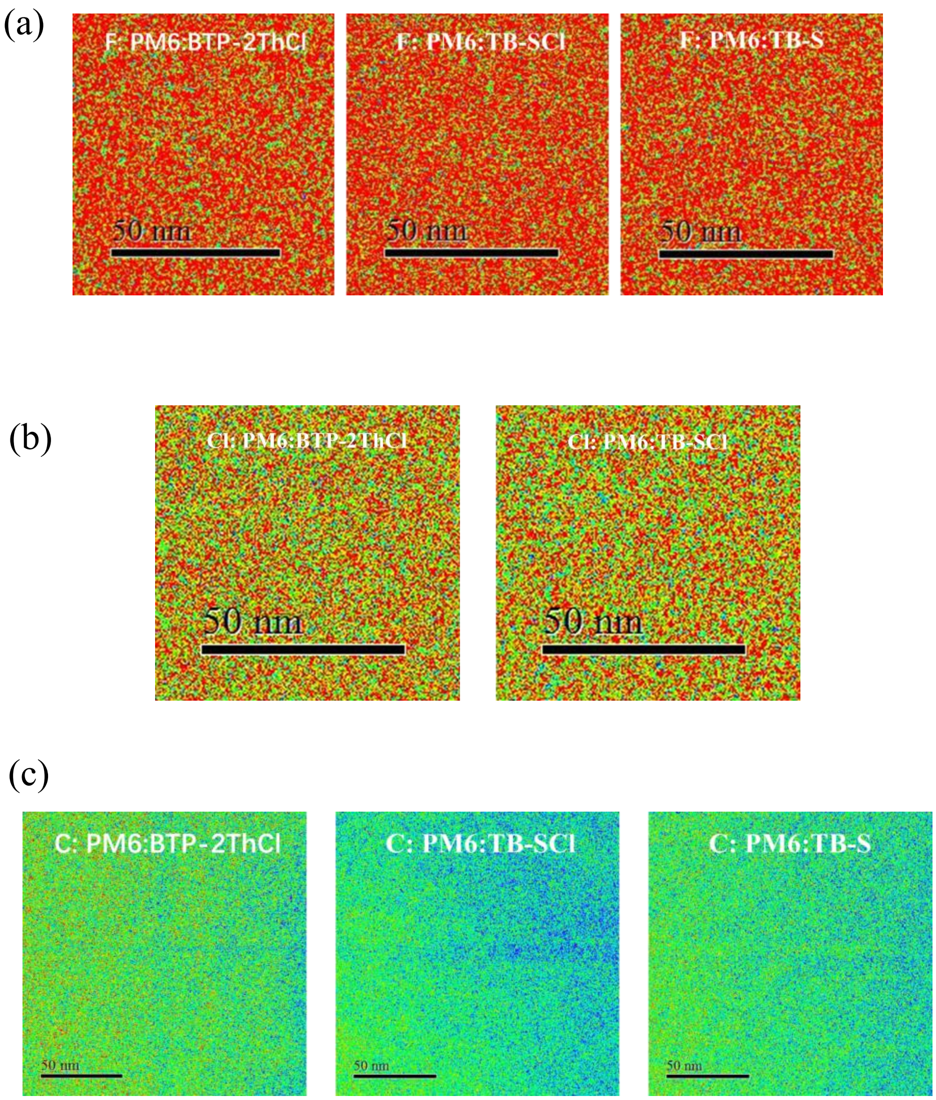

Figure 5.21. (a) Green field fluorine map (F) for donor domain of PM6:BTP-2ThCl, PM6:TB-SCl, and PM6:TB-S based films. (b) green field chlorine map (Cl) for acceptor domain of PM6:BTP-2ThCl and PM6:TB-SCl based films. (c) Green field carbon map (C) for whole film of PM6:BTP-2ThCl, PM6:TB-SCl, and PM6:TB-S based films. Red field means element cannot be detected.

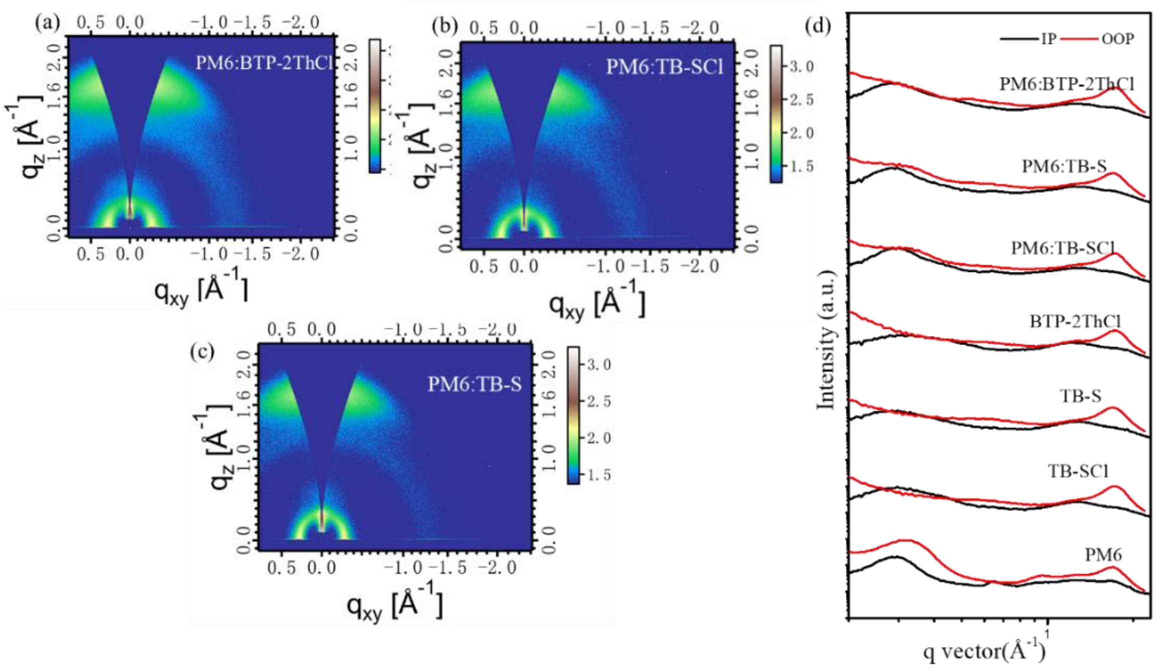

Figure 5.22. GIWAXS images of (a)PM6:BTP-2ThCl, (b)PM6:TB-SCl, and (c) PM6:TB-S. (d) scattering intensity curve of in plane (IP)and out of plane (OOP).

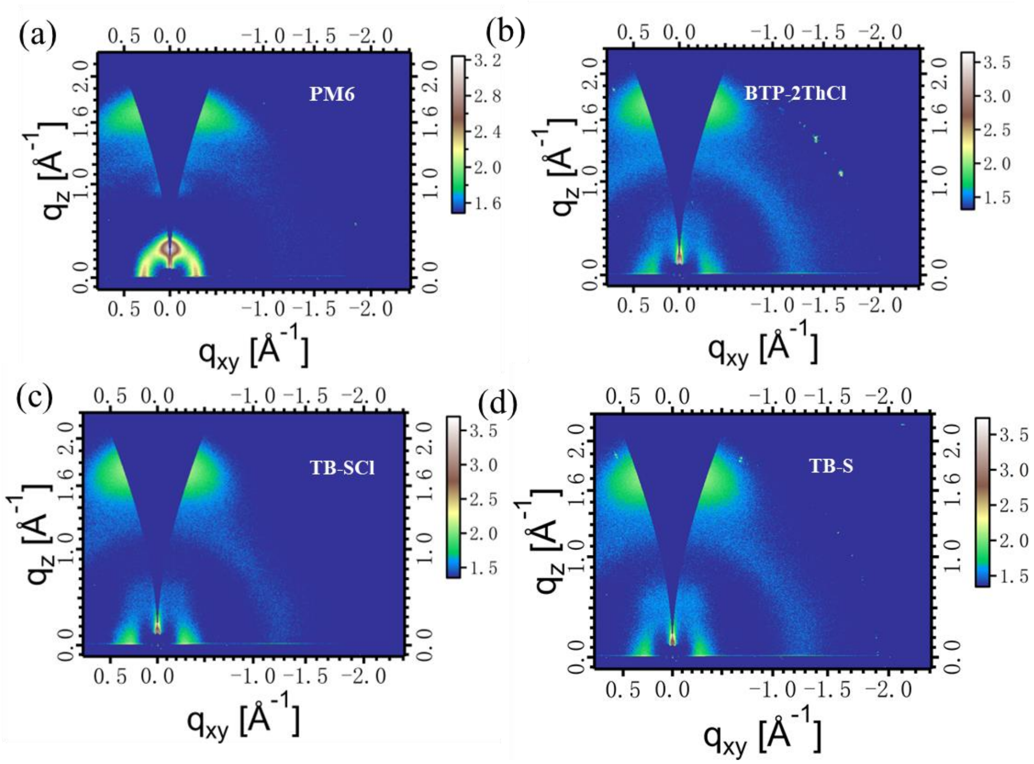

Figure 5.23. GIWAXS images of (a) PM6, (b)BTP-2ThCl, (c)TB-SCl, (d) TB-S.

Table 5.4. Detailed GIWAXS parameters along with out-of-plane direction.

	q(Å^{-1})	π-π distance (Å)	CCL (Å)	FWHM(Å^{-1})
PM6	1.703	3.687	24.179	0.260
TB-SCl	1.703	3.687	23.053	0.272
TB-S	1.703	3.687	22.787	0.276
BTP-2ThCl	1.703	3.687	22.232	0.282
PM6:TB-SCl	1.703	3.687	24.987	0.251
PM6:TB-S	1.703	3.687	24.219	0.259
PM6:BTP-2ThCl	1.703	3.687	23.209	0.271

5.2.4 Flexible IOPVs

Most highly efficient IOPVs spined on rigid substrates which is not practical for the applications utilized on the electronic textiles, curved surfaces, synthetic skin, etc. In this work, PM6:TB-S blended film has also been applied in the flexible substrate which indicates that TB-S is a good candidate for flexible IOPVs. The corresponding architecture is the configuration of PET/PH1000/PEDOT:PSS/PM6:TB-S/PDINO/Al, where the process technology for PH1000/PEDOT:PSS was reported in our previous work[232, 233]. The detailed device fabrication and test procedures were included in **section 3.5.2**. **Figure 5.24 a,b** present the *J-V* curve of PM6:TB-S illuminated under AM1.5 and 1000-lux LED, respectively. The flexible ITO-free OPV exhibited a PCE of 12.69% with a V_{OC}, a J_{SC}, and an FF of 0.94 V, 21.23 mA cm^{-2}, and 63.5% under the illumination of AM1.5, respectively. When the light source changed from AM1.5 to LED, the flexible device showed a PCE of 20.02%, accompanied with a V_{OC} of 0.801, a J_{SC} 108 μA cm^{-2}, and an FF of 71.75%. Subsequently, bending test with small radius of 2.5 mm was executed to assess its mechanical bending performance, where the active layer was suffered damage in the harsh bending condition. In **Figure 5.24 c**, after suffering bending cycles from the equipment, the result indicated that the efficiency decays small with 98% and 91.3% of its initial value after 400 /1000 times, respectively. This outstanding outcome deduces that the novel acceptor, TB-S, derived from Y6 backbone with an asymmetric structure and higher electronic density terminal groups can achieve remarkable PCE in the flexible architecture in the dim light environment.

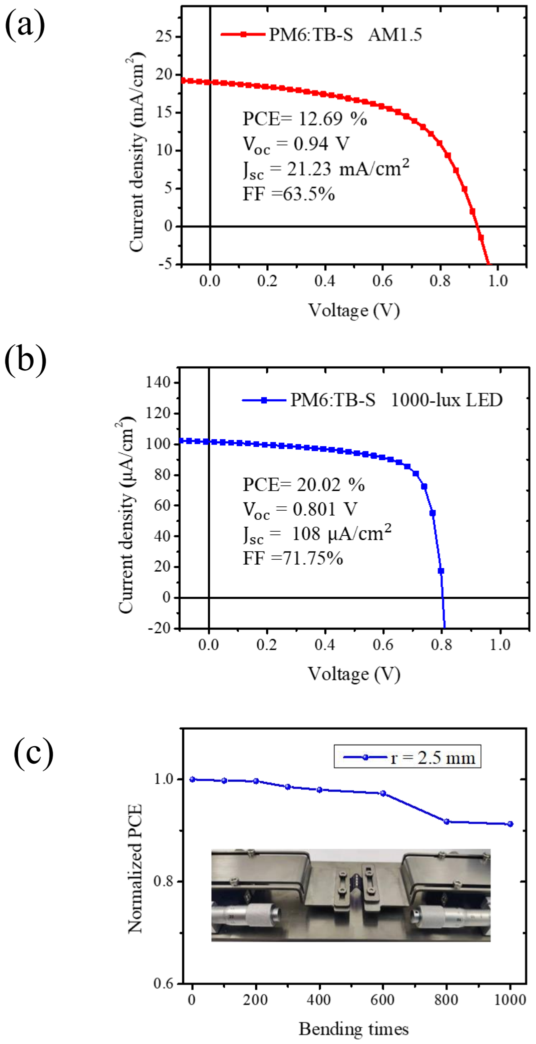

Figure 5.24. The *J-V* curve flexible device based on PM6:TB-S under the illumination of (a) AM1.5 and (b) 1000-lux LED. (c) bending performance versus bending times (2.5 radius) for PM6:TB-S based flexible device.

5.3 Conclusion

In summary, the impact of asymmetric skeleton and non-chlorination strategies on devices were systematically investigated through thoroughly evaluation of photovoltaic performance combined with analysis of intra-CT and inter-CT. Our result indicated that:

(i) the skeleton modified from symmetry to asymmetry by reducing a conjugate ring results in reduced intra-CT accounting for blue-shifted absorption and higher V_{OC}, enhanced inter-CT among acceptors benefiting for charge transfer and thus more efficient carrier collection resulting in elevated *FF*.

(ii) elevating electronic density of terminal group based on an asymmetric backbone through eliminating chlorine atom gives rise to further significantly decreased intra-CT resulting in more blue-shifted absorption and higher V_{OC} but reduced inter-CT owing to the lack of non-covalent bone leading to smaller binding energy and thus slightly negatively effect on carrier collection. Moreover, the elimination of chlorine in the terminal group for asymmetric molecules results in suppressed leakage current, mitigated carrier recombination, and mitigated non-radiative energy loss leading to surpassed PCE under the weak illumination.

Consequently, to achieve high-efficiency PCE under the illumination of artificial light source, trade-off among wide bandgap for high V_{OC}, efficient carrier generation and collection for high J_{SC}, mitigated leakage current for less V_{loss}, and minimized trap-state for higher *FF* and less V_{loss} should be taken into consideration. Therefore, molecular structure modification should consider the following aspects:

(i) a weak intra-CT is required to acquire wide bandgap to better match the emission spectrum of LED.

(ii) continuously weakening intra-CT may worsen inter-CT leading to inferior carrier generation and collection, which should be balanced.

(iii) the trap state should be mitigated to obtain suppressed V_{loss} and higher FF under weak illumination. The influence of interaction of donor and acceptor for utilizing weak illumination should be discussed in the further investigation.

Therefore, a novel acceptor TB-S possesses weak intra-CT and proper inter-CT along with mitigated trap state and V_{loss} yielding high-efficiency rigid PCE of 23.3% and flexible PCE of 20.02% under 1000-lux LED illumination. Our observation provides a new insight into molecule structure modification to promote the indoor photovoltaic performance.

Chapter 6

Alkoxy substitution on asymmetric conjugated molecule enabling over 18% efficiency in ternary organic solar cells by reducing non-radiative voltage loss

6.1 Synopsis

Ternary strategy is considered as an efficient and simple way to further enhance the performance of OPV. However, “structure-performance” correlation of the third component in the ternary device has rarely been clearly understood from the aspect of material’s eigen-properties. Herein, this relationship is investigated in depth by employing three asymmetric skeleton non-fullerene acceptors as the third component in the host system of PM6:BTP-eC9, respectively. Compared with TB-S and TB-S1, the alkoxy substituted TB-S1-O possesses more stable planar conformation, higher surface energy, and larger ordered stacking domain owing to the existence of non-covalent conformational locking (O···H). Consequently, the PM6:BTP-eC9:TB-S1-O device exhibits the highest efficiency of 18.14% as compared with the device based on PM6:BTP-eC9:TB-S (16.16%) and PM6:BTP-eC9:TB-S1 (16.18%). Most interestingly, only PM6:BTP-eC9:TB-S1-O device can maintain the positive effect of V_{OC} improvement, because a significant reduction in non-radiative voltage loss can be observed in this device. Moreover, the PM6:BTP-eC9:TB-S1-O blend film gives the optimal morphology with higher crystallinity and an interpenetrating network structure, thereby enhancing charge transfer and charge collection. Our systematic study reveals that alkoxy substitution on asymmetric backbone is an efficient method to construct the third component for high-performance ternary organic solar cells.

6.2 Introduction

OPVs with BHJ have attracted abundant attentions in the field of utilizing clean solar energy due to their promising advantages of solution processability, transparency, portability, and flexibility[2, 4, 190, 192, 211, 234-238]. Owing to continuous design of novel non-fullerene acceptors, the PCE of binary OPV under the illumination of 1-sun intensity has been increased from ~15% to ~18% [67, 75, 147, 239-243]. With morphology optimization, device’s structure development, the PCE of heterojunction OPVs has exceeded 19%[43-45]. To further improve the performance of

OPV, ternary strategy is considered as an efficient and simple way [43-45]. However, lots of these studies only focused on single guest component without systematic research on analogues. Therefore, the correlation among molecular structure of the third component, active layer morphology, and photovoltaic performance of the ternary device has rarely been clearly understood. In addition, the design of the third component molecule has reached a certain bottleneck, and the OPV field requires continuous development of more innovative chemical structure materials to further improve the efficiency of exciton generation, charge separation, and charge transfer, thereby further improving the energy conversion efficiency of photovoltaic devices. Hence, the study of asymmetric fused-ring third component small molecules is more innovative and meaningful in the OPV field.

6.2.1 Ternary strategy

In the past few years, many studies have demonstrated that the ternary strategy is a feasible way to further increase PCE of OPVs by simply adding the third material into the host materials. Ternary strategy maintains the simple process of binary devices, which contains three materials in active layers.

PM6:BTP-eC9 binary system achieved high efficiency of 17.8%[69]. Hence, lots of ternary system chose PM6:BTP-eC9 as the host system and added the third component to further increase its performance. PM6:BTP-eC9:MOIT-M showed a high PCE of 18.5%[74] and MOIT-M is indacene molecule. PM6:BTP-eC9:BTP-F produced an increased PCE of 18.45%[87]. Notably, PM6:BTP-eC9:ZY-4Cl achieved amazing PCE of 18.69%[77] which was ascribed to the symmetric Y-series acceptor possessing high V_{OC}.

Although many third component molecule designs meet the requirements of the ternary strategy and can provide cascading energy levels and complementary absorption for the main binary system, however, only a few third components can effectively improve the performance of the host binary system. The most common situation is that the doping of a guest molecule may significantly reduce the PCE of the device. This is because the addition of the third component molecule increases the complexity of intermolecular interactions and intermolecular stacking, which seriously disrupts the morphology of the original binary system, and the morphology of the active layer is closely related to the optoelectronic properties of OPVs. Notably, the morphology of the active layer directly affects the performance of OPVs such as absorption spectra, carrier separation and transport efficiency, and photovoltaic conversion efficiency. Incorporating the third component into the host mixed active layer may disrupt the nanoscale long-range order and morphology of the host system, for example, changing the π-π interaction effect between molecules, and after film formation, the stacking order of the morphology is disrupted, which greatly affects J_{SC} and FF, becoming a key factor limiting the photovoltaic efficiency. Therefore, the "structure-performance" correlation of the third component in ternary devices urgently needs to be studied and summarized to provide guidance for the effective design and screening of highly efficient third component molecules. Furthermore, the design of the third component molecule has been lacking in creativity, with most attention being given to modifying the symmetric molecules of the Y-series. Therefore, the OPV field needs to focus on continuous development of materials with innovative chemical structures, such as asymmetric molecules, to further improve the efficiency of exciton generation, charge separation, and charge transfer.

6.2.2 Asymmetric molecules

Since 2019, Y6 derivatives (especially for symmetric molecules) have become a hot topic of study in OPV due to their excellent properties such as low bandgaps and high electron mobility [234, 244]. Symmetric Y6 derivatives adopt a unique C-shaped skeleton, which can promote intra/intermolecular interactions, increase charge carrier mobility and molecular crystallinity. Therefore, Y-series have become a popular research topic in OPV due to their excellent performance. In addition to the symmetric non-fullerene acceptors, asymmetric non-fullerene (ANF) acceptors have recently been used successfully in OPV [170, 245-248]. Compared with symmetric structure, by employing the ANF design strategy, the molecule exhibits larger dipole moments and stronger binding energies, which enhance intermolecular interactions and enable clever modulation of photoelectric absorption properties. The configuration of the molecular backbone not only affects the absorption ability, orbital levels, molecular stacking, and compatibility with the acceptor, but also alters its crystallinity and charge transfer capacity.

In general, ANF acceptors are classified as asymmetry skeleton typed non-fullerene (ASNF, A-D_1A'D_2-A) and asymmetry terminal typed non-fullerene (ATNF, A_1-DA'D-A_2) acceptors. For ASNF, the number of fused rings on the central ring are different leading to asymmetric skeleton. Yang reported ATNF AY6 by reducing one fused ring on the skeleton[170]. This report claimed that large dipole moment can reinforce intermolecular interaction resulting in close packing of acceptor molecules and thus rendering more efficient charge transfer[172-175]. The intrinsic large dipole moment of asymmetric acceptor not only enhances intermolecular π-π stacking but also enable FF to be improved[174, 176]. Similarly, TB-4Cl reported by our group with the same skeleton of AY6 but with different end group showed the same characteristic of AY6[202]. Two ATNF acceptors were carried out by Jen, named BP5T-4F and ABP4T-4F with a different number of thiophene rings on either side of the central core leading to different configuration[249]. Hence, their aggregation behavior was different but they both showed decreased ΔE_{nonrad}. In terms of ATNF, the substitution of one of thermal groups is an effective way to improve the performance of device. Luo's group synthesized an ATNF called BTP-2F-ThCl by substituting one terminal group of Y6 from IC-2F to CPTCN-Cl. The result indicated that ATNF strategy adjusted molecular stacking to form better morphology so that reduced ΔE_{nonrad} and increased charge transfer and thus yielded a high PCE of 17.06%[147]. BT-S2 was developed by Chen which contained two different end groups, composed of halogenated indandione and 3-dicyanomethylene- 1-indanone, yielding higher PCE than Y6-based device[245]. Subsequently, Chen designed new ATNF BO-5Cl as the third component which was introduced into PM6:BO-4Cl system producing a high PCE of18.2%[245]. Very recently, ternary OPV devices using the ATNF acceptor as the third component had excellent PCEs of over 19% [14, 250]. However, the ASNF acceptor as the third component has never been studied and reported. Based on the studies of ASNF acceptors, the incorporation of asymmetrically fused third components molecules may enable the modulation of the aggregation behavior of the mixture, which can improve the kinetics of charge carrier transport, enhance exciton dissociation/extraction, and reduce ΔE_{nonrad} in devices.

6.2.3 Objective

In this work, the ATNF acceptors were adopted as the third component to study the impact of ATNF acceptors on the host system. This study can fill in the gap of ATNF as the third material in OSCs. In order to reveal the correlation between ASNF molecule's eigen-properties, active layer morphology, and photovoltaic performance of ternary OPV device, we synthesized two wider bandgap ASNF acceptors, named TB-S1 and TB-S1-O. Based on previous work, asymmetric skeleton-typed acceptor could be easily obtained by reducing one thiophene-ring of Y6 skeleton, resulting in a ~40 nm blue-shifted absorption in comparison with their symmetric molecule [202]. Moreover, the ASNF possessed a stronger dipole moment, which is favorable to enhanced intermolecular interaction, thereby promoting the J_{SC} and *FF*. To further acquire blue-shifted absorption, the engineering on the terminal groups is carried out. This is inspired by the report from Gao and co-authors in which the position of S substitution on isomerized thiophene-fused ending groups strongly influenced their optical absorption, and 40 nm blue-shifted absorption could be observed [251]. In addition, the alkoxy chains can have a significant impact on the electronic and morphological properties of OPV materials that has been reported [252]. Firstly, it can upshift the LUMO and widen optical bandgap of the materials due to the electron-donating effect [240, 253]. Secondly, the oxygen atoms can provide intramolecular conformational locking effect, which could regulate the aggregation property of the material and thus change the morphology of the blend film [254, 255]. These three ANF molecules have similar skeletons but different terminal groups or alkyl/alkoxy side chains are incorporated into the host system PM6:BTP-eC9 as a third component, respectively.

The molecular structures of the ASNF acceptors as the third components are shown in **Scheme 3.3**, which are TB-S, TB-S1, and TB-S1-O. The terminal group of TB-S is modified from 2-(6-oxo-5,6-dihydro-4H-cyclopenta [c] thiophen-4-ylidene) malononitrile to 2-(6-oxo-5,6-dihydro-4H-cyclopenta [b]thiophen-4-ylidene) malononitrile synthesizing TB-S1. Furthermore, the main difference between TB-S1 and TB-S1-O is the substitution of the alkoxy chain on the β-position of the outer thiophene moiety.

Ternary strategy is considered as an efficient and simple way to further enhance the performance of OPV. However, “structure-performance” correlation of the third component in the ternary device has rarely been clearly understood from the aspect of material’s eigen-properties. Herein, this relationship is investigated in depth by employing three asymmetric skeleton non-fullerene acceptors, TB-S, TB-S1, and TB-S1-O, as the third component into the host system of PM6:BTP-eC9, respectively. This work focuses on developing high performance devices under outdoor environment and the test under indoor condition is neglected.

6.3 Results and discussion

6.3.1 Quantum calculation

Gaussian simulation was performed to study the geometric configuration and Frontier orbits of the three analogues. Optimized molecular geometries, energy levels and wave function distributions of the frontier orbits for the four acceptors are shown in **Figure 6.1**. The incremental bandgaps for BTP-eC9, TB-S, TB-S1, and TB-S1-O are consistent with their absorption spectra. To understand the impact of the three ASNF acceptors, the relaxed potential surface energy scans of rotamer M1, M2, and M3 (**Figure 6.3b**) were studied by DFT calculation [152, 153]. Density functional theory (DFT) calculations based on B3LYP/6-31G(d,p) level.

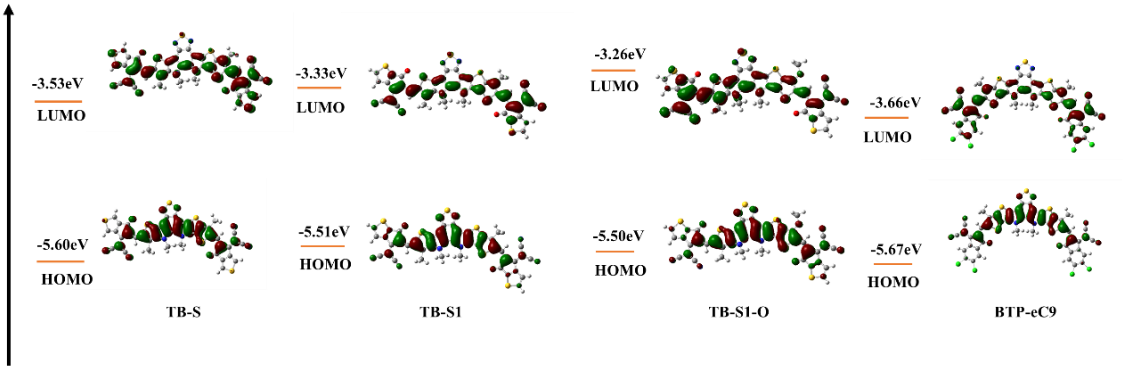

Figure 6.1. Optimized molecular geometry, energy levels and wave function distributions of the frontier orbits for TB-S, TB-S1, TB-S1-O, and BTP-eC9.

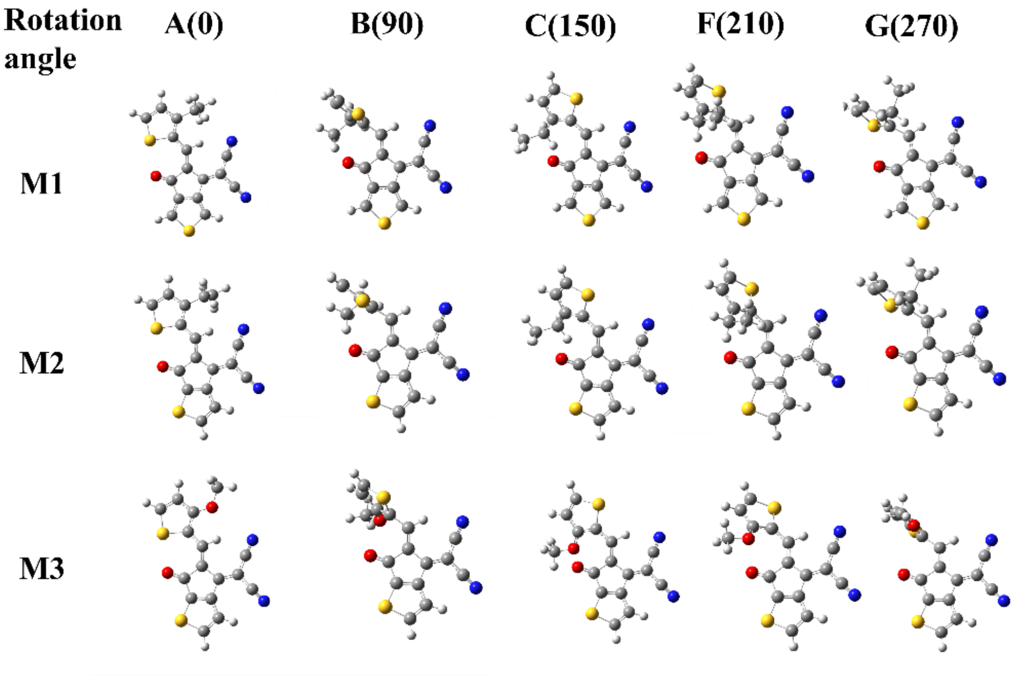

Figure 6.2. Conformations of M1, M2, and M3 at the rotation degrees of 0, 90, 150, 210, and 270.

The energy values of the three rotamers rotated along the single bone linking thiophene unit and the terminal groups are displayed in **Figure 6.5** and the corresponding conformations of M1, M2 and M3 at key rotation degree are shown in **Figure 6.2**. According to the result of **Figure 6.4**, the torsion barriers between A and B or A and F in M3 are significantly higher than those of M1 and M2 (around

60 *vs*. 49 and 43 KJ mol^{-1}), showing that A-conformation is more preferred in M3 than M1 and M2. The results indicated that the alkoxy substituted TB-S1-O has a stronger non-covalent conformational locking effect due to the existing intramolecular interaction O···H in addition to O···S, in comparison with the alkyl substituted TB-S and TB-S1, resulting in a more stable planar conformation.[255] Besides, this is benefit for enhancing the aggregation property of the molecule[255,256].

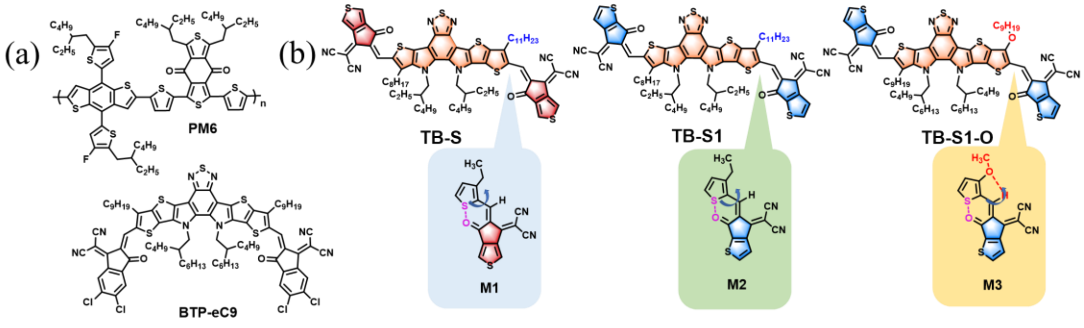

Figure 6.3. (a) Chemical structures of host system. (b) The Chemical structures of asymmetric acceptors for TB-S, TB-S1, and TB-S1-O and the conformations of rotamer for M1, M2, and M3.

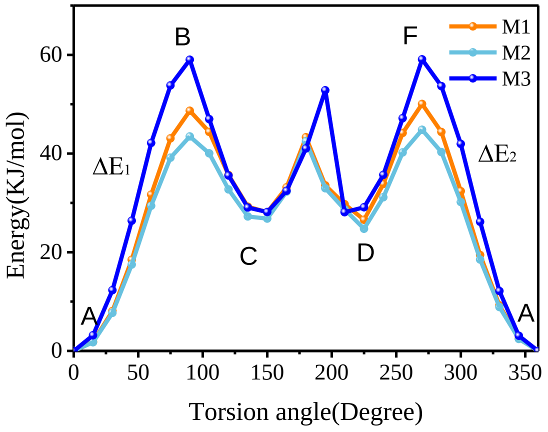

Figure 6.4. The energy levels plot of PM6, TB-S, TB-S1, TB-S1-O, and BTP-eC9.

6.3.2 Photovoltaics and photoelectric properties

As indicated in **Figure 6.5**, compared to the TB-S, TB-S1 shows a 60 nm blue-shifted absorption maximum, indicating a wider bandgap. For TB-S1-O, the absorption maximum is blue-shifted by 20 nm from that of TB-S1. The optical bandgaps of TB-S1 and TB-S1-O are calculated as 1.57 and 1.62 eV, respectively, which are higher than that of TB-S (1.47 eV). The result indicated that the terminal group substitution and alkoxy substitution can effectively blue shift the absorption and widen optical bandgap. The absorption spectra of TB-S1 and TB-S1-O show better complementary absorption property than that of TB-S for host material PM6 and BTP-eC9.

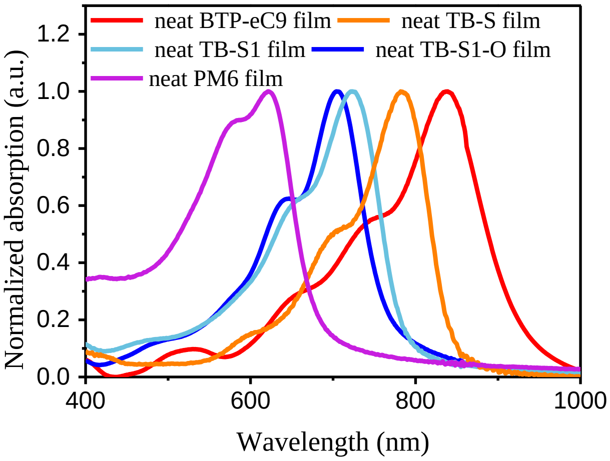

Figure 6.5. Normalized absorption spectra of all acceptors and PM6.

The CV was used to measure the HOMO and LUMO of these materials (**Figure 6.6**). the corresponding energy levels are depicted in **Figure 6.7**.

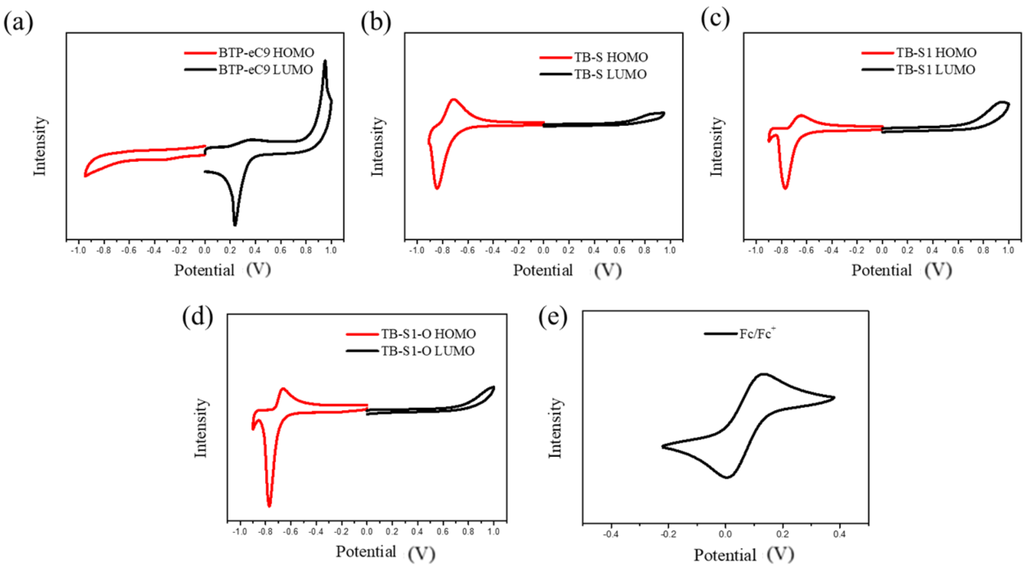

Figure 6.6. CV test for (a) BTP-eC9, (b)TB-S, (c)TB-S1, (d) TB-S1-O, (e) Fc/Fc+.

The corresponding energy levels are depicted in **Figure 6.7**. The energy levels of TB-S, TB-S1, and TB-S1-O as the third material are well-aligned with the host materials. Theoretically, they enable more efficient charge transfer at D-A interface which are beneficial to tune the voltage losses[257] and to improve V_{OC}.

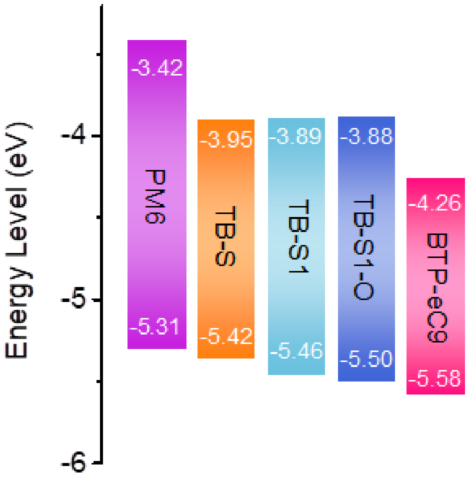

Figure 6.7. The energy levels plot of PM6, TB-S, TB-S1, TB-S1-O, and BTP-eC9.

Subsequently, contact angles were measured from spin-coated films by an optical contact angle meter (CAM 200). The contact angles (CA) of water and glycerol liquid drops was carried out to explore the compatibility of the third guest materials with the host materials, as displayed in **Figure 6.8**. The surface energy (γ_s) is analyzed by Wu's model [151]. The γ_s were calculated as 20.71, 20.60, 14.79, 15.99 and 21.87 mN m^{-1} for PM6, BTP-eC9, TB-S, TB-S1, and TB-S1-O, respectively. Therefore, TB-S1-O shows a significant higher surface energy than TB-S and TB-S1, and this is closer to the host materials (PM6 and BTP-eC9). TB-S1-O and BTP-eC9 have similar surface energy, which conduces to form alloy-like acceptor phase for these two acceptors.

Moreover, the degree of molecular miscibility for two molecules can be acquired by the Flory-Huggins interaction parameter χ[151]. Firstly, χ value for PM6 and the four acceptors were calculated which are 0.0001, 0.4970, 0.3050, and 0.0158 for BTP-eC9, TB-S, TB-S1, and TB-S1-O, respectively. The result indicates that BTP-eC9 and TB-S1-O perform superior compatibility between donor and acceptor than TB-S and TB-S1. Secondly, χ value for host acceptor BTP-eC9 and the guest acceptors were evaluated which are 0.480, 0.292, and 0.019 for TB-S, TB-S1, and TB-S1-O, respectively. The smallest χ value for BTP-eC9 and TB-S1-O suggests that TB-S1-O have the best compatibility with BTP-eC9 and thus the highest possibility to form well-mixed morphology.

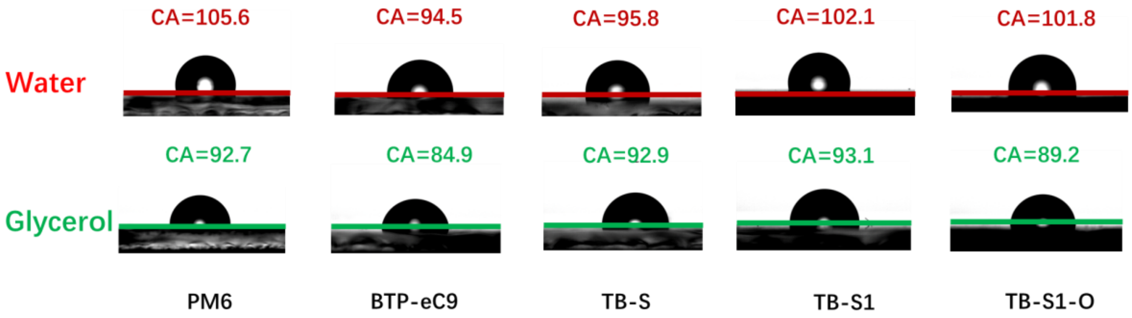

Figure 6.8. Contact angle test of all neat films by applying water and glycerol liquid drops.

Table 6.1. Photovoltaics parameters of the OPV cells under AM1.5 illumination.

Active layers	V_{OC} (V)	J_{SC} (mA cm^{-2})	$J^{a)}_{cal}$ (mA cm^{-2})	*FF*	R_SA (Ω cm^2)	$R_{Sh}A$ (Ω cm^2)	PCE$^{b)}$ (%)
PM6:BTP-eC9	0.837	26.72	25.68	77.7	2.17	1718	17.36 (17.28±0.07)
PM6:TB-S	0.949	20.67	20.19	72.4	3.55	1492	14.20 (14.04±0.13) $^{c)}$
PM6:TB-S1	1.030	13.82	14.04	44.9	17.9	297	6.41 (6.32±0.08)
PM6:TB-S1-O	1.120	13.62	12.67	60.0	8.02	647	9.09 (8.46±2.52)
PM6:BTP-eC9:TB-S	0.827	26.44	25.49	73.9	1.99	1436	16.16 (16.07±0.07)
PM6:BTP-eC9:TB-S1	0.828	27.27	26.22	71.6	2.08	1159	16.18 (16.06±0.05)
PM6:BTP-eC9:TB-S1-O	0.857	27.40	26.20	77.2	1.62	1150	18.14 (17.94 ± 0.11)

$^{a)}$Values were calculated from the integration of the EQE spectrum. $^{b)}$ Average values were obtained from 10 devices. $^{c)}$ Value was acquired from our previous work[2].

To explore the photovoltaic properties of TB-S, TB-S1, and TB-S1-O, their binary and ternary devices were fabricated, whose device performances are depicted in **Figure 6.9 a, c**, and **Table 6.1**. The V_{OC} of the devices are 0.837 V, 0.949 V, 1.030 V, and 1.120 V for BTP-eC9, TB-S, TB-S1, and TB-S1-O based binary system, indicating that the strategy to modulate acceptor molecules is effective to increase V_{OC}. As shown in **Figure 6.9b**,**d**, TB-S1 and TB-S1-O-based devices both exhibits significant lower external quantum efficiency (EQE) values from 400 to 800 nm range than that of TB-S, indicating that the end group substitution for TB-S1 and TB-S1-O compared with TB-S resulted in inferior carrier dissociation and transport [251]. Furthermore, the three ASNF acceptors were incorporated into host binary system, respectively. It was found that the incorporation of TB-S and TB-S1, respectively, into the host system PM6:BTP-eC9 failed to improve the device performance with an inferior PCE of 16.16% (V_{OC} = 0.827 V, J_{SC} = 26.44 mA cm^{-}

^{2}, FF = 73.9%) and 16.18% (V_{OC} = 0.828 V, J_{SC} = 27.27 mA cm^{-2}, FF = 71.6% despite the two acceptors satisfy the requirement of the cascade energy level and complementary absorption mentioned in lots of reported ternary OPV. Notably, the alkoxy substituted TB-S1-O, as the third component into the host system, yielded an optimized device with the highest PCE of 18.14% with an increased V_{OC} of 0.857 V, a superior J_{SC} of 27.4 mA cm^{-2}, and a comparable FF of 77.2% in comparison with PM6:BTP-eC9 based binary device. The EQE spectra were investigated to study the ability of photo response for these devices. It can be noticed in the **Figure 6.9b** that the devices of PM6:BTP-eC9:TB-S1 and PM6:BTP-eC9:TB-S1-O exhibit superior EQE responses especially in the wavelength range from 400 nm to 750 nm. This indicates that introducing TB-S1 and TB-S1-O into host system resulted in more efficient exciton dissociation and transport. However, the doping of TB-S yielded reduced EQE response. The integrated J_{SC} values based on EQE spectra are in line with the measurement values shown in J-V curves (within 5% error).

In order to evaluate exciton dissociation properties and charge collective properties of the devices, the η_{diss}/η_{coll} were calculated, which are 98.2%/87.4%, 97.1%/87.1%, 99.0%/86.2%, 98.4%/88.2% for PM6: BTP-eC9, PM6:BTP-eC9:TB-S, PM6:BTP-eC9:TB-S1, and PM6:BTP-eC9:TB-S1-O, respectively. As shown in **Figure 6.10**, in comparison to PM6:BTP-eC9, PM6:BTP-eC9:TB-S1-O performed higher η_{diss} and η_{coll} values. It indicated that higher exciton dissociation and carrier collection probabilities can be observed in PM6:BTP-eC9:TB-S1-O device, resulting in improved J_{SC} and comparable FF. For TB-S based ternary device, it displayed both inferior exciton dissociation and carrier collection probabilities[258, 259]. The TB-S1 exhibited higher exciton dissociation ability but produced lower charge collection ability resulting inferior FF. The above analysis figures out that the introduction of TB-S1-O into the binary system are beneficial to the charge generation, transport, and extraction.

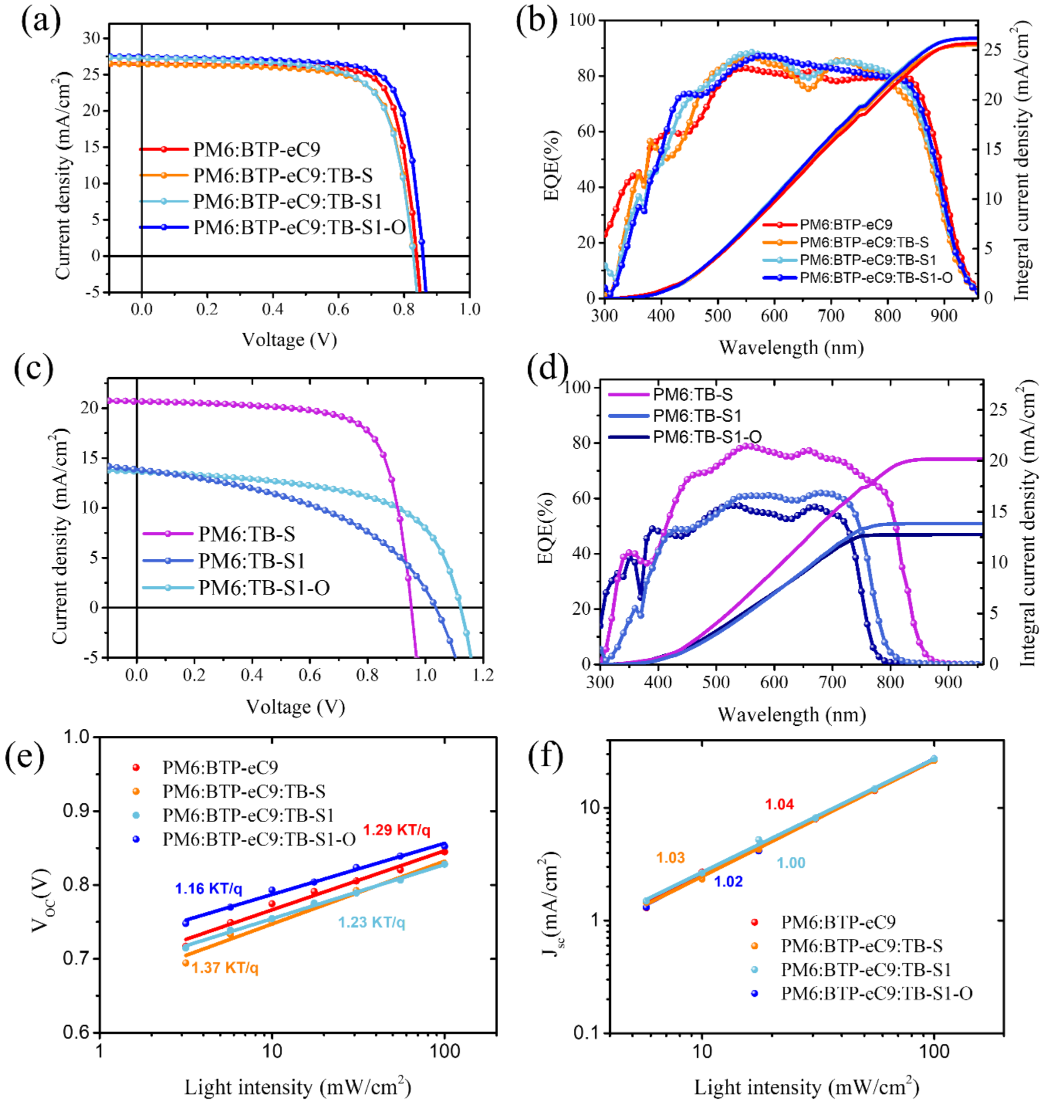

Figure 6.9. (a) *J-V* curves of devices fabricated by PM6:BTP-eC9, PM6:BTP-eC9:TB-S, PM6:BTP-eC9:TB-S1, and PM6:BTP-eC9:TB-S1-O. (b) EQE curves of the corresponding devices. (c) *J-V* curves of devices fabricated by PM6:TB-S, PM6:TB-S1, and PM6:TB-S1-O. (d) EQE curves of the corresponding devices. V_{OC} (e) and J_{SC} (f) depending on the variation of light intensity under solar simulator.

Space-charge-limited-current (SCLC) measurement was adopted to investigate the carrier mobilities for all the devices. The *J-V* curves of electron-only and hole-only devices are shown in **Figure 6.11**. The improved μ_e and μ_h for TB-S1 and TB-S1-O doped devices indicated that more charge transfer pathways were generated leading to the improved J_{SC}. Overall, as guest component, the isomerized thiophene-fused terminal group for TB-S1 and TB-S1-O doping into host system compared with that of TB-S is beneficial to improve carrier mobilities. For PM6:BTP-eC9 binary device, the electron mobility (μ_e) is 4.35 $\times 10^{-4}\ cm^2V^{-1}s^{-1}$ and the hole mobility (μ_h) is 3.54 $\times 10^{-4} cm^2V^{-1}s^{-1}$. When TB-S, TB-S1and TB-S1-O are introduced into the binary film, the μ_e / μ_h is $4.05 \times 10^{-4}/3.07 \times 10^{-4}(3.14 \times 10^{-4} \pm 1.05 \times 10^{-5})\ cm^2V^{-1}s^{-1}$, 4.52×10^{-4} / $3.87 \times 10^{-4}\ cm^2V^{-1}s^{-1}$, and 4.68×10^{-4} / $4.52 \times 10^{-4}\ cm^2V^{-1}s^{-1}$ for TB-S, TB-S1, and TB-S1-O-based ternary devices, respectively.

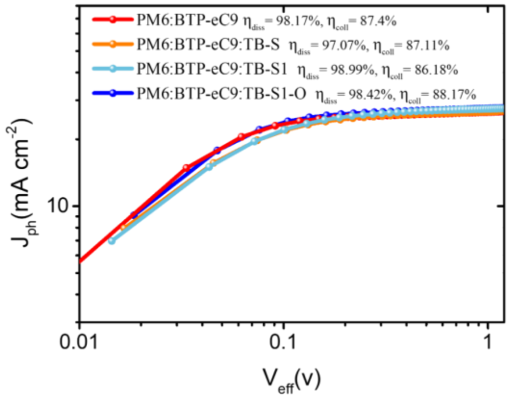

Figure 6.10. J_{ph}-V_{eff} curves of PM6:BTP-eC9, PM6:BTP-eC9:TB-S, PM6:BTP-eC9:TB-S1, and PM6:BTP-eC9:TB-S1-O.

To get insight of degrees of biomolecular recombination and trap-assisted recombination, the J_{SC} and V_{OC} values as a function of illumination intensity (P) were depicted. As shown in **Figure 6.9e**, the S values for all the devices are close to 1 suggesting that the less bimolecular recombination occurs. Moreover, the corresponding V_{OC} values is in the expression of $V_{OC} \propto$ n(KT/q)ln(P). As described in **Figure 6.9f**, the calculated slopes are 1.29, 1.37,1.23, and 1.16 KT/q for PM6:BTP-eC9, PM6:BTP-eC9:TB-S, PM6:BTP-eC9:TB-S1, and PM6:BTP-eC9:TB-S1-O, respectively. The result declares that the incorporation of TB-S1-O into host system can mitigate the trap-assisted state and thus the higher V_{OC} and Jsc can be observed. This may be ascribed to the good compatibility between TB-S1-O and BTP-eC9 and thus the highest possibility to form well-mixed morphology[227, 258, 259] which will be discussed later.

Table 6.2. Detailed V_{loss} for the OPV devices.

Devices	V_{OC} (V)	E_g (eV)	E_{loss} (eV)	E_{CT} (eV)	ΔE_{CT} (eV)	ΔE_{nonrad} (eV)
PM6:BTP-eC9	0.837	1.396	0.559	1.338	0.058	0.241
PM6:BTP-eC9:TB-S	0.828	1.411	0.583	1.350	0.061	0.244
PM6:BTP-eC9:TB-S1	0.828	1.394	0.566	1.343	0.051	0.244
PM6:BTP-eC9:TB-S1-O	0.857	1.399	0.542	1.345	0.054	0.228

Table 6.3. Photovoltaics parameters of the PM6:BTP-eC9:TB-S1-O based ternary devices with different doping ratio under AM1.5 illumination.

ratio	V_{OC} (V)	J_{SC} (mA cm^{-2})	*FF*	PCE (%)
1:1.2:0	0.845	26.35	78.41	17.46
1:1.1:0.1	0.853	26.16	78.53	17.52
1:1.05:0.15	0.857	27.4	77.22	18.14
1:1:0.2	0.861	25.78	77.62	17.22
1:0.15:1.05	0.946	10.19	34.74	3.35
1:0:1.2	1.12	13.62	60	9.09

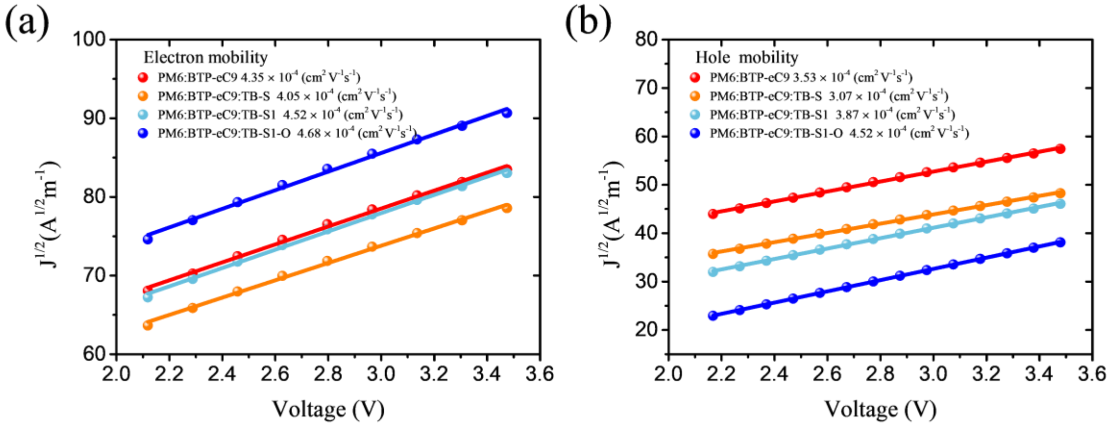

Figure 6.11. $J^{1/2}$ -V curves of electron (a) and hole (b) mobilities for all blended films.

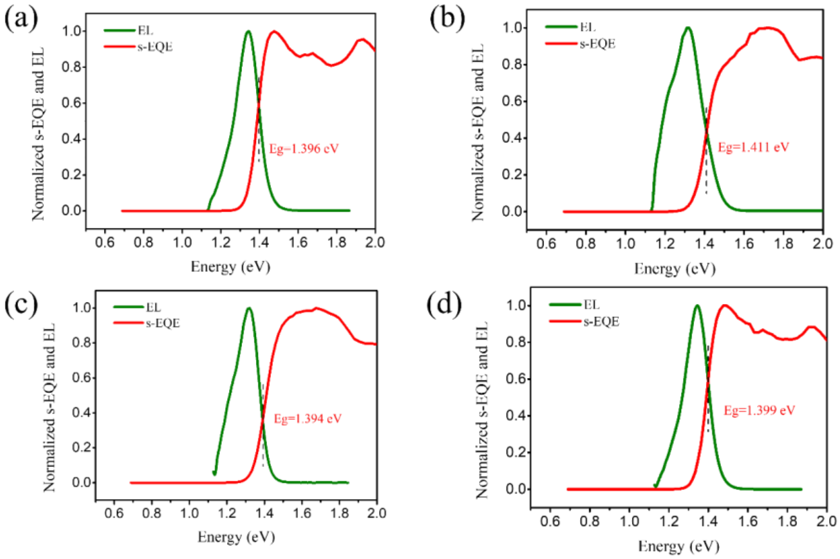

Figure 6.12. The normalized EL and the normalized s-EQE spectra of (a) PM6:BTP-eC9, (b) PM6:BTP-eC9:TB-S, (c) PM6:BTP-eC9:TB-S1, and (d) PM6:BTP-eC9:TB-S1-O.

To better understand the reason why the introduction of TB-S1-O can enhance device performance with higher V_{OC} whereas the incorporation of TB-S and TB-S1 result in inferior performance, the detailed energy loss E_{loss} was studied according to section 3.6.8. The schematic diagram is shown in **Figure 6.13g.**

The E_g values for blends are shown in **Table 6.2**. ΔE_{CT} was determined by the energetic difference between the singlet excited state and the CT state. E_{CT} was acquired from the intersection point of fitting s-EQE and EL curves by dual curve fitting based on Marcus theory as shown in **Figure 6.13a-b,d-e** [149, 150]. The ΔE_{CT} means the reduced voltage because of the CT process. The rest two parts of E_{loss} are radiative energy loss (ΔE_{rad}) and ΔE_{nonrad}. ΔE_{nonrad} is defined as $\Delta E_{nonrad} = -kT \ln(EQE_{EL})$, as shown in **Figure 6.13c**. Moreover, ΔE_{rad} can be calculated from the Equation 5.2. As summarized in the **Table 6.2**, PM6:BTP-eC9:TB-S1-O-based ternary device presents a lower E_{loss} of 0.542 eV than that of PM6:BTP-eC9-based device (0.559 eV). Whereas TB-S and TB-S1-based ternary devices perform higher E_{loss} than binary device which are 0.583 eV and 0.566 eV, respectively. It is well known that ΔE_{nonrad} is the main effect causing device voltage loss [87, 257]. An ΔE_{nonrad} of 0.228 eV is obtained for TB-S1-O doped ternary device which is lower than that of binary device (0.241 eV). Moreover, the introduction of TB-S and TB-S1 has the negative effect on the voltage losses resulting in larger ΔE_{nonrad}. This result implies that the third component TB-S1-O can disperse the aggregation of BTP-eC9 to mitigate aggregation-caused quenching leading to less ΔE_{nonrad} [260, 261]. Since TB-S1-O has a good compatibility with BTP-eC9, with increasing the third component content, the V_{OC}s of ternary devices increase with the content. As indicated in **Figure 6.14 and Table 6.3**, the V_{OC}s of ternary devices are tunable with the increase of the third component indicating the two similar acceptors tending to form alloy-like state [44, 262, 263]. **Table 6.4** summarizes the estimated E_{loss} for all binary devices.

The photoluminescence (PL) was performed to study the mechanism (energy transfer or charge transfer) for TB-S1-O promoting exciton dissociation and carrier transport for the host system. As shown in **Figure 6.15a**, the PL intensity of TB-S1-O is quenched while BTP-eC9 is introduced and the PL intensity of BTP-eC9 in the blended film increases compared with the neat BTP-eC9 film which implies that energy transfer[264] from TB-S1-O to BTP-eC9 occurs. From **Figure 6.15b,c**, it can be seen that when BTP-eC9 is added into TB-S1 and TB-S, respectively, the PL emissions of TB-S1 and TB-S in the blended films are quenched and the PL emissions of TB-S1 and TB-S in the blended films are lower than that of neat BTP-eC9 film, which implies that charge transfer[265] occurs from TB-S1 and TB-S to BTP-eC9, respectively.

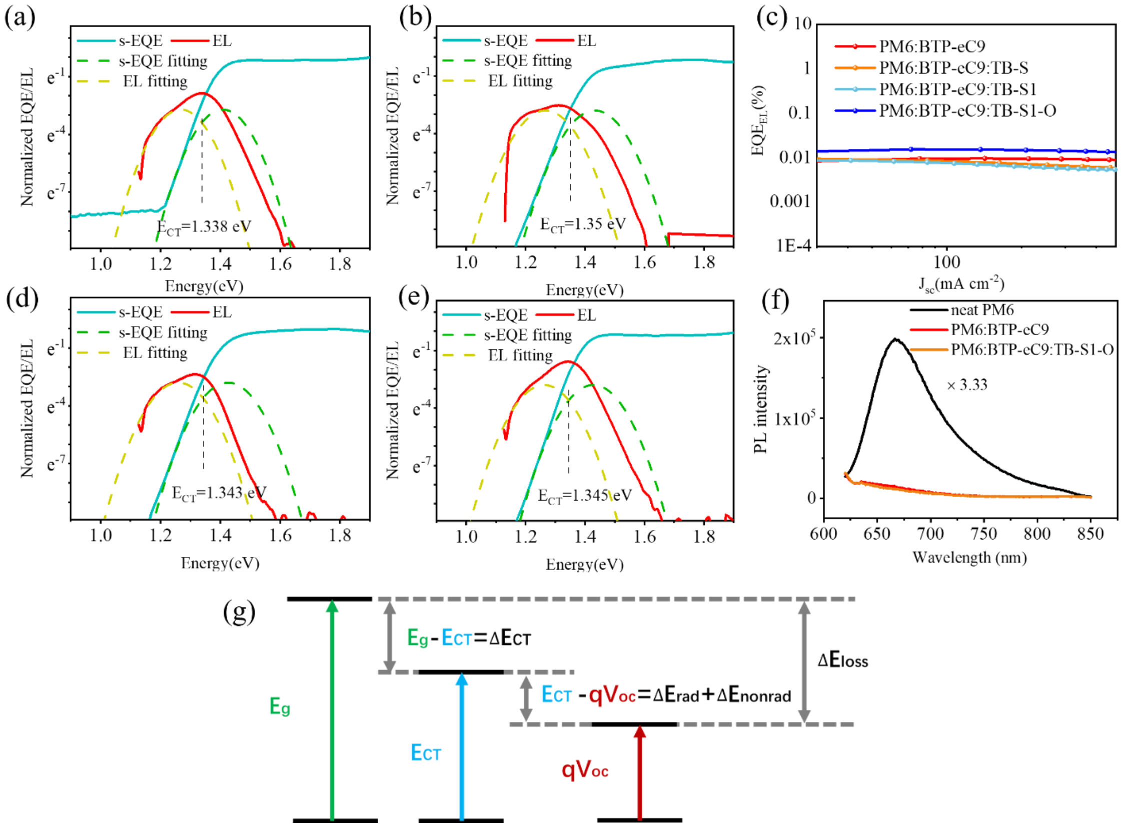

Figure 6.13. EL spectra and normalized s-EQE values of (a) PM6:BTP-eC9, (b) PM6:BTP-eC9:TB-S, (d) PM6:BTP-eC9:TB-S1, and (e) PM6:BTP-eC9:TB-S1-O. (c) EQE$_{EL}$ values of the devices. (f) The PL spectra of binary device PM6:BTP-eC9 and ternary device PM6:BTP-eC9:TB-S1-O. (g) Schematic diagram for energy losses of OSCs.

The quenching efficiency of PM6 emission in PM6:BTP-eC9:TB-S1-O blended film is higher than that of PM6:BTP-eC9 binary film, indicating that the introduction of TB-S1-O facilitated more efficient exciton dissociation. In terms of blended acceptors, if charge transfer occurs in two blended acceptors, the PL emission of TB-S1-O and BTP-eC9 will show quenched emissions [261, 266]. If the PL emission of TB-S1-O is quenched and that of BTP-eC9 is enhanced, indicating the existence of energy transfer mechanism [177, 267]. With increasing the doping content of TB-S1-O, the PL emission of BTP-eC9 increases and the PL emission of neat TB-S1-O is quenched, suggesting a possible energy transfer from TB-S1-O to BTP-eC9.

Table 6.4. V_{loss} for all binary devices.

Devices	V_{OC} (V)	E_g[a)] (eV)	E_{loss} (eV)
PM6:BTP-eC9	0.837	1.40	0.563
PM6:TB-S	0.949	1.47	0.521
PM6:TB-S1	1.030	1.57	0.540
PM6:TB-S1-O	1.120	1.62	0.500

a) E_g was estimated from the tangent line of the edge of absorption spectrum.

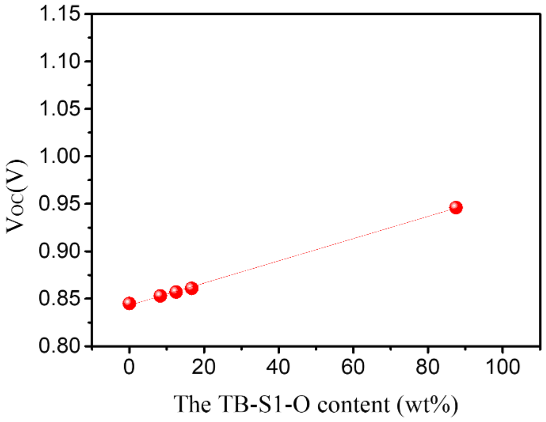

Figure 6.14. The evolution of V_{OC} of PM6:BTP-eC9:TB-S1-O based ternary devices by varying the blending ratio of TB-S1-O.

The alloy model mechanism describes that the guest material shows good compatibility with the host material resulting that the two components with similar electrical properties can form alloy state. Therefore, the energy level of alloy materials is able to be adjusted by adjusting the content of third component resulting in tunable V_{OC}[268, 269]. Compared with alloy model mechanism, the V_{OC} in the pure charge transfer model, pure energy transfer model, and pure parallel linkage model cannot be linearly adjusted.

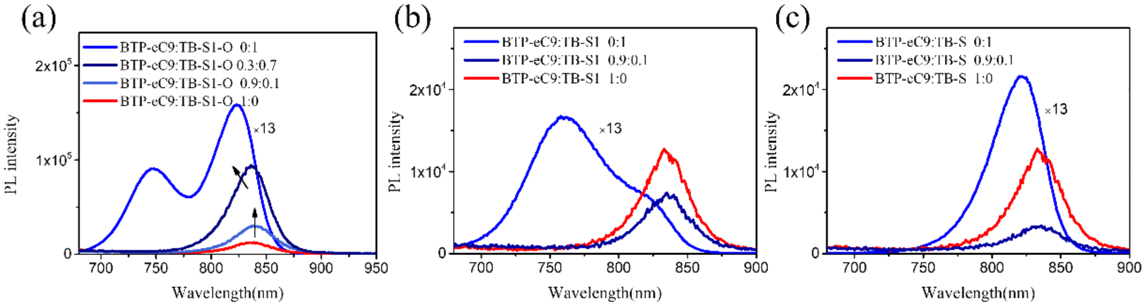

Figure 6.15. (a) The PL spectra of BTP-eC9:TB-S1-O films with different contents of TB-S1-O, under 550 nm light excitation.(b) The PL spectra of BTP-eC9:TB-S1 films with different contents of TB-S1, under 450 nm light excitation. (c) The PL spectra of BTP-eC9:TB-S films with different contents of TB-S, under 450 nm light excitation.

6.3.3 Morphology

The atomic force microscopy (AFM) and the transmission electron microscopy (TEM) were used to analyze the correlation between the morphology and device performance for binary and ternary films. The height and phase graphs are exhibited in **Figure 6.16a-h** for all the blended films. All the blended films possess small root-mean-square roughness (RMS) values which is good for the formation of compacted device, thereby facilitating charge transfer and collection.

PM6:BTP-eC9 film presents a nanofibrillar texture that is beneficial to exciton dissociation and transfer [262]. The doping of TB-S and TB-S1 into PM6:BTP-eC9 system produced smaller RMS values and smaller phase separation without obviously fibrillar structure owing to the impact of guest component for the molecular aggregation of host materials. The isolated domains can become the traps for free carriers owing to the over-mixed donor and acceptor phases.[258] Whereas the introduction of TB-S1-O into the binary system, the phase of film not only exhibited a smaller RMS value, but also possessed a better phase separation with an ideal interpenetrating biconticuous network which can facilitate exciton dissociation and free carrier transport [259].

As shown in **Figure 6.16i-l**, the results of TEM for PM6:BTP-eC9:TB-S1-O possesses enhanced nanoscale interconnecting networks than that of PM6:BTP-eC9 which is ascribed to the good compatibility between TB-S1-O and BTP-eC9. The better phase separation can facilitate mitigated charge recombination [270]. However, the incorporations of TB-S and TB-S1 showed blurry phase separation in the TEM because the self-aggregations of host materials have been interrupted, leading to severe carrier recombination and thus lower value of FF can be observed.

To figure out the molecular packing, structure ordering, and crystallinity of ASNF acceptors and their corresponding impact as the third component into the host system, grazing incidence wide-angle X-ray scattering (GIWAXS) measurements were adopted (as displayed in **Figure 6.18c-f and Figure 6.17**. **Figure 6.18a** displays out of plane (OOP) and in plane (IP) profiles of neat films for BTP-eC9, TB-S, TB-S1, and TB-S1-O. All neat films prefer to present face-on orientation which facilitates carrier transport.

As summarized in **Table 6.5**, The OOP (010) π-π distance and coherence length (CCL, according to Scherrer's equation[271]) for TB-S is 3.688 Å and 22.787 Å. For TB-S1, however, it exhibits weaker π-π stacking but longer CCL which are 3.718 Å and 24.822 Å, indicating that the replacement of terminal group results in weaker intermolecular interaction but bigger size of ordered domains. In addition, compared with TB-S1, TB-S1-O with the substation of alkoxy chain possesses the same π-π distance but significantly increased CCL (26.276 Å). This indicates that the substitution of alkoxy forms the additional conformation locking which is beneficial to form more orderly intermolecular packing and thus better morphology.

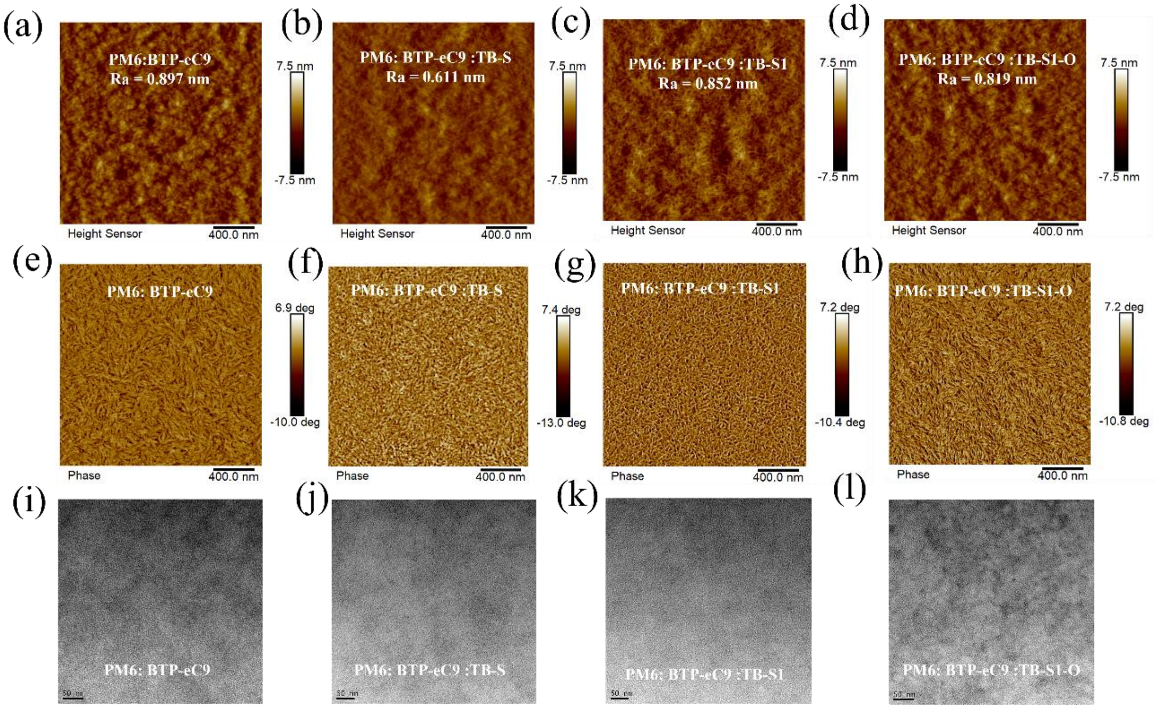

Figure 6.16. AFM height images of (a) PM6:BTP-eC9, (b) PM6:BTP-eC9:TB-S, (c) PM6:BTP-eC9:TB-S1, and (d) PM6:BTP-eC9:TB-S1-O. AFM phase images (e) PM6:BTP-eC9, (f) PM6:BTP-eC9:TB-S, (g) PM6:BTP-eC9:TB-S1, and (h) PM6:BTP-eC9:TB-S1-O. TEM images of (i) PM6:BTP-eC9, (j) PM6:BTP-eC9:TB-S, (k) PM6:BTP-eC9:TB-S1, and (l) PM6:BTP-eC9:TB-S1-O.

As indicated in **Table 6.6**, the IP (100) lamellar CCL of TB-S1-O is the largest (48.308 Å) among ASNF acceptors, indicating that TB-S1-O possessing additional conformation locking contributing to more ordered molecular packing. This deduction is consistent with the calculation of relaxed potential surface energy scans.

As shown in **Figure 6.18b**, all blended films possess face-on orientation. All ternary blended films show slightly enhanced π-π stacking (the peak at q =1.732 Å, π-π distance = 3.626 Å), whereas binary film produces π-π distance of 3.718 Å with the q of 1.689 Å. This implies that the doping of ASNF acceptors can induce enhanced π-π stacking for molecular packing.

The CCL are calculated to be 24.436 Å, 25.323 Å, 25.950 Å, and 25.528 Å for

PM6:BTP-eC9, PM6:BTP-eC9:TB-S, PM6:BTP-eC9:TB-S1, and PM6:BTP-eC9:TB-S1-O, respectively. The value of CCL corresponds the size of ordered domain where long-range ordering occurs[272]. Therefore, the doping of TB-S, TB-S1, and TB-S1-O acceptors caused larger ordered domains with less amorphous[273] evidenced by larger CCL in comparison with binary film, which is beneficial to carrier transport. Although TB-S and TB-S1 as guest components can induce larger ordered domains as well leading higher crystallinity, the poor nanoscale interconnecting networks displayed in AFM and TEM results inferior device performances. Only TB-S1-O based ternary film combines the advantages of enhanced π-π stacking, larger CCL, better phase separation with clear nanoscale interconnecting networks resulting in improved device performance.

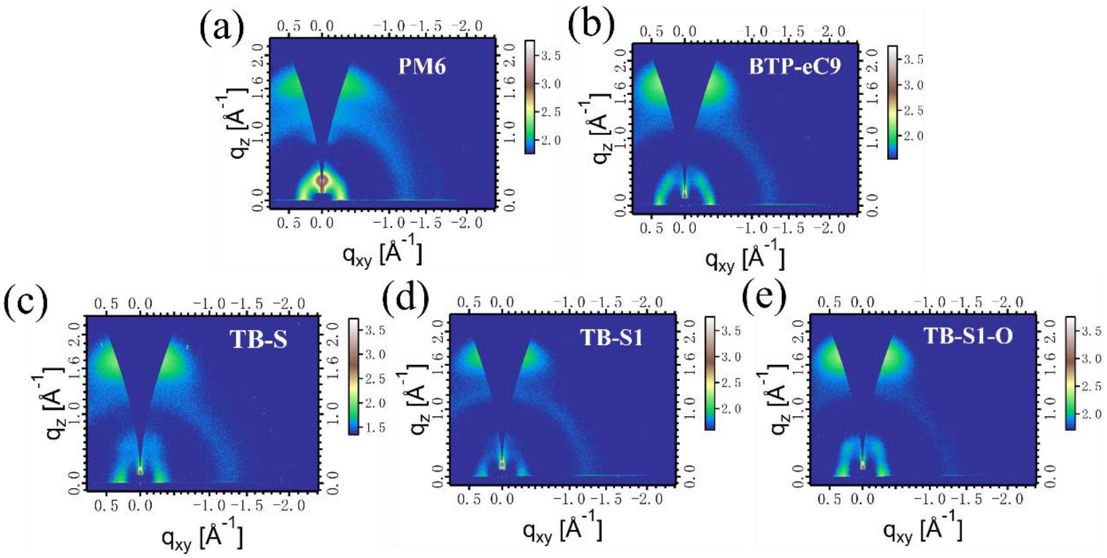

Figure 6.17. GIWAXS images of (a)PM6, (b)BTP-Ec9, and (c) TB-S(obtained from previous work)[2] (d) TB-S1, and (e) TB-S1-O.

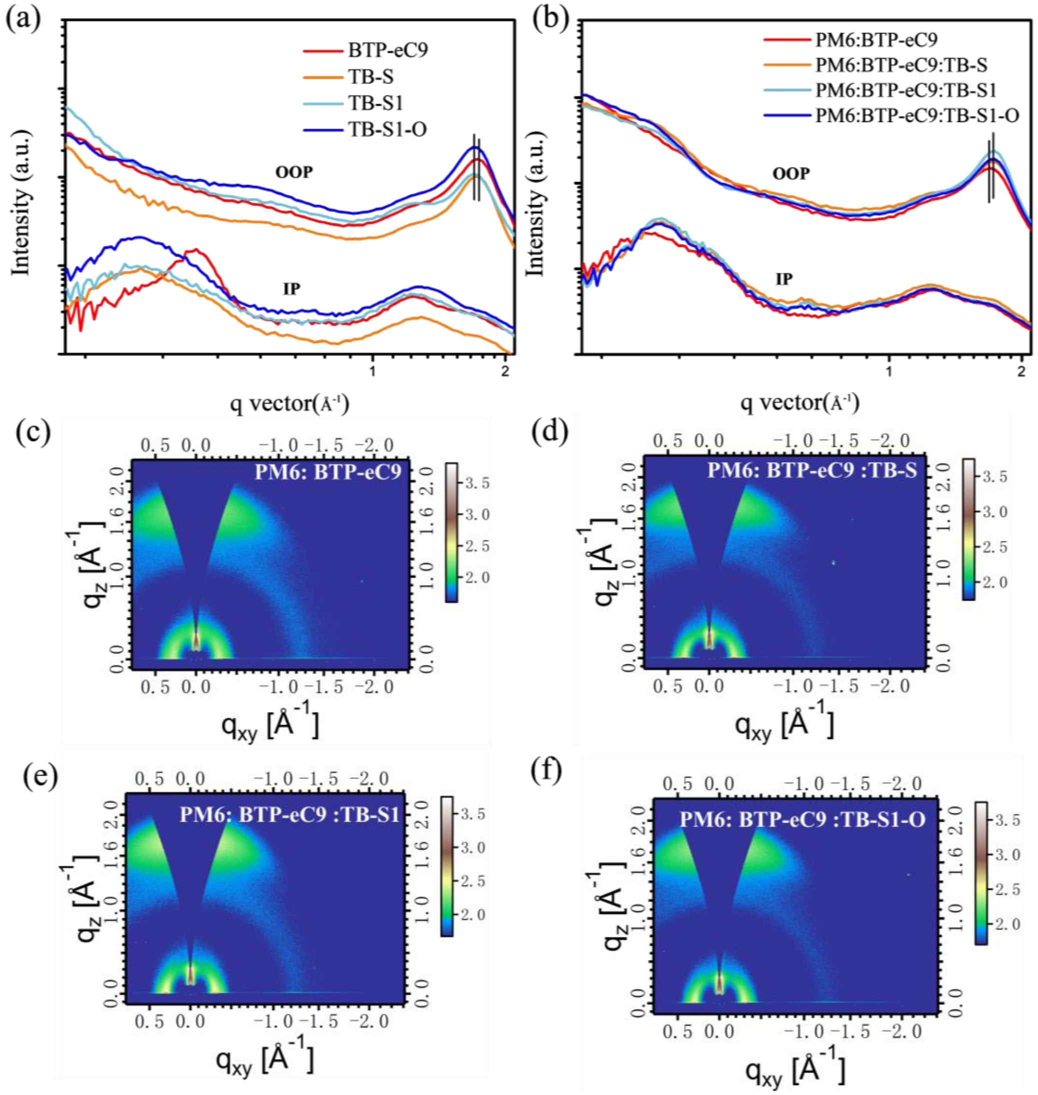

Figure 6.18. Out-of-plane and in-plane linecuts of 2D GIWAXS patterns for neat films (a) and (b) blended films. GIWAXS images of (c) PM6:BTP-eC9, (d)PM6:BTP-eC9:TB-S, (e) PM6: PM6:BTP-eC9:TB-S1, and (f) PM6:BTP-eC9:TB-S1-O.

Table 6.5. The diffraction vector (q) values of diffraction peaks, π-π distance, and FWHM crystal correlation lengths (CCLs) of neat films and the binary and ternary blend films along with out-of-plane direction.

	q($Å^{-1}$)	π-π distance (Å)	CCL (Å)	FWHM($Å^{-1}$)
PM6	1.647	3.813	22.920	0.274
BTP-eC9	1.732	3.626	23.878	0.263
TB-S	1.703	3.688	22.787	0.276
TB-S1	1.689	3.718	24.822	0.253
TB-S1-O	1.689	3.718	26.276	0.239
PM6: BTP-eC9	1.689	3.718	24.436	0.257
PM6: BTP-eC9:TB-S	1.732	3.626	25.323	0.248
PM6: BTP-eC9:TB-S1	1.732	3.626	25.950	0.243
PM6: BTP-eC9:TB-S1-O	1.732	3.626	25.528	0.246

Table 6.6. The diffraction vector (q) values of diffraction peaks, d spacing, and FWHM crystal correlation lengths (CCLs) of neat films and the binary and ternary blend films along with in-plane direction.

	q(Å^{-1})	d spacing (Å)	CCL (Å)	FWHM(Å^{-1})
PM6	0.288	21.806	60.971	0.103
BTP-eC9	0.397	15.819	68.261	0.092
TB-S	0.297	21.145	42.148	0.149
TB-S1	0.293	21.433	45.839	0.137
TB-S1-O	0.293	21.433	48.308	0.130
PM6: BTP-eC9	0.293	21.433	45.180	0.139
PM6: BTP-eC9:TB-S	0.304	20.658	66.105	0.095
PM6: BTP-eC9:TB-S1	0.304	20.658	68.261	0.092
PM6: BTP-eC9:TB-S1-O	0.304	20.658	67.527	0.093

6.4 Conclusion

In summary, a series ASNF acceptors, TB-S, TB-S1 and TB-S1-O, as the third components are introduced into the binary system PM6:BTP-eC9. The introduction of ASNF acceptor can induce smaller enhanced π-π stacking and more ordered molecular packing. Interestingly, only TB-S1-O based ternary device show improved performance and the reason is revealed in this work. The alkoxy substituted TB-S1-O with an additional non-covalent conformation locking, possesses a wide bandgap, good compatibility with the host materials, and stable planar conformation and larger ordered packing. TB-S1-O supplies a complementary absorption and energy transfer for BTP-eC9 increasing exciton generation and dissociation leading to high J_{SC}. The good compatibility between TB-S1-O and BTP-eC9 tends to form alloy-like acceptor phase, allowing the third component TB-S1-O to disperse the aggregation of BTP-eC9, and forming better phase separation with interpenetrating network structure and larger ordered domains to mitigate aggregation-caused quenching. Therefore, a reduction in ΔE_{nonrad} and an improvement in V_{OC} and J_{SC} can be observed in the PM6:BTP-eC9:TB-S1-O ternary device. Owing to the unstable conformation and incompatibility with BTP-eC9, the alkyl substituted TB-S and TB-S1 exhibit inferior morphologies in the ternary systems, leading to severe $\Delta E_{\mathrm{nonrad}}$ and carrier recombination, which reduces V_{OC} and FF. As a consequence, the ternary device based on PM6:BTP-eC9:TB-S1-O gives a significantly higher PCE of 18.14% than those of PM6:BTP-eC9:TB-S (16.16%) and PM6:BTP-eC9:TB-S1 devices (16.18%). The ternary strategy by introducing ASNF acceptor is the first time in the OPV and the correlation between molecular structure of the third component, active layer morphology and photovoltaic performance of the ternary device is carefully revealed, which gives a new point of view to in the ternary strategy to enhance device performance.

CHAPTER 7

Conclusion and future work

7.1 Synopsis

In conclusion, this study examined the potential of utilizing OPVs to utilize the irradiation under indoor and outdoor environment as a sustainable and renewable energy source to meet the growing global energy demand. The study proposed three main strategies to enhance the PCE of OPVs: (1) designing and synthesizing materials that match the spectrum wavelength (indoor or outdoor), (2) optimizing processing technology (C-BHJ and SD-BHJ) to improve carrier dissociation and collection, and enhance morphology, and (3) implementing a ternary strategy to incorporate a third material, which reduces non-radiative voltage loss, enhances stable planar conformation, and promotes ordered stacking domains.

7.2 Material design and processing optimization for both indoor and outdoor environment

A Y6's derivative, namely TB-4F, with blue-shifted absorption spectrum relative to Y6, and high EQE response, was designed and synthesized as an asymmetric acceptor with A−D1A′D2−A with a trade-off of absorption spectrum ranged from 600 to 850 nm and relatively high EQE. In this work, a novel asymmetric molecule TB-4F was synthesized to trade off absorption spectrum that can be applied indoor illuminated by both artificial light and sunlight. In the aspect of processing technology, the different technology will make different performance under solar light and artificial light. C-BHJ has been figured out that due to non-optimal morphology some carriers failed to be efficiently collected. Herein, SD-BHJ as an alternative fabrication method has successfully enhanced performance of OPVs, under both artificial light and sunlight, which was attributed to that favorable microstructure was vertically distributed in the active layer. PM6:TB-4F based OPVs were fabricated by C-BHJ and SD-BHJ, respectively. The optimal devices of PM6:TB-4F produced PCE of 14.44% and 15.24% for C-BHJ and SD-BHJ, respectively, under the illumination of AM1.5. There is not too much difference between C-BHJ and SD-BHJ. However, for 1000-lux LED illumination that produces low carrier density, devices showed PCE of 16.82% and 21.05% for C-BHJ and SD-BHJ, respectively. The PCE was significantly increased by 25% for SD-BHJ compared to C-BHJ under artificial light owing to the strong effect of trap-assisted recombination and dark current on PCE in the condition of low carrier density. Our result indicates that asymmetric molecule with blue-shifted spectrum fabricated by SD-BHJ can be a promising candidate which can be applied in the indoor environment to harvest sunlight and artificial light simultaneously.

7.3 Material design strategy via rational tuning of intermolecular and intramolecular interactions enabling high-efficiency indoor organic photovoltaics

IOPVs are one of promising candidates for transferring artificial illumination to power the IoT. However, their PCEs are limited by the fact that only a few efficient non-fullerene acceptors are available for IOPVs. Since Y6-series molecule has been figured out with a highly efficient performance owing to good phase separation, high charge carrier mobilities, and high external quantum efficiency (EQE), Y6-series molecule was chosen in this work to be reformed to better utilize the illumination of artificial light. Two design strategies are adopted in this work for high-efficiency IOPVs. **Strategy 1**: TB-SCl was designed and synthesized derived from symmetric BTP-2ThCl, the derivative of Y6, which produces higher V_{OC} and blue-shifted spectrum compared with Y6. Asymmetric backbone achieved by reducing a thiophene is chosen as the main chain inspired by numerous works showing that in comparison of symmetric analogue, asymmetric skeleton displayed higher FF and stronger intermolecular π-π stacking. **Strategy 2:** by modifying the terminals with a weaker acceptor (A) unit, removing chlorine in the thiophene-fused end groups from TB-SCl, TB-S was obtained. The study indicates that, in comparison with symmetric molecule BTP-2ThCl, asymmetric structure TB-SCl possesses a smaller intra-CT resulting in higher V_{OC} and strengthened inter-CT for neighboring acceptors resulting in more efficient carrier collection and thus higher FF. Moreover, the non-chlorine molecule TB-S exhibits smaller intra and inter-CT leading to further promoting V_{OC} but smaller *FF* compared with TB-SCl under 1-sun illumination. For TB-S based device, the trap state is mitigated, the leakage current is minimized, and non-radiative energy loss is suppressed. This allows for the novel acceptor TB-S to achieve high-efficiency rigid PCE of 23.3% under dim light condition, surpassing TB-SCl, and flexible PCE of 20.02%, one of the best PCEs for flexible IOPVs. Our findings demonstrate that modifying the molecule structure can enhance indoor photovoltaic performance.

7.4 Material design and ternary strategy

The asymmetric skeleton typed non-fullerene (ATNF) acceptors were adopted as the third component to study the impact of ATNF acceptors on the host system. This study can fill in the gap of ATNF as the third material in OSCs. In order to reveal the correlation between ASNF molecule's eigen-properties, active layer morphology, and photovoltaic performance of ternary OPV device, I synthesized two wider bandgap ASNF acceptors, named TB-S1 and TB-S1-O. Based on previous work, asymmetric skeleton-typed acceptor could be easily obtained by reducing one thiophene-ring of Y6 skeleton. Moreover, the ASNF possessed a stronger dipole moment, which is favorable to enhanced intermolecular interaction, thereby promoting the J_{SC} and *FF*. In addition, the alkoxy chains can have a significant impact on the electronic and morphological properties of OPV materials. First, it can upshift the LUMO and widen optical bandgap of the materials due to the electron-donating effect. Secondly, the oxygen atoms can provide intramolecular conformational locking effect, which could regulate the aggregation property of the material and thus change the morphology of the blend film. These three ASNF molecules, TB-S, TB-S1 and TB-S1-O, have similar skeletons but different terminal groups or alkyl/alkoxy side chains are incorporated into the host system PM6:BTP-eC9 as a third component, respectively. Introducing ASNF acceptor leads to smaller, enhanced π-π stacking and more ordered molecular packing. Notably, only the ternary device based on TB-S1-O shows improved performance, which is explained in this study. Compared to TB-S and TB-S1, TB-S1-O, which contains non-covalent conformational locking (O···H), has a more stable planar conformation, higher surface energy, and larger ordered stacking domain. As a result, the PM6:BTP-eC9:TB-S1-O device achieves the highest efficiency of 18.14%, surpassing devices based on PM6:BTP-eC9:TB-S (16.16%) and PM6:BTP-eC9:TB-S1 (16.18%). Additionally, only the PM6:BTP-eC9:TB-S1-O device maintains the positive effect of V_{OC} improvement by significantly reducing non-radiative voltage loss. Our study demonstrates that alkoxy substitution on the asymmetric backbone is an effective approach to construct high-performance ternary organic solar cells.

7.5 Future work

Over the last few decades, OPVs were viewed as a promising photovoltaic technology due to their reasonable PCE, low cost, and ease of processing. However, the main obstacles for OPVs to commercialize are high stability, large area processability, eco-compatible processability, and high efficiency. My future work will focus on development eco-compatible processable organic materials and improvement of stability of devices in the condition of air and strong illumination.

(1) Eco-compatible processability:

The commonly used solvents for high-performance OPV are chlorobenzene (CB) and CF, since they show superior dissolving capability for conjugated organic that is facilitate for the formation of organic material interaction and self-aggregation. Compared with CB and CF, o-xylene, 1,2,4-trimethylbenzene (1,2,4-TMB), and tetrahydrofuran (THF) are treated as relatively low toxic solvents but lower dissolving, which can be alternative solvents. However, the reports about eco-compatible solvent-processed are rare. In order to fulfill the requirements of practical production, the modification of acceptor molecules is necessary to make them acquire “suitable solubility” in eco-compatible solvent. Because the interaction between donor and acceptor in solvent is the key point for molecular pre-aggregation so that influent film morphology and thus device performance. Hence, I will modify alkyl side chains of Y6-dereivatives to tune their solubility in eco-compatible solvents to obtain high-efficiency OPVs.

(2) improvement of stability

Stability is a crucial factor for commercialization. OPV materials have poor stability under AM1.5 (strong illumination) which prevent them from entering the commercial market, despite several outstanding advantages such as their low cost, good flexibility, and transparency. Strong illumination and heat which come from solar irradiation are the two main reasons that cause OPV cells degradation and OPV performance decays. Therefore, stable molecule such as polymer molecule should be focused to improve OPVs stability under high temperature and can maintain high efficiency for a long time. Small organic molecules show advantages of batch-to-batch stability and consistent molecule weight which are critically important for large-scale fabrication. However, small molecules exhibit intrinsic disadvantages of thermal instability. Therefore, I focus on the development of polymer acceptor instead of small molecule acceptors in the future. Polymer acceptor in OPVs has been proved that it is useful to enhance stability. All polymer acceptors show advantage of inhibited degradation, aggregation and crystallization in the active layer. Naphthalene diimide (NDI)-based acceptors, such as poly[[N,N’-bis(2-octyldodecyl)-naph-thalene-1,4,5,8-bis(dicarboximide)-2,6-diyl-alt]-5,5’-(2,2’-bithiophene)] (N2200) attract lots of attentions as it exhibited high PCE and enhanced stability. Based on this, I will modify the molecules of N2200 derivatives by changing its skeleton so that increase device’s stability under the condition of air (high moisture) and high temperature (85℃).

Bibliography

1. Xie, L.; Lan, A.; Gu, Q.; Yang, S.; Song, W.; Ge, J.; Zhou, R.; Chen, Z.; Zhang, J.; Zhang, X.; Yang, D.; Tang, B.; Wu, T.; Ge, Z., Alkoxy Substitution on Asymmetric Conjugated Molecule Enabling over 18% Efficiency in Ternary Organic Solar Cells by Reducing Nonradiative Voltage Loss. *ACS Energy Letters* **2023,** *8* (1), 361-371.
2. Xie, L.; Zhang, J.; Song, W.; Ge, J.; Li, D.; Zhou, R.; Zhang, J.; Zhang, X.; Yang, D.; Tang, B.; Wu, T.; Ge, Z., Rational tuning of intermolecular and intramolecular interactions enabling high-efficiency indoor organic photovoltaics. *Nano Energy* **2022,** *99*, 107414.
3. Xie, L.; Zhang, J.; Song, W.; Hong, L.; Ge, J.; Wen, P.; Tang, B.; Wu, T.; Zhang, X.; Li, Y.; Ge, Z., Understanding the Effect of Sequential Deposition Processing for High-Efficient Organic Photovoltaics to Harvest Sunlight and Artificial Light. *ACS Appl Mater Interfaces* **2021,** *13* (17), 20405-20416.
4. Xie, L.; Song, W.; Ge, J.; Tang, B.; Zhang, X.; Wu, T.; Ge, Z., Recent progress of organic photovoltaics for indoor energy harvesting. *Nano Energy* **2021,** *82*, 105770.
5. Laboratory, N. R. Best Research-Cell Efficiency Chart. https://www.nrel.gov/pv/cell-efficiency.html.
6. Jørgensen, M.; Norrman, K.; Krebs, F. C., Stability/degradation of polymer solar cells. *Solar Energy Materials and Solar Cells* **2008,** *92* (7), 686-714.
7. Lee, T. D.; Ebong, A. U., A review of thin film solar cell technologies and challenges. *Renewable and Sustainable Energy Reviews* **2017,** *70*, 1286-1297.
8. Yan, C.; Barlow, S.; Wang, Z.; Yan, H.; Jen, A. K. Y.; Marder, S. R.; Zhan, X., Non-fullerene acceptors for organic solar cells. *Nature Reviews Materials* **2018,** *3* (3), 18003.
9. Li, Z.; Jiang, K.; Yang, G.; Lai, J. Y. L.; Ma, T.; Zhao, J.; Ma, W.; Yan, H., Donor polymer design enables efficient non-fullerene organic solar cells. *Nature Communications* **2016,** *7* (1), 13094.
10. Ouyang, X.; Peng, R.; Ai, L.; Zhang, X.; Ge, Z., Efficient polymer solar cells employing a non-conjugated small-molecule electrolyte. *Nature Photonics* **2015,** *9* (8), 520-524.
11. Qiu, N.; Yang, X.; Zhang, H.; Wan, X.; Li, C.; Liu, F.; Zhang, H.; Russell, T. P.; Chen, Y., Nonfullerene Small Molecular Acceptors with a Three-Dimensional (3D) Structure for Organic Solar Cells. *Chemistry of Materials* **2016,** *28* (18), 6770-6778.
12. Cheng, P.; Zhang, M.; Lau, T.-K.; Wu, Y.; Jia, B.; Wang, J.; Yan, C.; Qin, M.; Lu, X.; Zhan, X., Realizing Small Energy Loss of 0.55 eV, High Open-Circuit Voltage >1 V and High Efficiency >10% in Fullerene-Free Polymer Solar Cells via Energy Driver. *Advanced Materials* **2017,** *29* (11), 1605216.
13. Queisser, W. S. H. J., Detailed Balance Limit of Efficiency of p-n Junction Solar Cells. *Journal of Applied Physics* **1961,** *32*, 510-519.
14. Sun, R.; Wu, Y.; Yang, X.; Gao, Y.; Chen, Z.; Li, K.; Qiao, J.; Wang, T.; Guo, J.; Liu, C.; Hao, X.; Zhu, H.; Min, J., Single-Junction Organic Solar Cells with 19.17% Efficiency Enabled by Introducing One Asymmetric Guest Acceptor. *Advanced Materials* **2022,** *34* (26), 2110147.
15. Ma, L.-K.; Chen, Y.; Chow, P. C. Y.; Zhang, G.; Huang, J.; Ma, C.; Zhang, J.; Yin, H.; Hong Cheung, A. M.; Wong, K. S.; So, S. K.; Yan, H., High-Efficiency Indoor Organic Photovoltaics with a Band-Aligned Interlayer. *Joule* **2020,** *4* (7), 1486-1500.
16. Huang, H.; Yang, L.; Sharma, B., Recent advances in organic ternary solar cells. *Journal of Materials Chemistry A* **2017,** *5* (23), 11501-11517.
17. Kearns, D.; Calvin, M., Photovoltaic Effect and Photoconductivity in Laminated Organic Systems. *The Journal of Chemical Physics* **1958,** *29* (4), 950-951.
18. Tang, C. W., Two-layer organic photovoltaic cell. *Applied Physics Letters* **1986,** *48* (2), 183-185.
19. Jacobson, M. Z., Review of solutions to global warming, air pollution, and energy security. *Energy and Environmental Science* **2009,** *2* (2), 148-173.
20. Chow, J.; Kopp, R. J.; Portney, P. R., Energy Resources and Global Development. *Science* **2003,** *302* (5650), 1528-1531.

21. Bose, B. K., Global Warming: Energy, Environmental Pollution, and the Impact of Power Electronics. *IEEE Industrial Electronics Magazine* **2010,** *4* (1), 6-17.
22. Dincer, I., Renewable energy and sustainable development: a crucial review. *Renewable and Sustainable Energy Reviews* **2000,** *4* (2), 157-175.
23. Dai, S.; Zhan, X., Nonfullerene Acceptors for Semitransparent Organic Solar Cells. *Advanced Energy Materials* **2018,** *8* (21), 1800002.
24. Søndergaard, R.; Hösel, M.; Angmo, D.; Larsen-Olsen, T. T.; Krebs, F. C., Roll-to-roll Fabrication of Polymer Solar Cells. *Materials Today* **2012,** *15* (1), 36-49.
25. Kaltenbrunner, M.; White, M. S.; Głowacki, E. D.; Sekitani, T.; Someya, T.; Sariciftci, N. S.; Bauer, S., Ultrathin and lightweight organic solar cells with high flexibility. *Nature Communications* **2012,** *3* (1), 770.
26. Sun, C.; Xia, R.; Shi, H.; Yao, H.; Liu, X.; Hou, J.; Huang, F.; Yip, H.-L.; Cao, Y., Heat-Insulating Multifunctional Semitransparent Polymer Solar Cells. *Joule* **2018,** *2* (9), 1816-1826.
27. Virtuani, A.; Lotter, E.; Powalla, M., Influence of the light source on the low-irradiance performance of Cu(In,Ga)Se2 solar cells. *Solar Energy Materials and Solar Cells* **2006,** *90* (14), 2141-2149.
28. Yang, S.-S.; Hsieh, Z.-C.; Keshtov, M. L.; Sharma, G. D.; Chen, F.-C., Toward High-Performance Polymer Photovoltaic Devices for Low-Power Indoor Applications. *Solar RRL* **2017,** *1* (12), 1700174.
29. Wu, J.-L.; Chen, F.-C.; Chuang, M.-K.; Tan, K.-S., Near-infrared Laser-driven Polymer Photovoltaic Devices and Their Biomedical Applications. *Energy & Environmental Science* **2011,** *4* (9), 3374-3378.
30. Dennler, G.; Bereznev, S.; Fichou, D.; Holl, K.; Ilic, D.; Koeppe, R.; Krebs, M.; Labouret, A.; Lungenschmied, C.; Marchenko, A.; Meissner, D.; Mellikov, E.; Méot, J.; Meyer, A.; Meyer, T.; Neugebauer, H.; Öpik, A.; Sariciftci, N. S.; Taillemite, S.; Wöhrle, T., A self-rechargeable and flexible polymer solar battery. *Solar Energy* **2007,** *81* (8), 947-957.
31. Mathews, I.; Kantareddy, S. N.; Buonassisi, T.; Peters, I. M., Technology and Market Perspective for Indoor Photovoltaic Cells. *Joule* **2019,** *3* (6), 1415-1426.
32. Chen, F.-C., Emerging Organic and Organic/Inorganic Hybrid Photovoltaic Devices for Specialty Applications: Low-Level-Lighting Energy Conversion and Biomedical Treatment. *Advanced Optical Materials* **2019,** *7* (1), 1800662.
33. Freunek, M.; Freunek, M.; Reindl, L. M., Maximum efficiencies of indoor photovoltaic devices. *IEEE Journal of Photovoltaics* **2013,** *3* (1), 59-64.
34. Sacco, A.; Rolle, L.; Scaltrito, L.; Tresso, E.; Pirri, C. F., Characterization of photovoltaic modules for low-power indoor application. *Applied Energy* **2013,** *102*, 1295-1302.
35. Randall, J. F.; Jacot, J., Is AM1.5 applicable in practice? Modelling eight photovoltaic materials with respect to light intensity and two spectra. *Renewable Energy* **2003,** *28* (12), 1851-1864.
36. Randall, J. F., Designing Indoor Solar Products: Photovoltaic Technologies for AES. In *Designing Indoor Solar Products*, John Wiley & Sons, Ltd: 2005; pp 79-94.
37. Di Giacomo, F.; Zardetto, V.; Lucarelli, G.; Cinà, L.; Di Carlo, A.; Creatore, M.; Brown, T. M., Mesoporous perovskite solar cells and the role of nanoscale compact layers for remarkable all-round high efficiency under both indoor and outdoor illumination. *Nano Energy* **2016,** *30*, 460-469.
38. Conings, B.; Baeten, L.; Jacobs, T.; Dera, R.; D'Haen, J.; Manca, J.; Boyen, H. G., An easy-to-fabricate low-temperature TiO2 electron collection layer for high efficiency planar heterojunction perovskite solar cells. *APL Materials* **2014,** *2* (8), 081505.
39. De Rossi, F.; Pontecorvo, T.; Brown, T. M., Characterization of photovoltaic devices for indoor light harvesting and customization of flexible dye solar cells to deliver superior efficiency under artificial lighting. *Applied Energy* **2015,** *156*, 413-422.
40. Cutting, C. L.; Bag, M.; Venkataraman, D., Indoor light recycling: a new home for organic photovoltaics. *Journal of Materials Chemistry C* **2016,** *4* (43), 10367-10370.
41. Mathews, I.; Kantareddy, S. N. R.; Sun, S.; Layurova, M.; Thapa, J.; Correa-Baena, J.-P.; Bhattacharyya, R.; Buonassisi, T.; Sarma, S.; Peters, I. M., Self-Powered

Sensors Enabled by Wide-Bandgap Perovskite Indoor Photovoltaic Cells. *Advanced Functional Materials* **2019,** *29* (42), 1904072.

42. Ann, M. H.; Kim, J.; Kim, M.; Alosaimi, G.; Kim, D.; Ha, N. Y.; Seidel, J.; Park, N.; Yun, J. S.; Kim, J. H., Device design rules and operation principles of high-power perovskite solar cells for indoor applications. *Nano Energy* **2020,** *68*, 104321.

43. Gasparini, N.; Salleo, A.; McCulloch, I.; Baran, D., The role of the third component in ternary organic solar cells. *Nature Reviews Materials* **2019,** *4* (4), 229-242.

44. Doumon, N. Y.; Yang, L.; Rosei, F., Ternary organic solar cells: A review of the role of the third element. *Nano Energy* **2022,** *94*, 106915.

45. Li, M.; Zhou, Y.; Zhang, M.; Liu, Y.; Ma, Z.; Liu, F.; Qin, R.; Bo, Z., Ternary Strategy Enabling High-Performance Organic Solar Cells with Optimized Film Morphology and Reduced Nonradiative Energy Loss. *Solar RRL* **2021,** *5* (12), 2100806.

46. Bai, F.; Zhang, J.; Zeng, A.; Zhao, H.; Duan, K.; Yu, H.; Cheng, K.; Chai, G.; Chen, Y.; Liang, J.; Ma, W.; Yan, H., A highly crystalline non-fullerene acceptor enabling efficient indoor organic photovoltaics with high EQE and fill factor. *Joule* **2021,** *5* (5), 1231-1245.

47. Yu, L.; Stingelin, N., Controlling the solid-state microstructure of organic semiconducting materials by molecular compound formation. *Journal of Organic Semiconductors* **2013,** *1* (1), 16-21.

48. Halls, J. J. M.; Walsh, C. A.; Greenham, N. C.; Marseglia, E. A.; Friend, R. H.; Moratti, S. C.; Holmes, A. B., Efficient photodiodes from interpenetrating polymer networks. *Nature* **1995,** *376* (6540), 498-500.

49. Dang, M. T.; Hirsch, L.; Wantz, G., P3HT:PCBM, Best Seller in Polymer Photovoltaic Research. *Advanced Materials* **2011,** *23* (31), 3597-3602.

50. Lee, S.-H.; Kim, J.-H.; Shim, T.-H.; Park, J.-G., Effect of interface thickness on power conversion efficiency of polymer photovoltaic cells. *Electronic Materials Letters* **2009,** *5* (1), 47-50.

51. Hou, J.; Tan, Z. a.; Yan, Y.; He, Y.; Yang, C.; Li, Y., Synthesis and Photovoltaic Properties of Two-Dimensional Conjugated Polythiophenes with Bi(thienylenevinylene) Side Chains. *Journal of the American Chemical Society* **2006,** *128* (14), 4911-4916.

52. Huo, L.; Zhou, Y.; Li, Y., Alkylthio-Substituted Polythiophene: Absorption and Photovoltaic Properties. *Macromolecular Rapid Communications* **2009,** *30* (11), 925-931.

53. Qian, D.; Ye, L.; Zhang, M.; Liang, Y.; Li, L.; Huang, Y.; Guo, X.; Zhang, S.; Tan, Z. a.; Hou, J., Design, Application, and Morphology Study of a New Photovoltaic Polymer with Strong Aggregation in Solution State. *Macromolecules* **2012,** *45* (24), 9611-9617.

54. Xue, L.; Yang, Y.; Zhang, Z.-G.; Dong, X.; Gao, L.; Bin, H.; Zhang, J.; Yang, Y.; Li, Y., Indacenodithienothiophene–naphthalene diimide copolymer as an acceptor for all-polymer solar cells. *Journal of Materials Chemistry A* **2016,** *4* (16), 5810-5816.

55. Li, Y.; Zhong, L.; Wu, F.-P.; Yuan, Y.; Bin, H.-J.; Jiang, Z.-Q.; Zhang, Z.; Zhang, Z.-G.; Li, Y.; Liao, L.-S., Non-fullerene polymer solar cells based on a selenophene-containing fused-ring acceptor with photovoltaic performance of 8.6%. *Energy & Environmental Science* **2016,** *9* (11), 3429-3435.

56. Liu, Q.; Jiang, Y.; Jin, K.; Qin, J.; Xu, J.; Li, W.; Xiong, J.; Liu, J.; Xiao, Z.; Sun, K.; Yang, S.; Zhang, X.; Ding, L., 18% Efficiency organic solar cells. *Science Bulletin* **2020,** *65* (4), 272-275.

57. Yao, H.; Ye, L.; Zhang, H.; Li, S.; Zhang, S.; Hou, J., Molecular Design of Benzodithiophene-Based Organic Photovoltaic Materials. *Chem Rev* **2016,** *116* (12), 7397-457.

58. Zhang, M.; Guo, X.; Ma, W.; Ade, H.; Hou, J., A Large-Bandgap Conjugated Polymer for Versatile Photovoltaic Applications with High Performance. *Advanced Materials* **2015,** *27* (31), 4655-4660.

59. Fan, Q.; Zhu, Q.; Xu, Z.; Su, W.; Chen, J.; Wu, J.; Guo, X.; Ma, W.; Zhang, M.; Li, Y., Chlorine substituted 2D-conjugated polymer for high-performance polymer solar cells with 13.1% efficiency via toluene processing. *Nano Energy* **2018,** *48*, 413-420.

60. Zhou, Z.; Xu, S.; Song, J.; Jin, Y.; Yue, Q.; Qian, Y.; Liu, F.; Zhang, F.; Zhu, X., High-efficiency small-molecule ternary solar cells with a hierarchical morphology enabled by synergizing fullerene and non-fullerene acceptors. *Nature Energy* **2018,** *3* (11), 952-959.

61. He, Y.; Chen, H.-Y.; Hou, J.; Li, Y., Indene−C60 Bisadduct: A New Acceptor for High-Performance Polymer Solar Cells. *Journal of the American Chemical Society* **2010,** *132* (4), 1377-1382.

62. Lin, Y.; Wang, J.; Zhang, Z.-G.; Bai, H.; Li, Y.; Zhu, D.; Zhan, X., An Electron Acceptor Challenging Fullerenes for Efficient Polymer Solar Cells. **2015,** *27* (7), 1170-1174.

63. Li, C.; Xie, Y.; Fan, B.; Han, G.; Yi, Y.; Sun, Y., A nonfullerene acceptor utilizing a novel asymmetric multifused-ring core unit for highly efficient organic solar cells. *Journal of Materials Chemistry C* **2018,** *6* (18), 4873-4877.

64. Yin, H.; Yan, J.; Ho, J. K. W.; Liu, D.; Bi, P.; Ho, C. H. Y.; Hao, X.; Hou, J.; Li, G.; So, S. K., Observing electron transport and percolation in selected bulk heterojunctions bearing fullerene derivatives, non-fullerene small molecules, and polymeric acceptors. *Nano Energy* **2019,** *64*, 103950.

65. Ma, Y.; Cai, D.; Wan, S.; Wang, P.; Wang, J.; Zheng, Q., Ladder-Type Heteroheptacenes with Different Heterocycles for Nonfullerene Acceptors. *Angewandte Chemie International Edition* **2020,** *59* (48), 21627-21633.

66. Yuan, J.; Zhang, Y.; Zhou, L.; Zhang, G.; Yip, H.-L.; Lau, T.-K.; Lu, X.; Zhu, C.; Peng, H.; Johnson, P. A.; Leclerc, M.; Cao, Y.; Ulanski, J.; Li, Y.; Zou, Y., Single-Junction Organic Solar Cell with over 15% Efficiency Using Fused-Ring Acceptor with Electron-Deficient Core. *Joule* **2019,** *3* (4), 1140-1151.

67. Liu, S.; Yuan, J.; Deng, W.; Luo, M.; Xie, Y.; Liang, Q.; Zou, Y.; He, Z.; Wu, H.; Cao, Y., High-efficiency organic solar cells with low non-radiative recombination loss and low energetic disorder. *Nature Photonics* **2020,** *14* (5), 300-305.

68. Sutherland, B. R., Charging up Stationary Energy Storage. *Joule* **2019,** *3* (1), 1-3.

69. Cui, Y.; Yao, H.; Zhang, J.; Xian, K.; Zhang, T.; Hong, L.; Wang, Y.; Xu, Y.; Ma, K.; An, C.; He, C.; Wei, Z.; Gao, F.; Hou, J., Single-Junction Organic Photovoltaic Cells with Approaching 18% Efficiency. *Advanced Materials* **2020,** *32* (19), e1908205.

70. Kim, Y. J.; Hong, J.; Park, C. E., Schematic Studies on the Structural Properties and Device Physics of All Small Molecule Ternary Photovoltaic Cells. *ACS Applied Materials & Interfaces* **2015,** *7* (38), 21423-21432.

71. Ge, J.; Wei, Q.; Peng, R.; Zhou, E.; Yan, T.; Song, W.; Zhang, W.; Zhang, X.; Jiang, S.; Ge, Z., Improved Efficiency in All-Small-Molecule Organic Solar Cells with Ternary Blend of Nonfullerene Acceptor and Chlorinated and Nonchlorinated Donors. *ACS Applied Material Interfaces* **2019,** *11* (47), 44528-44535.

72. Dong, Y.; Zou, Y.; Yuan, J.; Yang, H.; Wu, Y.; Cui, C.; Li, Y., Ternary Polymer Solar Cells Facilitating Improved Efficiency and Stability. *Advanced Materials* **2019,** *31* (52), e1904601.

73. Yan, T.; Song, W.; Huang, J.; Peng, R.; Huang, L.; Ge, Z., 16.67% Rigid and 14.06% Flexible Organic Solar Cells Enabled by Ternary Heterojunction Strategy. *Advanced Materials* **2019,** *31* (39), e1902210.

74. Yan, X.; Wu, J.; Lv, J.; Zhang, L.; Zhang, R.; Guo, X.; Zhang, M., Highly efficient ternary solar cells with reduced non-radiative energy loss and enhanced stability via two compatible non-fullerene acceptors. *Journal of Materials Chemistry A* **2022,** *10* (29), 15605-15613.

75. He, C.; Pan, Y.; Ouyang, Y.; Shen, Q.; Gao, Y.; Yan, K.; Fang, J.; Chen, Y.; Ma, C.-Q.; Min, J.; Zhang, C.; Zuo, L.; Chen, H., Manipulating the D:A interfacial energetics and intermolecular packing for 19.2% efficiency organic photovoltaics. *Energy & Environmental Science* **2022**, 2537-2544.

76. Yan, T.; Song, W.; Huang, J.; Peng, R.; Huang, L.; Ge, Z., 16.67% Rigid and 14.06% Flexible Organic Solar Cells Enabled by Ternary Heterojunction Strategy. *Advanced Materials* **2019,** *31* (39), 1902210.

77. Duan, X.; Song, W.; Qiao, J.; Li, X.; Cai, Y.; Wu, H.; Zhang, J.; Hao, X.; Tang, Z.; Ge, Z.; Huang, F.; Sun, Y., Ternary strategy enabling high-efficiency rigid and flexible organic solar cells with reduced non-radiative voltage loss. *Energy & Environmental Science* **2022,** *15* (4), 1563-1572.

78. Yang, D.; Wang, Y.; Sano, T.; Gao, F.; Sasabe, H.; Kido, J., A minimal non-radiative recombination loss for efficient non-fullerene all-small-molecule organic solar cells with

a low energy loss of 0.54 eV and high open-circuit voltage of 1.15 V. *Journal of Materials Chemistry A* **2018,** *6* (28), 13918-13924.

79. Liu, J.; Chen, S.; Qian, D.; Gautam, B.; Yang, G.; Zhao, J.; Bergqvist, J.; Zhang, F.; Ma, W.; Ade, H.; Inganäs, O.; Gundogdu, K.; Gao, F.; Yan, H., Fast charge separation in a non-fullerene organic solar cell with a small driving force. *Nature Energy* **2016,** *1* (7), 16089.

80. Qian, D.; Zheng, Z.; Yao, H.; Tress, W.; Hopper, T. R.; Chen, S.; Li, S.; Liu, J.; Chen, S.; Zhang, J.; Liu, X.-K.; Gao, B.; Ouyang, L.; Jin, Y.; Pozina, G.; Buyanova, I. A.; Chen, W. M.; Inganäs, O.; Coropceanu, V.; Bredas, J.-L.; Yan, H.; Hou, J.; Zhang, F.; Bakulin, A. A.; Gao, F., Design rules for minimizing voltage losses in high-efficiency organic solar cells. *Nature Materials* **2018,** *17* (8), 703-709.

81. Wang, J.; Han, C.; Bi, F.; Huang, D.; Wu, Y.; Li, Y.; Wen, S.; Han, L.; Yang, C.; Bao, X.; Chu, J., Overlapping fasten packing enables efficient dual-donor ternary organic solar cells with super stretchability. *Energy & Environmental Science* **2021,** *14* (11), 5968-5978.

82. Bi, P.; Zhang, S.; Chen, Z.; Xu, Y.; Cui, Y.; Zhang, T.; Ren, J.; Qin, J.; Hong, L.; Hao, X.; Hou, J., Reduced non-radiative charge recombination enables organic photovoltaic cell approaching 19% efficiency. *Joule* **2021,** *5* (9), 2408-2419.

83. Yoon, S.; Park, S.; Park, S. H.; Nah, S.; Lee, S.; Lee, J.-W.; Ahn, H.; Yu, H.; Shin, E.-Y.; Kim, B. J.; Min, B. K.; Noh, J. H.; Son, H. J., High-performance scalable organic photovoltaics with high thickness tolerance from 1 cm2 to above 50 cm2. *Joule* **2022**.

84. Khlyabich, P. P.; Burkhart, B.; Thompson, B. C., Efficient Ternary Blend Bulk Heterojunction Solar Cells with Tunable Open-Circuit Voltage. *Journal of the American Chemical Society* **2011,** *133* (37), 14534-14537.

85. Huang, J.-S.; Goh, T.; Li, X.; Sfeir, M. Y.; Bielinski, E. A.; Tomasulo, S.; Lee, M. L.; Hazari, N.; Taylor, A. D., Polymer bulk heterojunction solar cells employing Förster resonance energy transfer. *Nature Photonics* **2013,** *7* (6), 479-485.

86. Zhang, G.; Zhang, K.; Yin, Q.; Jiang, X.-F.; Wang, Z.; Xin, J.; Ma, W.; Yan, H.; Huang, F.; Cao, Y., High-Performance Ternary Organic Solar Cell Enabled by a Thick Active Layer Containing a Liquid Crystalline Small Molecule Donor. *Journal of the American Chemical Society* **2017,** *139* (6), 2387-2395.

87. Li, Y.; Cai, Y.; Xie, Y.; Song, J.; Wu, H.; Tang, Z.; Zhang, J.; Huang, F.; Sun, Y., A facile strategy for third-component selection in non-fullerene acceptor-based ternary organic solar cells. *Energy & Environmental Science* **2021,** *14* (9), 5009-5016.

88. Shockley, W.; Queisser, H. J., Detailed Balance Limit of Efficiency of p-n Junction Solar Cells. *Journal of Applied Physics* **1961,** *32* (3), 510-519.

89. Teran, A. S.; Wong, J.; Lim, W.; Kim, G.; Lee, Y.; Blaauw, D.; Phillips, J. D., AlGaAs Photovoltaics for Indoor Energy Harvesting in mm-Scale Wireless Sensor Nodes. *IEEE Transactions on Electron Devices* **2015,** *62* (7), 2170-2175.

90. You, Y. J.; Song, C. E.; Hoang, Q. V.; Kang, Y.; Goo, J. S.; Ko, D. H.; Lee, J. J.; Shin, W. S.; Shim, J. W., Highly Efficient Indoor Organic Photovoltaics with Spectrally Matched Fluorinated Phenylene-Alkoxybenzothiadiazole-Based Wide Bandgap Polymers. *Advanced Functional Materials* **2019**.

91. Cui, Y.; Yao, H.; Zhang, T.; Hong, L.; Gao, B.; Xian, K.; Qin, J.; Hou, J., 1 cm(2) Organic Photovoltaic Cells for Indoor Application with over 20% Efficiency. *Adavnced Materials* **2019,** *31* (42), e1904512.

92. Li, Y.; Grabham, N. J.; Beeby, S. P.; Tudor, M. J., The effect of the type of illumination on the energy harvesting performance of solar cells. *Solar Energy* **2015,** *111*, 21-29.

93. Reich, N. H.; van Sark, W. G. J. H. M.; Alsema, E. A.; Lof, R. W.; Schropp, R. E. I.; Sinke, W. C.; Turkenburg, W. C., Crystalline silicon cell performance at low light intensities. *Solar Energy Materials and Solar Cells* **2009,** *93* (9), 1471-1481.

94. Cui, Y.; Wang, Y.; Bergqvist, J.; Yao, H.; Xu, Y.; Gao, B.; Yang, C.; Zhang, S.; Inganäs, O.; Gao, F.; Hou, J., Wide-gap non-fullerene acceptor enabling high-performance organic photovoltaic cells for indoor applications. *Nature Energy* **2019,** *4* (9), 768-775.

95. Mainville, M.; Leclerc, M., Recent Progress on Indoor Organic Photovoltaics: From Molecular Design to Production Scale. *ACS Energy Letters* **2020,** *5* (4), 1186-1197.

96. Lee, H. K. H.; Li, Z.; Durrant, J. R.; Tsoi, W. C., Is organic photovoltaics promising for indoor applications? *Applied Physics Letters* **2016,** *108* (25), 253301.
97. Gupta, V.; Kyaw, A. K. K.; Wang, D. H.; Chand, S.; Bazan, G. C.; Heeger, A. J., Barium: An Efficient Cathode Layer for Bulk-heterojunction Solar Cells. *Scientific Reports* **2013,** *3* (1), 1965.
98. Fukuhara, T.; Tamai, Y.; Ohkita, H., Nongeminate charge recombination in organic photovoltaics. *Sustainable Energy & Fuels* **2020**.
99. Elumalai, N. K.; Uddin, A., Open circuit voltage of organic solar cells: an in-depth review. *Energy & Environmental Science* **2016,** *9* (2), 391-410.
100. Je, H.-I.; Shin, E.-Y.; Lee, K. J.; Ahn, H.; Park, S.; Im, S. H.; Kim, Y.-H.; Son, H. J.; Kwon, S.-K., Understanding the Performance of Organic Photovoltaics under Indoor and Outdoor Conditions: Effects of Chlorination of Donor Polymers. *ACS Applied Materials & Interfaces* **2020,** *12* (20), 23181-23189.
101. Vandewal, K.; Tvingstedt, K.; Gadisa, A.; Inganäs, O.; Manca, J. V., On the origin of the open-circuit voltage of polymer–fullerene solar cells. *Nature Materials* **2009,** *8* (11), 904-909.
102. Vandewal, K.; Benduhn, J.; Nikolis, V. C., How to determine optical gaps and voltage losses in organic photovoltaic materials. *Sustainable Energy & Fuels* **2018,** *2* (3), 538-544.
103. Yang, W.; Luo, Y.; Guo, P.; Sun, H.; Yao, Y., Leakage Current Induced by Energetic Disorder in Organic Bulk Heterojunction Solar Cells: Comprehending the Ultrahigh Loss of Open-Circuit Voltage at Low Temperatures. *Physical Review Applied* **2017,** *7* (4), 044017.
104. Zhang, Z.-G.; Qi, B.; Jin, Z.; Chi, D.; Qi, Z.; Li, Y.; Wang, J., Perylene diimides: a thickness-insensitive cathode interlayer for high performance polymer solar cells. *Energy & Environmental Science* **2014,** *7* (6), 1966-1973.
105. Li, N.; Lassiter, B. E.; Lunt, R. R.; Wei, G.; Forrest, S. R., Open circuit voltage enhancement due to reduced dark current in small molecule photovoltaic cells. *Applied Physics Letters* **2009,** *94* (2), 023307.
106. Yin, H.; Ho, J. K. W.; Cheung, S. H.; Yan, R. J.; Chiu, K. L.; Hao, X.; So, S. K., Designing a ternary photovoltaic cell for indoor light harvesting with a power conversion efficiency exceeding 20%. *Journal of Materials Chemistry A* **2018,** *6* (18), 8579-8585.
107. Proctor, C. M.; Nguyen, T.-Q., Effect of leakage current and shunt resistance on the light intensity dependence of organic solar cells. *Applied Physics Letters* **2015,** *106* (8), 083301.
108. Steim, R.; Ameri, T.; Schilinsky, P.; Waldauf, C.; Dennler, G.; Scharber, M.; Brabec, C. J., Organic photovoltaics for low light applications. *Solar Energy Materials and Solar Cells* **2011,** *95* (12), 3256-3261.
109. Xu, X.; Yu, T.; Bi, Z.; Ma, W.; Li, Y.; Peng, Q., Realizing Over 13% Efficiency in Green-Solvent-Processed Nonfullerene Organic Solar Cells Enabled by 1,3,4-Thiadiazole-Based Wide-Bandgap Copolymers. *Advanced Materials* **2018,** *30* (3), 1703973.
110. Baran, D.; Kirchartz, T.; Wheeler, S.; Dimitrov, S.; Abdelsamie, M.; Gorman, J.; Ashraf, R. S.; Holliday, S.; Wadsworth, A.; Gasparini, N.; Kaienburg, P.; Yan, H.; Amassian, A.; Brabec, C. J.; Durrant, J. R.; McCulloch, I., Reduced voltage losses yield 10% efficient fullerene free organic solar cells with >1 V open circuit voltages. *Energy & Environmental Science* **2016,** *9* (12), 3783-3793.
111. Minnaert, B.; Veelaert, P., A Proposal for Typical Artificial Light Sources for the Characterization of Indoor Photovoltaic Applications. *Energies* **2014,** *7* (3), 1500-1516.
112. Janglin Chen, W. C., Mark Fihn, *Handbook of Visual Display Technology*. Springer: Berlin, Heidelberg, 2012.
113. Lee, H. K. H.; Wu, J.; Barbé, J.; Jain, S. M.; Wood, S.; Speller, E. M.; Li, Z.; Castro, F. A.; Durrant, J. R.; Tsoi, W. C., Organic photovoltaic cells – promising indoor light harvesters for self-sustainable electronics. *Journal of Materials Chemistry A* **2018,** *6* (14), 5618-5626.
114. Heo, Y.-J.; Jung, Y.-S.; Hwang, K.; Kim, J.-E.; Yeo, J.-S.; Lee, S.; Jeon, Y.-J.; Lee, D.; Kim, D.-Y., Small-Molecule Organic Photovoltaic Modules Fabricated via Halogen-Free Solvent System with Roll-to-Roll Compatible Scalable Printing Method. *ACS Applied Materials & Interfaces* **2017,** *9* (45), 39519-39525.
115. You, Y.-J.; Song, C. E.; Hoang, Q. V.; Kang, Y.; Goo, J. S.; Ko, D.-H.; Lee, J.-

J.; Shin, W. S.; Shim, J. W., Highly Efficient Indoor Organic Photovoltaics with Spectrally Matched Fluorinated Phenylene-Alkoxybenzothiadiazole-Based Wide Bandgap Polymers. *Advanced Functional Materials* **2019,** *29* (27), 1901171.
116. Mori, S.; Gotanda, T.; Nakano, Y.; Saito, M.; Todori, K.; Hosoya, M., Investigation of the organic solar cell characteristics for indoor LED light applications. *Japanese Journal of Applied Physics* **2015,** *54* (7), 071602.
117. Cui, Y.; Yao, H.; Zhang, T.; Hong, L.; Gao, B.; Xian, K.; Qin, J.; Hou, J., 1 cm2 Organic Photovoltaic Cells for Indoor Application with over 20% Efficiency. *Advanced Materials* **2019,** *31* (42), 1904512.
118. Shin, S.-C.; Koh, C. W.; Vincent, P.; Goo, J. S.; Bae, J.-H.; Lee, J.-J.; Shin, C.; Kim, H.; Woo, H. Y.; Shim, J. W., Ultra-thick semi-crystalline photoactive donor polymer for efficient indoor organic photovoltaics. *Nano Energy* **2019,** *58*, 466-475.
119. Wei, J.; Zhang, C.; Ji, G.; Han, Y.; Ismail, I.; Li, H.; Luo, Q.; Yang, J.; Ma, C.-Q., Roll-to-roll printed stable and thickness-independent ZnO:PEI composite electron transport layer for inverted organic solar cells. *Solar Energy* **2019,** *193*, 102-110.
120. Gasparini, N.; Salvador, M.; Heumueller, T.; Richter, M.; Classen, A.; Shrestha, S.; Matt, G. J.; Holliday, S.; Strohm, S.; Egelhaaf, H.-J.; Wadsworth, A.; Baran, D.; McCulloch, I.; Brabec, C. J., Polymer:Nonfullerene Bulk Heterojunction Solar Cells with Exceptionally Low Recombination Rates. *Advanced Energy Materials* **2017,** *7* (22), 1701561.
121. Zhang, K.; Chen, Z.; Armin, A.; Dong, S.; Xia, R.; Yip, H.-L.; Shoaee, S.; Huang, F.; Cao, Y., Efficient Large Area Organic Solar Cells Processed by Blade-Coating With Single-Component Green Solvent. *Solar RRL* **2018,** *2* (1), 1700169.
122. Small, C. E.; Tsang, S.-W.; Chen, S.; Baek, S.; Amb, C. M.; Subbiah, J.; Reynolds, J. R.; So, F., Loss Mechanisms in Thick-Film Low-Bandgap Polymer Solar Cells. *Advanced Energy Materials* **2013,** *3* (7), 909-916.
123. Lenes, M.; Koster, L. J. A.; Mihailetchi, V. D.; Blom, P. W. M., Thickness dependence of the efficiency of polymer:fullerene bulk heterojunction solar cells. *Applied Physics Letters* **2006,** *88* (24), 243502.
124. Ryu, H. S.; Park, S. Y.; Lee, T. H.; Kim, J. Y.; Woo, H. Y., Recent progress in indoor organic photovoltaics. *Nanoscale* **2020,** *12* (10), 5792-5804.
125. Lin, Y.; Wang, J.; Zhang, Z.-G.; Bai, H.; Li, Y.; Zhu, D.; Zhan, X., An Electron Acceptor Challenging Fullerenes for Efficient Polymer Solar Cells. *Advanced Materials* **2015,** *27* (7), 1170-1174.
126. Wadsworth, A.; Moser, M.; Marks, A.; Little, M. S.; Gasparini, N.; Brabec, C. J.; Baran, D.; McCulloch, I., Critical review of the molecular design progress in non-fullerene electron acceptors towards commercially viable organic solar cells. *Chemical Society Reviews* **2019,** *48* (6), 1596-1625.
127. Zhang, G.; Zhao, J.; Chow, P. C. Y.; Jiang, K.; Zhang, J.; Zhu, Z.; Zhang, J.; Huang, F.; Yan, H., Nonfullerene Acceptor Molecules for Bulk Heterojunction Organic Solar Cells. *Chemical Reviews* **2018,** *118* (7), 3447-3507.
128. Cheng, P.; Li, G.; Zhan, X.; Yang, Y., Next-generation organic photovoltaics based on non-fullerene acceptors. *Nature Photonics* **2018,** *12* (3), 131-142.
129. Lin, Y.; Zhang, Z.-G.; Bai, H.; Wang, J.; Yao, Y.; Li, Y.; Zhu, D.; Zhan, X., High-performance fullerene-free polymer solar cells with 6.31% efficiency. *Energy & Environmental Science* **2015,** *8* (2), 610-616.
130. Lin, Y.; He, Q.; Zhao, F.; Huo, L.; Mai, J.; Lu, X.; Su, C.-J.; Li, T.; Wang, J.; Zhu, J.; Sun, Y.; Wang, C.; Zhan, X., A Facile Planar Fused-Ring Electron Acceptor for As-Cast Polymer Solar Cells with 8.71% Efficiency. *Journal of the American Chemical Society* **2016,** *138* (9), 2973-2976.
131. Bi, P.; Hao, X., Versatile Ternary Approach for Novel Organic Solar Cells: A Review. *Solar RRL* **2019,** *3* (1), 1800263.
132. Lu, L.; Xu, T.; Chen, W.; Landry, E. S.; Yu, L., Ternary blend polymer solar cells with enhanced power conversion efficiency. *Nature Photonics* **2014,** *8* (9), 716-722.
133. Nam, M.; Cha, M.; Lee, H. H.; Hur, K.; Lee, K.-T.; Yoo, J.; Han, I. K.; Kwon, S. J.; Ko, D.-H., Long-term efficient organic photovoltaics based on quaternary bulk heterojunctions. *Nature Communications* **2017,** *8* (1), 14068.

134. Nam, M.; Noh, H. Y.; Cho, J.; Park, Y.; Shin, S.-C.; Kim, J.-A.; Kim, J.; Lee, H. H.; Shim, J. W.; Ko, D.-H., All-Day Operating Quaternary Blend Organic Photovoltaics. *Advanced Functional Materials* **2019,** *29* (16), 1900154.
135. Yu, R.; Yao, H.; Hou, J., Recent Progress in Ternary Organic Solar Cells Based on Nonfullerene Acceptors. *Advanced Energy Materials* **2018,** *8* (28), 1702814.
136. Ho, C. H. Y.; Cheung, S. H.; Li, H.-W.; Chiu, K. L.; Cheng, Y.; Yin, H.; Chan, M. H.; So, F.; Tsang, S.-W.; So, S. K., Using Ultralow Dosages of Electron Acceptor to Reveal the Early Stage Donor–Acceptor Electronic Interactions in Bulk Heterojunction Blends. *Advanced Energy Materials* **2017,** *7* (12), 1602360.
137. Costantini, J.-M.; Lelong, G.; Guillaumet, M.; Weber, W. J.; Takaki, S.; Yasuda, K., Color-center production and recovery in electron-irradiated magnesium aluminate spinel and ceria. *Journal of Physics: Condensed Matter* **2016,** *28* (32), 325901.
138. Nam, M.; Kang, J.-h.; Shin, J.; Na, J.; Park, Y.; Cho, J.; Kim, B.; Lee, H. H.; Chang, R.; Ko, D.-H., Ternary Organic Blend Approaches for High Photovoltaic Performance in Versatile Applications. *Advanced Energy Materials* **2019,** *9* (38), 1901856.
139. Wang, C.; Xu, X.; Zhang, W.; Dkhil, S. B.; Meng, X.; Liu, X.; Margeat, O.; Yartsev, A.; Ma, W.; Ackermann, J.; Wang, E.; Fahlman, M., Ternary organic solar cells with enhanced open circuit voltage. *Nano Energy* **2017,** *37*, 24-31.
140. Li, S.; Ye, L.; Zhao, W.; Zhang, S.; Mukherjee, S.; Ade, H.; Hou, J., Energy-Level Modulation of Small-Molecule Electron Acceptors to Achieve over 12% Efficiency in Polymer Solar Cells. *Advanced Materials* **2016,** *28* (42), 9423-9429.
141. Li, S.; Ye, L.; Zhao, W.; Zhang, S.; Ade, H.; Hou, J., Significant Influence of the Methoxyl Substitution Position on Optoelectronic Properties and Molecular Packing of Small-Molecule Electron Acceptors for Photovoltaic Cells. *Advanced Energy Materials* **2017,** *7* (17), 1700183.
142. Yang, K.; Liao, Q.; Koh, C. W.; Chen, J.; Su, M.; Zhou, X.; Tang, Y.; Wang, Y.; Zhang, Y.; Woo, H. Y.; Guo, X., Improved photovoltaic performance of a nonfullerene acceptor based on a benzo[b]thiophene fused end group with extended π-conjugation. *Journal of Materials Chemistry A* **2019,** *7* (16), 9822-9830.
143. Wang, W.; Zhao, B.; Cong, Z.; Xie, Y.; Wu, H.; Liang, Q.; Liu, S.; Liu, F.; Gao, C.; Wu, H.; Cao, Y., Nonfullerene Polymer Solar Cells Based on a Main-Chain Twisted Low-Bandgap Acceptor with Power Conversion Efficiency of 13.2%. *ACS Energy Letters* **2018,** *3* (7), 1499-1507.
144. Roncali, J., Molecular Engineering of the Band Gap of π-Conjugated Systems: Facing Technological Applications. *Macromolecular Rapid Communications* **2007,** *28* (17), 1761-1775.
145. Alamoudi, M. A.; Khan, J. I.; Firdaus, Y.; Wang, K.; Andrienko, D.; Beaujuge, P. M.; Laquai, F., Impact of Nonfullerene Acceptor Core Structure on the Photophysics and Efficiency of Polymer Solar Cells. *ACS Energy Letters* **2018,** *3* (4), 802-811.
146. Zhang, J.; Han, Y.; Zhang, W.; Ge, J.; Xie, L.; Xia, Z.; Song, W.; Yang, D.; Zhang, X.; Ge, Z., High-Efficiency Thermal-Annealing-Free Organic Solar Cells Based on an Asymmetric Acceptor with Improved Thermal and Air Stability. *ACS Applied Materials & Interfaces* **2020,** *12* (51), 57271-57280.
147. Luo, Z.; Ma, R.; Liu, T.; Yu, J.; Xiao, Y.; Sun, R.; Xie, G.; Yuan, J.; Chen, Y.; Chen, K.; Chai, G.; Sun, H.; Min, J.; Zhang, J.; Zou, Y.; Yang, C.; Lu, X.; Gao, F.; Yan, H., Fine-Tuning Energy Levels via Asymmetric End Groups Enables Polymer Solar Cells with Efficiencies over 17%. *Joule* **2020,** *4* (6), 1236-1247.
148. Braun, S.; Salaneck, W. R.; Fahlman, M., Energy-Level Alignment at Organic/Metal and Organic/Organic Interfaces. *Advanced Materials* **2009,** *21* (14-15), 1450-1472.
149. Cheng, Y.; Huang, B.; Huang, X.; Zhang, L.; Kim, S.; Xie, Q.; Liu, C.; Heumüller, T.; Liu, Z.; Zhang, Y.; Wu, F.; Yang, C.; Brabec, C. J.; Chen, Y.; Chen, L., Oligomer-Assisted Photoactive Layers Enable >18 % Efficiency of Organic Solar Cells. *Angewandte Chemie International Edition* **2022,** *61* (21), e202200329.
150. Vandewal, K.; Tvingstedt, K.; Gadisa, A.; Inganäs, O.; Manca, J. V., Relating the open-circuit voltage to interface molecular properties of donor:acceptor bulk heterojunction solar cells. *Physical Review B* **2010,** *81* (12), 125204.
151. Nilsson, S.; Bernasik, A.; Budkowski, A.; Moons, E., Morphology and Phase

Segregation of Spin-Casted Films of Polyfluorene/PCBM Blends. *Macromolecules* **2007,** *40* (23), 8291-8301.
152. Yang, L.; Song, X.; Yu, J.; Wang, H.; Zhang, Z.; Geng, R.; Cao, J.; Baran, D.; Tang, W., Tuning of the conformation of asymmetric nonfullerene acceptors for efficient organic solar cells. *Journal of Materials Chemistry A* **2019,** *7* (39), 22279-22286.
153. Chen, Y.; Bai, F.; Peng, Z.; Zhu, L.; Zhang, J.; Zou, X.; Qin, Y.; Kim, H. K.; Yuan, J.; Ma, L. K.; Zhang, J.; Yu, H.; Chow, P. C. Y.; Huang, F.; Zou, Y.; Ade, H.; Liu, F.; Yan, H., Asymmetric Alkoxy and Alkyl Substitution on Nonfullerene Acceptors Enabling High-Performance Organic Solar Cells. *Advanced Energy Materials* **2020,** *11* (3), 2003141.
154. Lu, T.; Chen, F., Multiwfn: A multifunctional wavefunction analyzer. *Journal of Computational Chemistry* **2012,** *33* (5), 580-592.
155. Rühle, K.; Kasemann, M. In *Approaching High Efficiency Wide Range Silicon Solar Cells*, 2013 IEEE 39th Photovoltaic Specialists Conference (PVSC), 16-21 June 2013; 2013; pp 2651-2654.
156. Ding, Z.; Zhao, R.; Yu, Y.; Liu, J., All-polymer Indoor Photovoltaics with High Open-circuit Voltage. *Journal of Materials Chemistry A* **2019,** *7* (46), 26533-26539.
157. Xie, L.; Song, W.; Ge, J.; Tang, B.; Zhang, X.; Wu, T.; Ge, Z., Recent progress of organic photovoltaics for indoor energy harvesting. *Nano Energy* **2021**, 105770.
158. Zhou, Y.; Khan, T. M.; Shim, J. W.; Dindar, A.; Fuentes-Hernandez, C.; Kippelen, B., All-plastic solar cells with a high photovoltaic dynamic range. *Journal of Materials Chemistry A* **2014,** *2* (10), 3492-3497.
159. Cui, Y.; Hong, L.; Hou, J., Organic Photovoltaic Cells for Indoor Applications: Opportunities and Challenges. *ACS Applied Materials & Interfaces* **2020,** *12* (35), 38815-38828.
160. Dennler, G.; Scharber, M. C.; Brabec, C. J., Polymer-Fullerene Bulk-Heterojunction Solar Cells. *Advanced Materials* **2009,** *21* (13), 1323-1338.
161. Huang, Y.; Kramer, E. J.; Heeger, A. J.; Bazan, G. C., Bulk Heterojunction Solar Cells: Morphology and Performance Relationships. *Chemical Reviews* **2014,** *114* (14), 7006-7043.
162. Sun, R.; Guo, J.; Sun, C.; Wang, T.; Luo, Z.; Zhang, Z.; Jiao, X.; Tang, W.; Yang, C.; Li, Y.; Min, J., A universal layer-by-layer solution-processing approach for efficient non-fullerene organic solar cells. *Energy & Environmental Science* **2019,** *12* (1), 384-395.
163. Yao, H.; Ye, L.; Hou, J.; Jang, B.; Han, G.; Cui, Y.; Su, G. M.; Wang, C.; Gao, B.; Yu, R.; Zhang, H.; Yi, Y.; Woo, H. Y.; Ade, H.; Hou, J., Achieving Highly Efficient Nonfullerene Organic Solar Cells with Improved Intermolecular Interaction and Open-Circuit Voltage. *Advanced Materials* **2017,** *29* (21), 1700254.
164. Zhang, J.; Kan, B.; Pearson, A. J.; Parnell, A. J.; Cooper, J. F. K.; Liu, X.-K.; Conaghan, P. J.; Hopper, T. R.; Wu, Y.; Wan, X.; Gao, F.; Greenham, N. C.; Bakulin, A. A.; Chen, Y.; Friend, R. H., Efficient non-fullerene organic solar cells employing sequentially deposited donor–acceptor layers. *Journal of Materials Chemistry A* **2018,** *6* (37), 18225-18233.
165. Cheng, P.; Hou, J.; Li, Y.; Zhan, X., Layer-by-Layer Solution-Processed Low-Bandgap Polymer-PC61BM Solar Cells with High Efficiency. *Advanced Energy Materials* **2014,** *4* (9), 1301349.
166. Weng, K.; Ye, L.; Zhu, L.; Xu, J.; Zhou, J.; Feng, X.; Lu, G.; Tan, S.; Liu, F.; Sun, Y., Optimized active layer morphology toward efficient and polymer batch insensitive organic solar cells. *Nature Communications* **2020,** *11* (1), 2855.
167. Nam, M.; Na, J.; Shin, J.; Lee, H. H.; Chang, R.; Ko, D.-H., Alternative sequential deposition for optimization-free multi-component organic bulk heterojunctions. *Nano Energy* **2020,** *74*, 104883.
168. Fu, H.; Gao, W.; Li, Y.; Lin, F.; Wu, X.; Son, J. H.; Luo, J.; Woo, H. Y.; Zhu, Z.; Jen, A. K.-Y., A Generally Applicable Approach Using Sequential Deposition to Enable Highly Efficient Organic Solar Cells. *Small Methods* **2020,** *4* (12), 2000687.
169. Sun, R.; Wu, Q.; Guo, J.; Wang, T.; Wu, Y.; Qiu, B.; Luo, Z.; Yang, W.; Hu, Z.; Guo, J.; Shi, M.; Yang, C.; Huang, F.; Li, Y.; Min, J., A Layer-by-Layer Architecture for Printable Organic Solar Cells Overcoming the Scaling Lag of Module Efficiency. *Joule* **2020,** *4* (2), 407-419.
170. Gao, W.; Ma, X.; An, Q.; Gao, J.; Zhong, C.; Zhang, F.; Yang, C., An asymmetrical fused-ring electron acceptor designed by a cross-conceptual strategy achieving

15.6% efficiency. *Journal of Materials Chemistry A* **2020,** *8* (29), 14583-14591.
171. Zhao, W.; Li, S.; Yao, H.; Zhang, S.; Zhang, Y.; Yang, B.; Hou, J., Molecular Optimization Enables over 13% Efficiency in Organic Solar Cells. *Journal of the American Chemical Society* **2017,** *139* (21), 7148-7151.
172. Li, C.; Fu, H.; Xia, T.; Sun, Y., Asymmetric Nonfullerene Small Molecule Acceptors for Organic Solar Cells. *Advanced Energy Materials* **2019,** *9* (25), 1900999.
173. Gao, W.; Liu, T.; Sun, R.; Zhang, G.; Xiao, Y.; Ma, R.; Zhong, C.; Lu, X.; Min, J.; Yan, H.; Yang, C., Dithieno[3,2-b:2′,3′-d]pyrrol-Fused Asymmetrical Electron Acceptors: A Study into the Effects of Nitrogen-Functionalization on Reducing Nonradiative Recombination Loss and Dipole Moment on Morphology. *Advanced Science* **2020,** *7* (5), 1902657.
174. Gao, W.; Zhang, M.; Liu, T.; Ming, R.; An, Q.; Wu, K.; Xie, D.; Luo, Z.; Zhong, C.; Liu, F.; Zhang, F.; Yan, H.; Yang, C., Asymmetrical Ladder-Type Donor-Induced Polar Small Molecule Acceptor to Promote Fill Factors Approaching 77% for High-Performance Nonfullerene Polymer Solar Cells. *Advanced Materials* **2018,** *30* (26), 1800052.
175. Zhang, H.; Yao, H.; Hou, J.; Zhu, J.; Zhang, J.; Li, W.; Yu, R.; Gao, B.; Zhang, S.; Hou, J., Over 14% Efficiency in Organic Solar Cells Enabled by Chlorinated Nonfullerene Small-Molecule Acceptors. *Advanced Materials* **2018,** *30* (28), 1800613.
176. Gao, W.; Liu, T.; Zhong, C.; Zhang, G.; Zhang, Y.; Ming, R.; Zhang, L.; Xin, J.; Wu, K.; Guo, Y.; Ma, W.; Yan, H.; Liu, Y.; Yang, C., Asymmetrical Small Molecule Acceptor Enabling Nonfullerene Polymer Solar Cell with Fill Factor Approaching 79%. *ACS Energy Letters* **2018,** *3* (7), 1760-1768.
177. Song, J.; Li, C.; Zhu, L.; Guo, J.; Xu, J.; Zhang, X.; Weng, K.; Zhang, K.; Min, J.; Hao, X.; Zhang, Y.; Liu, F.; Sun, Y., Ternary Organic Solar Cells with Efficiency >16.5% Based on Two Compatible Nonfullerene Acceptors. *Advanced Materials* **2019,** *31* (52), 1905645.
178. Bi, P.; Zheng, F.; Yang, X.; Niu, M.; Feng, L.; Qin, W.; Hao, X., Dual Förster resonance energy transfer effects in non-fullerene ternary organic solar cells with the third component embedded in the donor and acceptor. *Journal of Materials Chemistry A* **2017,** *5* (24), 12120-12130.
179. Baumann, A.; Lorrmann, J.; Rauh, D.; Deibel, C.; Dyakonov, V., A New Approach for Probing the Mobility and Lifetime of Photogenerated Charge Carriers in Organic Solar Cells Under Real Operating Conditions. *Advanced Materials* **2012,** *24* (32), 4381-4386.
180. McNeill, C. R.; Hwang, I.; Greenham, N. C., Photocurrent transients in all-polymer solar cells: Trapping and detrapping effects. *Journal of Applied Physics* **2009,** *106* (2), 024507.
181. Kyaw, A. K. K.; Wang, D. H.; Gupta, V.; Leong, W. L.; Ke, L.; Bazan, G. C.; Heeger, A. J., Intensity Dependence of Current–Voltage Characteristics and Recombination in High-Efficiency Solution-Processed Small-Molecule Solar Cells. *ACS Nano* **2013,** *7* (5), 4569-4577.
182. Khlyabich, P. P.; Burkhart, B.; Thompson, B. C., Compositional Dependence of the Open-Circuit Voltage in Ternary Blend Bulk Heterojunction Solar Cells Based on Two Donor Polymers. *Journal of the American Chemical Society* **2012,** *134* (22), 9074-9077.
183. Li, H.; Cao, J.; Zhou, Q.; Ding, L.; Wang, J., High-performance inverted PThTPTI:PC71BM solar cells. *Nano Energy* **2015,** *15*, 125-134.
184. Peng, R.; Liu, Z.; Guan, Q.; Hong, L.; Song, W.; Wei, Q.; Gao, P.; Huang, J.; Fan, X.; Wang, M.; Ge, Z., Highly efficient non-fullerene polymer solar cells enabled by novel non-conjugated small-molecule cathode interlayers. *Journal of Materials Chemistry A* **2018,** *6* (15), 6327-6334.
185. Lim, S. B.; Ji, C. H.; Oh, I. S.; Oh, S. Y., Reduced leakage current and improved performance of an organic photodetector using an ytterbium cathode interlayer. *Journal of Materials Chemistry C* **2016,** *4* (22), 4920-4926.
186. Liu, Y.; Zhao, J.; Li, Z.; Mu, C.; Ma, W.; Hu, H.; Jiang, K.; Lin, H.; Ade, H.; Yan, H., Aggregation and morphology control enables multiple cases of high-efficiency polymer solar cells. *Nature Communications* **2014,** *5* (1), 5293.
187. Jiang, K.; Wei, Q.; Lai, J. Y. L.; Peng, Z.; Kim, H. K.; Yuan, J.; Ye, L.; Ade, H.; Zou, Y.; Yan, H., Alkyl Chain Tuning of Small Molecule Acceptors for Efficient Organic Solar Cells. *Joule* **2019,** *3* (12), 3020-3033.

188. Kawashima, K.; Fukuhara, T.; Suda, Y.; Suzuki, Y.; Koganezawa, T.; Yoshida, H.; Ohkita, H.; Osaka, I.; Takimiya, K., Implication of Fluorine Atom on Electronic Properties, Ordering Structures, and Photovoltaic Performance in Naphthobisthiadiazole-Based Semiconducting Polymers. *Journal of the American Chemical Society* **2016,** *138* (32), 10265-10275.

189. Xie, L.; Zhang, J.; Song, W.; Hong, L.; Ge, J.; Wen, P.; Tang, B.; Wu, T.; Zhang, X.; Li, Y.; Ge, Z., Understanding the Effect of Sequential Deposition Processing for High-Efficient Organic Photovoltaics to Harvest Sunlight and Artificial Light. *ACS Applied Materials & Interfaces* **2021,** *13* (17), 20405-20416.

190. Ge, J.; Hong, L.; Ma, H.; Ye, Q.; Chen, Y.; Xie, L.; song, W.; Li, D.; Chen, Z.; Yu, K.; Zhang, J.; Wei, Z.; Huang, F.; Ge, Z., Asymmetric Substitution of End-Groups Triggers 16.34% Efficiency for All-Small-Molecule Organic Solar Cells. *Advanced Materials* **2022,** *34*, 10.1002/adma.202202752.

191. Song, W.; Yu, K.; Zhou, E.; Xie, L.; Hong, L.; Ge, J.; Zhang, J.; Zhang, X.; Peng, R.; Ge, Z., Crumple Durable Ultraflexible Organic Solar Cells with an Excellent Power-per-Weight Performance. *Matter* **2021,** *31* (30), 2102694.

192. Li, D.; Wang, J.; Xie, L.; Ge, J.; Zhou, R.; Gu, Q.; Yang, D.; Zhang, J.; Ge, Z., Crystallinity modulation of donors by heteroatom side-chain engineering and solvent additive achieving 14.3% all-small-molecule organic solar cells. *Journal of Materials Chemistry A* **2022,** *10* (17), 9635-9642.

193. Song, W.; Liu, Y.; Fanady, B.; Han, Y.; Xie, L.; Chen, Z.; Yu, K.; Peng, X.; Zhang, X.; Ge, Z., Ultra-flexible light-permeable organic solar cells for the herbal photosynthetic growth. *Nano Energy* **2021,** *86*, 106044.

194. Cui, Y.; Hong, L.; Zhang, T.; Meng, H.; Yan, H.; Gao, F.; Hou, J., Accurate photovoltaic measurement of organic cells for indoor applications. *Joule* **2021,** *5* (5), 1016-1023.

195. Gupta, V.; Kyaw, A. K.; Wang, D. H.; Chand, S.; Bazan, G. C.; Heeger, A. J., Barium: an efficient cathode layer for bulk-heterojunction solar cells. *Sci Rep* **2013,** *3*, 1965.

196. Li, X.; Luo, S.; Sun, H.; Sung, H. H.-Y.; Yu, H.; Liu, T.; Xiao, Y.; Bai, F.; Pan, M.; Lu, X.; Williams, I. D.; Guo, X.; Li, Y.; Yan, H., Medium band-gap non-fullerene acceptors based on a benzothiophene donor moiety enabling high-performance indoor organic photovoltaics. *Energy & Environmental Science* **2021,** *14* (8), 4555-4563.

197. Yang, S.-S.; Hsieh, Z.-C.; Keshtov, M. L.; Sharma, G. D.; Chen, F.-C., Toward High-Performance Polymer Photovoltaic Devices for Low-Power Indoor Applications. **2017,** *1* (12), 1700174.

198. Mori, S.; Gotanda, T.; Nakano, Y.; Saito, M.; Todori, K.; Hosoya, M., Investigation of the organic solar cell characteristics for indoor LED light applications. *Japanese Journal of Applied Physics* **2015,** *54* (7).

199. Cui, Y.; Yao, H.; Zhang, T.; Hong, L.; Gao, B.; Xian, K.; Qin, J.; Hou, J., 1 cm2 Organic Photovoltaic Cells for Indoor Application with over 20% Efficiency. **2019,** *31* (42), 1904512.

200. Gao, W.; Liu, T.; Li, J.; Xiao, Y.; Zhang, G.; Chen, Y.; Zhong, C.; Lu, X.; Yan, H.; Yang, C., Simultaneously increasing open-circuit voltage and short-circuit current to minimize the energy loss in organic solar cells via designing asymmetrical non-fullerene acceptor. *Journal of Materials Chemistry A* **2019,** *7* (18), 11053-11061.

201. Gao, W.; An, Q.; Zhong, C.; Luo, Z.; Ming, R.; Zhang, M.; Zou, Y.; Liu, F.; Zhang, F.; Yang, C., Designing an asymmetrical isomer to promote the LUMO energy level and molecular packing of a non-fullerene acceptor for polymer solar cells with 12.6% efficiency. *Chemical Science* **2018,** *9* (42), 8142-8149.

202. Zhang, J.; Han, Y.; Zhang, W.; Ge, J.; Xie, L.; Xia, Z.; Song, W.; Yang, D.; Zhang, X.; Ge, Z., High-Efficiency Thermal-Annealing-Free Organic Solar Cells Based on an Asymmetric Acceptor with Improved Thermal and Air Stability. *ACS Applied Material Interfaces* **2020,** *12* (51), 57271-57280.

203. Gao, W.; Fu, H.; Li, Y.; Lin, F.; Sun, R.; Wu, Z.; Wu, X.; Zhong, C.; Min, J.; Luo, J.; Woo, H. Y.; Zhu, Z.; Jen, A. K. Y., Asymmetric Acceptors Enabling Organic Solar Cells to Achieve an over 17% Efficiency: Conformation Effects on Regulating Molecular Properties and Suppressing Nonradiative Energy Loss. *Advanced Energy Materials* **2020,** *11* (4).

204. Zhang, J.; Li, Y.; Hu, H.; Zhang, G.; Ade, H.; Yan, H., Chlorinated Thiophene End Groups for Highly Crystalline Alkylated Non-Fullerene Acceptors toward Efficient Organic Solar Cells. *Chemistry of Materials* **2019,** *31* (17), 6672-6676.
205. Roy, P.; Jha, A.; Yasarapudi, V. B.; Ram, T.; Puttaraju, B.; Patil, S.; Dasgupta, J., Ultrafast bridge planarization in donor-pi-acceptor copolymers drives intramolecular charge transfer. *Nature Communications* **2017,** *8* (1), 1716.
206. Carsten, B.; Szarko, J. M.; Son, H. J.; Wang, W.; Lu, L.; He, F.; Rolczynski, B. S.; Lou, S. J.; Chen, L. X.; Yu, L., Examining the effect of the dipole moment on charge separation in donor-acceptor polymers for organic photovoltaic applications. *Journal Of The American Chemical Society* **2011,** *133* (50), 20468-75.
207. Yao, H.; Cui, Y.; Yu, R.; Gao, B.; Zhang, H.; Hou, J., Design, Synthesis, and Photovoltaic Characterization of a Small Molecular Acceptor with an Ultra-Narrow Band Gap. *Angew Chem Int Ed Engl* **2017,** *56* (11), 3045-3049.
208. Li, W.; Ye, L.; Li, S.; Yao, H.; Ade, H.; Hou, J., A High-Efficiency Organic Solar Cell Enabled by the Strong Intramolecular Electron Push-Pull Effect of the Nonfullerene Acceptor. *Advanced Materials* **2018,** *30* (16), e1707170.
209. Tautz, R.; Da Como, E.; Limmer, T.; Feldmann, J.; Egelhaaf, H. J.; von Hauff, E.; Lemaur, V.; Beljonne, D.; Yilmaz, S.; Dumsch, I.; Allard, S.; Scherf, U., Structural correlations in the generation of polaron pairs in low-bandgap polymers for photovoltaics. *Nature Communications* **2012,** *3,* 970.
210. Li, Z.; Zhu, Z.; Chueh, C. C.; Jo, S. B.; Luo, J.; Jang, S. H.; Jen, A. K., Rational Design of Dipolar Chromophore as an Efficient Dopant-Free Hole-Transporting Material for Perovskite Solar Cells. *Journal Of The American Chemical Society* **2016,** *138* (36), 11833-9.
211. Xia, Z.; Zhang, J.; Gao, X.; Song, W.; Ge, J.; Xie, L.; Zhang, X.; Liu, Z.; Ge, Z., Fine-Tuning the Dipole Moment of Asymmetric Non-Fullerene Acceptors Enabling Efficient and Stable Organic Solar Cells. *ACS Applied Materials & Interfaces* **2021,** *13* (20), 23983-23992.
212. Sajjad, M. T.; Ruseckas, A.; Samuel, I. D. W., Enhancing Exciton Diffusion Length Provides New Opportunities for Organic Photovoltaics. *Matter* **2020,** *3* (2), 341-354.
213. Lunt, R. R.; Benziger, J. B.; Forrest, S. R., Relationship between crystalline order and exciton diffusion length in molecular organic semiconductors. *Advanced Materials* **2010,** *22* (11), 1233-6.
214. Yao, H.; Qian, D.; Zhang, H.; Qin, Y.; Xu, B.; Cui, Y.; Yu, R.; Gao, F.; Hou, J., Critical Role of Molecular Electrostatic Potential on Charge Generation in Organic Solar Cells. *Chinese Journal of Chemistry* **2018,** *36* (6), 491-494.
215. Yao, H.; Cui, Y.; Qian, D.; Ponseca, C. S.; Honarfar, A.; Xu, Y.; Xin, J.; Chen, Z.; Hong, L.; Gao, B.; Yu, R.; Zu, Y.; Ma, W.; Chabera, P.; Pullerits, T.; Yartsev, A.; Gao, F.; Hou, J., 14.7% Efficiency Organic Photovoltaic Cells Enabled by Active Materials with a Large Electrostatic Potential Difference. *Journal of the American Chemical Society* **2019,** *141* (19), 7743-7750.
216. Kesava, S. V.; Fei, Z.; Rimshaw, A. D.; Wang, C.; Hexemer, A.; Asbury, J. B.; Heeney, M.; Gomez, E. D., Domain Compositions and Fullerene Aggregation Govern Charge Photogeneration in Polymer/Fullerene Solar Cells. *Advanced Energy Materials* **2014,** *4* (11).
217. Hu, Z.; Wang, J.; Wang, Z.; Gao, W.; An, Q.; Zhang, M.; Ma, X.; Wang, J.; Miao, J.; Yang, C.; Zhang, F., Semitransparent ternary nonfullerene polymer solar cells exhibiting 9.40% efficiency and 24.6% average visible transmittance. *Nano Energy* **2019,** *55,* 424-432.
218. Zhang, M.; Ming, R.; Gao, W.; An, Q.; Ma, X.; Hu, Z.; Yang, C.; Zhang, F., Ternary polymer solar cells with alloyed non-fullerene acceptor exhibiting 12.99% efficiency and 76.03% fill factor. *Nano Energy* **2019,** *59,* 58-65.
219. Yao, H.; Ye, L.; Hou, J.; Jang, B.; Han, G.; Cui, Y.; Su, G. M.; Wang, C.; Gao, B.; Yu, R.; Zhang, H.; Yi, Y.; Woo, H. Y.; Ade, H.; Hou, J., Achieving Highly Efficient Nonfullerene Organic Solar Cells with Improved Intermolecular Interaction and Open-Circuit Voltage. *Advanced Materials* **2017,** *29* (21).
220. Zhou, X.; Wu, H.; Lin, B.; Naveed, H. B.; Xin, J.; Bi, Z.; Zhou, K.; Ma, Y.; Tang, Z.; Zhao, C.; Zheng, Q.; Ma, Z.; Ma, W., Different Morphology Dependence for Efficient Indoor Organic Photovoltaics: The Role of the Leakage Current and Recombination

Losses. *ACS Applied Material Interfaces* **2021,** *13* (37), 44604-44614.
221. Cui, Y.; Hong, L.; Hou, J., Organic Photovoltaic Cells for Indoor Applications: Opportunities and Challenges. *ACS Applied Material Interfaces* **2020,** *12* (35), 38815-38828.
222. Chen, Z.; Wang, T.; Wen, Z.; Lu, P.; Qin, W.; Yin, H.; Hao, X.-T., Trap State Induced Recombination Effects on Indoor Organic Photovoltaic Cells. *ACS Energy Letters* **2021,** *6* (9), 3203-3211.
223. Sun, R.; Wang, W.; Yu, H.; Chen, Z.; Xia, X.; Shen, H.; Guo, J.; Shi, M.; Zheng, Y.; Wu, Y.; Yang, W.; Wang, T.; Wu, Q.; Yang, Y.; Lu, X.; Xia, J.; Brabec, C. J.; Yan, H.; Li, Y.; Min, J., Achieving over 17% efficiency of ternary all-polymer solar cells with two well-compatible polymer acceptors. *Joule* **2021,** *5* (6), 1548-1565.
224. Eisner, F. D.; Azzouzi, M.; Fei, Z.; Hou, X.; Anthopoulos, T. D.; Dennis, T. J. S.; Heeney, M.; Nelson, J., Hybridization of Local Exciton and Charge-Transfer States Reduces Nonradiative Voltage Losses in Organic Solar Cells. *Journal of the American Chemical Society* **2019,** *141* (15), 6362-6374.
225. Kozub, D. R.; Vakhshouri, K.; Orme, L. M.; Wang, C.; Hexemer, A.; Gomez, E. D., Polymer Crystallization of Partially Miscible Polythiophene/Fullerene Mixtures Controls Morphology. *Macromolecules* **2011,** *44* (14), 5722-5726.
226. Egerton, R. F. J. P. P., Electron Energy-Loss Spectroscopy in the Electron Microscope. **2011**.
227. Lee, H.; Park, C.; Sin, D. H.; Park, J. H.; Cho, K., Recent Advances in Morphology Optimization for Organic Photovoltaics. *Advanced Materials* **2018**, e1800453.
228. Luo, Z.; Liu, T.; Wang, Y.; Zhang, G.; Sun, R.; Chen, Z.; Zhong, C.; Wu, J.; Chen, Y.; Zhang, M.; Zou, Y.; Ma, W.; Yan, H.; Min, J.; Li, Y.; Yang, C., Reduced Energy Loss Enabled by a Chlorinated Thiophene-Fused Ending-Group Small Molecular Acceptor for Efficient Nonfullerene Organic Solar Cells with 13.6% Efficiency. *Advanced Energy Materials* **2019,** *9* (18).
229. He, C.; Pan, Y.; Ouyang, Y.; Shen, Q.; Gao, Y.; Yan, K.; Fang, J.; Chen, Y.; Ma, C.-Q.; Min, J.; Zhang, C.; Zuo, L.; Chen, H., Manipulating the D:A interfacial energetics and intermolecular packing for 19.2% efficiency organic photovoltaics. *Energy & Environmental Science* **2022**.
230. Zhang, J.; Zhang, Y.; Fang, J.; Lu, K.; Wang, Z.; Ma, W.; Wei, Z., Conjugated Polymer-Small Molecule Alloy Leads to High Efficient Ternary Organic Solar Cells. *Journal of the American Chemical Society* **2015,** *137* (25), 8176-83.
231. Chiu, M.-Y.; Jeng, U. S.; Su, M.-S.; Wei, K.-H., Morphologies of Self-Organizing Regioregular Conjugated Polymer/Fullerene Aggregates in Thin Film Solar Cells. *Macromolecules* **2009,** *43* (1), 428-432.
232. Chen, Z.; Song, W.; Yu, K.; Ge, J.; Zhang, J.; Xie, L.; Peng, R.; Ge, Z., Small-molecular donor guest achieves rigid 18.5% and flexible 15.9% efficiency organic photovoltaic via fine-tuning microstructure morphology. *Joule* **2021,** *5* (9), 2395-2407.
233. Song, W.; Fan, X.; Xu, B.; Yan, F.; Cui, H.; Wei, Q.; Peng, R.; Hong, L.; Huang, J.; Ge, Z., All-Solution-Processed Metal-Oxide-Free Flexible Organic Solar Cells with Over 10% Efficiency. *Advanced Materials* **2018,** *30* (26), 1800075.
234. Yao, H.; Hou, J., Recent Advances in Single-Junction Organic Solar Cells. *Angewandte Chemie International Edition* **2022,** *61* (37), e202209021.
235. Song, W.; Yu, K.; Zhou, E.; Xie, L.; Hong, L.; Ge, J.; Zhang, J.; Zhang, X.; Peng, R.; Ge, Z., Crumple Durable Ultraflexible Organic Solar Cells with an Excellent Power-per-Weight Performance. *Matter* **2021,** *31* (30), 2102694.
236. Xie, L.; Zhang, J.; Song, W.; Hong, L.; Ge, J.; Wen, P.; Tang, B.; Wu, T.; Zhang, X.; Li, Y.; Ge, Z., Understanding the Effect of Sequential Deposition Processing for High-Efficient Organic Photovoltaics to Harvest Sunlight and Artificial Light. *ACS Applied Material Interfaces* **2021,** *13* (17), 20405-20416.
237. Ye, Q.; Ge, J.; Li, D.; Chen, Z.; Shi, J.; Zhang, X.; Zhou, E.; Yang, D.; Ge, Z., Modulation of the Fluorination Site on Side-Chain Thiophene Improved Efficiency in All-Small-Molecule Organic Solar Cells. *ACS Applied Materials & Interfaces* **2022,** *14* (29), 33234-33241.
238. Riede, M.; Spoltore, D.; Leo, K., Organic Solar Cells—The Path to Commercial

Success. *Advanced Energy Materials* **2021,** *11* (1), 2002653.
239. Cui, Y.; Yao, H.; Zhang, J.; Xian, K.; Zhang, T.; Hong, L.; Wang, Y.; Xu, Y.; Ma, K.; An, C.; He, C.; Wei, Z.; Gao, F.; Hou, J., Single-Junction Organic Photovoltaic Cells with Approaching 18% Efficiency. *Advanced Materials* **2020,** *32* (19), e1908205.
240. Chen, Y.; Bai, F.; Peng, Z.; Zhu, L.; Zhang, J.; Zou, X.; Qin, Y.; Kim, H. K.; Yuan, J.; Ma, L.-K.; Zhang, J.; Yu, H.; Chow, P. C. Y.; Huang, F.; Zou, Y.; Ade, H.; Liu, F.; Yan, H., Asymmetric Alkoxy and Alkyl Substitution on Nonfullerene Acceptors Enabling High-Performance Organic Solar Cells. *Advanced Energy Materials* **2021,** *11* (3), 2003141.
241. Ge, J.; Hong, L.; Ma, H.; Ye, Q.; Chen, Y.; Xie, L.; Song, W.; Li, D.; Chen, Z.; Yu, K.; Zhang, J.; Wei, Z.; Huang, F.; Ge, Z., Asymmetric Substitution of End-Groups Triggers 16.34% Efficiency for All-Small-Molecule Organic Solar Cells. *Advanced Materials* **2022,** *34* (29), 2202752.
242. Liu, Y.; Liu, B.; Ma, C.-Q.; Huang, F.; Feng, G.; Chen, H.; Hou, J.; Yan, L.; Wei, Q.; Luo, Q.; Bao, Q.; Ma, W.; Liu, W.; Li, W.; Wan, X.; Hu, X.; Han, Y.; Li, Y.; Zhou, Y.; Zou, Y.; Chen, Y.; Liu, Y.; Meng, L.; Li, Y.; Chen, Y.; Tang, Z.; Hu, Z.; Zhang, Z.-G.; Bo, Z., Recent progress in organic solar cells (Part II device engineering). *Science China Chemistry* **2022,** *65* (8), 1457-1497.
243. Liu, Y.; Liu, B.; Ma, C.-Q.; Huang, F.; Feng, G.; Chen, H.; Hou, J.; Yan, L.; Wei, Q.; Luo, Q.; Bao, Q.; Ma, W.; Liu, W.; Li, W.; Wan, X.; Hu, X.; Han, Y.; Li, Y.; Zhou, Y.; Zou, Y.; Chen, Y.; Li, Y.; Chen, Y.; Tang, Z.; Hu, Z.; Zhang, Z.-G.; Bo, Z., Recent progress in organic solar cells (Part I material science). *Science China Chemistry* **2022,** *65* (2), 224-268.
244. Li, S.; Li, C.-Z.; Shi, M.; Chen, H., New Phase for Organic Solar Cell Research: Emergence of Y-Series Electron Acceptors and Their Perspectives. *ACS Energy Letters* **2020,** *5* (5), 1554-1567.
245. Li, S.; Zhan, L.; Jin, Y.; Zhou, G.; Lau, T.-K.; Qin, R.; Shi, M.; Li, C.-Z.; Zhu, H.; Lu, X.; Zhang, F.; Chen, H., Asymmetric Electron Acceptors for High-Efficiency and Low-Energy-Loss Organic Photovoltaics. *Advanced Materials* **2020,** *32* (24), 2001160.
246. Liu, T.; Zhang, Y.; Shao, Y.; Ma, R.; Luo, Z.; Xiao, Y.; Yang, T.; Lu, X.; Yuan, Z.; Yan, H.; Chen, Y.; Li, Y., Asymmetric Acceptors with Fluorine and Chlorine Substitution for Organic Solar Cells toward 16.83% Efficiency. *Advanced Functional Materials* **2020,** *30* (24), 2000456.
247. Luo, Z.; Gao, Y.; Lai, H.; Li, Y.; Wu, Z.; Chen, Z.; Sun, R.; Ren, J.; Zhang, C. e.; He, F.; Woo, H. Y.; Min, J.; Yang, C., Asymmetric Side-Chain Substitution Enables a 3D Network Acceptor with Hydrogen Bond Assisted Crystal Packing and Enhanced Electronic Coupling for Efficient Organic Solar Cells. *Energy & Environmental Science* **2022**, 4601-4611.
248. Feng, S.; Zhang, C. e.; Liu, Y.; Bi, Z.; Zhang, Z.; Xu, X.; Ma, W.; Bo, Z., Fused-Ring Acceptors with Asymmetric Side Chains for High-Performance Thick-Film Organic Solar Cells. *Advanced Materials* **2017,** *29* (42), 1703527.
249. Gao, W.; Fu, H.; Li, Y.; Lin, F.; Sun, R.; Wu, Z.; Wu, X.; Zhong, C.; Min, J.; Luo, J.; Woo, H. Y.; Zhu, Z.; Jen, A. K.-Y., Asymmetric Acceptors Enabling Organic Solar Cells to Achieve an over 17% Efficiency: Conformation Effects on Regulating Molecular Properties and Suppressing Nonradiative Energy Loss. *Advanced Energy Materials* **2021,** *11* (4), 2003177.
250. Zhan, L.; Li, S.; Li, Y.; Sun, R.; Min, J.; Chen, Y.; Fang, J.; Ma, C.-Q.; Zhou, G.; Zhu, H.; Zuo, L.; Qiu, H.; Yin, S.; Chen, H., Manipulating Charge Transfer and Transport via Intermediary Electron Acceptor Channels Enables 19.3% Efficiency Organic Photovoltaics. *Advanced Energy Materials* **2022,** *12*, 2201076.
251. Wu, H.; Bian, Q.; Zhao, B.; Zhao, H.; Wang, L.; Wang, W.; Cong, Z.; Liu, J.; Ma, W.; Gao, C., Effects of the Isomerized Thiophene-Fused Ending Groups on the Performances of Twisted Non-Fullerene Acceptor-Based Polymer Solar Cells. *ACS Applied Material Interfaces* **2020,** *12* (21), 23904-23913.
252. Zhu, J.; Xiao, Y.; Wang, J.; Liu, K.; Jiang, H.; Lin, Y.; Lu, X.; Zhan, X., Alkoxy-Induced Near-Infrared Sensitive Electron Acceptor for High-Performance Organic Solar Cells. *Chemistry of Materials* **2018,** *30* (12), 4150-4156.

253. Xu, Y.; Yao, H.; Ma, L.; Wu, Z.; Cui, Y.; Hong, L.; Zu, Y.; Wang, J.; Woo, H. Y.; Hou, J., Organic photovoltaic cells with high efficiencies for both indoor and outdoor applications. *Materials Chemistry Frontiers* **2021,** *5* (2), 893-900.
254. Shi, S.; Liao, Q.; Tang, Y.; Guo, H.; Zhou, X.; Wang, Y.; Yang, T.; Liang, Y.; Cheng, X.; Liu, F.; Guo, X., Head-to-Head Linkage Containing Bithiophene-Based Polymeric Semiconductors for Highly Efficient Polymer Solar Cells. *Advanced Materials* **2016,** *28* (45), 9969-9977.
255. Liu, Y.; Zhang, Z.; Feng, S.; Li, M.; Wu, L.; Hou, R.; Xu, X.; Chen, X.; Bo, Z., Exploiting Noncovalently Conformational Locking as a Design Strategy for High Performance Fused-Ring Electron Acceptor Used in Polymer Solar Cells. *Journal of the American Chemical Society* **2017,** *139* (9), 3356-3359.
256. Xu, L.; Tao, W.; Liu, H.; Ning, J.; Huang, M.; Zhao, B.; Lu, X.; Tan, S., Achieving 17.38% efficiency of ternary organic solar cells enabled by a large-bandgap donor with noncovalent conformational locking. *Journal of Materials Chemistry A* **2021,** *9* (19), 11734-11740.
257. He, D.; Zhao, F.; Wang, C.; Lin, Y., Non-Radiative Recombination Energy Losses in Non-Fullerene Organic Solar Cells. *Advanced Functional Materials* **2022,** *32* (19), 2111855.
258. Bartelt, J. A.; Beiley, Z. M.; Hoke, E. T.; Mateker, W. R.; Douglas, J. D.; Collins, B. A.; Tumbleston, J. R.; Graham, K. R.; Amassian, A.; Ade, H.; Fréchet, J. M. J.; Toney, M. F.; McGehee, M. D., The Importance of Fullerene Percolation in the Mixed Regions of Polymer–Fullerene Bulk Heterojunction Solar Cells. *Advanced Energy Materials* **2013,** *3* (3), 364-374.
259. Proctor, C. M.; Kher, A. S.; Love, J. A.; Huang, Y.; Sharenko, A.; Bazan, G. C.; Nguyen, T.-Q., Understanding Charge Transport in Molecular Blend Films in Terms of Structural Order and Connectivity of Conductive Pathways. *Advanced Energy Materials* **2016,** *6* (9), 1502285.
260. Yu, R.; Yao, H.; Cui, Y.; Hong, L.; He, C.; Hou, J., Improved Charge Transport and Reduced Nonradiative Energy Loss Enable Over 16% Efficiency in Ternary Polymer Solar Cells. *Advanced Materials* **2019,** *31* (36), 1902302.
261. Liu, Q.; Wang, Y.; Fang, J.; Liu, H.; Zhu, L.; Guo, X.; Gao, M.; Tang, Z.; Ye, L.; Liu, F.; Zhang, M.; Li, Y., Synergistically minimized nonradiative energy loss and optimized morphology achieved via the incorporation of small molecule donor in 17.7% efficiency ternary polymer solar cells. *Nano Energy* **2021,** *85*, 105963.
262. Lan, A.; Lv, Y.; Zhu, J.; Lu, H.; Do, H.; Chen, Z.-K.; Zhou, J.; Wang, H.; Chen, F.; Zhou, E., High-Performance Ternary Organic Solar Cells through Incorporation of a Series of A2-A1-D-A1-A2 Type Nonfullerene Acceptors with Different Terminal Groups. *ACS Energy Letters* **2022,** *7* (8), 2845-2855.
263. Liu, F.; Zhou, L.; Liu, W.; Zhou, Z.; Yue, Q.; Zheng, W.; Sun, R.; Liu, W.; Xu, S.; Fan, H.; Feng, L.; Yi, Y.; Zhang, W.; Zhu, X., Organic Solar Cells with 18% Efficiency Enabled by an Alloy Acceptor: A Two-in-One Strategy. *Advanced Materials* **2021,** *33* (27), 2100830.
264. Li, W.; Yan, Y.; Gong, Y.; Cai, J.; Cai, F.; Gurney, R. S.; Liu, D.; Pearson, A. J.; Lidzey, D. G.; Wang, T., Contrasting Effects of Energy Transfer in Determining Efficiency Improvements in Ternary Polymer Solar Cells. *Advanced Functional Materials* **2018,** *28* (5), 1704212.
265. Rao, A. D.; Murali, M. G.; Kesavan, A. V.; Ramamurthy, P. C., Experimental investigation of charge transfer, charge extraction, and charge carrier concentration in P3HT:PBD-DT-DPP:PC70BM ternary blend photovoltaics. *Solar Energy* **2018,** *174*, 1078-1084.
266. Xia, D.; Zhang, Z.; Zhao, C.; Wang, J.; Xia, J.; Chen, G.; Li, S.; Tang, Z.; You, S.; Li, W., Fullerene as an additive for increasing the efficiency of organic solar cells to more than 17%. *Journal of Colloid and Interface Science* **2021,** *601*, 70-77.
267. Gao, J.; Ma, X.; Xu, C.; Wang, X.; Son, J. H.; Jeong, S. Y.; Zhang, Y.; Zhang, C.; Wang, K.; Niu, L.; Zhang, J.; Woo, H. Y.; Zhang, J.; Zhang, F., Over 17.7% efficiency ternary-blend organic solar cells with low energy-loss and good thickness-tolerance. *Chemical Engineering Journal* **2022,** *428*, 129276.
268. Zhou, D.; You, W.; Xu, H.; Tong, Y.; Hu, B.; Xie, Y.; Chen, L., Recent progress in ternary organic solar cells based on solution-processed non-fullerene acceptors. *Journal of*

Materials Chemistry A **2020,** *8* (44), 23096-23122.

269. Wan, J.; Chen, Z.; Zeng, L.; Liao, X.; He, Q.; Liu, S.; Zhu, P.; Zhu, H.; Chen, Y., Realizing high-performance organic solar cells through precise control of HOMO driving force based on ternary alloy strategy. *Journal of Energy Chemistry* **2022,** *65*, 133-140.

270. Yang, D.; Yang, R.; Priya, S.; Liu, S., Recent Advances in Flexible Perovskite Solar Cells: Fabrication and Applications. *Angew. Chem. Int. Ed* **2019,** *58* (14), 4466-4483.

271. Smilgies, D. M., Scherrer grain-size analysis adapted to grazing-incidence scattering with area detectors. *Journal of Applied Crystallography* **2009,** *42* (6), 1030-1034.

272. Minassian-Saraga, L. T., Thin films including layers: terminology in relation to their preparation and characterization (IUPAC Recommendations 1994). *Pure and Applied Chemistry* **1994,** *66* (8), 1667-1738.

273. He, C.; Chen, Z.; Wang, T.; Shen, Z.; Li, Y.; Zhou, J.; Yu, J.; Fang, H.; Li, Y.; Li, S.; Lu, X.; Ma, W.; Gao, F.; Xie, Z.; Coropceanu, V.; Zhu, H.; Bredas, J.-L.; Zuo, L.; Chen, H., Asymmetric electron acceptor enables highly luminescent organic solar cells with certified efficiency over 18%. *Nature Communications* **2022,** *13* (1), 2598.